LUND UNIVERSITY

Laser Diagnostic Techniques with Ultra-High Repetition Rate for Studies in Combustion Environments

Olofsson, Jimmy

2007

Total number of authors:
1

Laser Diagnostic Techniques with Ultra-High Repetition Rate for Studies in Combustion Environments

Doctoral Thesis

Jimmy Olofsson

Division of Combustion Physics
Department of Physics

LUND UNIVERSITY

Lund 2007

Jimmy Olofsson
Division of Combustion Physics
Department of Physics
Lund University
P.O. Box 118
SE-211 00 Lund, Sweden

Abstract

When conducting laser based diagnostics in combustion environments it is often desirable to obtain temporally resolved information. This can be due to several factors such as combustion taking place in a turbulent flow field, flame propagation from a spark plug in an initially quiescent combustible mixture, or rapid, multi-point fuel consumption in a homogeneous charge as a result of compression ignition in an engine cycle. A multi-YAG laser cluster and a high-speed framing camera capable of recording sequences of up to eight image frames, and having a framing rate up to the megahertz range were originally set up for these types of studies. Within the framework of this thesis, further developments of this high-speed diagnostic system aiming at extending the wavelength palette and thus the range of detectable species, was carried out. In addition, the system was used for measurements with ultra-high repetition rates for the detection of different flame species in a variety of combustion devices.

The high-speed laser system was redesigned for the generation of laser radiation at 355 nm, in addition to the original 532 nm and 266 nm, and a successful feasibility test for high-speed formaldehyde planar laser-induced fluorescence (PLIF) was carried out for the new design. Moreover, a novel multi-dye laser cluster has been set up. By pumping each of the four dye lasers individually using the Nd:YAG lasers in the multi-YAG cluster, tunable laser radiation with an ultra-high repetition rate can be produced, without the drawback of either losses in laser pulse energy or significant deterioration of the beam intensity profile often occurring when a single dye laser is pumped at ultra-high repetition rates.

The multi-YAG and multi-dye laser clusters were used for high-speed visualization of the OH radical by means of planar laser-induced fluorescence in a low-swirl methane/air flame for tracking flame front movements over time while simultaneously measuring the flow-velocity field. Simultaneous high-speed OH visualization and imaging of the temperature field was also performed. The work carried out was a first step in the development of a detailed Large Eddy Simulation validation database for turbulent, premixed methane/air flames. High-speed OH PLIF using a single dye laser was employed in several other studies of the reaction

zone, including an investigation of the ignition properties of hot jets in explosive environments, a study of combustion processes in a pulse combustor, and an investigation of the governing processes leading to electrical signals in an ion-current sensor. The last of these also included high-speed fuel tracer LIF.

An alternative technique for flame studies involving measurement of the chemiluminescence from OH and CH in order to determine the equivalence ratio was investigated in terms of spatial and temporal resolution. The capability of the technique for resolving flame fronts was compared to reference measurements of OH PLIF. The tests showed that the spatial resolution in the depth direction suffered from line-of-sight detection, which significantly reduced the resolution. As the sensor was designed for monitoring spatial and temporal inhomogenities in mixtures within industrial gas turbine combustors, the temporal and spatial scales in such a combustor were evaluated using the high-speed laser diagnostic system for time-resolved visualization of OH. Also, fuel tracer PLIF was performed in order to visualize the fuel distribution in the combustor.

The multi-YAG laser cluster was used in several studies of combustion processes in a homogeneous charge compression ignition (HCCI) engine, involving both high-speed fuel tracer PLIF and formaldehyde PLIF, with the aim of studying different types of ignition control. Acetone was used as a fuel tracer in investigating the effects of combustion chamber geometry on combustion. In studies of spark-assisted HCCI operation, the engine was run on a fuel mixture containing n-heptane, which produces formaldehyde early in the cool-flame region. Formaldehyde can thus be used as a fuel marker, eliminating the need of an added fuel tracer in this situation.

Furthermore, three-dimensional imaging of formaldehyde in a laboratory flame as well as of Jet-A vapour in a slow non-reacting flow was demonstrated. This was achieved by rapidly scanning the laser sheet across a measurement volume spatially separating the eight laser pulses. A stack of closely spaced PLIF images was acquired by the framing camera, which could be used to re-create the three-dimensional shape of the investigated species by means of interpolation between the sheets.

List of Papers

I.   R. Sadanandan, D. Markus, R. Schießl, U. Maas, J. Olofsson, H. Seyfried, M. Richter, M. Aldén
Detailed investigation of ignition by hot gas jets
Proceedings of the Combustion Institute, 31: p. 719-726, 2007.

II.   A. Franke, W. Koban, J. Olofsson, C. Schulz, W. Bessler, R. Reinmann, A. Larsson, M. Aldén
Application of advanced laser diagnostics for the investigation of the ionization sensor signal in a combustion bomb
Applied Physics B, 81: p. 1135-1142, 2005.

III.   A, Lindholm, J. Olofsson, S.I. Möller, J. Hult, M. Aldén
Ignition, flame growth and extinction in premixed combustion dominated by a strongly oscillating flow field
In preparation.

IV.   P. Petersson, J. Olofsson, C. Brackmann, H. Seyfried, J. Zetterberg, M. Richter, M. Aldén, M. A. Linne, R. K. Cheng, A. Nauert, D. Geyer, A. Dreizler
Simultaneous PIV/OH PLIF, Rayleigh thermometry/OH PLIF and stereo PIV measurements in a low-swirl flame
Submitted to Applied Optics, LACSEA Feature Issue.

V.   Y. Hardalupas, M. Orain, C. S. Panoutsos, A.M.K.P. Taylor, J. Olofsson, H. Seyfried, M. Richter, J. Hult, M. Aldén, F. Hermann, J. Klingmann
Chemiluminescence sensor for local equivalence ratio of reacting mixtures of fuel and air (FLAMESEEK)
Applied Thermal Engineering, 24: p. 1619–1632, 2004.

VI.   H. Seyfried, J. Olofsson, J. Sjöholm, M. Richter, M. Aldén, A. Vressner, A. Hultqvist, B. Johansson
High-Speed PLIF Imaging for Investigation of Turbulence Effects on Heat Release Rates in HCCI Combustion
SAE Technical Report No. 2007-01-0521, 2007.

iv

VII.   J. Olofsson, M. Richter, M. Aldén, M. Augé
Development of High Temporally and Spatially (Three-Dimensional) Resolved Formaldehyde Measurements in Combustion Environments
Review of Scientific Instruments, 77, 013104, 2006.

VIII.   J. Olofsson, H. Seyfried, M. Richter, M. Aldén, A. Vressner, A. Hultqvist, B. Johansson, K. Lombaert
High-Speed LIF Imaging for Cycle-Resolved Formaldehyde Visualization in HCCI Combustion
SAE Technical Report No. 2005-01-0641, 2005.

IX.   M. Weinrotter, E. Wintner, K. Iskra, T. Neger, J. Olofsson, H. Seyfried, M. Aldén, M. Lackner, F. Winter, A. Vressner, A. Hultqvist, B. Johansson
Optical Diagnostics of Laser-Induced and Spark Plug-Assisted HCCI Combustion
SAE Technical Report No. 2005-01-0129, 2005.

Related Work

A.   Y. Hardalupas, M. Orain, C. S. Panoutsos, A.M.K.P. Taylor, J. Olofsson, H. Seyfried, M. Richter, J. Hult, M. Aldén
Chemiluminescence sensor for local equivalence ratio of reacting mixtures of liquid fuel vapour and air (MAST B LIQUID)
First International Conference on Gas Turbine Technologies, Brussels, Belgium, July 10-11, 2003.

B.   C. S. Panoutsos, Y. Hardalupas, A.M.K.P. Taylor, J. Olofsson, H. Seyfried, M. Richter, J. Hult, M. Aldén
Evaluation of the Spatial Response of a Chemiluminescence Sensor using OH PLIF
Proceedings of the European Combustion Meeting (ECM), Orléans, France, October 25-28, 2003.

C.   R. Sadanandan, D. Markus, M. Spilling, R. Schiessl, U. Maas, J. Olofsson, H. Seyfried, M. Richter, M. Aldén
Observation of the transmission of gas explosions through narrow gaps using time–resolved laser/Schlieren techniques
Loss Prevention Conference, 2004.

D.   K-J. Nogenmyr, P. Petersson, X. S. Bai, A. Nauert, J. Olofsson, C. Brackman, H. Seyfried, J. Zetterberg, Z.S. Li, M. Richter, A. Dreizler, M. Linne, M. Aldén
Large Eddy Simulation and experiments of stratified lean premixed methane/air turbulent flames
Proceedings of the Combustion Institute, 31: p. 1467-1475, 2007.

E.   R.X. Yu, X.S. Bai, A. Vressner, A. Hultqvist, B. Johansson, J. Olofsson, H. Seyfried, J. Sjöholm, M. Richter, M. Aldén
Effect of Turbulence on HCCI Combustion
SAE Technical Report No. 2007-01-0183, 2007.

Contents

Chapter 1

Introduction

During the past year, issues concerning human related impact on global climate have climbed once again to the top of the international political agenda. Still in the beginning of the 21st century, the predominant source of energy in the world is based on one of the oldest technologies known to man; combustion. Today more than 90% of the total global energy demands are met by combustion-related processes, and prognoses point to fossil fuels most likely remaining the dominant energy source in the coming decades. Oil, coal, and natural gas alone satisfy some 80% of the energy demands, a fact which is clearly problematical since resources of these fuels are limited [1,2]. In addition, combustion processes have a negative impact on the environment due to emissions of e.g. NOx, CO, particulate matter, and SOx. These emissions lead to air pollution and acid rain, which in turn affect our own health and that of other life forms. Recently, the attention has shifted to carbon-dioxide, CO_2, which is a natural product of the combustion of hydrocarbon fuels. The levels of CO_2 in the atmosphere are rising, and since CO_2 is a greenhouse gas, the increasing levels contribute to global warming [3]. New energy sources and alternative fuels, as well as the improvement of existing technologies in terms of fuel economy and pollutant reduction are of great interest and importance, and for this reason research on combustion aimed at improving our understanding of these processes is clearly needed.

Practical applications of combustion, such as internal combustion (IC) engines and gas turbine combustors, often involve turbulent flow fields in which the chemical reactions take place. Turbulence can be regarded as irregular motion in time and space, and such flows significantly improve the mixing of fuel and oxidizer, which in turn leads to increased efficiency of the combustion process. This is due to convection of the separate fluids flows into each other, as well as to an increase in the contact surfaces between them, which through molecular diffusion increases the mixing. Turbulence alone is a very complex phenomenon. Adding to this the chemistry involved, comprising thousands of reactions and the participation of several hundred different species results in a still further increase in complexity [4]. The characteristic time scales on which turbulence in reacting flows occurs usually

range from 10^{-2} to 10^{-5} seconds, whereas the chemical reactions occur on a broader time range. This is shown in Figure 1.1, redrawn from a similar diagram by Warnatz et al. [5]. In order to improve our knowledge of such processes, specialized measurement techniques are needed, able to cope with the harsh combustion environments. A high temporal resolution of the measurements is needed because of the rapid processes involved. It is also important that the influence the measurements have on the combustion process be kept at a minimum.
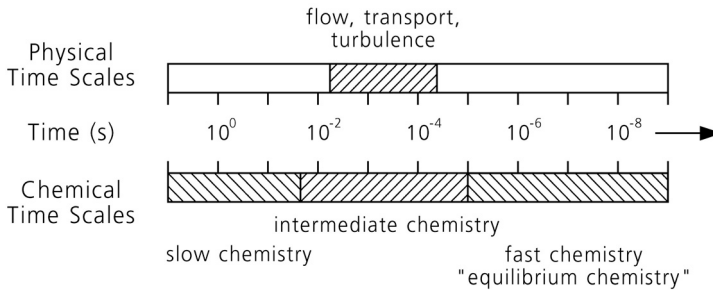
Figure 1.1 *Physical and chemical time scales in turbulent reacting flows.*

Laser diagnostic techniques have found widespread application in fields including medical diagnostics, environmental monitoring, and chemical processing, and have over the past decades proven to be suitable for applications also in combustion environments [6]. High spatial resolution can be achieved by focusing a laser beam to a small point and detecting the subsequent signal from this point. Pulsed lasers with a pulse duration in the range of 10 nanoseconds can be used to obtain a high temporal resolution. During this short period of time the combustion process can often be considered to be "frozen", meaning that measurements can be carried out faster than the characteristic time scales of the flow field and many reactions, thus making instantaneous measurements feasible. Measurements can also be made *in situ*, without their affecting the ongoing combustion significantly, provided appropriate methods are employed. Important combustion parameters such as temperature, species concentrations, and flow fields can be monitored by means of laser diagnostics [7,8]. There are certain disadvantages, however, with applications of this type. For example, optical access is required for the laser beam to be able to reach the combustion chamber, as well as for the detector to record the generated signal. This can be a problem particularly in production-type internal combustion devices in which some of the metal parts need to be replaced by glass counterparts in order to create small windows through which laser beams and signals can be directed in and out. Expensive and highly specialized equipment is needed to perform such measurements, and because of this, the techniques are often complicated to use,

requiring personnel with special skills to operate the systems employed. Despite these disadvantages, however, laser diagnostics is sometimes the only competitive alternative.

One important development in the field of laser based combustion diagnostics is that of two-dimensional visualization of fluorescence emission, planar laser-induced fluorescence (PLIF). The technique utilizes a laser beam expanded to a sheet of laser light to illuminate a thin slice of the combustion environment, the subsequent fluorescence being recorded perpendicular to the plane, often by use of an intensified CCD detector. Up until the late nineteen nineties, the technique has been more or less limited to single-shot registration or to repetition rates of up to about 100 Hz, which is clearly not sufficient for capturing the temporal evolution of turbulent combustion processes and rapidly propagating flames. However, such investigations are of great interest, and at the end of last century a laser and detector system capable of recording PLIF sequences with repetition rates of up to the megahertz range was set up for this type of studies [9]. Within the framework of the thesis, further development of this high-speed diagnostic system aimed at extending the wavelength palette, and thus the range of detectable species, as well as applications of the system to measurements involving ultra-high repetition rates for the detection of a number of flame species in a variety of combustion devices has been carried out.

Chapter 2 deals primarily with the background physics to the laser techniques employed in this work. The basic principles of laser-induces fluorescence are presented and how this technique can be used to monitor certain flame species is discussed. Chapter 3 deals with the experimental equipment involved. The high-speed laser diagnostic system is presented, together with different ways of utilizing it in practical applications for both two-dimensional and three-dimensional imaging. Various alternative approaches to high-speed measurements are likewise discussed. The combustion devices which were investigated using the high-speed diagnostic system are described briefly in Chapter 4. In Chapter 5 a selection of examples of applications and the results obtained, including investigations of the ignition properties of hot jets in explosive environments, flame front visualization in a low-swirl methane/air flame, characterization of temporal and spatial scales in a gas turbine combustor, cycle resolved fuel visualization in an internal combustion engine and three-dimensional imaging of formaldehyde in a flame, are presented. In Chapter 6 a brief summary of the work is provided, and some ideas concerning future developments and applications are discussed.

Chapter 2

Laser-Induced Fluorescence

This chapter deals with the basic principles of the laser diagnostic technique used in the experiments reported in the thesis, namely laser-induced fluorescence. A brief theoretical background to the technique is provided, after which a discussion regarding the probed species is given.

2.1   Laser-Induced Fluorescence Theory

Laser-induced fluorescence (LIF) has become a versatile tool in combustion diagnostics. It enables several different aspects of the combustion process to be studied, such as species distributions, flame front propagation and temperature fields. The technique utilizes laser radiation of well-defined wavelength to illuminate the part of the flame to be studied. If the wavelength of the laser radiation matches an energy transition in one of the molecules present, this molecule can absorb a photon and thereby becomes excited from a ground state level to a vibrational and rotational level in a higher electronic state. Due to collations between the molecules, an energy redistribution occurs immediately after the excitation, causing a population of closely lying rotational levels. Shortly thereafter, the molecules return to the ground state again, loosing part of their excess energy through spontaneous emission of radiation in the form of fluorescence. As a result of the energy redistribution, the fluorescence occurs not only at the excitation wavelength (resonant fluorescence), but also at other wavelengths, shifted mainly towards longer wavelengths. Detection of the fluorescence is generally done at the non-resonant wavelengths so as to minimize interference from scattered laser light. Since the absorption and fluorescence patterns are specific for each species, the technique allows for species-selective measurements. Another great advantage of LIF is the high sensitivity that can be achieved, due to the relatively large cross-sections of the resonant absorption process. This permits measurements of flame radical species to be made at sub-ppm levels. Moreover, the high level of sensitivity enables the laser beam to be expanded to form a laser sheet,

which in turn permits planar laser-induced fluorescence (PLIF) imaging to be carried out. This is often the case in combustion diagnostics [8].

   To describe the principles that apply to single-photon LIF, a simple two-energy-level model can be employed. The two-level system is shown in Figure 2.1, levels 1 and 2 being the lower and the upper energy level, respectively. The populations of these two levels are denoted as N_1 and N_2, respectively. The arrows, representing the processes connecting the two levels, are denoted by their corresponding rate constants.
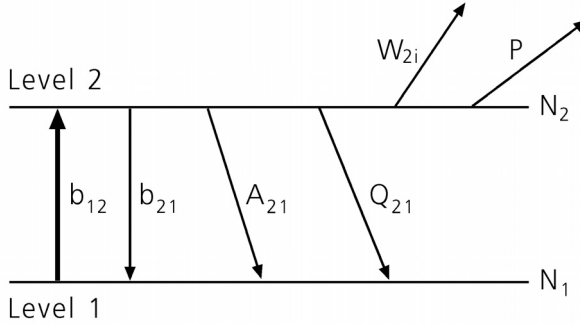
Figure 2.1 *A simple two-energy-level model used for explaining the basic principals of single-photon LIF.*

The rate constants for stimulated absorption and stimulated emission, denoted as b_{12} and b_{21}, are related to the Einstein coefficient for the corresponding process, B. The relation can be written as

$$b = \frac{BI_v}{c} \tag{2.1}$$

where I_v is the spectral irradiance of the incident laser light and c is the speed of light. The rate constant for spontaneous emission is denoted as A_{21} and is given by the Einstein A coefficient. Q_{21} represents the rate constant for collisional quenching. Finally, the last two arrows denoted as W_{2i} and P correspond to the rate constants for photo ionization and predissociation, respectively. The rate equations for the populations of the two levels can then be written as

$$\frac{dN_1}{dt} = -N_1 b_{12} + N_2 (b_{21} + A_{21} + Q_{21}) \tag{2.2}$$

$$\frac{dN_2}{dt} = N_1 b_{12} - N_2 (b_{21} + A_{21} + Q_{21} + P + W_{2i}) \tag{2.3}$$

These two loss terms are included in the model to provide a complete description of the two-level system. It should be noted, however, that the influence of the two is usually neglected. The reason for this simplification of the model is that photo ionization can be avoided by simply adjusting the laser power, and that most excited states are not predissociative. It follows that if no loss terms are present, the number of states in the two levels is constant, which can be expressed as

$$N_1 + N_2 = N_{tot} \approx N_1^0 = \text{const.} \tag{2.4}$$

where N_1^0 is the population of level 1 prior to excitation. Here it is assumed that the population of level 2 prior to excitation is negligible, i.e. that $N_2(t=0) = 0$. Combining this assumption with expressions 2.3 and 2.4 and solving for N_2 allows the population of level 2 to be expressed as

$$N_2(t) = \frac{b_{12} N_1^0}{(b_{12} + b_{21} + A_{21} + Q_{21})} (1 - e^{-(b_{12} + b_{21} + A_{21} + Q_{21})t}) \tag{2.5}$$

After a short period of time (typically shorter than a standard 10 ns laser pulse) a steady state between the energy transfer processes shown in Figure 2.1 is reached, and as a result the population progresses towards the value of the first term in expression 2.5. Assuming a steady state and rearranging allows the population to be written as

$$N_2 = N_1^0 \frac{b_{12}}{b_{12} + b_{21}} \cdot \frac{1}{1 + \dfrac{A_{21} + Q_{21}}{b_{12} + b_{21}}} = N_1^0 \frac{B_{12}}{B_{12} + B_{21}} \cdot \frac{1}{1 + \dfrac{I_{sat}^v}{I_v}} \tag{2.6}$$

where the saturated spectral irradiance is defined as

$$I_{sat}^v \equiv \frac{(A_{21} + Q_{21})c}{B_{12} + B_{21}} \tag{2.7}$$

Since the fluorescence signal power, F, is proportional to $N_2 A_{21}$ it can be written as

$$F = h\nu N_2 A_{21} \frac{\Omega}{4\pi} lA = h\nu \frac{\Omega}{4\pi} lA N_1^0 \frac{B_{12}}{B_{12} + B_{21}} \cdot \frac{A_{21}}{1 + \dfrac{I_{sat}^v}{I_v}} \tag{2.8}$$

In this expression, h is Planck's constant, ν is the frequency of the fluorescence light, $h\nu$ thus being the photon energy. Moreover, Ω is the collection solid angle, l is the

length along the laser beam from which fluorescence is detected, and A is the cross-sectional area of the laser beam. Expression 2.8 can be simplified if a low laser excitation irradiance is assumed to be employed, i.e. $I_v << I_{sat}^v$. If this is indeed the case, the signal is in the linear regime, and the fluorescence signal power can be written as

$$F = \frac{h\nu}{c} \cdot \frac{\Omega}{4\pi} l A N_1^0 B_{12} I_v \frac{A_{21}}{A_{21} + Q_{21}} \tag{2.9}$$

From this expression it is clear that the fluorescence signal power is linearly proportional to the laser irradiance. In addition, the fluorescence is proportional to the number of molecules of the probed species, lAN_0^1, in the measurement volume. One drawback however, is that the process is sensitive to collisional quenching. This means that the time between excitation and fluorescence emission is long enough for some of the molecules to lose their excitation energy in collisions with other molecules before fluorescence is emitted, making it very difficult to quantify species concentration on the basis of the recorded signal. Generally quenching is dominant over spontaneous emission, $A_{21} << Q_{21}$, resulting in the fluorescence efficiency, $A_{21}/(A_{21} + Q_{21})$, being much smaller than unity, which means that a great part of the excited molecules lose their excitation energy through non-radiative processes. Therefore it is necessary to be able to handle the quenching rate constant when using LIF in the linear regime, if quantitative results are desired. This is not an easy task, however, since the quenching rate is dependent on temperature, pressure and species composition. Evaluations of this type can be done in some situations, such as in stationary flames where these parameters, and thus also the quenching rate, are constant over time. However, emphasis in the thesis is placed on diagnostics performed in transient and turbulent combustion events, where such evaluations are very difficult. In such situations, other strategies are needed, and one alternative is to increase one of the loss terms sufficiently to make it dominant over the quenching rate, so that the quenching can be neglected. This is the idea behind photo ionization LIF and predissociative LIF, but due to the great losses the fluorescence signal power is very low, which makes these approaches difficult to use. Another strategy that can be used in order to eliminate the effects of quenching is saturated LIF. In this approach a very high level of laser irradiance is used, $I_v >> I_{sat}^v$. From equation 2.8 it is evident then that the fluorescence signal power is independent of laser irradiance in this saturated regime. Moreover, since it is independent of quenching, no quenching corrections of the measurements are required. A difficulty with this approach is that of achieving complete saturation due partly to wing effects of the laser profiles in the spatial, temporal and spectral domains.

   LIF in the linear regime is still the most commonly used technique, despite the difficulties in achieving quantitative results. Under certain assumptions such that the

quenching is reasonably constant throughout the measurement volume, linear LIF still provides a good qualitative overview of e.g. the spatial distribution of the species which is studied.

2.2 Flame Front Markers

The region of a flame in which most of the chemical reactions convert fuel and oxidizer into combustion products is referred to as the reaction zone, or flame front. Because of the many reactions occurring in the flame front, this region is very important to study in combustion research. The many reactions result in a high local heat release rate, and thus in a high temperature. However, since it may not be possible to monitor the flame front directly, some other property closely connected with the flame front, a so called flame front marker, has to be monitored instead.

The hydroxyl radical, OH, is an important intermediate species in the oxidation process of hydrocarbon fuels. Since OH is formed in the high-temperature regions it is commonly employed as a flame front marker. In Papers I-V PLIF of OH is used in various applications to visualize flame front structures as well as the start of combustion and regions of burned gases. Excitation can be achieved by use of the $Q_1(8)$ transition in the (1,0) vibrational band of the $A^2\Sigma^+$-$X^2\Pi$ electronic band system, and it is usually performed using an Nd:YAG laser pumped dye laser near 283 nm. This transition is relatively temperature insensitive, making it suitable for LIF measurements in flames. The excitation and fluorescence scheme of OH is displayed in Figure 2.2. In the initially excited $v' = 1$ state, rotational energy transfer (RET) starts immediately after excitation, and the population is distributed among the neighbouring rotational levels. In addition, vibrational energy transfer (VET) also occurs, populating the $v' = 0$, and the fluorescence in the (0,0) band is shifted towards longer wavelengths around 308 nm, as compared with the fluorescence from the (1,0) band. In performing OH LIF measurements this is advantageous, since by the use of proper filters only fluorescence from the (0,0) band is detected, and hence interference from scattered laser light can be avoided [10]. Dreizler et al. used OH LIF to characterize a spark ignition system [11]. Details on molecular spectroscopy are presented by Banwell and McCash [12].

OH occurs in relatively high concentrations in the reaction zone, which is a great advantage when using OH LIF for flame front studies. However, since OH is relatively long lived, this radical does not only mark the primary hydrocarbon reaction zone. CH is a short lived intermediate species, formed during the primary reactions of hydrocarbons and air, and is then rapidly converted to other species [13]. This makes CH a more effective marker of the hydrocarbon reactions, but it usually occurs in very low concentration, which makes it difficult to detect. Detection is
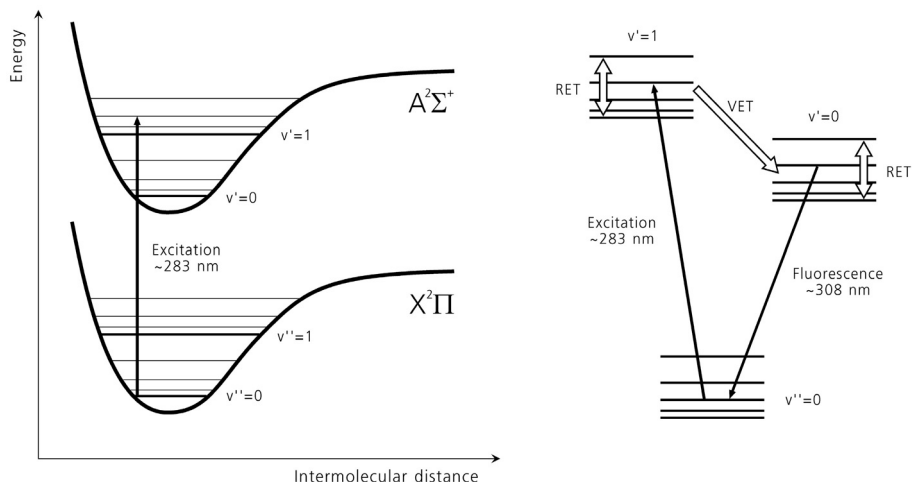
Figure 2.2 *Schematic energy-level diagram of the energy transitions involved in laser excitation and fluorescence of the OH radical.*

further complicated by overlapping fluorescence from polycyclic aromatic hydrocarbons (PAH). Carter et al. has demonstrated measurements of flame front location by means of CH PLIF employing an Nd:YAG pumped dye laser, in combination with particle imaging velocimetry (PIV) for velocity field measurements, in order to study the effects of the flow field on the flame front in a turbulent, non-premixed flame [14]. Li et al. has reported on the development of CH PLIF in turbulent premixed flames using a pulsed alexandrite laser [15].

2.3   Fuel Tracers

In practical combustion devices, such as IC engines and gas turbines, perhaps one of the most interesting properties to study is the distribution of fuel concentration. Fuel visualization can provide information concerning not only the fuel distribution but also flame propagation, if it occurs. Fuel visualization is generally performed by exciting a fluorescent tracer molecule added to a non-fluorescing fuel. For most gaseous fuels, adding a fluorescent tracer molecule to the fuel is necessary to make it visible for the LIF technique, since they do not fluoresce when illuminated by UV radiation. Many commercial liquid fuels, however, fluoresce when illuminated by UV radiation, but they consist of a wide variety of hydrocarbon fuel components, several of which fluoresce. Since it is not known which species contribute to the fluorescence, the dependence on pressure and temperature, and on the quenching rate is unknown. Furthermore, the fuel composition, and thus its absorption and

fluorescence properties, often varies from batch to batch for these fuels. When using LIF for fuel visualization, commercial fuels are often replaced by a one-component fuel or a mixture of a number of one-component fuels, all of them non-fluorescent, to which a small fraction of a fluorescent tracer is added.

There are a number of important characteristics a suitable tracer should have. It is crucial that the tracer follow the fuel flow and that it be consumed in the combustion process in the same manner as the fuel. To ensure this, the tracer should have physical and chemical properties similar to those of the fuel to which it is added, such as evaporation, diffusion and reactivity [16,17]. Furthermore, the tracer should generate strong fluorescence when excited by a commercially available laser wavelength. It is desirable that the absorption and fluorescence regions be separated spectrally, and that the fluorescence be independent of variations in temperature, pressure and species composition in the gas. However, it should be noted that the fluorescence of most tracers shows at least some dependence on these parameters.

A most frequently used class of tracers is the ketones, among which acetone ($[CH_3]_2CO$) and 3-pentanone ($[CH_3CH_2]_2CO$) are commonly used. The first report on the use of 3-pentanone as a fluorescent tracer for iso-octane was published in 1992 by Neij et al., who also reported for the first time the use of acetone as a fuel tracer in an engine experiment the same year [18,19]. The broad absorption spectrum of acetone ranges from 225 nm to 320 nm (similar to 3-pentanone), making the molecule accessible to common pulsed, high-power lasers, such as Nd:YAG lasers. Fluorescence, occurring between 350 nm and 550 nm, is well separated from the absorption region. Thurber and Hanson have shown that acetone has a number of advantages as a fuel tracer, e.g. that the fluorescence signal is linearly dependent on the laser energy when excited at 248, 266 or 308 nm [20-22]. Another advantage is the short lifetime (<2 ns) of the excited state, which minimizes the influence of quenching [23]. For the purpose of visualizing fuel distribution in an IC engine using acetone as a tracer, laser radiation of 266 nm wavelength can be used. It should be pointed out, however, that the optimum choice of wavelength with respect to independence of variations in temperature and pressure would be in the range of 275-290 nm [21,24].

2.4   Formaldehyde

Formaldehyde, CH_2O, appears as an intermediate species in combustion of many hydrocarbon fuels. It is formed in the low temperature oxidation process, often referred to as the cool-flame region, and is consumed thereafter during the main combustion process. Formaldehyde is an important species in the low temperature region of combustion and a key species in auto-ignition and knock phenomena.

Recently its presence in Homogeneous Charge Compression Ignition, HCCI, engines has also been demonstrated [25,26].

LIF measurements of formaldehyde can be used for investigations of the initial stages of combustion, and in Papers VIII-IX formaldehyde was utilized as a naturally occurring fuel marker in HCCI combustion. The absorption spectrum ranges from 270 nm to 360 nm, and excitation of the molecule can be achieved by using a frequency tripled Nd:YAG laser at 355 nm [27]. Although the band excited at 355 nm (band $\tilde{A}^1A_2 - \tilde{X}^1A_1\ 4_0^1$) shows a weak absorption coefficient [28], it is still an attractive choice of excitation wavelength since it is easily obtained at high energy levels from the laser source. Another advantage of this approach is that it simplifies the experimental setup as compared to using a dye laser to tune the laser radiation to a strong transition. Fluorescence occurs within a broad range of wavelengths, between 350 and 550 nm. A more detailed description of the approach of using a frequency tripled Nd:YAG laser for formaldehyde LIF is provided by Brackmann et al. [27].

Chapter 3

High-Speed Laser Diagnostic System

3.1   Multi-YAG Laser Cluster

In order for a laser diagnostic system to be able to follow the processes occurring in turbulent reacting flows, the repetition rate of the system must be in the range of the turbulent timescales of the flow, which is usually in the kHz or even MHz range. However, most high power laser sources have a repetition rate in the range of 10-100 Hz, which is clearly much slower than the required repetition rate. For these studies a multiple laser design can be used. More information about the principles of lasers can be found in [29].

The laser source of the high-speed laser diagnostic system used in the work presented in the thesis consists of four individual, Q-switched, flash lamp-pumped solid state lasers, all mounted on the same base plate (BMI, CSF-Thomson). Each laser is of Nd:YAG type and has an oscillator and a single amplifier, each with a rod of YAG ($Y_3Al_5O_{12}$) crystal doped with Nd^{3+} ions as the active lasing medium. The lasers produce pulses with a repetition rate of 10 Hz at the fundamental wavelength of 1064 nm. For generating laser radiation at 532 nm and for combining the four laser beams the frequency doubling and beam combining scheme shown in Figure 3.1 is used. The fundamental beam from laser 1 is frequency doubled to 532 nm in a second harmonic generation (SHG) crystal, and this beam is then spectrally isolated from the fundamental beam by means of a dichroic mirror reflecting 532 nm and transmitting 1064 nm. An additional dichroic mirror is used to combine the second harmonic beam from laser 1 with the fundamental beam from laser 2. After the two beams have been combined they are directed through the SHG crystal of laser 2. Ideally, the second harmonic beam from laser 1 passes the crystal unaffected whereas the fundamental beam from laser 2 is frequency doubled. A weak absorption of the second harmonic from the first laser occurs, however. The procedure is repeated for all four lasers until the beams are frequency doubled and aligned onto a single output beam path. Optionally, a fourth harmonic generation
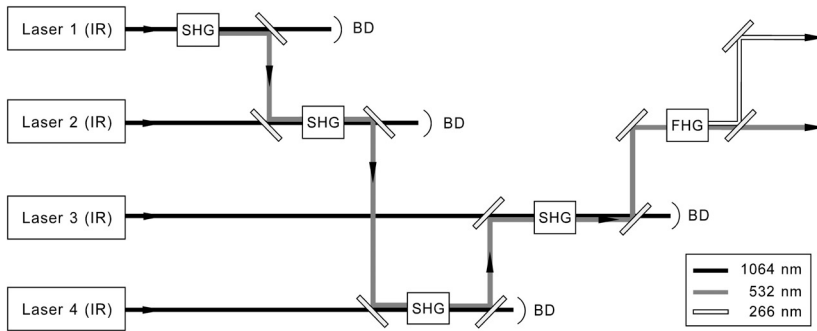
Figure 3.1 *The optical layout of the original multi-YAG laser cluster for generation of 532 nm or 266 nm laser radiation. Second and fourth harmonic generation (SHG and FHG) crystals are used for conversion of the fundamental Nd:YAG laser radiation, and the beam paths are superimposed by means of dichroic mirrors.*

crystal (FHG) can be placed just before the exit of the laser, enabling laser radiation at 266 nm to be generated as well.

This frequency doubling and beam combining scheme was also redesigned in order to frequency triple the fundamental beams from the Nd:YAG lasers to 355 nm. In Figure 3.2 the layout of this scheme is shown, where third harmonic generation crystals (THG) have been added and the dichroic mirrors have been replaced by ones reflecting at 355 nm and transmitting longer wavelengths. Before the laser pulses exit the system, they are reflected by a pair of dichroic mirrors of the same type as those used in the beam combination scheme. Thus, most of the residuals are transmitted, whereas the desired output wavelength is reflected, further enhancing the spectral isolation of 532 nm, 355 nm or 266 nm, depending on the configuration.

Figure 3.2 *The optical layout of the redesigned multi-YAG laser. Third harmonic generation (THG) crystals were added to the original design for generation of 355 nm.*

The four lasers can be fired in a sequence in which the time-separation between the pulses can be individually set from 0 to 100 ms, resulting in a rapid burst of laser pulses from the cluste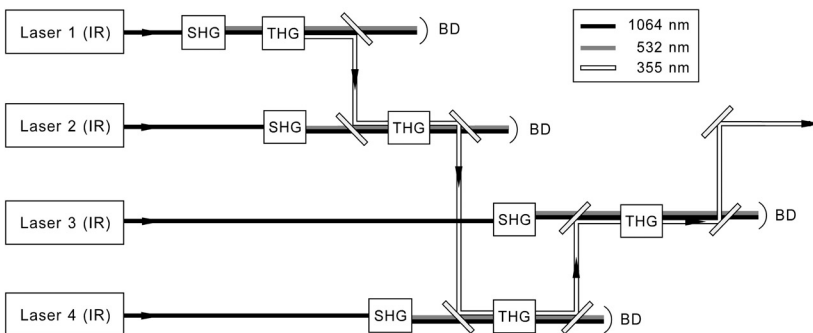r. However, each of the lasers can optionally be operated in double pulse mode, meaning that the Q-switch is opened twice during a flash lamp discharge. This increases the maximum number of pulses to eight. The time-separation between the two double pulses can be adjusted from 25 µs up to 145 µs, where the lower limit is governed by the gain build-up time in the cavity and the upper limit is given by the length of the flash lamp discharge. In order to achieve shorter time-separations, the pulses from the four lasers can be interleaved. In this manner time-separations as short as 6.25 µs (= 25 µs/4) can be achieved, with equidistant spacing between the pulses.

Table 3.1 *Output pulse energies of the multi-YAG laser.*

Wavelength (nm)	Pulse Energy (mJ)
532	500
355	100
266	90

The maximum laser pulse energies at the output of the multi-YAG laser cluster are given in Table 3.1 for the three different wavelengths. The values are given for single pulse operation, since the pulse energies in double pulse operation are dependent on the time-separation between the double pulses. Note that, due to the different path lengths through the harmonic generation and beam combining optics, the output pulse energies vary between the four lasers in the cluster. This is caused partly by absorption in the doubling and tripling crystals, and the effect is noticeable especially for generation of 355 nm, for which the output energies vary between 100 mJ and 200 mJ for the four lasers.

3.2   Multi-Dye Laser Cluster

In order to generate other laser wavelengths and thus enable other species to be detected, the multi-YAG laser cluster can be used to pump a dye laser. A dye laser using a fluorescing dye in a solvent and having an adjustable grating as a part of the resonator was used in some of the applications presented, in which a tunable laser source was required. For example, this approach was used in some of the OH PLIF work, in which a dye solution of Rhodamine 590 in methanol was used to generate laser radiation at 566 nm, which was subsequently converted to 283 nm by means of a second harmonic generation crystal.

An important issue that arises in pumping a dye laser with a rapid sequence of pulses from the multi-YAG cluster is the deterioration of the output energy and the spatial energy profile of the output beam of the dye laser. It has been shown that if the time-separation between two consecutive pulses is decreased to values below the time it takes for the circulation pump to replace all of the solution in the cell, effects of the previous pump beam that was present in parts of the solution, becomes evident [30]. The energy of the output pulses thereafter is significantly reduced as compared with the output of the first pulse. In order to produce a pulse sequence with an even energy distribution, the energy of the first pulses needs to be reduced to the level of the last and weakest pulse. The drawback of doing so is evident, since it results in a pulse sequence of significantly lower pulse energy than if the dye laser is pumped by a single pulse. Moreover, the quality of the intensity profile across the laser beam deteriorates when the dye laser is pumped with a rapid sequence from the multi-YAG. In two-dimensional imaging where the laser beam is expanded to a sheet, this is seen in the form of alternating darker and brighter stripes along the direction of propagation of the laser sheet. This effect can be compensated for, but to achieve this an on-line beam profile measurement is required since the phenomenon varies from pulse to pulse.
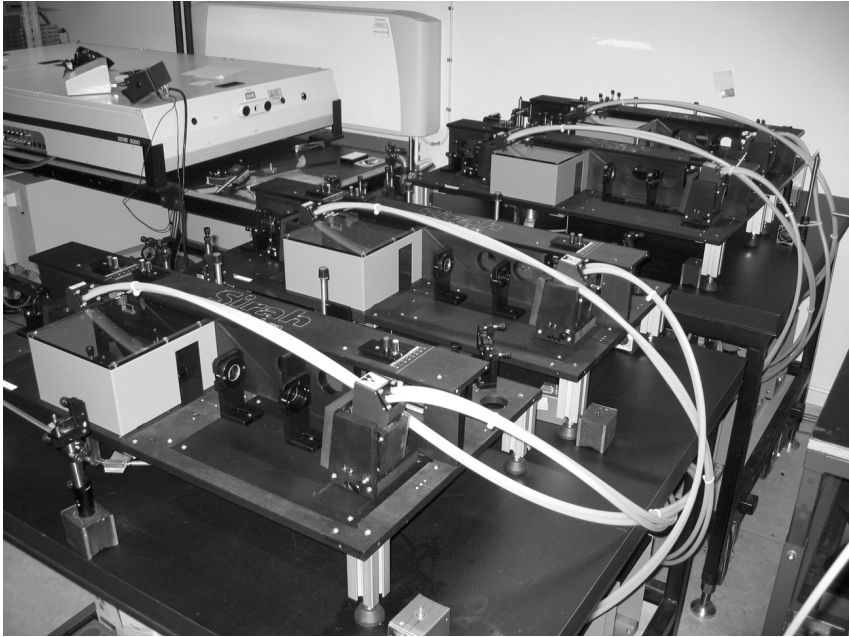

Figure 3.3 *A photograph of the multi-dye laser cluster and the multi-YAG laser.*
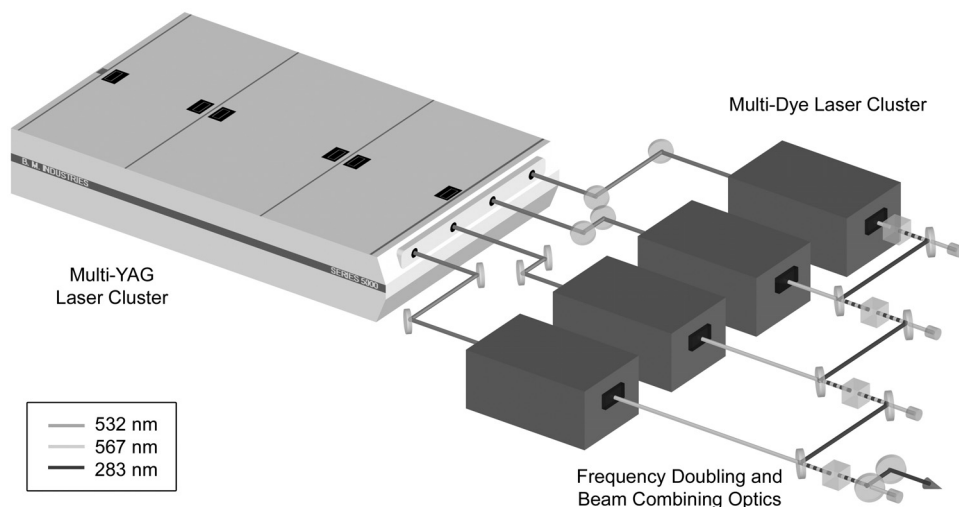
Figure 3.4 *The optical layout for pumping the multi-dye laser cluster with the multi-YAG to generate laser radiation at 283 nm used for LIF imaging of the OH radical.*

To enhance the performance at high repetition rates, one can either increase the flow rate of the dye solution through the cell or use the multi-YAG to pump several dye lasers. In the present work, the latter approach was employed. A multi-dye laser cluster was set up consisting of four individual dye lasers (Cobra-Stretch, Sirah), see Figure 3.3. Each of the four dye lasers can be pumped by the pulses from one of the Nd:YAG lasers in the multi-YAG cluster. Figure 3.4 shows how the second harmonics of the Nd:YAG beams were used for individual pumping of the four dye lasers using a solution of Rhodamine 590 in methanol. By frequency doubling the dye laser output and superimposing the four beam paths in the same manner as described for the multi-YAG cluster, a rapid burst of up to eight laser pulses at 283 nm could be obtained. This setup was used for the high framing rate measurements of OH.

The optical layout of the Cobra-Stretch dye laser is shown in Figure 3.5. The dye laser has two dye cells, the first of which is used for both the resonator and the pre-amplifier. To achieve this, the beam is turned 180° by means of a set of prisms after the output coupler has been passed, in order to pass through the cell a second time. The resonator uses a 60 mm grating of 2400 l/mm, resulting in a linewidth of 0.09 cm^{-1} at 566 nm and approximately 0.13 cm^{-1} for the frequency doubled radiation at 283 nm. The second dye cell is used for the main amplifier of the laser. The energy of the incoming pump beam from the Nd:YAG cluster is distributed to the resonator, the pre-amplifier and the main amplifier by means of two beam splitters, M_1 and M_4. The beam path created by the mirrors M_2, M_3 and M_5

constitutes a delay line for the pump beam so as to guarantee optimal timing of the three pumping volumes. By exchanging the mirrors, the dye laser can be pumped by either 532 nm or 355 nm from the multi-YAG cluster.
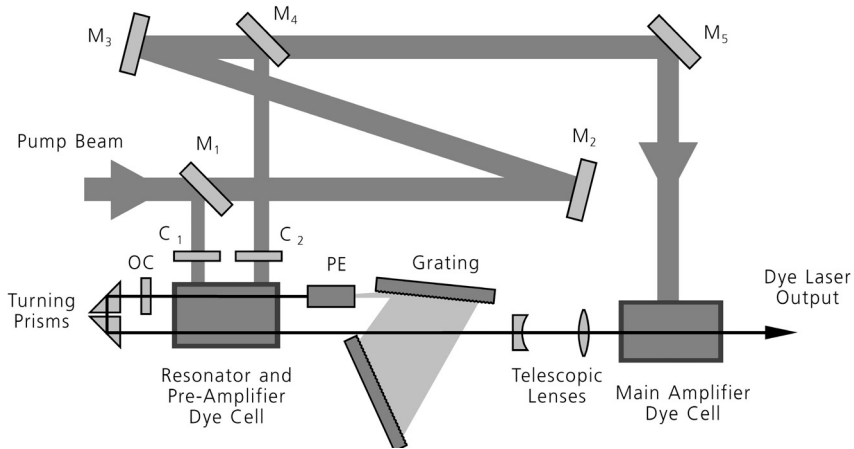
Figure 3.5 *Schematic overview of the Cobra-Stretch dye laser.*

3.3   High-Speed Framing Camera

Since the laser sources used in this experimental approach have a repetition rate in the range of MHz, a detector system with an equally high acquisition rate is required. For detecting the fluorescence induced by the burst of laser pulses from the cluster, a high-speed framing camera (Imacon 468, DRS Hadland) was used. The commercially available detector system has been modified for improved triggering capabilities and to permit synchronization with an additional image intensifier. This detector employs a single optical input with a standard Nikon lens mount. By means of an eight-facet pyramid beam splitter the collected image is redirected into eight separate channels, each with an intensified charge coupled device (ICCD) module. The high framing rate is achieved by exposing the eight ICCD modules in a sequence synchronized with the laser pulses. A schematic of the optical layout of the framing camera is shown in Figure 3.6.

Each ICCD module consists of a micro channel plate (MCP) and a CCD image sensor. The MCP is used for both image intensification and gating of the image acquisition. With this technique, exposures as short as 10 ns can be achieved. To ensure maximum coupling efficiency, the MCP is fibre-optically coupled to the CCD detector. The CCD detector consists of 384×576 pixels, and the recorded

Figure 3.6 *The high-speed framing camera employs an eight-facet pyramid beam splitter for redirecting the collected light onto eight individual ICCD detectors.*

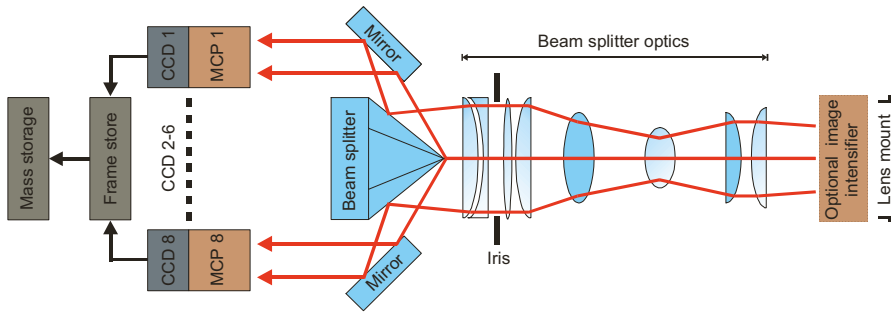image is read out and digitized to 8 bits and then stored in an internal memory in the camera. The gate time, delay time and gain can be set for each of the eight channels individually. This configuration allows sequences of eight images to be recorded at a framing rate as high as 100 MHz, assuming that no temporal overlap of the images is desired.

As already indicated, the camera has been modified to function together with an additional three-stage image intensifier, which can be mounted at the image plane behind the camera lens at the optical input, and this has two major advantages. It increases the sensitivity of the detector system and it also makes the system UV-sensitive, through converting UV radiation into visible light, detectable by the remainder of the system. When this option is selected, sequential gating of this additional intensifier is generally employed, defining the exposure time for the acquisition of each of the eight images. Sequential gating at a high repetition rate calls for the use of a fast phosphor. However, the full framing rate of the original camera system cannot be reached due to the lifetime of the phosphor, and thus in using this option the maximum framing rate is reduced to ~1 MHz.

3.4   Synchronization of the System

Several different alternatives are available for triggering the laser and the detector system to the experimental situation. When studying a continuous combustion process, the laser cluster is triggered internally at 10 Hz and the lasers are then fired individually according to pre-programmed delays with respect to the master trigger. If a periodically occurring process is studied, such as combustion in an internal combustion engine, and the periodicity can be related to 10 Hz, the laser cluster can

be triggered externally at 10 Hz, after which the system behaves in the same manner as when triggered internally.

Trigger the system to a single external event requires a slightly more sophisticated triggering scheme. This is referred to as Synchro Shot by the laser manufacturer, where the trigger pulse works as an arm-and-fire sequence to the laser. Prior to the external event, the laser is triggered internally at a 10 Hz repetition rate, so as to maintain the thermal stability in the YAG crystals. Continuous operation of the laser is interrupted at the rising edge of the external trigger pulse, the laser being adjusted to firing on demand. The falling edge of the trigger pulse, set to correspond with the start of the external event, starts the firing sequence of the laser in accordance with the preset delays. Note that in order for the start of the external event to be registered by the diagnostic system, the falling edge must be reached slightly before the start of the event. This is because it takes about 125 μs for the flash lamp to build up the necessary gain in the cavity, this being the minimum time delay, therefore, between the falling edge of the trigger pulse and the first laser pulse. For technical reasons, the arm-and-fire trigger pulse length should be in the range of 200 – 800 ms. A short period of time (~1 s) after the laser is interrupted by the rising slope of the external trigger pulse, it returns to continuous operation again at 10 Hz.

Each image frame acquired by the framing camera is triggered individually by a pulse from the laser 500 ns before the opening of the respective Q-switch. The four lasers in the cluster have individual outputs for their respective trigger pulses, and the four channels are added to a single output channel using a CINEMAX unit, which is
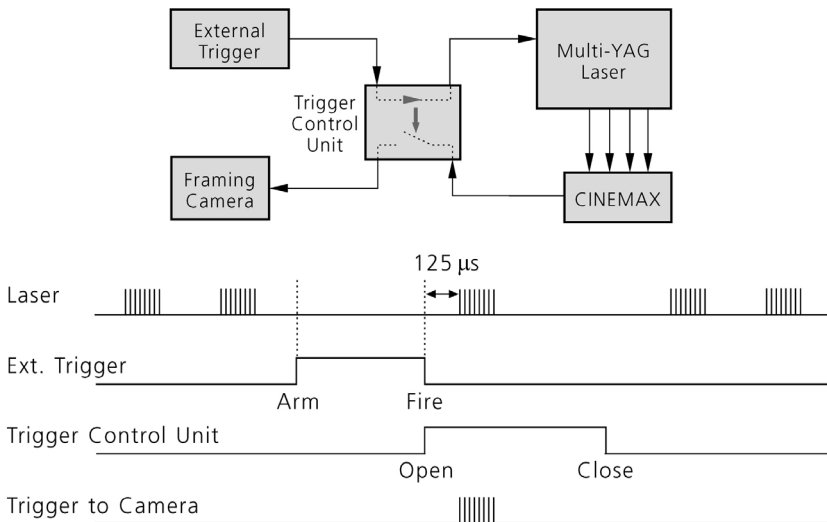

Figure 3.7 *A typical triggering scheme utilizing the Synchro Shot capability of the multi-YAG laser, in order to trigger the system to a single external event.*

also used for controlling the gain and gate settings on the extra image intensifier of the framing camera. The delays of the actual image acquisition can then be programmed individually with respect to the trigger pulses. For continuous operation the framing camera is normally triggered by the laser at 10 Hz. However, when a single external event is to be captured and the laser system is operated in synchro shot mode it is desired that the camera only acquires a sequence after the falling edge of the trigger pulse to the laser has been reached, and not during the continuous operation prior to this event. For this reason, a small electronic device was constructed which blocks the burst of trigger pulses from the laser to the camera and is temporally opened only after the falling edge of the trigger to the laser has been reached. A typical triggering scheme is shown in Figure 3.7.

3.5   Experimental Overview

3.5.1   Planar Laser-Induced Fluorescence at High Repetition Rate

The basic experimental setup for planar laser-induced fluorescence imaging at high repetition rates is shown in Figure 3.8. In the various applications presented in the thesis some different species have been probed, such as formaldehyde, OH and acetone (as a fuel tracer), and for each species a suitable wavelength has to be chosen. For formaldehyde and fuel tracer PLIF the multi-YAG laser cluster is employed with in a configuration producing the third and fourth harmonic, respectively, whereas for OH PLIF the multi-YAG is employed together with one or more dye lasers. By means of cylindrical and spherical lenses the beam is expanded to a collimated laser sheet with a height of generally around 50 mm and is focused to a thickness in the range of 100-300 µm. In the intersection region of the sheet with the flame, the probed species is excited and subsequent fluorescence is detected by the framing
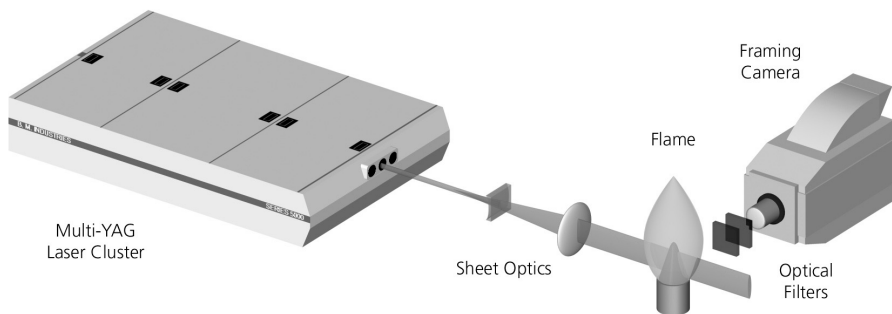

Figure 3.8 *A basic experimental setup for planar laser-induced fluorescence.*
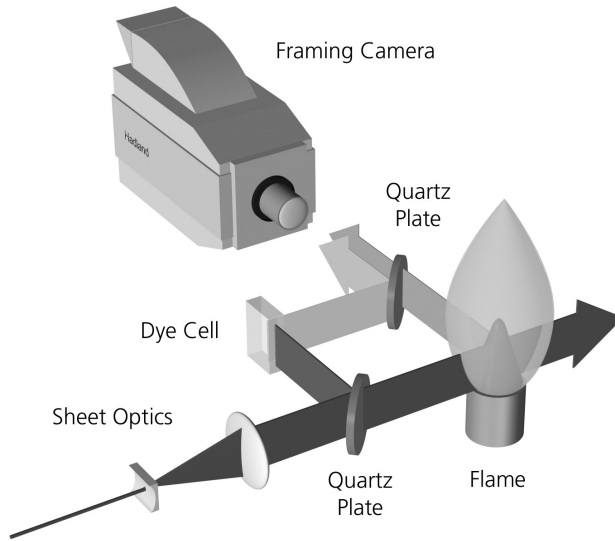
Figure 3.9 *An approach for on-line laser beam profile monitoring.*

camera, perpendicular to the sheet. The fluorescence is collected by an achromatic quartz lens with a focal length of 100 mm and with an f-number of 2, and suitable filters are placed in front of the camera lens so as to minimize any interference from unwanted reflections of laser light or potential Mie scattering. Short exposure times in the range of 50-300 ns are selected to avoid spectral interference from background radiation.

Fluctuations in the laser pulse energy as well as variations in the beam intensity profile can in some applications be a significant problem. These variations can be compensated for after measurements have been made if the sheet intensity profile has also been measured, yet since the profile varies from pulse to pulse there is a need of on-line monitoring of the beam or of the sheet profile. The approach employed here for this type of monitoring is shown in Figure 3.9. A quartz plate is inserted after the sheet-forming optics, to reflect a small fraction of the sheet intensity. Most of the sheet intensity is transmitted through the plate to reach the flame under investigation, whereas the reflected fraction of the sheet is directed into a cell containing a fluorescing dye. The fluorescence response of the dye must be linear to the laser intensity and be homogeneously mixed, to ensure that the fluorescence has the same intensity profile as the impinging laser sheet. A second quartz plate placed in front of the camera lens at a 45° angle directs some of the fluorescence from the cell onto the camera, whereas the fluorescence from the flame is transmitted through the plate. Adjusting the angle of the second quartz plate enables the fluorescence from the flame and the cell to be imaged on separate parts of the same CCD

detector. This allows an on-line sheet profile to be recorded for each individual PLIF measurement.

3.5.2   An Approach for Measurements in Three Dimensions

Adding a rapidly scanning mirror to the high-speed diagnostic system enables the species distribution to be visualized in three dimensions. A schematic of the technique is shown in Figure 3.10. The laser sheet is swept across the measurement volume so that the position of the sheet is altered slightly between consecutive laser pulses. In this manner, a stack of up to eight closely spaced 2D images can be acquired, which can be used to recreate the three-dimensional distribution of the species.
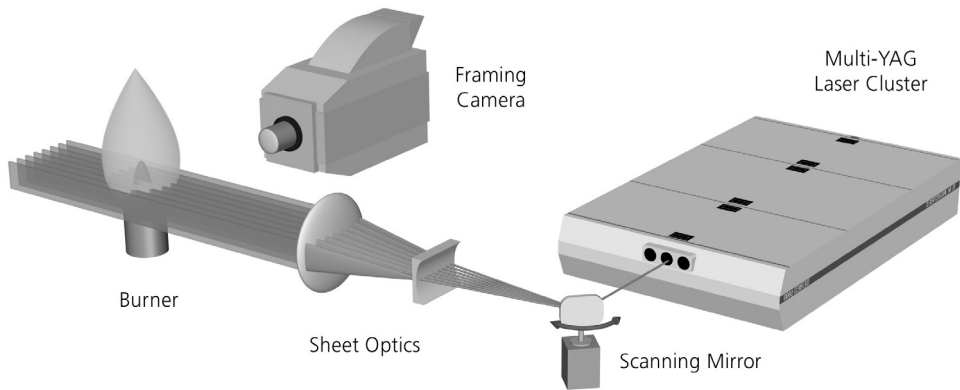
Figure 3.10 *By using a rapidly scanning mirror for displacing the laser sheet from pulse to pulse, a stack of closely spaced 2D images can be acquired, which can be assembled to a 3D image of the investigated species.*

In the work presented in this thesis a galvanometric mirror scanner (GSI Lumonics, G330) was used for scanning of the laser beam, see Figure 3.11. The laser beam was reflected by the scanning mirror through a series of lenses to create a laser sheet, and by placing the mirror at the focal point of the spherical focusing lens, the sheets were made parallel. The demands placed on the temporal resolution can be very high in performing measurements of this type, the temporal resolution required depending on e.g. the turbulent time scales of the process being studied. All the eight images have to be acquired during a time period sufficiently short for the flame structures to not change noticeably. As previously mentioned, the minimum time-separation between the laser pulses is 6.25 μs, which means that the minimum acquisition time for a single three-dimensional measurement is $7 \times 6.25\ \mu s \approx 44\ \mu s$. Note, however,

that since the pulse energies are significantly lower at this pulse separation, a longer separation is preferred if the phenomena being studied permits it.

The spatial resolution in the depth direction is given by the sheet separation, which in turn is dependent on both the temporal pulse separation and the sweep speed of the mirror at the time of measurement. Since the temporal pulse separation is kept as short as possible so as to ensure that the flow field is frozen during the entire acquisition, a relatively high sweep speed is needed to spatially separate the sheets. This should, however, not be mistaken for a need of a high scanning frequency. On the contrary, a modest scanning frequency and a large sweep amplitude also result in a high sweep speed and is advantageous to a higher frequency in several ways. First, the sweep amplitude on many commercially available scanners of this type decreases rapidly as the maximum frequency increases, limited partly by the mechanical inertia of the mirror mounted on the armature of the scanner. Since it is the combination of the two parameters rather than the frequency alone that is important, a scanner with a higher maximum frequency generally needs to be operated closer to its performance limits than a corresponding low-frequency scanner does. Secondly, with a larger amplitude it is possible to use only the central part of the scan, hence firing all of the laser pulses in the linear part of the sinusoidal scan, as shown in the right section of Figure 3.11. This provides equidistant laser sheets, whereas with use of a smaller amplitude the entire scan has to be employed, resulting in more closely spaced sheets at the turning points.

Synchronization of the mirror scan to the laser and the detector system can be achieved in several ways. The easiest way is to drive the scanner with a function generator, generating a sinusoidal signal with a frequency which is a multiple of 10 Hz. This signal can then be sampled down to 10 Hz with which the laser can be triggered. This approach is suitable when there is no need for synchronization of the system to an external combustion event. If that is required, other approaches are possible.
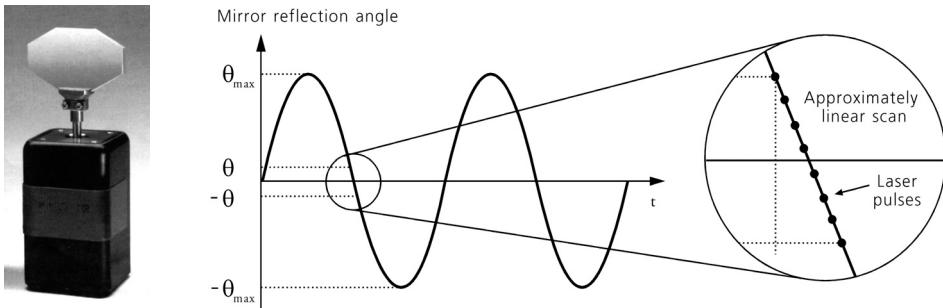

Figure 3.11 *Photo of the mirror scanner (left). By using a large scanning amplitude, the laser pulses may be fired in the linear regime of the scan to provide a suitable equidistant sheet spacing (right).*

3.6   Alternative Approaches to High-Speed Diagnostics

The system with the multi-laser design described in the thesis has the capability of generating a burst of laser pulses with very short time-separations and with relatively high pulse energy. In combination with the high-speed framing camera two-dimensional LIF measurements with ultra-high framing rates are feasible. However, it is limited to eight image frames and in some applications it would be advantageous to have even longer sequences. In addition, a detector with a wider dynamic range than that of the framing camera could be useful in some situations. In the present section some examples of other approaches for measurements with high repetition rates are briefly presented.

The first laser ever constructed was the ruby laser built in 1960 [29]. An early laser system with ultra-high repetition rate was reported by Theocaris et al. in 1981 [31], which was also based on the ruby laser design. This laser consisted of 16 Q-switched ruby lasers and was capable of producing 200 mJ/pulse with repetition rates in the MHz range. The laser was designed for studies using sequential photography of dynamic phenomena such as crack propagation, however, with a wavelength of 694 nm, the ruby laser is not very well suited for LIF measurements of combustion species.

An Nd:YAG laser system capable of generating a burst of up to 30 pulses has been reported by Wu and Miles [32]. The system consists of a cw master oscillator and a pulse slicer (two Pockels cells) for chopping the cw beam. With a five stage amplifier system pulses of 70 mJ can be produced at 1 MHz repetition rate and 1064 nm wavelength. By frequency doubling the radiation and reducing the repetition rate to 0.5 MHz pulse energies of 25 mJ at 532 nm can be generated, and this approach has been used for visualization in supersonic flows by means of Rayleigh scattering. However, because of the low pulse energies obtained if the radiation is converted to the UV region, its use for PLIF in combustion environments is probably limited.

Another Nd:YAG laser based high-speed system has been presented by Fajardo, Smith and Sick [33,34]. Fuel tracer PLIF measurements in an engine have been performed using a frequency tripled, diode-pumped laser at a repetition rate of 12 kHz, providing crank angle resolution. The great advantage with this system is that the number of pulses is not limited, since it operates continuously at 12 kHz, and in combination with a high-speed CMOS camera (Phantom 7.1) and an external two-stage image intensifier several thousand image frames can be recorded sequentially. Because of the high repetition rate, however, the pulse energy is only 0.4 mJ making PLIF measurements difficult. For fuel tracer PLIF experiments with 355 nm laser radiation, well known tracers such as acetone or 3-pentanone cannot be used, and in the experiments presented in [33,34] biacetyl was used as fuel tracer for which the absorption and fluorescence spectra overlap. In addition, CMOS detectors

generally have a limited data read out rate, and when the framing rate is increased the recording suffers in terms of resolution. Thus to achieve the same framing rates as can be reached by the framing camera employing multiple ICCD detectors, the imaged area needs to be reduced in size to some tens of pixels. The described system has also been used for sequential PIV measurements in an engine, were a repetition rate of 16 kHz was used to record four velocity fields per crank angle degree [35].

Gas lasers such as excimer and Cu vapour lasers generally have a higher repetition rate than conventional solid state lasers, and can generate pulses in the kHz range. The pulse energies of excimer lasers are sufficient for fuel tracer LIF, while the pulse energies of Cu vapour lasers are generally too low for these applications. Nevertheless, flame front studies have been conducted using Cu vapour lasers. In a paper by Renou et al. [36] a high-speed diagnostic system is presented, consisting of a Cu vapour laser and a high-speed Cordin camera for ordinary 35 mm film. To visualize the flame front, scattering of the laser light on silicon oil droplets, which were evaporated when entering the flame front, was utilized. High-speed film cameras in combination with high-resolution film has the advantage of recording images with higher resolution than a camera using CCD detector technology, and can in general reach very high repetition rates e.g. by means of a rotating mirror sweeping the image over the film. However, the image frames must be developed before the result can be studies, which is one disadvantage with this type of detection. Moreover, post-processing of the image data using computers is often desired, for which reason the images still have to be digitized frame by frame.

Chapter 4

Investigated Combustion Devices

Several different types of combustion devices have been investigated in the thesis, ranging from laboratory burners to commercial truck-sized internal combustion (IC) engines and gas turbine combustors. In this chapter the different combustion devices that have been investigated in the papers are presented briefly. The experiments carried out in the different combustion environments of these devices and the results obtained are presented in the following chapter.

4.1   Laboratory Burners

Laboratory burners range from small laminar burners and Bunsen burners to larger turbulent jet burners and more sophisticated swirl burners. The more advanced burners are often used for studying certain aspects of the combustion process, whereas simple burners can come in handy when developing new diagnostic techniques. In Paper V and VII a small water-cooled cone burner was used in order to study e.g. the spatial resolution of a chemiluminescence diagnostic technique rather than the flame itself. The burner consists of a long vertical pipe at the bottom of which fuel and air are supplied and premixed. The mixture flows to a nozzle at the top of the pipe with a nozzle diameter of 10 mm. To provide a stable temperature of the burner over long periods of time, the cone-shaped nozzle is water cooled. The burner provides a laminar, stable cone-shaped flame, which have been used for evaluation purposes in the papers mentioned above.

4.1.1   Low-Swirl Burner

In Paper IV the combustion and flow fields in a low-swirl methane/air flame were studied. The burner design is based on lean premixing of the fuel and air in order to achieve low levels of NOx emissions, and was initiated by Cheng and co-workers in 1995 [37,38]. It is characterized by a detached flame that propagates freely in a divergent and turbulent flow field.

In the study presented in the thesis an annular swirler consisting of eight curved vanes was used in connection with a perforated plate fitted to the entrance of the centre channel. Figure 4.1 shows the inner parts of the burner. The burner was mounted in a co-flow of air 600 mm in width. The wide co-flow is used to prevent dust particles from the surrounding laboratory air from entering. Moreover, the burner has a nozzle with a long bezel on the outside in order to maintain the area of the inner flow when exiting into the surrounding co-flow, and it also prevents the generation of recirculation zones at the exit of the nozzle. The mass flows are controlled by electronic mass flow controllers (Bronckhorst).
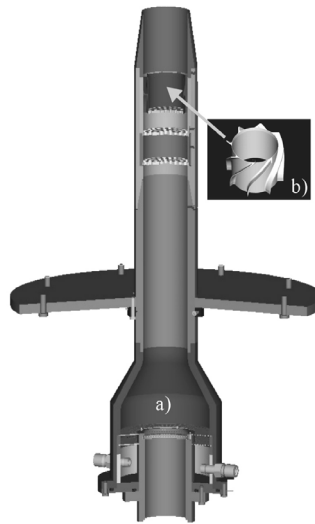
Figure 4.1 *The inner parts of the low-swirl burner.*

4.2   Constant-Volume Combustion Chambers

4.2.1   Combustion Chamber for Ion Current Studies

For the purpose of studying spark-ignition and ion-current phenomena a constant-volume combustion chamber has been constructed. The chamber is built in a block of stainless steel in which there are three orthogonal intersecting cylindrical passages having a total inner volume of 167 cm^3. Each of the passages can be used either for optical access by attaching a fused silica window to it or for inserting electrodes and pressure transducers into it, mounted on plugs of stainless steel. In addition, the

chamber is also equipped with smaller diagonal passages used for air and fuel injection, for exhaust and for evacuation of the cell, all of these functions being controlled by electromagnetic valves. Instead of using a conventional spark plug, two electrodes of straight threaded stainless steel are employed, each 2 mm in diameter, inserted from opposite sides of the chamber. This arrangement provides an adjustable electrode gap. The entire cell can be heated up to about 400 K, and together with the heating of the injected gases, this ensures a homogeneous temperature in the chamber. The heating of the cell also prevents water from condensing on the windows and other cool parts, and helps to keep the windows clean.

4.2.2 Two-Chamber Optical Combustion Cell

The ignition process that occurs when a hot gas jet impinges on a mixture of fuel and air is important in many fields, ranging from the development of combustion engines to industrial explosions. In an explosive environment, ignition can occur as a result of a jet of hot gas escaping through inevitable gaps in a flameproof enclosure. A two-chamber optical combustion cell can be used to study phenomena of this kind, see Figure 4.2.

The cell employed consists of two separate chambers interconnected by means of a small nozzle. In the smaller of the two chambers which is cylindrical in shape, 80 mm long and 60 mm in diameter (volume of 0.226 litre), a combustible gas mixture can be ignited by a spark plug located at an adjustable distance X_i from the nozzle. In the work presented in the thesis the fuel mixture in both chambers consisted of 28 mole% hydrogen and 72 mole% air. As combustion progresses the
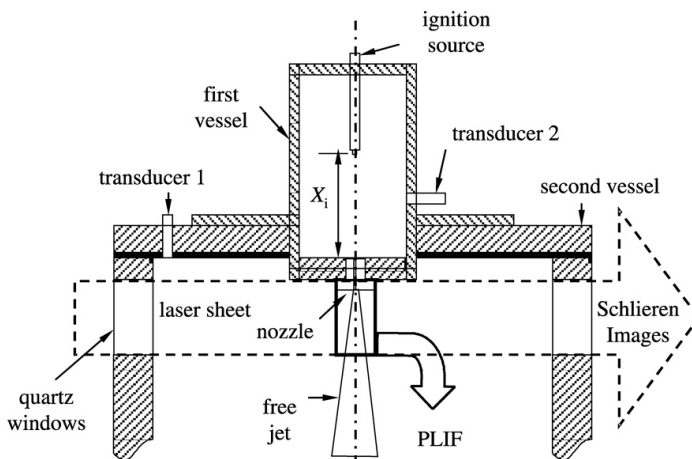

Figure 4.2 *Schematic view of the two-chamber optical combustion cell.*

pressure increases in the first chamber, and some of the hot gases being forced to expand through the nozzle into the second chamber (with a 12 litre volume). The hot jet of burned gases impinging upon the unburned gases can potentially cause ignition, even though no flame is propagating through the nozzle. When the experiments were performed, a pressure transducer was placed in each of the two chambers for monitoring of the pressure trace during the process. The second chamber has been equipped with three side windows to provide optical access.

4.3   Helmholtz Type Pulse Combustor

Paper III deals with both experimental and theoretical work concerning the ignition, combustion and extinction processes in a strongly oscillating flow field. A Helmholtz type pulse combustor was used for this purpose, consisting of a flapper valve, a combustion chamber and a tail pipe. A schematic view of the combustor is shown in Figure 4.3.
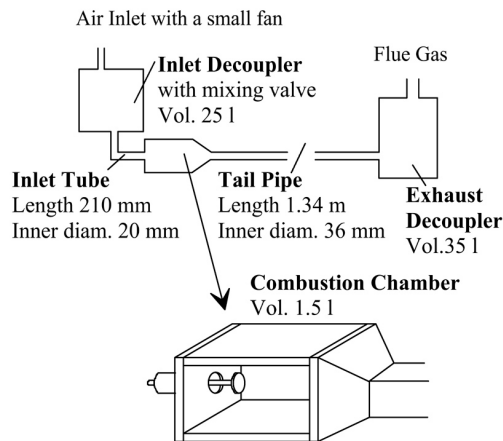
Figure 4.3 *Schematic view of the Helmholtz type pulse combustor.*

A decoupler is connected to each side of the combustion chamber via the inlet tube and the tail pipe, respectively. The combustion chamber has a square cross-sectional area of 80×80 mm^2 and was 150 mm in length. It has a total volume of 1.5 litres including the contraction cone connecting the chamber to the tail pipe. The injection of fuel and air into the chamber is governed by a pressure-activated valve. A 5 mm rod, on which a circular stagnation plate 25 mm in diameter was mounted, was centred on the inlet to the combustion chamber. Adjusting the position of this

plate alters the inlet geometry which in turn affects the operating conditions, such as the operating frequency and the fuel/air ratio [39]. To provide optical access to the combustion zone, the four walls of the chamber were all made of quartz.

4.4 Internal Combustion Engines

The two dominant branches of internal combustion (IC) engines used today are spark-ignition (SI) engines and compression ignition (CI) engines. These types of engines are frequently employed for transportation and for power generation, and their contribution to pollutant emissions is thus significant. Further development of engine design can improve efficiency and reduce the emissions. This is the major motivation for conducting combustion research in these engines. A more thorough description of IC engine technology is provided by Heywood [40].

The time for completion of the combustion process in an IC engine is limited to a fraction of the engine cycle around the top dead centre (TDC). In an IC engine operated in a range extending from hundreds up to several thousand revolutions per minute (rpm) the combustion process must thus be very rapid, often completed within 1-10 ms. The conventional approach to studies of fuel distribution by means of PLIF imaging in such environments employs single-frame detection in each cycle, at successive crank angle degrees, and combines the results from different cycles to encompass the entire combustion event. However, due to cycle-to-cycle variations in engines, data acquired in this manner suffers from an averaging effect, and to avoid this, single-cycle-resolved measurements are needed. In performing such measurements, higher repetition rates than standard laser sources normally provide are needed.

In testing the capabilities of new diagnostic techniques in engine environments a small SI engine was used. The engine, originally designed for production of electrical power, has a single cylinder with a side-valve design. To enable optical access to the combustion chamber, the flat cylinder head was equipped with three quartz windows. This engine was used in Paper VII for investigating the feasibility of obtaining formaldehyde PLIF measurements in engine environments using the redesigned multi-YAG laser cluster. Since it is a production type engine, lubricant oil is likely to escape past the piston rings and into the combustion chamber, which worsen the conditions for laser based diagnostics. However, if a particular technique is found to work even in such an environment it is indeed likely to work in a more refined optical engine.

4.4.1   HCCI – Homogeneous Charge Compression Ignition

Over the last decade or so homogeneous charge compression ignition (HCCI) combustion has proven to be a promising engine concept [41]. An HCCI engine can be regarded as a hybrid between the two well established engine concepts, spark-ignition and diesel ignition. In order to form a homogeneous charge, the fuel and air are premixed, just as in an SI engine. As the charge is compressed, the pressure and the temperature increase sufficiently to auto-ignite the charge, the combustion event being initiated by auto-ignition, just as in a diesel engine. Due to the homogeneous charge ignition occurs at multiple points simultaneously, resulting in rapid rate of heat release. Most of the charge is consumed within a few crank angle degrees and combustion occurs without the presence of flame front propagation. Too high a combustion rate can result in knock-like phenomena and high NOx productions. To prevent this, diluted mixtures are employed. Dilution can be achieved by simply using a very lean mixture or by use of exhaust gas recirculation (EGR).

For diesel engines there is a trade-off between reduction of NOx and soot; a reduction of NOx usually results in an increase of soot, and vice versa. A major advantage of HCCI as compared with diesel engines is the low NOx emissions in combination with significantly reduced soot formation. This is a result of the lean and homogeneous charge, which leads to a lower combustion temperature. Another advantage is the higher part-load efficiency as compared with that of SI engines, which is a result of the fact that the HCCI engine runs unthrottled.
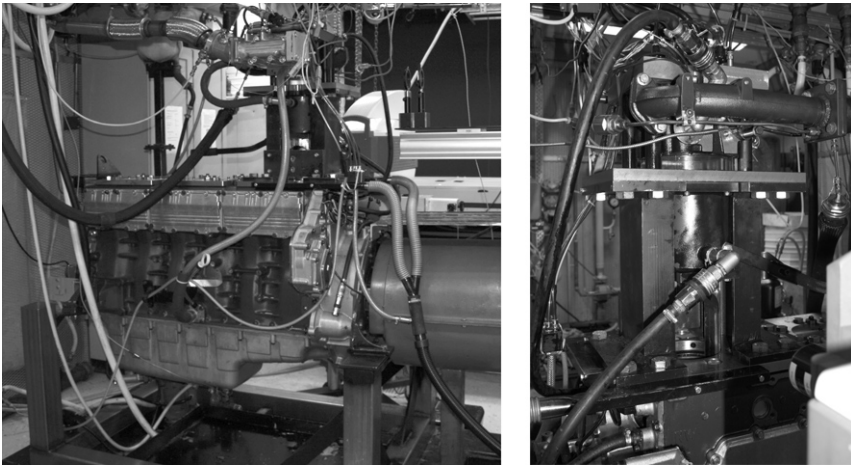

Figure 4.4 *The Scania D12 diesel engine converted to HCCI operation (left) and the Bowditch extension design for providing optical access to the combustion chamber (right).*

In this thesis a six-cylinder, 2 litre/cylinder Scania D12 diesel engine converted to single-cylinder HCCI operation was studied, see Figure 4.4. The engine has been modified to operate with use of port-fuel injection, which generates a basically homogeneous charge. The inlet air is preheated by an electronic heater to initiate HCCI combustion with the selected combination of compression ratio and type of fuel. In order to achieve optical access to the engine, it was equipped with an elongated piston, according to the Bowditch design. A quartz window in the piston crown and a 45 degree mirror placed in the extension below the window makes fluorescence detection from below possible. In Figure 4.5 the principle of the Bowditch extension design is shown [42]. The piston is exchangeable, to allow studies of different combustion chamber geometries to be carried out. To provide optical access from the side, the cylinder was also equipped with a 30 mm high quartz liner.

Despite HCCI engines having many advantages compared with the two well-established engine concepts, there is much work yet to be done before these engines can be used for production applications. The greatest challenge is that of ignition control. Since the charge auto-ignites when it has reached a certain temperature, there is no way of controlling the time of ignition directly. This can only be accomplished indirectly by changing parameters, such as the inlet air temperature, the compression ratio, the fuel properties or the EGR rate. In Paper VI, VIII, and IX single-cycle investigations of e.g. fuel distribution and fuel consumption were performed in HCCI combustion as well as in spark-assisted HCCI, and the experiments and results are discussed in the next chapter.
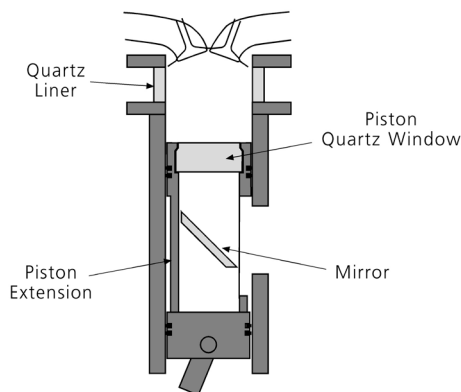

Figure 4.5 *The Bowditch extension design for obtaining optical access to the cylinder of an IC engine.*

4.5 Gas Turbine Combustor

The combustion chamber investigated originates from a commercial Volvo VT 40 micro-turbine. It was originally designed for a maximum thermal power of around 145 kW at full load and 4 bar, which corresponds to a thermal power of around 40 kW when operated under atmospheric conditions. The flow scheme of the atmospheric combustor is shown in Figure 4.6. The combustor is run on natural gas supplied either to the pilot burner (providing a diffusion flame) or to the main burner (providing a premixed flame). Hence, the combustion chamber has the capabilities of both premixed and non-premixed operating modes. The air split between the primary and the dilution zone is 35/65. Air flow to the primary zone also cools the backside liner of the combustion chamber. Before the main flame is swirl-stabilized in the combustion chamber, the fuel and air are premixed. The mixing process starts in the secondary swirl, where the fuel is injected perpendicularly to the air flow. Additional air is then added to the flow in the tertiary swirl. To further improve the mixing, the two swirls are counter-flowing. Further downstream, the remaining airflow is added to the dilution zone. Optionally, the inlet air flow can be humidified up to 20% at full load before entering the combustor chamber.

Optical access to the combustion chamber is provided by adding two side windows and a bottom window. The side windows are placed opposite to each other and are double-walled, providing optical access from the fuel/air inlet in the primary zone down to the dilution zone. The bottom window allows for additional optical imaging of the flame structure from below [43].
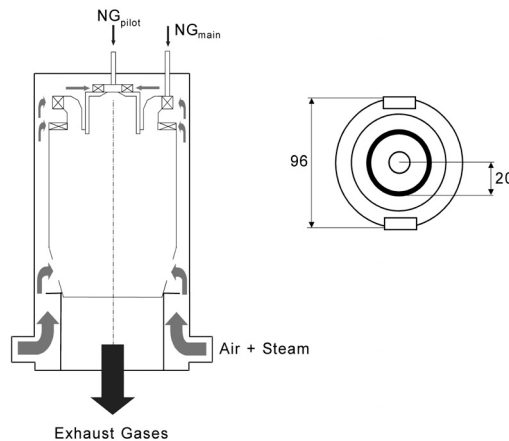

Figure 4.6 *Flow scheme of the atmospheric gas turbine combustor.*

Chapter 5

Applications and Results

The measurements and results presented in this chapter are mainly selected from the published papers included in the thesis, but also from unpublished work that was likewise carried out. The chapter is divided into four sections dealing with visualization of flame fronts, fuel, formaldehyde and visualizations performed in 3D. In addition to the laser based flame front measurements presented in the first section, it also includes a discussion and evaluation of an alternative technique for flame front studies, aiming at determining the equivalence ratio in a point. The first section concerns studies of specific combustion properties in laboratory burners and combustion cells, whereas sections two and three, dealing with fuel tracer and formaldehyde visualization, are directed more at studies of combustion in applied environments, such as in IC engines and in gas turbine combustors. In the last section, a motivation for 3D measurements is given and examples are presented involving 3D imaging of formaldehyde in a laboratory flame as well as of a cold flow of Jet-A vapour.

5.1   Flame Front Visualization

Laser-induced fluorescence imaging of OH is a widely employed technique for flame front studies in reacting flows. Already in 1982 Aldén et al. [44] reported on a technique for mapping the OH profile in a methane/air flame using frequency-doubled radiation from a YAG pumped dye laser and a gated and intensified diode array. This was the first set of one-dimensional measurements of this type ever reported, and was a first step towards 2D imaging. In the work reported by Watson et al. [13], simultaneous PLIF of OH and of CH was performed in a methane jet diffusion flame to determine the relative location and thickness of the two radical fields, as well as to investigate possible mechanisms leading to e.g. local extinction in these types of flames. Within the framework of the thesis OH PLIF with high

repetition rates was utilized to study the temporal evolution of several different combustion processes, and some examples are given in this section.

5.1.1   High-Speed OH PLIF Applications Using a Single Dye Laser

A study of the spatial and temporal evolution of the ignition process induced by a hot jet impinging upon an explosive environment was reported on in Paper I. The experiment was carried out in the two-chamber optical combustion cell described in section 4.2.2. A hydrogen/air mixture was first ignited by a spark plug in the small chamber, and during the combustion process the pressure increased rapidly, forcing hot gases through a small nozzle leading into the second chamber. Potentially, the hot gas jet could cause ignition of the hydrogen/air mixture present in the second chamber. These events were studied by means of high-speed planar laser-induced fluorescence of OH in combination with Schlieren imaging. OH was used as a marker for the reaction zone to monitor whether, where and when ignition occurred, and by means of the Schlieren technique the entire hot jet was imaged. The multi-YAG laser cluster was operated in double pulse mode to generate a rapid pulse train of eight pulses at 532 nm, used to pump a single dye laser. A Rhodamine 590 solution in methanol was used as dye to generate 566 nm and after frequency doubling, laser radiation of 283 nm was reached. A horizontal laser sheet was formed and was directed into the second chamber through a side window as shown in Figure 4.2. The sheet was positioned in front of the nozzle and fluorescence from the OH radical was detected by means of the high-speed framing camera through a third window perpendicular to the sheet. To eliminate spectral interference from reflections and from scattering of laser radiation, a high-reflection filter (HR 275-295 nm) and a UG11 (Schott) filter were mounted in front of the camera lens. Since a single dye laser was pumped by a rapid burst of laser pulses from the YAG cluster, the intensity profile of the output beam suffered from deterioration, and for this reason the on-line beam profile monitoring described in section 3.5.1 was utilized. This profile information was used in the post-processing of the image data to correct for such imperfections.

Figure 5.1 shows a series of four simultaneous Schlieren (a) and OH PLIF (b) images, the white lines in the OH PLIF sequence corresponding to the jet as determined from the Schlieren sequence. The upper edge of each image is located 29 mm downstream from the nozzle and the imaged area covers a 26.5×39 mm^2 area. From the combined measurements, it can be seen that ignition occurred between the first and second image frame, far from the nozzle. One should bear in mind the fact that Schlieren imaging is a line-of-sight technique whereas OH PLIF contain genuine planar information. Accordingly, despite the OH appearing well inside the boundaries of the Schlieren image, this does not necessarily mean that
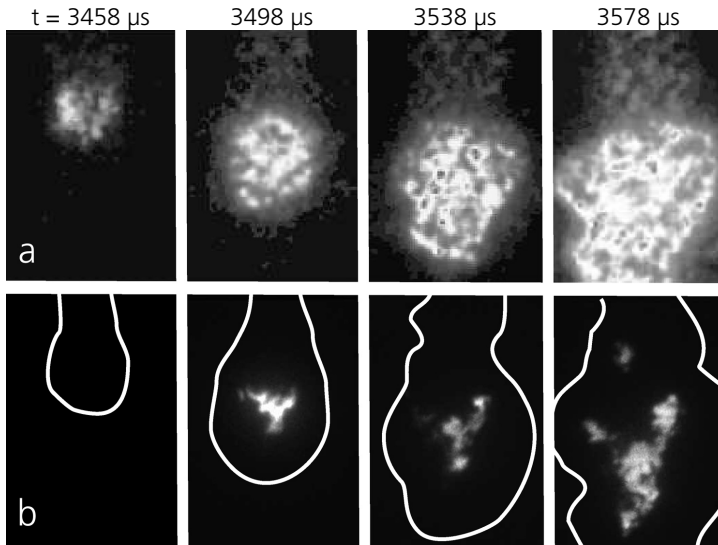
Figure 5.1 *Simultaneous Schlieren imaging (a) and OH PLIF (b) showing the ignition process induced by a jet of hot gases impinging upon a hydrogen/air mixture.*

ignition occurred inside the jet. It might as well have occurred at the boundaries of the jet. Detailed information about the results of this study is reported in Paper I.

Similar experiments in which the multi-YAG laser cluster was used to pump a single dye laser were carried out in other studies as well. In Paper II high-speed OH PLIF was used to study flame front propagation from a spark plug in the constant-volume chamber described in section 4.2.1. In this study the technique was combined with LIF of NO to investigate the governing processes that lead to an electrical signal being sent from an ionization sensor. Furthermore, high-speed fuel tracer LIF was also used in this study. In Paper III high-speed OH PLIF was performed to investigate the combustion in a pulse combustor, and here laser system was phase-locked to the pulsation frequency. Details of the experiments are reported in the respective papers.

5.1.2   Studies in a Low-Swirl Flame Using a Multi-Dye Laser Cluster

In the methane/air flame produced by the low-swirl burner described in section 4.1.1, high-speed OH PLIF was used for tracking of the movements of the flame front over time simultaneous with particle imaging velocimetry (PIV) for imaging the flow field. In addition, filtered Rayleigh scattering (FRS) was employed for imaging the temperature field simultaneous with high-speed OH PLIF. The work was a first step in the development of a detailed Large Eddy Simulation validation
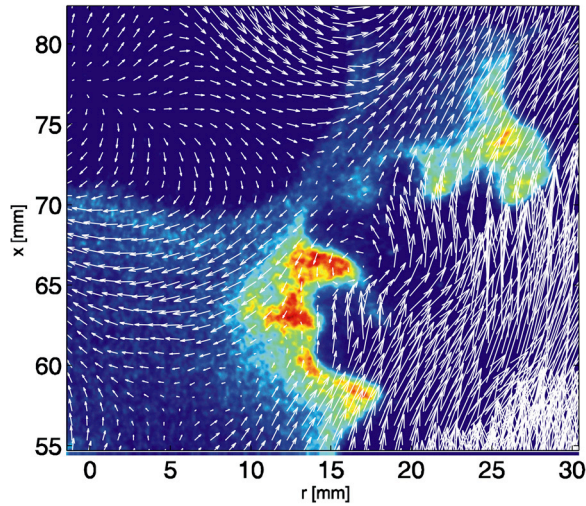
Figure 5.2 *Combined OH PLIF and flow field images from PIV measurements obtained in a low-swirl flame.*

database for this turbulent, premixed methane/air flame. A thorough account of this work and of the background of the study is found in Paper IV.

Four pulses from the multi-YAG laser were used to pump the multi-dye laser cluster for the first time, as shown in Figure 3.4. For some of the measurements, also on-line monitoring of the sheet intensity profile was utilized, allowing corrections of intensity inhomogenities to be made. However, the marked deterioration of the beam quality observed when the YAG cluster pumps a single dye laser was not present here, since the dye cells in each of the four lasers were pumped at the comparatively slow repetition rate of 10 Hz. When carrying out simultaneous OH PLIF and PIV measurements two counter-propagating sheets were overlapped above the burner, and for simultaneous OH PLIF and FRS measurements a similar arrangement was used. PIV was performed using two pulses from a frequency doubled Nd:YAG laser, whereas for FRS an alexandrite laser generating laser radiation at 254 nm was utilized. Figure 5.2 presents an example of the OH distribution together with the flow field from the PIV for the upper part of the flame. In the displayed region, the flow field which has a Reynolds number of 30 000 at the exit of the nozzle, gets increasingly complex and shows strong interaction between the flame and flow. In addition, dilution of the mixture occurs due to entrainment of air from the surrounding co-flow, and extinction finally occurs.

A temperature map generated from the FRS measurement is shown in Figure 5.3 together with four corresponding OH PLIF images. The consecutive OH PLIF images have a 400 µs temporal separation. The temperature image is measured
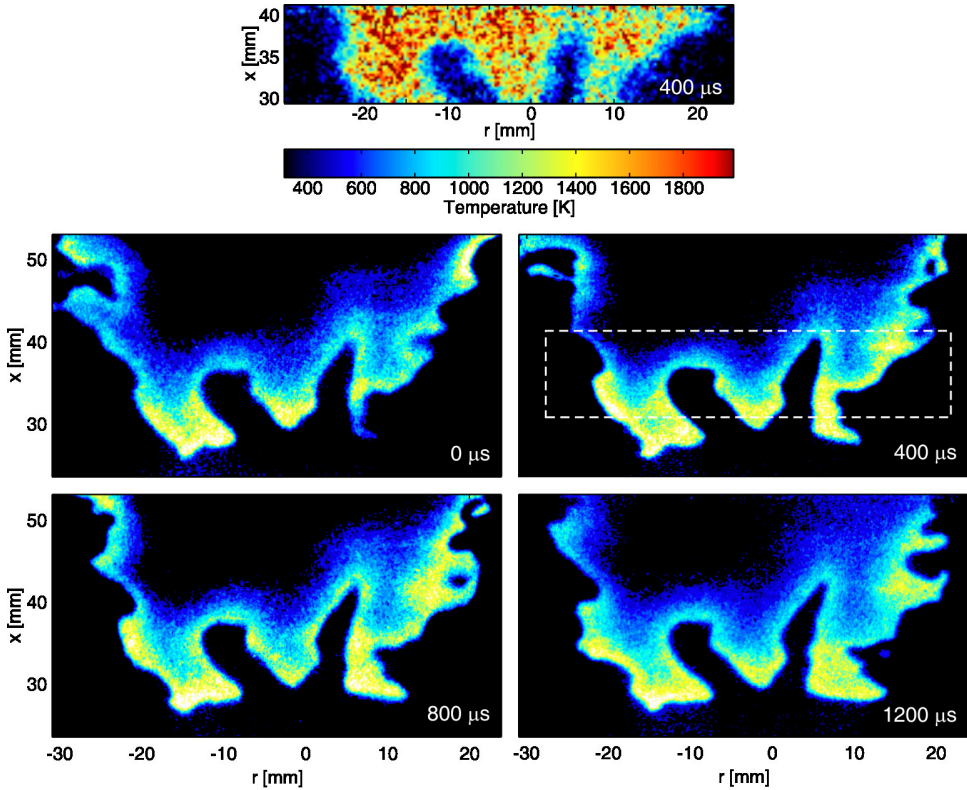
Figure 5.3 *Simultaneous OH PLIF and temperature field measurements using filtered Rayleigh scattering, in the low-swirl flame.*

simultaneously with the second OH image, and the dotted line in the figure indicates the area covered by the temperature map. As can be seen in the OH sequence, the central parts of the flame structures show only slow movements and are nearly two-dimensional in appearance, whereas in the outer regions the effects of the swirl are more pronounced. The reader is referred to Paper IV for detailed information about the experiments.

5.1.3   Evaluation of a Chemiluminescence Sensor

As an alternative to laser diagnostics, chemiluminescence from excited flame radicals, such as OH^*, CH^*, and C_2^*, can be utilized to measure various combustion characteristics. Chemiluminescence from OH^* and CH^* has been used earlier to measure the global equivalence ratio in lean flames of premixed methane and air, as reported by Higgins et al. [45,46] and Docquier et al. [47]. Spatially resolved measurements of the three radicals carried out in fuel rich premixed methane/air

flames have been reported by Kojima et al. [48]. In Paper V a chemiluminescence sensor (CS) is presented, with potential for monitoring spatial and temporal inhomogenities in lean premixed mixtures in industrial gas turbine combustors. The sensor collects the chemiluminescence by means of Cassegrain optics, as shown in Figure 5.4, similar to the one presented by Akamatsu et al. [49]. The light is focused on an optical fibre and led to a photo-detector unit, where it is divided up by means of dichroic mirrors and interference filters into the three spectral regions of the emissions that the radicals produce, and the light is finally detected by photomultipliers.
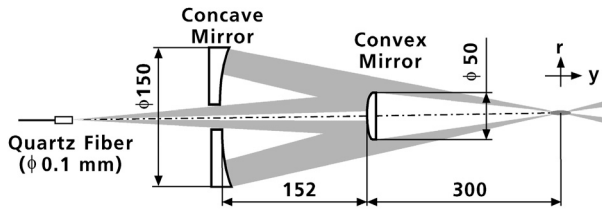
Figure 5.4 *The Cassegrain optics of the chemiluminescence sensor. Two mirrors are used to collect light from the probe volume and focus it onto an optical fibre.*

Measurements to evaluate the spatial and temporal response of the sensor were made in a small laminar cone-shaped flame produced by the water-cooled burner, described briefly in section 4.1, as well as in the combustion environment of an atmospheric gas turbine combustor. Both sets of measurements were compared with reference data from PLIF experiments carried out in the same flames. The results from the laboratory flame used in evaluating the sensor resolution are described here, whereas the laser diagnostics performed in the gas turbine combustor are presented in section 5.2.1.

    According to Akamatsu et al. [49], the focus of the Cassegrain optics, i.e. the probe volume, is 200 μm in diameter and 1.6 mm long. Provided that no light is collected from outside this probe volume, this was claimed to define the spatial resolution of the sensor. The spatial resolution was evaluated by testing the sensor's ability to detect the thin flame front (OH*) in the cone flame, horizontally traversing the probe volume across the flame both in the y- (longitudinal) and the r-direction (transverse) as shown in Figure 5.4, and the obtained data was compared with the OH LIF data. Since a stable flame was used for the study, the high-speed capability of the laser system was not utilized. The results are summarized in Figure 5.5. As indicated in the figure, the spatial resolution is a complex parameter to evaluate, since it is not the same in all three spatial directions. As can be seen in the figure the peaks of OH detected by the LIF and detected by the sensor when scanning in the

transverse direction coincide rather well. It should be noted that the LIF measurements also show a lower plateau outside the peaks of the flame front, since some of the OH is present in the post flame gases as well. However, the sensor measurements only detect chemically excited OH*, present only in the reaction zone. With this in mind the match of the two flame front positions appear very good. However, the longitudinal scan by the sensor does not show any indication of a flame front at the expected positions, but instead a rather constant chemiluminescence intensity is detected, independent of the position of the probe volume. Thus, light is in fact collected not only from the probe volume as claimed but also from the cone-shaped field of view of the collecting optics as shown in Figure 5.4. In Paper B a more thorough theoretical investigation of these effects is reported.
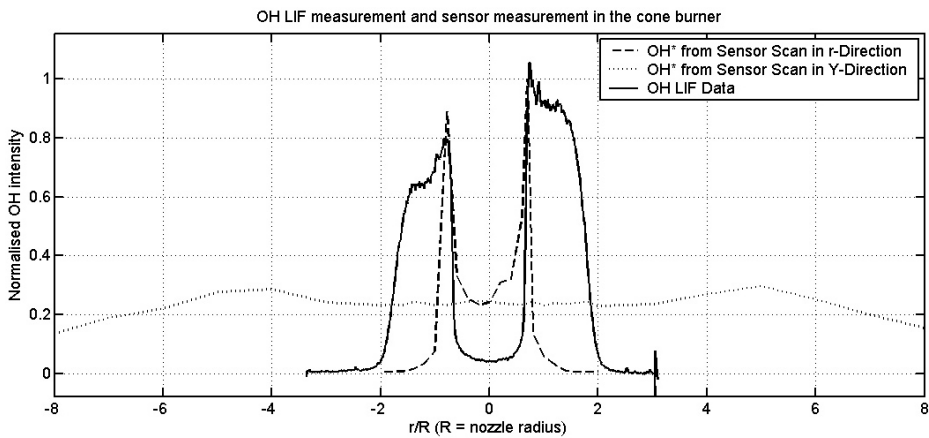
Figure 5.5 *OH distribution across the cone flame as measured by OH PLIF and the chemiluminescence sensor.*

An initial and very straightforward experiment for testing the temporal response of the sensor was performed in the conical burner by positioning the probe volume at the flame front and stepwise shortening the data acquisition time. It was found that for data acquisition times shorter than 200 μs, the measured equivalence ratios deviated noticeably from corresponding values retrieved with longer integration times. For accurate measurements of the equivalence ratio it is thus not advisable to use acquisition times shorter than 200 μs. In order to determine whether the spatial and the temporal response of the sensor was satisfactory for applications in gas turbine combustors, an atmospheric gas turbine combustor was characterized by means of laser diagnostic techniques as presented in section 5.2.1. More information about the evaluation of the performance of the sensor is reported in Paper V.

5.2   Fuel Tracer PLIF

Fuel visualization is an important part of the diagnostics of combustion processes and can serve as a valuable tool e.g. for engine developers. The capability of tracking the evolution of combustion over time in such a device adds a useful dimension in terms of measurement data. PLIF can be used for fuel visualization experiments, and is generally performed by excitation of a fluorescent fuel tracer that is added to a non-fluorescent fuel. In Paper VI the multi-YAG and the framing camera system has been utilized for multi-frame fuel visualization in an HCCI engine. The same diagnostic approach was used to visualize temporally resolved OH distribution in a small atmospheric gas turbine combustor in which also fuel tracer LIF was performed using an excimer laser. Part of this study is presented in Paper V. As mentioned earlier, high-speed fuel tracer PLIF was also used together with OH and NO PLIF in the study involving the ionization sensor in Paper II.

5.2.1   Fuel and OH Visualization in a Gas Turbine Combustor

To evaluate the capabilities of the chemiluminescence sensors to measure in industrial gas turbine combustors, the micro-turbine combustor described in section 4.5, run on natural gas, was evaluated in terms of temporal and spatial scales by means of laser diagnostics, with which measurements from the sensor could be compared, see Paper V. The fuel distribution in this combustor was visualized by single-shot fuel tracer PLIF using an excimer laser, whereas temporally resolved OH PLIF was performed employing the framing camera and a dye laser pumped by the multi-YAG laser cluster.

Natural gas consists mainly of methane, which does not show any fluorescence when illuminated by laser radiation in the wavelength region of these lasers. Since natural gas is generally not a fuel of fixed composition, the composition is varying from one batch to another, it can contain fluorescent impurities. However, in order to adequately visualize the fuel distribution by means of LIF, it is essential to have a sufficiently strong and repeatable fluorescence signal. To achieve this a fluorescent tracer species must be added to the gaseous fuel. In the presented measurements acetone was chosen to mark the fuel. For seeding the acetone to the natural gas a device letting the fuel bubble through liquid acetone was designed.

A krypton-fluoride (KrF) excimer laser was selected as the means for exciting the acetone. This laser produced pulsed UV radiation of 248 nm wavelength with a pulse energy of around 200 mJ and a pulse duration of 20 ns. The laser beam was formed into a horizontal sheet and was directed into the combustion chamber through one of the side windows on the turbine combustor. Fluorescence was detected from below (see Figure 5.6) by means of an image intensified CCD camera (La Vision

FlameStar). In using a Nikon f50 mm/f#1.2 glass lens for signal collection, some of the fluorescence is lost since it partly occurs in the UV spectral region, where glass does not transmit. On the other hand, for the same reason, interference from scattered laser radiation is effectively discriminated. In the performed measurements the signal levels were sufficiently high to allow a glass lens assembly to be used.
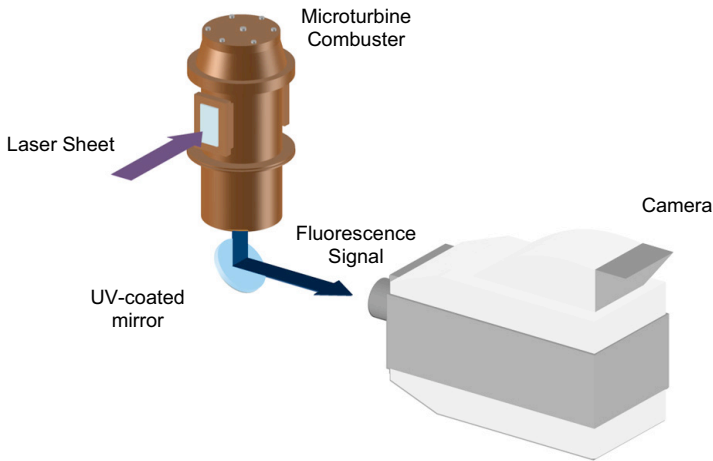
Figure 5.6 *Utilization of optical access to the gas turbine combustor for PLIF measurements of OH and fuel tracer distribution.*

The position of the flame front is an important consideration, and in order to determine the flame front position in the gas turbine combustor, OH PLIF measurements were performed. The OH radical is formed close to the flame front and was used as a flame front marker, but the lifetime of the OH is long enough for it to also mark some of the post flame gases in the atmospheric gas turbine combustor. In the OH visualization experiment, the high-speed framing camera was used together with the Nd:YAG laser cluster operating in single pulse mode for pumping a dye laser, producing a pulse train of four rapid pulses with a time-separation ranging from 25 µs to 40 µs. The laser beam was formed into a laser sheet and was directed into the combustion chamber, in the same manner as for the fuel tracer PLIF, as shown in Figure 5.6. The fluorescence from OH located in the intersection region of the sheet and the gases in the combustion chamber, was imaged on four of the CCD detectors in the framing camera, providing a field of view of nearly the entire width of the burner (100 mm).

A comparison of the distributions of the fuel and the OH is shown in Figure 5.7. The images are centred on the pilot fuel nozzle and images were acquired at three different distances downstream from the nozzle. The position of the outlet for the

Figure 5.7 *This image set shows a comparison of the OH distribution (left) and the fuel distribution (right) in the three measurement planes. Note that these images are not recorded simultaneously and are thus showing physically uncorrelated events.*

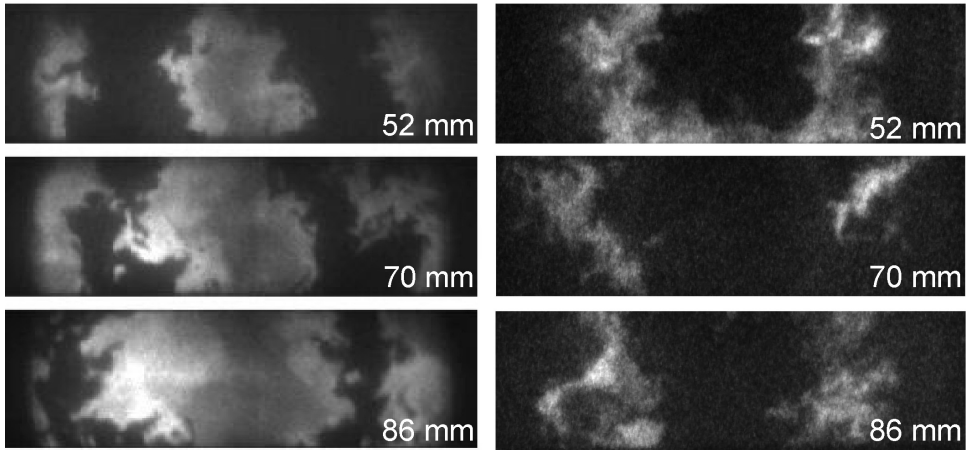premixed natural gas and air corresponds well with the fuel distribution in the upper right corner the figure. It is interesting to note that the unburned fuel is never transported to the centre of the combustor. Nevertheless, OH radicals are found in reasonably high concentrations at this location, leading one to conclude that there are recirculation zones that transport burnt gases, containing OH, into this region. This means that in the upper parts of the combustor, no combustion takes place in the centre. Note that this can be concluded from neither the OH measurements nor the fuel measurements alone, hence only by the combination of the two techniques this important result can be revealed.

By comparing OH images with different time-separations it was possible to determine at what time scales the flame front structures change. In Figure 5.8 a section of an OH image is enlarged and compared with the same section in three consecutive images. The fact that after a period of 25 µs the structures of the flame front do not appear to have changed appreciably, but that after 75 µs the structures are no longer recognizable indicates that a measurement acquisition time significantly longer than ~50 µs cannot be considered as instantaneous in this type of burner. Since the measurement times of the chemiluminescence sensor range from milliseconds up to several seconds, the sensor measurements must thus be considered to be time averages. Further information about the experiments and the evaluation of the chemiluminescence sensor is reported in Paper V.
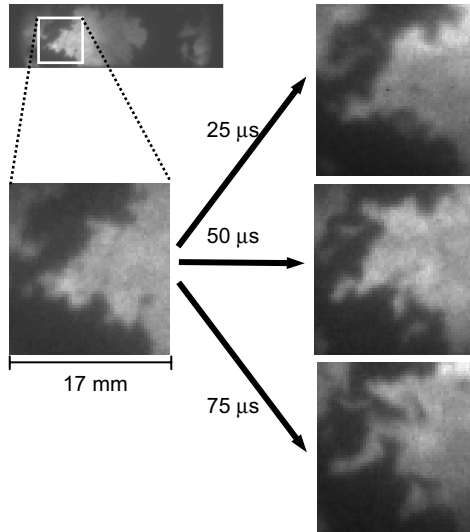
Figure 5.8 *Comparison of images showing OH structures with different time delays.*

5.2.2   Fuel Visualization in an HCCI Engine

As mentioned previously, controlling combustion phasing is one of the major issues with HCCI combustion. Strategies for decreasing the combustion rate are of interest and one such strategy could be to change the flow conditions in the cylinder. One way of achieving this is by using geometry generated turbulence, and in Paper VI high-speed fuel tracer PLIF was utilized to study the effects this had. The Scania D12 engine redesigned for HCCI operation described in section 4.4.1 was used in the study, and to vary the degree of turbulence two different piston crown geometries were employed. Both piston crowns were made of quartz to enable optical access, one of them being flat, resulting in a disk shaped combustion chamber at top dead centre (TDC), and the other one with a deep square bowl in the piston. The narrow squish in the latter case was expected to generate a swirling motion of the charge into the bowl during the compression stroke. Ethanol was used as fuel and since it is a non-fluorescent fuel, a fluorescent tracer had to be added. Acetone and 3-pentanone would both have been suitable tracers for the fuel but since previous work had shown that 3-pentanone, as opposed to acetone, suffers from a decrease in the fluorescence signal later in the compression stroke and after the onset of combustion, acetone was selected [50,51].

The high-speed laser and detector system was used for single-cycle-resolved PLIF imaging of the fuel distribution for both piston geometries. Laser radiation of 266 nm was used to excite the acetone, and the laser beam was formed into a

horizontal sheet and was directed into the combustion chamber through the quartz cylinder liner, see Figure 5.9. In the case of the square bowl piston, the sheet was positioned half way up from the bottom of the bowl. Subsequent fluorescence was imaged through the quartz piston via a UV-enhanced mirror, located in the piston extension, onto the framing camera. To prevent scattered laser light at 266 nm from reaching the detectors a quartz cuvette containing liquid n.n.-dimethyl-formamide was used as a long-pass filter mounted in front of the camera lens. In addition, a short-pass filter with a cut-off wavelength at 500 nm was used to eliminate interference from residual 532 nm laser light. The engine speed was kept constant at 1200 rpm, corresponding to a combustion cycle frequency of 10 Hz, and a pulse from a crank-angle encoder was used for continuous triggering of the laser and detector system.
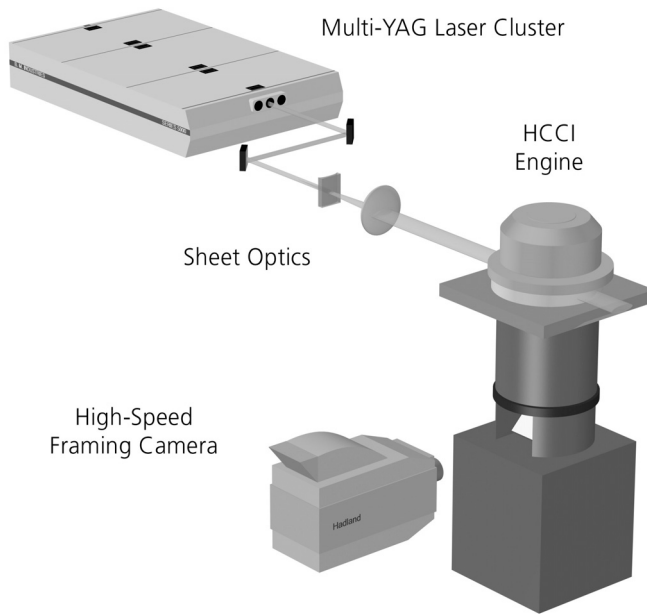
Figure 5.9 *Schematic presentation of the experimental setup used for high-speed fuel visualization in an HCCI engine.*

A PLIF image sequence of seven images showing the fuel distribution in a single cycle for each of the two geometries is displayed in Figure 5.10. The initial width of the laser sheet was 31 mm, however, for the square bowl geometry the sheet had to pass through the solid quartz piston in order to reach the inside of the bowl, and this has a strong focusing effect on the sheet. To compensate for this effect, the sheet was made divergent before entering the combustion chamber. However, with the optics
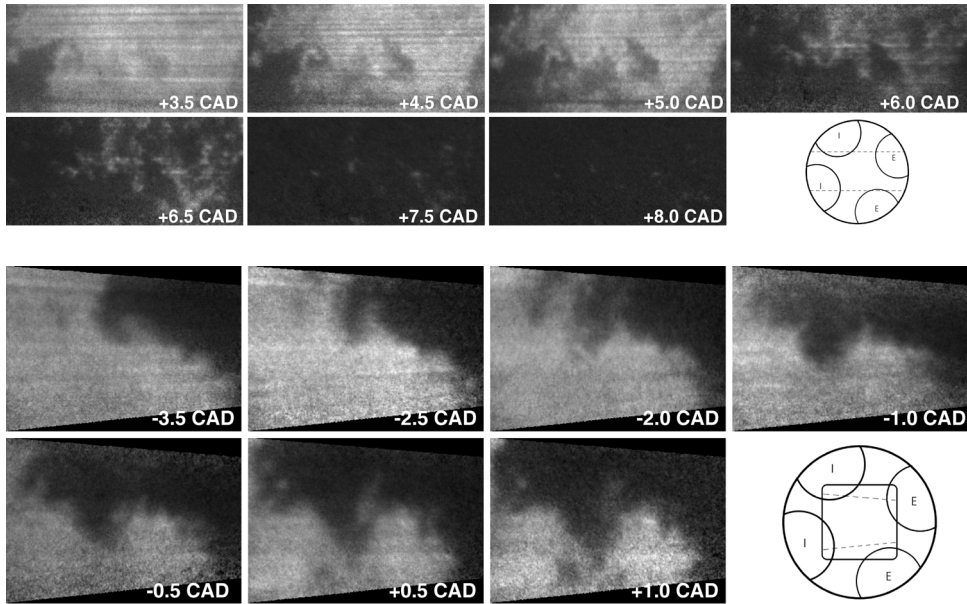
Figure 5.10 *Image sequences of seven single-shot PLIF images showing the fuel consumption for the two piston geometries at λ = 3.3. The upper sequence represents the case of the disc piston in which a 30 mm × 67 mm area was imaged, whereas the lower sequence represents the case of the square bowl piston in which a 30 mm × 45 mm area was imaged.*

available it was not possible to fully compensate for this and therefore a slight convergence remain, as can be seen in the lower sequence in the figure.

   For the case of the disk geometry the fuel consumption starts at multiple ignition points, most likely due to temperature inhomogenities in the charge, and the progress through distributed reactions. This behaviour would be expected under standard HCCI operation. However, a clearly different behaviour can be seen in the fuel consumption process in the case of the square bowl geometry. Here ignition appears to occur at only a few points, which gives rise to a more flame-front-like combustion, thus to much sharper concentration gradients. It is also clear that the fuel consumption process for this case is much slower. To more adequately distinguish between flame-front-like combustion and combustion with multiple ignition points and more gradual fuel consumption, the intensity histograms of the image sequences were examined, an example being shown in Figure 5.11. Because of the sharp gradients connected with images of flame front propagation, this type of combustion gives rise to well-separated groups of intensity levels, corresponding to burnt and unburnt regions, respectively, whereas a more gradual fuel consumption results in a more even intensity distribution. In the histograms for the square bowl

geometry, a clear bimodal structure can be seen which is not present for the disk geometry. For further details regarding the experiments and the results obtained, the reader is referred to Paper VI.
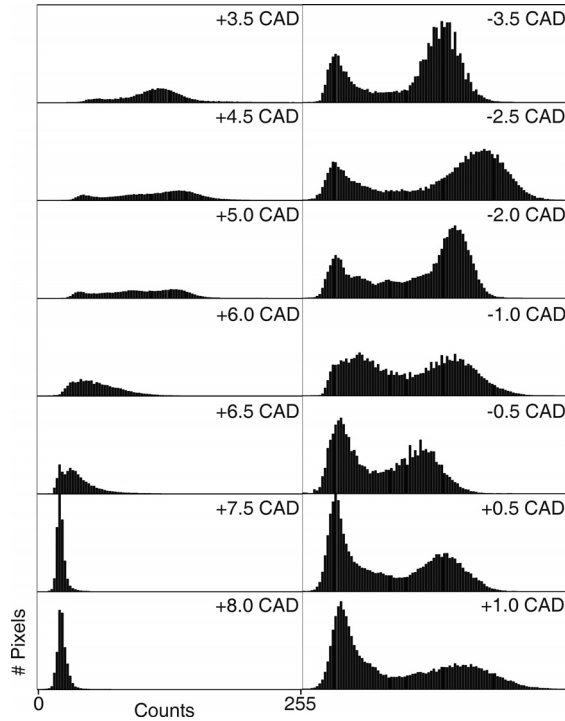
Figure 5.11 *Intensity histograms for the disc geometry (left) and the square bowl geometry (right), both determined from the sequences for λ = 3.3 shown in Figure 5.10.*

5.3   Visualization of Formaldehyde

For the purpose of extending the wavelength palette of the multi-YAG laser system from the original second and fourth harmonic, the harmonic generation and beam combining scheme was redesigned. With the new design also the third harmonic of the Nd:YAG, 355 nm, can be generated. This wavelength is of great interest for diagnostic purposes since it enables high repetition rate pumping of dye lasers in a different wavelength region than those the original system could reach, thus making the probing of new species, such as CH, C_2 and NO, feasible. As mentioned in section 2.4, this wavelength can also be employed for formaldehyde measurements

with the use of PLIF. In Paper VII, the performance of the redesigned laser system is demonstrated by the successful high-speed imaging of formaldehyde in a laboratory flame and in an SI engine. In Papers VIII and IX the system was utilized in single-cycle resolved studies of formaldehyde distribution in the combustion chamber of a truck-size HCCI engine with the aim of tracking the evolution of the combustion in terms of rate and of spatial structures, and for comparing standard HCCI operation with spark-plug and laser spark-assisted HCCI operation.

5.3.1 Initial Testing of High-Speed Formaldehyde PLIF

The objective of the work presented in Paper VII was to determine the feasibility of ultra-high-speed formaldehyde PLIF in flames as well as in engines, using the multi-YAG laser cluster with the redesigned harmonic generation and beam combining scheme for operation at 355 nm. Experiments were carried out both in a flame and in a small engine using the experimental setup shown in Figure 5.12. The beam from the multi-YAG laser was shaped into a narrow sheet that was directed into the ongoing combustion process (flame or engine). Formaldehyde was excited in the intersection region with the laser sheet, and the subsequent fluorescence occurring between 350 and 550 nm was detected either by the framing camera for the high-speed imaging tests, or by a CCD detector mounted on a spectrometer (ACTON)
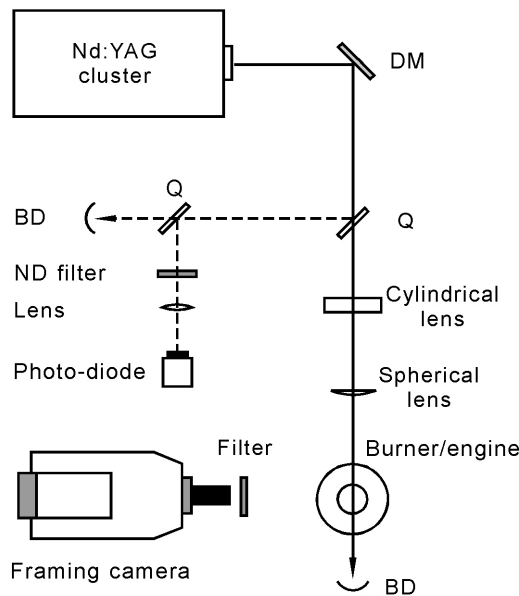
Figure 5.12 *Experimental setup used for testing the redesigned multi-YAG laser cluster for high-speed formaldehyde PLIF.*

for spectroscopic investigation of the fluorescence. To eliminate interference from reflections of laser light, a set of filters was placed in front of the collection optics. Reflections at 355 nm were eliminated using a long-pass GG385 filter, whereas reflections from residual 532 nm were eliminated by use of a band-pass filter, BG3, centred at 360 nm.

A quartz plate (Q) was used to link off a small fraction of the laser beam, and the intensity of this reflection was further reduced by means of neutral density filters before the beam was focused on a UV sensitive photo-diode. The signal from the photo-diode was used for on-line monitoring of the individual laser pulse intensities and the time-separations between them.

The water-cooled cone burner producing a stable flame as mentioned in section 4.1 was used for the flame experiments. The burner was supplied with air and DME $((CH_3)_2O)$ as fuel, the latter being selected primarily because of the high concentrations of formaldehyde it produces [52]. Prior to the high-speed measurements, a spectroscopic investigation of the fluorescence was made so as to ensure that the fluorescence emission originated from formaldehyde. This was done by comparing the experimental spectrum to known flame emission spectra exhibiting the features characterizing formaldehyde [53]. An example of the fluorescence spectrum from the flame is displayed in Figure 5.13, curve A.
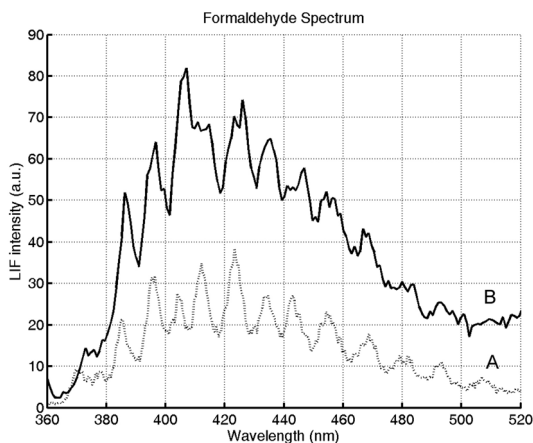
Figure 5.13 *Spectra of laser-induced fluorescence from formaldehyde in a flame (A) and in an engine (B).*

For time-resolved measurements of formaldehyde in the flame the multi-YAG cluster was operated in both single and double pulse mode. In the example presented in Figure 5.14 the laser was operated in single pulse mode, producing a burst of four laser pulses with a pulse energy of 70 mJ and with time-separations of 100 µs. In the
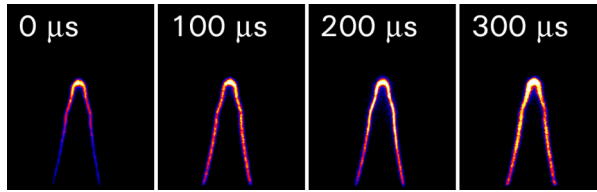
Figure 5.14 *An image sequence of high-speed formaldehyde PLIF in a laminar premixed DME/air flame.*

image sequence a thin, cone-shaped region can clearly be seen, corresponding to the reaction zone in which intermediate species such as formaldehyde are formed [54]. Due to the laminar flame and the short time-separation between images, virtually no changes in the flame structures can be observed in the sequence. Nevertheless, the experiment shows that high-speed formaldehyde PLIF experiments using the multi-YAG laser operating at 355 nm are feasible, at least in laboratory flames, and that they can provide data with a decent signal-to-noise ratio.

Tests for evaluating the system's capabilities of high-speed formaldehyde PLIF measurements in engine environments were carried out in a small four-stroke spark-ignition engine. The optical engine was described briefly in section 4.4, and in the tests presented here, optical-grade methanol was used as fuel. Spectroscopic measurements were performed for the same reason as for the flame, and an example of the spectrum of the fluorescence induced in the engine is shown in Figure 5.13, curve B. As can be seen in the figure, the emission spectrum from the engine resembles rather closely the spectrum from the flame.

By synchronizing the laser and the detector system to the engine cycle, using a crank-angle encoder, entire image sequences showing the time evolution of the formaldehyde distribution in the engine could be recorded. Because of the lack of
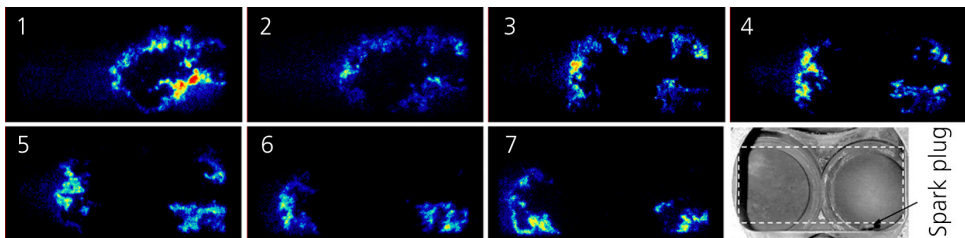
Figure 5.15 *A sequence of seven formaldehyde PLIF images from a single engine cycle, showing the propagation of a flame front initiated by the spark plug, shown at the lower right. The time-separations between the successive images were 80 μs, and the engine was running at 2400 rpm.*

laser sources of high repetition rate and suitable wavelengths, this has not previously been feasible for formaldehyde. An example of this is shown in Figure 5.15 involving seven image frames of formaldehyde fluorescence induced by laser pulses with a pulse energy of ~25 mJ, and with time-separations of 80 µs, corresponding to 1.15 CAD at an engine speed of 2400 rpm. The dotted line in the photograph at the lower right in the figure marks the imaged area, shown in relation to the spark plug. In the seven-frame sequence, formaldehyde can be seen in the pre-heat zone in front of a flame front propagating from the spark plug.

Regarding the optical properties, the environment in this type of production-type engine is quite harsh, since lubricant oil is likely to escape past the piston rings and entering the combustion chamber, interfering with the formaldehyde fluorescence by fluorescence and Mie scattering from the oil. Despite this problem, the results revealed an acceptable signal-to-noise ratio (~10), indicating a high potential for cycle-resolved measurements also in more refined optical engine with a dry liner and dry piston rings.

5.3.2   Cycle-Resolved Formaldehyde PLIF in an HCCI Engine

Formaldehyde is formed through the low-temperature oxidation in the early stage of the ignition process of hydrocarbons and air, and consumed later in the main combustion process. In HCCI combustion certain fuels generate low-temperature reactions (cool-flames) prior to the main combustion event, thus by studying the formation and consumption of formaldehyde, these cool-flame regions as well as the early phase of the main combustion can be investigated. It has also been shown that, after the cool-flame region, formaldehyde can serve as a fuel marker, just as well as an added tracer [55]. This allows fuel visualization of non-fluorescent fuels to be made without having to add a tracer to the fuel mixture.

In Paper VIII the redesigned multi-YAG cluster for generation of 355 nm was used together with the high-speed framing camera to generate unique single-cycle resolved measurements of formaldehyde distribution in a Scania D12 truck-size HCCI engine. N-heptane was used as fuel, which shows characteristic cool-flame behaviour. The laser diagnostic technique was used to study the formation and consumption of formaldehyde in terms of rate and of the spatial structures for different stoichiometries. The experimental setup was quite similar to that used for fuel tracer PLIF as shown in Figure 5.9. A sequence of seven formaldehyde PLIF images is presented in Figure 5.16, for which the image time-separation is 70 µs, corresponding to 0.5 CAD at an engine speed of 1200 rpm. Interference from scattered laser light at 355 nm was eliminated by the use of a long-pass GG385 filter placed in front of the camera lens and residual 532 nm was blocked by a short-pass filter with a cut-off wavelength at 500 nm. By utilizing high-speed laser diagnostics, the averaging effects introduced by the cycle-to-cycle variations in combustion
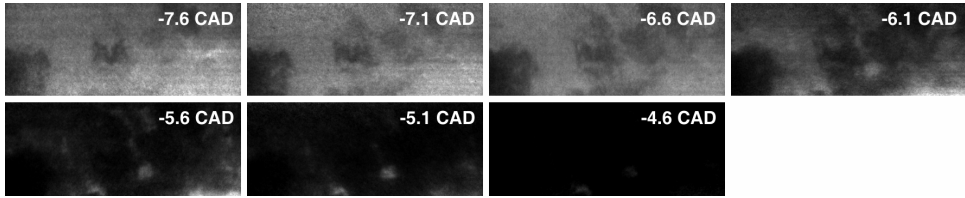
Figure 5.16 *A sequence of seven single-shot PLIF images seprated by 70 μs, showing the formaldehyde consumption in an HCCI engine running at 1200 rpm for λ = 3.5.*

phasing were avoided. In the figure it can be seen that the formaldehyde is gradually consumed from multiple ignition points. The heterogenous structure is a result of varying combustion phasing in the different parts of the combustion chamber.

Binary images were created by applying a threshold to the greyscale images. The threshold level was placed just above the noise level of the detector to separate areas containing formaldehyde fluorescence signal from areas without fluorescence signal. The binary images were then integrated in order to determine the fraction of surface covered by formaldehyde in each image frame. In Figure 5.17 the results from single engine cycles are plotted together with the corresponding heat-release curves for four different stoichiometries. As can be seen in the figure, the formaldehyde consumption was found to be clearly more rapid for richer mixtures. Similar
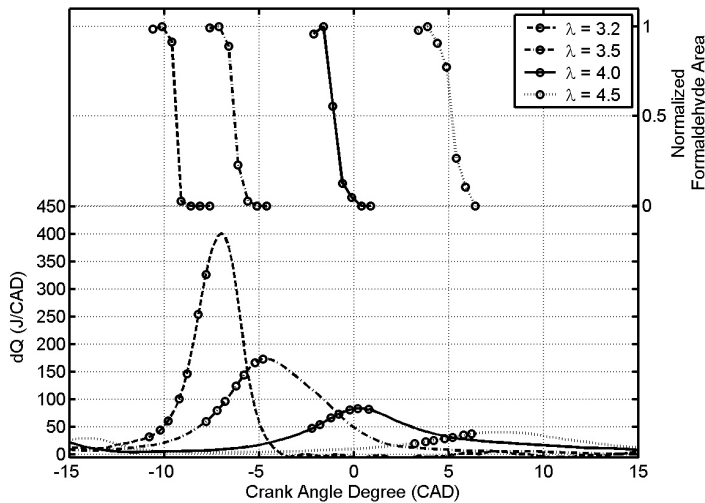
Figure 5.17 *Cycle resolved formaldehyde surface fraction in the acquired images at the main combustion event is shown together with the corresponding rate of heat-release curves for four different stoichiometries.*

diagrams from earlier in the engine cycle showed that the time of formaldehyde formation seemed less dependent on stoichiometry.

The approach of probing formaldehyde by use of the high-speed diagnostic system enabled us to perform for the first time single-cycle resolved measurements of a non-fluorescent fuel without having to add a fluorescent tracer. This is of particular interest when an engine is run on heavier fuel fractions for which no suitable tracers exist. Further details of the measurements and the results are reported in Paper VIII.

In Paper IX the same experimental approach was used in an investigation aimed at determining how and to what extent a controlled spark influences the auto-ignition process in HCCI combustion, and whether spark-assistance can be used for ignition control. The effects of a laser-induced spark as well as of the spark from a spark-plug were compared with conventional HCCI operation. The laser spark was generated by a second Nd:YAG laser with a pulse energy of 25 mJ at 1064 nm, and the laser beam was focused in the centre of the combustion chamber, producing a plasma that could potentially initiate combustion. A mixture of 80% iso-octane and 20% n-heptane (PRF80) was used as fuel, the latter component being responsible for the cool-flame characteristics and hence for the early formaldehyde formation. From the heat-release curves no clear difference could be seen between the three cases of ignition, however, with the optical techniques this could be evaluated. Formaldehyde PLIF imaging with high repetition rate was used to detect any changes in the spatial behaviour of the combustion, such as revealing whether any flame-front-like propagation from the position of the spark was present. Simultaneous with the PLIF, also Schlieren imaging and chemiluminescence imaging was performed. Further information on the results can be found in Paper IX.

5.4   Visualization in Three Dimensions

Combustion processes, especially in turbulent flows, are truly three-dimensional phenomena. Visualization of combustion species in two dimensions provides important information about the processes being studied, and by extending the technique by use of high repetition rate imaging, also the time evolution of the processes can be studied. In some applications, however, two-dimensional information is not sufficient to obtain all the desired information. One problem connected with conventional planar laser-induced fluorescence arises when images show small flame islands, which appear to have no physical connection with the main flame zone surrounding them. With only two-dimensional information one cannot conclude with certainty whether these flame islands are in fact isolated or if they are simply an effect of the three-dimensional main flame bending in and out of the laser sheet. Such information can only be revealed by measurements involving all three

spatial dimensions. Three-dimensional laser-induced fluorescence (3D LIF) measurements can be performed by recording a stack of closely spaced PLIF images. The first report made on three-dimensional measurements in an IC engine was made by Mantzaras et al. [56], who employed four closely spaced laser sheets of different wavelengths to visualize burned and unburned regions in the engine. This was done by detecting Mie scattered light from particles seeded into the engine, the light being recorded from all four planes simultaneously. Another approach to obtaining three-dimensional information is to use a rapidly scanning mirror to sweep a laser sheet through the measurement volume, as described in section 3.5.2. In this approach, it is highly important that the signals from all planes be recorded faster than the characteristic time scale of the process being studied. This approach has previously been used for 3D visualization, see [57,58].

5.4.1   3D Visualization of Formaldehyde in a DME/Air Flame

In Paper VII the high repetition rate of the multi-YAG laser/framing camera system was used to capture 3D LIF images of the formaldehyde distribution in a small premixed DME/air flame, as described in section 5.3.1. The experimental setup was similar to that shown in Figure 3.10. The configuration for third-harmonic generation of the multi-YAG system was utilized, and the laser was operated in double pulse mode, delivering a burst of eight laser pulses at 355 nm. The time-separation between the pulses was set to 13 µs. To sweep the laser beams, the galvanometric scanning mirror (GSI Lumonics) described in section 3.5.2 was used, with the scanning frequency set to 40 Hz and the sweep amplitude adjusted to obtain a suitable sheet spacing. The mirror directed the beams through a cylindrical and a spherical lens, and for obtaining parallel laser sheets, the scanning mirror was placed in the focal plane of the spherical lens. This created laser sheets ~45 mm in height and with a sheet spacing of 1.1 mm. The focus of the laser sheets was positioned above the centre of the burner nozzle. Formaldehyde fluorescence from the planes was detected by the framing camera with a Nikon f = 50 mm camera lens and the same optical filters as described in section 5.3.1.

To ensure that the laser was firing at the same position in the mirror scan each time, the laser/detector system was synchronized with the scanning of the mirror. This was achieved by using the 40 Hz signal from the function generator to create a 10 Hz trigger signal for the laser, phase-locked to the signal, which governed the scanning of the mirror.

To separate fluorescence areas from the background, each 2D image was converted from an 8-bit greyscale image to a binary image by means of signal thresholding before the images were assembled to create a 3D surface. Such a 3D surface of the formaldehyde distribution in the flame was finally produced by shape-

based interpolation between the laser planes [59]. An example of the results is shown in Figure 5.18.
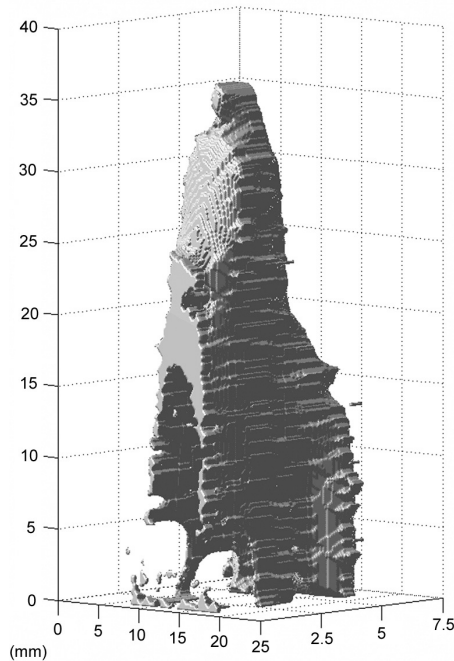
Figure 5.18 *A three-dimensional measurement of the formaldehyde distribution in a slightly turbulent DME/air flame.*

5.4.2   3D Visualization of Jet-A Vapour

Jet-A is a multi-component fuel containing several fluorescent and non-fluorescent species. A potential problem related to LIF measurements of this type of fuel is the high absorption of laser radiation in the UV region by large hydrocarbon species. In a study by Löfström et al. [60] the absorption properties of Jet-A were investigated in order to determine the expected attenuation of a laser beam at different wavelengths. According to the study, Jet-A generates a broadband fluorescence spectrum between 300 nm and 420 nm when excited at around 290 nm. Jet-A can be excited by laser radiation of 266 nm wavelength, however, above 310 nm the fuel is practically transparent making LIF measurements infeasible.

Three-dimensional imaging of Jet-A using LIF was performed in the thesis work as a demonstration. The experimental setup is depicted in Figure 5.19, and shows the multi-YAG cluster together with the galvanometric scanning mirror and framing
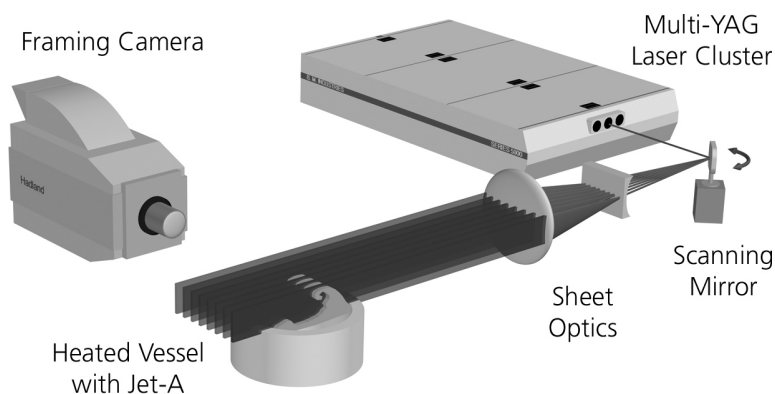
Figure 5.19 *Experimental setup for 3D imaging of Jet-A vapour from a heated vessel.*

camera used in the same manner as in the formaldehyde 3D imaging described in the previous section.

A small heated vessel containing liquid Jet-A was used to create Jet-A vapour. A burst of seven pulses at 266 nm was generated by the multi-YAG system, and the time-separation between the consecutive pulses was set to 23 µs. This is generally regarded as a rather long time-separation for 3D measurements, since the acquisition time for an entire measurement is nearly 140 µs. However, the flow of Jet-A was very slow and non-reacting, and previous tests conducted on a similar flow using the high repetition rate laser/detector system without the scanning mirror had shown that for a time-separation of 200 µs the flow appeared to be completely frozen, whereas at 400 µs minor movements between the individual image frames were visible. This permitted a lower framing rate to be used than in the 3D imaging of formaldehyde in the flame described in the previous section. The advantage of this is that the double pulsing of the individual lasers can be operated close to the optimum time-separation in terms of laser pulse energy, which significantly improves the individual pulse energy and beam profile, and thus the image quality. Setting the scanning frequency to 40 Hz resulted in a sheet spacing of 1 mm. A 3D surface of the Jet-A distribution was created using shape-based interpolation between the laser planes, see Figure 5.20. The figure shows how the Jet-A vapour rising from the heated vessel, swirls slowly with a puff of air, one generated by the author with use of a small pipette.
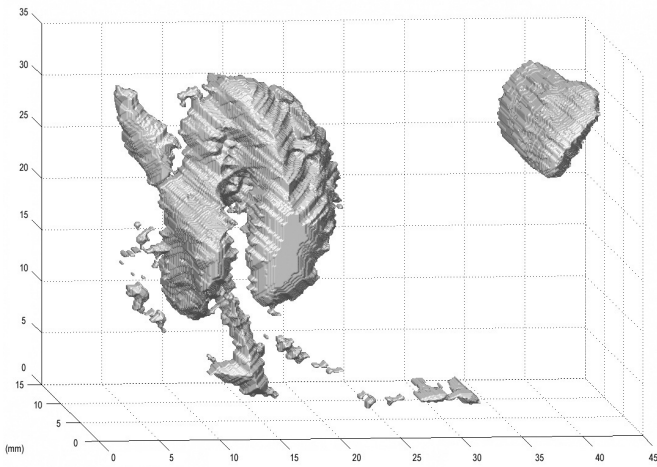
Figure 5.20 *A 3D surface visualizing the Jet-A vapour distribution from a heated vessel, swirling slowly with a puff of air generated by the author using a small pipette.*

Chapter 6

Summary and Future Outlook

For several reasons, temporally resolved measurements are often of considerable interest in combustion research. This is the case for example, in studying turbulent reacting flow fields, flame propagation and rapid fuel consumption in IC engines. A laser diagnostic system with the capability of recording image sequences of up to eight image frames was originally set up for investigations in turbulent reacting flows. The system consists of a multi-YAG laser and a high-speed framing camera, and the system has the capability of achieving framing rates of up to the megahertz range, which is well suited to combustion studies. In the present work, the system was further developed to reach new laser wavelengths, and thus enabling measurements of high repetition rates of new flame species. For the generation of laser radiation of 355 nm the harmonic generation and beam combining scheme of the multi-YAG cluster was redesigned, and a successful feasibility test for high-speed formaldehyde PLIF was carried out for the new design. Furthermore, a novel multi-dye laser cluster has been set up based on the design of four Cobra-Stretch dye lasers (Sirah) and a harmonic and beam combining scheme resembling the one used for the multi-YAG cluster. By individual pumping of the dye lasers with the multi-YAG laser, tunable laser radiation with ultra-high repetition rate can be achieved, avoiding the drawbacks of losses in laser pulse energy and intensity profile deterioration related to pumping a single dye laser with repetition rates in this range. As a part of this work, the laser/detector system has also been utilized in a variety of combustion diagnostic applications, ranging from flame front visualization in laboratory flames and combustion cells to fuel and reaction zone visualization in a gas turbine combustor and several studies in an HCCI engine where single-cycle resolved investigations of the ignition and combustion processes were carried out. Furthermore, three-dimensional imaging of formaldehyde in a laboratory flame as well as of Jet-A vapour in a slow non-reacting flow was demonstrated.

Continuation of this work will undoubtedly involve use of the high-speed laser and detector system in a variety of applications, including further studies of the HCCI engine concept with the purpose of improving the knowledge of the combustion processes involved in order to find e.g. suitable ways of controlling the

ignition timing. Studies in laboratory flames as for example the low-swirl methane/air flame will also continue, and three-dimensional imaging will be employed in this situation. Three-dimensional imaging of OH in this type of flame would be of interest because of the swirling flow field involved, as the three-dimensional effects become increasingly prominent farther away from the symmetry axis of the burner. By utilizing 3D imaging one could reduce uncertainties regarding whether flame movements seen in 2D images are the result of the flame moving in and out of the sheet in the outer parts of the flow.

Ways of extending the technique to 4D imaging, through producing two 3D images separated by a short time interval, have been discussed. One way of achieving this could be to utilize the laser beams from the four dye lasers without superimposing the four beam paths, and instead creating four parallel, closely spaced laser sheets. By firing the four lasers in a rapid sequence and synchronizing this with the action of the framing camera, four single-shot PLIF images could be obtained, which could be used for creating a 3D surface of the flame species being investigated. By operating the YAG lasers in double pulse mode for pumping of the dye lasers, two such images could be recorded. One drawback of this approach, however, is that the time-separation between the two 3D images would be limited to the range of the double pulsing of the YAG lasers, thus by the gain build-up time in the crystals and by the flash lamp pumping time, and hence the longest time-separation feasible with use of this approach would be around 145 μs. Nevertheless, 4D measurements of e.g. OH would be possible in this way, and such data would be of interest in studies of the sort carried out in the low-swirl burner, especially in combination with stereo PIV for measuring the flow velocity field in all three spatial components in order to investigate flame/flow interaction.

The redesigning of the multi-YAG laser cluster for operation at 355 nm opens possibilities not only for formaldehyde detection but also for high repetition rate detection of flame species for which pumping of tunable dye lasers at 355 nm is required. Species such as CH, absorbing at 430 nm, C_2, absorbing at 516 nm, and NO, absorbing at 226 nm (which can be achieved by frequency doubling of 452 nm) may now in principle be investigated either in 2D at high repetition rates or in 3D. Plans for the near future have also been made for investigating the possibilities for CH detection at high repetition rates, using the multi-dye laser cluster pumped by the multi-YAG laser at 532 nm. Excitation of CH at 387 nm can be achieved by frequency doubling the dye laser output at around 774 nm, after which fluorescence can be detected around 430 nm.

Temperature measurements could also be extended to the temporal domain in several ways, one approach being to use the multi-YAG and multi-dye clusters for two-line atomic fluorescence (TLAF). In the general TLAF technique, a fluorescent atomic substance (e.g. indium) is seeded at tracer levels into the flame, and two

temperature sensitive electronic levels in the tracer substance are excited to a common upper level by laser radiation at two different wavelengths. The temperature can be evaluated from the ratio of the fluorescence signals to each other following excitation. In using indium as a tracer, excitations at 410 nm and 451 nm can be employed and dyes suitable for these wavelengths are available if 355 nm is used for pumping. Hence in principle it is possible to pump two of the dye lasers with four pulses each from the multi-YAG cluster, to generate four rapid pulses at the two required wavelengths, and thus obtain high-speed temperature measurements with four image frames.

Finally, from the experience gained in working with and developing the present high-speed laser/detector system for applications in combustion environments, some areas where improvement of the system would be beneficial have been identified. These areas have been carefully considered when just recently ordering a new laser and detector system for high-speed measurements. The new multi-YAG laser cluster will utilize an optical layout similar to that in the present system, however, according to the specifications of the laser, the pulse energies will be significantly higher. Higher pulse energies is an advantage, especially when the laser is operated in double pulse mode, since the energy in each pulse is significantly reduced as compared with single pulse mode operation. In situations where the induced fluorescence is weak, the signal can be increased by use of a higher pulse energy, and thus enhancing the image quality. In addition, the new system will be easier to operate in terms of adjusting pulse separations and balancing pulse energies. The framing camera of the new high-speed diagnostic system will have a higher resolution than the present system, providing sharper images, but the main advantage of the new system, however, is its dynamic range. With the present framing camera the detected signal is digitized to a dynamic range of 8 bit, whereas the new system will have a 12 bit dynamic range. This enhances the image quality and also extends the ability of the system to record transient processes in which the fluorescence varies from very bright to very dark both in space and time. The sensitivity will also be improved, increasing the detectability of the being species studied. By combining the present high-speed system with the new system, simultaneous measurements at high repetition rate of several different species will be feasible for many new and exciting applications.

Acknowledgements

The major part of the work presented in this thesis was carried out at the division of Combustion Physics at Lund University, however, some of the applications were performed at the department of Energy Sciences. During my research studies I have met many friendly and helpful people, and all deserve credit for making the work truly pleasant. Some of them I would like to mention here.

First of all, I would like to thank Professor Marcus Aldén for giving me the opportunity to work in the field of laser-based combustion diagnostics, and for his encouragement and support. Marcus is an ever-lasting source of ideas for new and exciting experiments and the discussions with him have always been inspiring.

I would also like to thank Mattias Richter for being an excellent supervisor. Among other things, Mattias has a magical ability to make malfunctioning experimental equipment work by his mere presence in the laboratory, something that has come in handy several times during the various measurements. Without his support the work would have been very difficult.

Johan Hult deserves great thanks for teaching me all the tricks and secrets of the multi-YAG laser and the high-speed framing camera and for being a great supervisor during my first time at the division.

Professor Per-Erik Bengtsson was one of my supervisors during my first time at the division, and he has always helped me in straitening out my numerous question marks regarding combustion, for which I am very grateful.

Hans Seyfried and I have worked a lot together, especially on the engine related experiments. He deserves credit for being an excellent co-pilot on the multi-YAG laser, for his ever-lasting good spirit during the measurement campaigns, and for being a good friend.

Although I have worked very little in the lab together with Johan Zetterberg, this guy strongly contributes to the good atmosphere at the division. His laid-back style makes him easy to be around, which is something that I learned during a great conference week in Chicago. Johan has also proven to be an inspiring chef as well as a good friend.

In 1995 I started my undergraduate studies, and already during the first weeks I met Henrik Bladh. We soon realized that we shared each others passion for music, which became a solid foundation for our friendship. Since then Henrik and I have done lots of things together, such as attending physics courses, working on laboratory exercises, playing music, being neighbours, doing a masters thesis, starting our graduate studies the very same day and sharing office for the past five years. Henrik

has supported me throughout the years and I am grateful for having him as my friend. I will truly miss our endless lunch discussion about everything from the scalar dissipation rate to how a laser TV actually works.

During my undergraduate studies I also got to know Martin Linvin, and it was a nice surprise when he decided to join the team at the division. Martin is a great guy and he has a deep knowledge about home electronics, which has come in handy ones or twice. He is also very passionate about travelling to Thailand, which he does every now and then.

I would like to thank Fredrik Vestin for being a good room mate at the Gordon conference. Fredrik and I have also spent a great week in New York together with Hans, where Fredrik and I proved that it is possible (although quite hard) to walk through the entire Central Park area in the summer heat at about 35°C.

I have been fortunate enough to have been working together with Sven-Inge Möller, Annika Lindholm, Per Petersson, Christian Brackmann, and Axel Franke in the various projects concerning burners and combustion cells. They are all great people, and have contributed in different ways to creating a pleasant atmosphere at the division.

Robert Collin and Gustaf Särner are two great guys who I have worked with in trying to teach young physics students about how to use thermocouples, amongst other things. They are always really helpful and it has been a pleasure working with them.

I would also like to mention Johan Sjöholm and Elias Kristensson and take the opportunity to whish them the best of luck with the continuation of the work related to the high-speed diagnostic system. I am certain that they will engage in many exciting new applications.

The administrative staff, Anneli Nilsson, Cecilia Bille, Marie Persson and Elna Brodin, are excellent at handling the administrical issues, and they have all been a great support throughout the work.

Thomas Wendel is the guy to consult regarding malfunctioning electronic equipment. His support has been valuable when working in the lab as well as when having computer and printer problems.

Rutger Lorensson and Jonny Nyman are two skilful men who deserve credit for their excellent support with designing and constructing all sorts of mechanical equipment needed for the experimental work.

During most of my years at the division I have been a member of Trivselkommittén, and I would like to thank all the other members for the good work and for all the fun we have had when planning the social events for the division.

I would also like to thank all my other fellow graduate students and the rest of the staff at the division of Combustion Physics for contributing to the friendly atmosphere at work as well as during our numerous social activities.

During the work at the department of Energy Sciences I got to know several nice people. I would like to thank Andreas Vressner, Leif Hildingsson, Anders Hultqvist, and Professor Bengt Johansson for the nice collaboration on the engine related work, and also Bertil Andersson and Jan-Erik Nilsson for keeping the optical engines running smoothly. I would also like to thank Fredrik Hermann and Jens Klingmann together with whom the gas turbine related work was performed.

I would like to thank all the people outside Lund University together with whom I have worked on the various measurement campaigns, for very fruitful collaborations.

I would like to take the opportunity to thank all my great friends who have patiently waited, but several times so eagerly asked me: When are you going to finish school?!

Finally I would like to thank my parents, Monica and Tommy, for your unconditional support during my work as well as in life. Without your invaluable encouragements I would never have made it this far.

References

1.   IEA, *World Energy Outlook 2006*, International Energy Agency, 2006.

2.   IEA, *Key World Energy Statistics 2006*, International Energy Agency, 2006.

3.   Griffiths, J.F. and Barnard, J.A., *Flame and combustion*. 3. ed, Blackie Academic & Professional, London, 1995.

4.   Tennekes, H. and Lumley, J.L., *A first course in turbulence*, The MIT Press, Cambridge, MA, 1972.

5.   Warnatz, J., Maas, U., and Dibble, R.W., *Combustion: Physical and chemical fundamentals, modelling and simulation, experiments, pollutant formation*, Springer-Verlag, Berlin ; New York, 1996.

6.   Svanberg, S., *Atomic and molecular spectroscopy: Basic aspects and practical applications*, Springer-Verlag, Berlin ; New York, 1991.

7.   Kohse-Höinghaus, K., Barlow, R.S., Aldén, M., and Wolfrum, J., *Combustion at the focus: laser diagnostics and control*, Proceedings of the Combustion Institute, 30: p. 89-123, 2005.

8.   Eckbreth, A.C., *Laser diagnostics for combustion temperature and species*. 2. ed, Gordon & Breach, Amsterdam, 1996.

9.   Kaminski, C.F., Hult, J., and Aldén, M., *High repetition rate planar laser induced fluorescence of OH in a turbulent non-premixed flame*, Applied Physics B, 68: p. 757-760, 1999.

10.   Kohse-Höinghaus, K. and Jeffries, J.B., *Applied Combustion Diagnostics*, Taylor and Francis, New York, 2002.

11.   Dreizler, A., Lindenmaier, S., Maas, U., Hult, J., Aldén, M., and Kaminski, C.F., *Characterisation of a spark ignition system by planar laser-induced fluorescence of OH at high repetition rates and comparison with chemical kinetic calculations*, Applied Physics B, 70: p. 287-294, 2000.

12.   Banwell, C.N. and McCash, E.M., *Fundamentals of molecular spectroscopy*. 4 ed, McGraw-Hill Book, London ; New York, 1994.

13. Watson, K.A., Lyons, K.M., Donbar, J.M., and Carter, C.D., *Scalar and velocity field measurements in a lifted CH4-air diffusion flame*, Combustion and Flame, 117: p. 257-271, 1999.

14. Carter, C.D., Donbar, J.M., and Driscoll, J.F., *Simultaneous CH planar laser-induced fluorescence and particle imaging velocimetry in turbulent nonpremixed flames*, Applied Physics B, 66: p. 129-132, 1998.

15. Li, Z.S., Kiefer, J., Zetterberg, J., Linvin, M., Leipertz, A., Bai, X.S., and Aldén, M., *Development of improved PLIF CH detection using an Alexandrite laser for single-shot investigation of turbulent and lean flames*, Proceedings of the Combustion Institute, 31: p. 727-735, 2007.

16. Schulz, C. and Sick, V., *Tracer-LIF diagnostics: quantitative measurement of fuel concentration, temperature and fuel/air ratio in practical combustion systems*, Progress in Energy and Combustion Science, 31: p. 75-121, 2005.

17. Neij, H., *Development of laser-induced fluorescence for precombustion diagnostics in spark-ignition engines*. Doctoral Thesis, Lund University, Lund, 1998.

18. Neij, H., Aldén, M., and Magnusson, I., *Investigations of the influences of inhomogenities in the air/fuel/exhaust mixture on cyclic variations in spark ignition engines*, Contract JOUE CT-90-0066, 3rd Periodic Progress Report, July-December, 1992.

19. Neij, H., Georgiev, N., and Aldén, M., *Application of laser-induced fluorescence to spark-ignition engines*, 2nd International Workshop on Fluidmechanics, Combustion, Emissions and Reliability in Reciprocating Engines, Capri, 1992.

20. Thurber, M.C., Grisch, F., and Hanson, R.K., *Temperature imaging with single- and dual-wavelength acetone planar laser-induced fluorescence*, Optics Letters, 22: p. 251-253, 1997.

21. Thurber, M.C., Grisch, F., Kirby, B.J., Votsmeier, M., and Hanson, R.K., *Measurements and modeling of acetone laser-induced fluorescence with implications for temperature-imaging diagnostics*, Applied Optics, 37: p. 4963-4978, 1998.

22. Thurber, M.C. and Hanson, R.K., *Pressure and composition dependences of acetone laser-induced fluorescence with excitation at 248, 266, and 308 nm*, Applied Physics B, 69: p. 229-240, 1999.

23. Ossler, F. and Aldén, M., *Measurements of picosecond laser induced fluorescence from gas phase 3-pentanone and acetone: Implications to combustion diagnostics*, Applied Physics B, 64: p. 493-502, 1997.

24. Einecke, S., Schulz, C., Sick, V., Dreizler, A., Schießl, R., and Maas, U., *Two-Dimensional Temperature Measurements in an SI Engine Using Two-Line Tracer LIF*, SAE Technical Report No. 982468, 1998.

25. Graf, N., Gronki, J., Schulz, C., Baritaud, T., Cherel, J., Duret, P., and Lavy, J., *In-Cylinder Combustion Visualization in An Auto-Igniting Gasoline Engine Using Fuel Tracer- and Formaldehyde-Lif Imaging*, SAE Technical Report No. 2001-01-1924, 2001.

26. Collin, R., Nygren, J., Richter, M., Aldén, M., Hildingsson, L., and Johansson, B., *Simultaneous OH- and formaldehyde-LIF measurements in an HCCI engine*, SAE Technical Report No. 2003-01-3218, 2003.

27. Brackmann, C., Nygren, J., Bai, X., Li, Z.S., Bladh, H., Axelsson, B., Denbratt, I., Koopmans, L., Bengtsson, P.E., and Aldén, M., *Laser-induced fluorescence of formaldehyde in combustion using third harmonic Nd : YAG laser excitation*, Spectrochimica Acta Part a-Molecular and Biomolecular Spectroscopy, 59: p. 3347-3356, 2003.

28. Harrington, J.E. and Smyth, K.C., *Laser-Induced Fluorescence Measurements of Formaldehyde in a Methane Air Diffusion Flame*, Chemical Physics Letters, 202: p. 196-202, 1993.

29. Svelto, O. and Hanna, D.C., *Principles of lasers*. 4. ed, Plenum Press, New York, 1998.

30. Hult, J., Richter, M., Nygren, J., Aldén, M., Hultqvist, A., Christensen, M., and Johansson, B., *Application of a high-repetition-rate laser diagnostic system for single-cycle-resolved imaging in internal combustion engines*, Applied Optics, 41: p. 5002-5014, 2002.

31. Theocaris, P.S., Serafetinides, A.A., and Andrianopoulos, N.P., *A high-power multiple ruby laser system for recording dynamic events*, Journal of Physics E: Scientific Instruments, 14: p. 705-708, 1981.

32.   Wu, P.P. and Miles, R.B., *High-energy pulse-burst laser system for megahertz-rate flow visualization*, Optics Letters, 25: p. 1639-1641, 2000.

33.   Fajardo, C.M., Smith, J.D., and Sick, V., *PIV, high-speed PLIF and chemiluminescence imaging for near-spark-plug investigations in IC engines*, Journal of Physics: Conference Series, 45: p. 19-26, 2006.

34.   Smith, J.D. and Sick, V., *Quantitative, dynamic fuel distribution measurements in combustion-related devices using laser-induced fluorescence imaging of biacetyl in iso-octane*, Proceedings of the Combustion Institute, 31: p. 747-755, 2007.

35.   Fajardo, C.M. and Sick, V., *Flow field assessment in a fired spray-guided spark-ignition direct-injection engine based on UV particle image velocimetry with sub crank angle resolution*, Proceedings of the Combustion Institute, 31: p. 3023-3031, 2007.

36.   Renou, B., Boukhalfa, A., Puechberty, D., and Trinité, M., *Local Scalar Flame Properties of Freely Propagating Premixed Turbulent Flames at Various Lewis Numbers*, Combustion and Flame, 123: p. 507-521, 2000.

37.   Cheng, R.K., Yegian, D.T., Miyasato, M.M., Samuelsen, G.S., Benson, C.E., Pellizzari, R., and Loftus, P., *Scaling and development of low-swirl burners for low-emission furnaces and boilers*, Proceedings of the Combustion Institute, 28: p. 1305-1313, 2000.

38.   Chan, C.K., Lau, K.S., Chin, W.K., and Cheng, R.K., *Freely propagating open premixed turbulent flames stabilized by swirl*, Proceedings of the Combustion Institute, 24: p. 511-518, 1992.

39.   Möller, S.-I. and Lindholm, A., *Theoretical and experimental investigation of the operating characteristics of a Helmholtz type pulse combustor due to changes in the inlet geometry*, Combustion Science and Technology, 149: p. 389-406, 1999.

40.   Heywood, J.B., *Internal combustion engine fundamentals*, McGraw-Hill, New York, 1988.

41.   Onishi, S., Hong Jo, S., Shoda, K., Do Jo, P., and Kato, S., *Active Thermo-Atmosphere Combustion (Atac)--A New Combustion Process for Internal Combustion Engines*, SAE Technical Report No. 790501, 1979.

42.   Bowditch, F.W., *A new tool for combustion research–A quartz piston engine*, SAE Transaction, 69: p. 17-23, 1961.

43.   Hermann, F., *Investigation of Emission Characteristics for Diluted Flames and Renewable Fuels in Gas Turbine Combustors*. Doctoral Thesis, Lund Institute of Technology, Lund, 2005.

44.   Aldén, M., Edner, H., Holmstedt, G., Svanberg, S., and Hogberg, T., *Single-Pulse Laser-Induced Oh Fluorescence in an Atmospheric Flame, Spatially Resolved with a Diode-Array Detector*, Applied Optics, 21: p. 1236-1240, 1982.

45.   Higgins, B., McQuay, Q., Lacas, F., and Candel, S., *An experimental study on the effect of pressure and strain rate on CH chemiluminescence of premixed fuel-lean methane/air flames*, Fuel, 80: p. 1583-1591, 2001.

46.   Higgins, B., McQuay, Q., Lacas, F., and Candel, S., *Systematic measurements of OH chemiluminescence for fuel-lean, high-pressure, premixed, laminar flames*, Fuel, 80: p. 67-74, 2001.

47.   Docquier, N., Lacas, F., and Candel, S., *Closed-loop equivalence ratio control of premixed combustors using spectrally resolved chemiluminescence measurements*, Proceedings of the Combustion Institute, 29: p. 139-145, 2002.

48.   Kojima, J., Ikeda, Y., and Nakajima, T., *Spatially resolved measurement of OH*, CH*, And C_2* chemiluminescence in the reaction zone of laminar methane/air premixed flames*, Proceedings of the Combustion Institute, 28: p. 1757-1763, 2000.

49.   Akamatsu, F., Wakabayashi, T., Tsushima, S., Katsuki, M., Mizutani, Y., Ikeda, Y., Kawahara, N., and Nakajima, T., *The development of a light-collecting probe with high spatial resolution applicable to randomly fluctuating combustion fields*, Measurement Science and Technology, 10: p. 1240-1246, 1999.

50.   Richter, M., *Combustion Engine Characterization and Development by Means of Laser Diagnostics*. Doctoral Thesis, Lund Institute of Technology, Lund, 2002.

51.   Fujikawa, T., Hattori, Y., and Akihama, K., *Quantitative 2-D fuel distribution measurements in an SI engine using laser-induced fluorescence with suitable combustion of fluorescence tracer and excitation wavelength*, SAE Technical Report No. 972944, 1997.

52.   Konno, M., Kajitani, S., Chen, Z., Yoneda, K., Matsui, H., and Goto, S., *Investigation of the Combustion Process of a Di Ci Engine Fueled With Dimethyl Ether*, SAE Technical Report No. 2001-01-3504, 2001.

53.   Klein-Douwel, R.J.H., Luque, J., Jeffries, J.B., Smith, G.P., and Crosley, D.R., *Laser-induced fluorescence of formaldehyde hot bands in flames*, Applied Optics, 39: p. 3712-3715, 2000.

54.   Burkert, A., Grebner, D., Muller, D., Triebel, W., and Konig, J., *Single-shot imaging of formaldehyde in hydrocarbon flames by XeF excimer laser-induced fluorescence*, Proceedings of the Combustion Institute, 28: p. 1655-1661, 2000.

55.   Särner, G., Richter, M., Aldén, M., Hildingsson, L., Hultqvist, A., and Johansson, B., *Simultaneous PLIF Measurements for Visualization of Formaldehyde- and Fuel- Distributions in a DI HCCI Engine*, SAE Technical Report No. 2005-01-3869, 2005.

56.   Mantzaras, J., Felton, P.G., and Bracco, F.V., *Three-Dimensional Visualization of Premixed-Charge Engine Flames: Islands of Reactants and Products; Fractal Dimensions; and Homogenity*, SAE Technical Report No. 881635, 1988.

57.   Kychakoff, G., Paul, P.H., Vancruyningen, I., and Hanson, R.K., *Movies and 3-D Images of Flowfields Using Planar Laser-Induced Fluorescence*, Applied Optics, 26: p. 2498-2500, 1987.

58.   Yip, B., Schmitt, R.L., and Long, M.B., *Instantaneous 3-Dimensional Concentration Measurements in Turbulent Jets and Flames*, Optics Letters, 13: p. 96-98, 1988.

59.   Andersson, M., *Three-dimensional visualization of turbulent flames using shape-based interpolation*. Master's Thesis, 2000:E12, Lund Institute of Technology, Lund, 2000.

60.   Löfström, C., Engström, J., Richter, M., Kaminski, C.F., Johansson, P., Nyholm, K., Hult, J., Nygren, J., and Aldén, M., *Feasibility Studies and Application of Laser /Optical Diagnostics for Characterisation of a Practical Low-Emission Gas Turbine Combustor*, Proceedings of ASME TURBO EXPO, 2000-GT-0124, 2000.

Summary of Papers

Paper I

In this study the multi-YAG laser cluster was used to pump a single dye laser for high-speed OH visualization, conducted simultaneously with laser Schlieren imaging, for investigating the ignition properties of jets of hot exhaust gas impinging upon a quiescent hydrogen/air mixture after passing through a small nozzle. In addition to the experimental work, numerical modeling was performed. It was concluded that the ignition process is influenced by the temperature of the jet and the speed of mixing of the hot and cold gases. Ignition was found to occur near the jet tip rather than at the sides of the jet, which is explained by reduced mixing at the tip of the jet as compared with the sides.

The experiments were carried out together with Rajesh Sadanandan, Detlef Markus and Robert Schiessl, who performed the Schlieren imaging as well as the numerical modeling and also wrote the major part of the manuscript. Hans Seyfried and I conducted the high-speed LIF measurements, and I did the post processing of the LIF data.

Paper II

In this paper the processes governing generation of the signal in an ionization sensor was investigated. High-speed LIF measurements of OH were conducted in combination with LIF of NO for monitoring the flame propagation in a constant-volume combustion cell. Also fuel tracer LIF was used in this study. On the basis of the measurements, it could be concluded that cycle-to-cycle fluctuations in the ion current could be attributed to stochastic contact between the electrodes and the flame.

I conducted the high-speed measurements and also performed the data post-processing of the data. The NO imaging was done by Wieland Koban. Axel Franke operated the combustion cell, measured the ion currents, and also did most of the writing of the manuscript.

Paper III

A study of the effects of interaction between fluid dynamics and combustion in a pulse combustor is presented. The study focuses on the ignition, combustion and extinction processes occurring in the oscillating flow field in the burner. The multi-YAG laser was used to pump a dye laser for performing high-speed OH PLIF measurements phase-locked to the pulsation frequency of the combustor. The distribution of heat release over the combustion cycle was found to be dependent on the injection velocity. Mixing in the chamber is increased with increasing velocity, which in turn affects the ignition process.

The LIF experiments were performed by Johan Hult and me, and we also did the post-processing of the LIF image data. Annika Lindholm operated the pulse combustor and she and Sven-Inge Möller prepared the manuscript with contributions from Johan and me.

Paper IV

In this work a low-swirl methane/air flame was investigated as a first step in the development of an LES validation data base for a turbulent, premixed flame. Simultaneous measurements of the velocity fields and the OH distribution, as well as simultaneous measurements of the temperature fields and the OH distribution are presented. OH PLIF with high repetition rate was performed using the multi-dye laser cluster for the first time, pumped by the multi-YAG. Properties such as conditional velocities and scalar flux were extracted from the measurement data.

I shared responsibility for performing the high-speed OH PLIF measurements with Christian Brackmann and Hans Seyfried, whereas Per Petersson and Johan Zetterberg performed the velocity and the temperature measurements, respectively. Andreas Nauert operated the burner and extracted the data from the measurements. Per had the main responsibility for preparing the manuscript to which I contributed.

Paper V

A Cassegrain optics-based chemiluminescence sensor is proposed for monitoring of fluctuations in the equivalence ratio in industrial gas turbine combustors. The spatial and temporal response of the sensor was evaluated by comparison of sensor measurements with OH PLIF measurements in a stable, laminar flame. To investigate the ability of the sensors to measure in a practical turbine combustor application, laser diagnostics was used for characterizing the temporal scales and the

spatial distribution of fuel and reaction zones in a modified atmospheric micro-gas turbine combustor running on natural gas, in which measurements using the sensor were also made.

The high-speed OH PLIF measurements were performed by Johan Hult and me. Visualization of the fuel distribution (not explicitly mentioned in the paper) was performed mainly by Mattias Richter and me. All three of us did the post-processing of the LIF data and we also contributed to the manuscript. The measurements carried out using the sensor were done by Christos Panoutsos, and the combustor was operated by Fredrik Hermann.

Paper VI

High-speed fuel tracer LIF was used for studies of the effects of geometry generated turbulence in a truck-size HCCI engine. The combustion evolution was studied when using a piston crown with a deep square bowl and a flat piston crown, and a clearly slower process was seen for the square bowl case. Moreover, the square bowl geometry showed much more flame-front-like combustion, with only few ignition points, which would not be expected for conventional HCCI operation. This difference in combustion behavior observed by use of high-speed laser diagnostics, would not have been detected on the basis of the pressure trace and rate of heat release curves.

I performed the laser measurements together with Hans Seyfried and Johan Sjöholm, whereas Andreas Vressner operated the engine. Hans and I shared the main responsibility for preparing the manuscript and Johan Sjöholm carried out the data post-processing.

Paper VII

For the first time high-speed PLIF imaging of formaldehyde is reported, using the redesigned multi-YAG laser cluster at 355 nm and the framing camera. Successful demonstrations of formaldehyde measurements were made in a laboratory flame as well as in a small spark-ignition engine. Spectroscopic investigations of the fluorescence emission were conducted, and the results were compared to known flame emission spectra showing formaldehyde features. In addition, three-dimensional imaging of formaldehyde in a flame was demonstrated, by use of a rapidly scanning mirror for displacing the position of the laser sheet between the pulses. Stacks of PLIF images were recorded, from which the three-dimensional shape of the formaldehyde distribution in the flame could be recreated.

The high-speed measurements of formaldehyde in the flame and engine and the corresponding spectroscopic measurements were carried out by Micheline Augé, Mattias Richter and me and I conducted the three-dimensional visualization myself. I also had the main responsibility for the post-processing of the acquired data, and of the preparation of the manuscript.

Paper VIII

The multi-YAG laser, operating at 355 nm, was used together with the framing camera for single-cycle-resolved investigations of the formation and consumption processes of formaldehyde in a truck-size HCCI engine run on n-heptane. After being formed in the early cool-flame region, formaldehyde can be used as a marker of fuel. For the first time the diagnostic system could be used for multi-frame visualization of a non-fluorescent fuel in a single engine cycle, without having to add a tracer.

Hans Seyfried and I shared the main responsibility for the laser diagnostic measurements, as well as for the data post-processing and for preparing the manuscript. Andreas Vressner operated the engine and was also responsible for the heat-release analysis and the sections related to the engine hardware in the manuscript.

Paper IX

Laser spark-assisted and spark plug-assisted HCCI were investigated by means of cycle-resolved formaldehyde PLIF imaging, using the high-speed laser diagnostic system, and the results were compared with those for conventional HCCI operation. In addition, Schlieren photography and chemiluminescence imaging was also performed. From the heat-release analysis no clear difference could be seen between the different cases, however, by use of the optical diagnostics, evaluation of these differences could be made.

Hans Seyfried and I performed the LIF measurements, whereas the Schlieren imaging and the controlling of the laser spark were carried out by Martin Weinrotter, Kurt Iskra and Max Lackner. The engine operation as well as the heat-release analysis were done by Andreas Vressner. Hans Seyfried and I shared the responsibility for the LIF data post-processing and contributed to the manuscript.

Detailed investigation of ignition by hot gas jets

R. Sadanandan [a,*], D. Markus [a], R. Schießl [b], U. Maas [b],
J. Olofsson [c], H. Seyfried [c], M. Richter [c], M. Aldén [c]

[a] *Physikalisch Technische Bundesanstalt, Braunschweig, Germany*
[b] *Universität Karlsruhe, Institut für Technische Thermodynamik, Germany*
[c] *Lund Institute of Technology, Division of Combustion Physics, Sweden*

Abstract

Experimental and numerical investigations of the ignition of hydrogen/air mixtures by jets of hot exhaust gases are reported. An experimental realisation of such an ignition process, where a jet of hot exhaust gas impinges through a narrow nozzle into a quiescent hydrogen/air mixture, possibly initiating ignition and combustion, is studied. High-speed laser-induced fluorescence (LIF) image sequences of the hydroxyl radical (OH) and laser Schlieren methods are used to gain information about the spatial and temporal evolution of the ignition process. Recording temporally resolved pressure traces yields information about ambient conditions for the process. Numerical experiments are performed that allow linking these observables to certain characteristic states of the gas mixture. The outcome of numerical modelling and experiments indicates the important influence of the hot jet temperature and speed of mixing between the hot and cold gases on the ignition process. The results show the quenching of the flame inside the nozzle and the subsequent ignition of the mixture by the hot exhaust jet. These detailed examinations of the ignition process improve the knowledge concerning flame transmission out of electrical equipment of the type of protection flameproof enclosure.
© 2006 The Combustion Institute. Published by Elsevier Inc. All rights reserved.

1. Introduction and theoretical background

Ignition of fuel/air mixtures by impinging hot gas jets is a very important process in various fields ranging from industrial explosions and nuclear safety to supersonic combustors and to the development of combustion engines [1]. In explosive environments, hot jet ignition may take place due to a hot jet escaping from flameproof enclosures through inevitable gaps [2], e.g., like the ones present at the shaft bearing of an electrical motor. Closer analysis shows that hot jet ignition is a complicated process involving turbulent mixing of exhaust and fresh gas coupled with chemical reactions. It becomes even more complex at supersonic flow regimes when gas dynamic effects on the jet temperature can have a profound influence on the ignition process. The influence of pressure, temperature, and chemical kinetics on the ignition process has been examined widely for premixed H_2/air mixtures [3]. The role of strain and turbulence has been studied for nonpremixed H_2/air mixtures experimentally [4] and

---

[*] Corresponding author. Present address: German Aerospace Center (DLR), Institute of Combustion Technology, Pfaffenwaldring 38-40, D-70569 Stuttgart, Germany. Fax: +49 711 6862 578.
  E-mail address: Rajesh.Sadanandan@dlr.de (R. Sadanandan).

numerically [5]. However, theoretical and experimental investigations on the fundamental mechanisms behind the complex coupling of chemical reactions and turbulence are very sparse for hot jet ignition. Literature on the effects of mixing and chemistry on the ignition initiation by hot turbulent jets can be found in the earlier works done by Meyer et al. [6] and Philips [7]. More recent studies have examined the ignition processes from the view of explosion protection determining critical nozzle diameters for flame transmission [8,9].

The current study focuses on the ignition of 28 mol%/72 mol% hydrogen/air mixtures, which is a standard test gas concentration for gas group IIC [2,10], following the gas grouping for electrical apparatus in IEC 60079-0 [11]. The strategy is to use a combination of experimental observation and numerical simulation to identify the dominating processes. Experiments were performed in an optically accessible, constant volume combustion cell. In this cell, a jet of burned gases impinging into an unburned hydrogen/air mixture at room temperature is created. The hydroxyl radical (OH) is used as a marker of the reaction zone as it is an important intermediate species that is formed during the combustion process [12,13]. The temporal development of the hot jet penetration into the fresh mixture is observed using combined laser Schlieren and OH-LIF [14] visualisation sequenced at high repetition rates. Experiments were performed with different pressure ratios over the nozzle and different nozzle diameters in order to study the influence of different jet velocities on the gas expansion and ignition processes. To aid the interpretation of the measured OH-LIF signals, simple numerical simulations were carried out yielding detailed information on the mechanisms involved in the ignition process.

2. Methodology

The measurement object was a jet of hot exhaust gas impinging into a quiescent hydrogen/air mixture which was generated in a dedicated test cell with optical access. A schematic of the combustion cell is shown in Fig. 1. It consists of two chambers which are interconnected by means of a nozzle. The cylindrical smaller chamber (length 80 mm, diameter 60 mm, volume 0.226 L) was flanged to a second chamber (volume 12 L) which is equipped with three quartz windows for optical access. In each experiment, both chambers were filled with 28 mol%/72 mol% hydrogen/air mixtures up to atmospheric pressure. The H_2/air mixture in the first chamber was then ignited by means of a spark plug located at an ignition distance X_i, defined as the distance between the spark plug centre and the nozzle. This
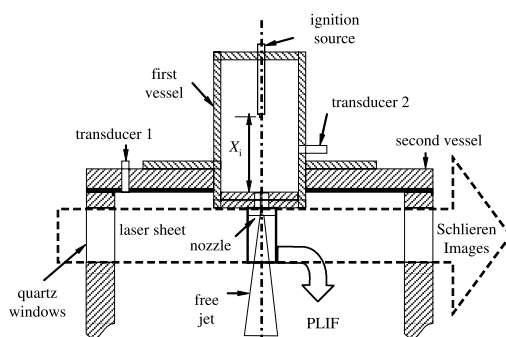

Fig. 1. Schematic of the combustion chamber.

distance can be adjusted by moving the spark plug along its axial direction.

The combustion leads to a pressure increase in the first chamber. The hot burned gases therefore expand through the nozzle into the second chamber, rendering a jet of hot burned gases that impinges into the unburned gas, possibly causing ignition. For this process, the ignition distance has an important effect: Reducing the ignition distance causes the resulting flame in the first chamber to reach the nozzle earlier. Therefore, a smaller fraction of the gas in the first chamber is burned at the time at which the flame enters the nozzle, and the pressure difference between the first and second chamber is smaller. The development of the hot jet and the subsequent ignition processes is imaged perpendicularly to the flow using ICCD cameras. The pressure trace in both chambers is recorded by means of transducers (Kistler Model 6031).

Figure 2 is a schematic sketch of the optical set-up used for the experiment. As excitation source for OH-LIF a multiple Nd:YAG laser cluster consisting of four standard flash-lamp-pumped Nd:YAG lasers, each operated in double
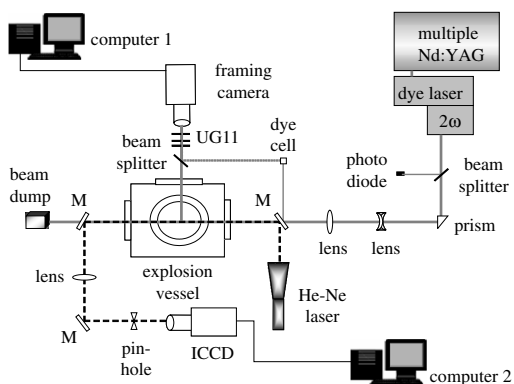

Fig. 2. Schematic of the optical set-up used for simultaneous OH-PLIF and Schlieren imaging.

pulse mode with a variable pulse interval of 25–145 μs was used. The beams from the four lasers were superimposed to a common optical axis and frequency doubled to 532 nm. By interleaving the double pulses of the four lasers, the time delay between the pulses could be reduced down to 6.25 μs in an eight-pulse sequence. The laser pulses for OH-PLIF were obtained by pumping a dye laser (operating on Rhodamine 590 as laser dye) with the Nd:YAG laser cluster and frequency doubling the dye laser output. For exciting the OH radical the dye laser was tuned to the $Q_1(9)$ transition near 283 nm in the $v'' = 0$, $v' = 1$ vibrational band of the $A^2\Sigma^+ - X^2\Pi$ electronic system of OH. By means of cylindrical lenses and mirrors the laser beam was formed into a vertical sheet of approximately 39 mm in height and 200 μm in thickness, and guided into the optically accessible test chamber described below. Subsequent fluorescence from the OH radical was observed using a combination of a high reflection filter (HR 275–295 nm) and a UG11 filter in front of the camera lens which eliminates reflections and scattering of the laser wavelength. A small part of the incoming laser sheet was reflected by a beam splitter and directed to a fluorescent dye cell. The resulting fluorescence from this dye cell was reflected onto the side of the same CCD as used for the OH-LIF detection to enable correction for laser profile inhomogeneities. A small part of the output beam from the dye laser was guided onto a photodiode by means of a beam splitter. This allowed additional on-line monitoring of the laser pulse energies on a shot-to-shot basis.

The detector system used for the visualisation of planar OH-LIF is an ultra fast CCD camera (Imacon 468, dynamic range 8 bit, 576×385 pixels). High framing speed is achieved by sequential exposure of eight individual CCD detectors with short exposure times. The CCD signals are digitised to 8 bits, and transferred to the controlling computer. Exposure times, gains and trigger delays are individually programmable for each CCD, providing full timing control. More details of the laser cluster and the camera system can be found in [15].

The laser Schlieren optical system consists of a He–Ne laser (20 mW at 632.8 nm) as a point source and a beam expander for collimating the beam. The beam is passed through the chamber along the same optical path as the dye laser sheet by means of mirrors. It is then redirected to a lens, which focuses the beam onto a dot mask where the Schlieren image is formed because of the light deflection due to the refractive index gradient inside the probe volume. For the laser Schlieren imaging, a Streak Star high-speed ICCD camera (La-Vision, 14-bit dynamic range, 384×576-pixel array), coupled to a Sigma zoom lens (75–300, 4–5.6 f) was used. During each experiment four sequential Schlieren images with an exposure time of 1 μs were recorded simultaneously with the OH-LIF images. The timing between the laser pulses and the different camera gate openings are adjusted by means of a delay generator circuit.

3. Results and discussions

A change in the ignition distance X_i leads to a change in the pressure ratio p_1/p_2 over the nozzle as the jet emanates out of the nozzle. Table 1 summarises the different nozzle diameters d tested for each ignition distance X_i and the resulting pressure ratios over the nozzle. For a given ignition distance no fluctuations of the measured pressure ratio could be detected i.e., the uncertainty of this value is only determined by the inaccuracy of the pressure measuring system. Variations in ignition distances and nozzle diameters lead to a subsequent change in jet velocities and rate of cooling of the burned gas.

Experimental laser Schlieren and OH-LIF images for $p_1/p_2 = 2.21$ and $d = 0.8$ mm are shown in Figs. 3a and b, respectively. The boundary contours of the corresponding Schlieren images are drawn into the OH-LIF images for better comparison of the Schlieren- and LIF-images. The spatial and temporal evolution of the hot burned gas as it expands into the second chamber from the nozzle exit can be seen in the Schlieren sequences (Fig. 3a). The imaged area covers 16×24.5 mm. The first frame is taken 2678 μs

Table 1
Measurement parameters

Ignition distance X_i (mm)	Nozzle diameter d (mm)	Pressure ratio p_1/p_2	Ignition probability (%)
24	0.7	1.50	0
24	0.8	1.44	61
24	0.9	1.44	100
32	0.8	2.21	15
32	0.9	2.19	67
32	1.0	2.06	100
56	0.8	5.22	0
56	1.1	4.75	89
56	1.3	4.63	100

$t = 2678$ μs $t = 2718$ μs $t = 2758$ μs $t = 2798$ μs

a)

b)

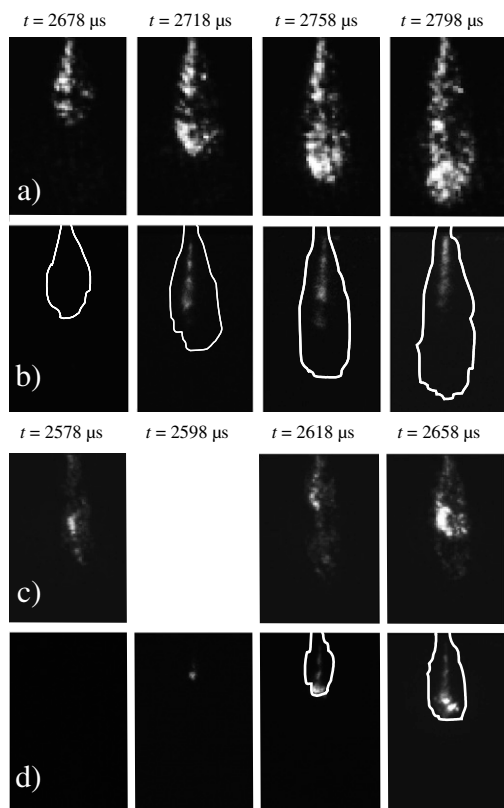$t = 2578$ μs $t = 2598$ μs $t = 2618$ μs $t = 2658$ μs

c)

d)

Fig. 3. (a) Simultaneous laser Schlieren and (b) OH-PLIF sequences, for $p_1/p_2 = 2.21$ and $d = 0.8$ mm. The height of imaged area in (a) and (b) is 24.5 mm. (c) Simultaneous laser Schlieren and (d) OH-PLIF sequences for $p_1/p_2 = 2.06$ and $d = 1.0$ mm. The height of the imaged area is 39 mm in (c) and (d). The PLIF images have been recorded approximately 2 μs after the corresponding Schlieren images. The extra OH-LIF image (2nd from the left) in (d) has no corresponding simultaneous Schlieren image; it is shown here because it contains the first evidence of ignition in the sequence.

after the spark in the first chamber was triggered, and the period between each frame is 40 μs. Although LIF images were taken with a time delay of 20 μs in the experiments, Fig. 3b shows only the time-resolved and simultaneous OH-LIF images corresponding to the Schlieren images of Fig. 3a recorded approximately 2 μs after the corresponding Schlieren images. From the recorded pressure trace and the OH-LIF images it can be inferred that there is no ignition in the second chamber in this case. Although some OH-LIF along the axis of the jet is visible, the absence of a significant amount of OH radicals at the nozzle exit indicates quenching caused by cooling due to the walls inside the nozzle before the gas expands into the second chamber. The structure that is visible in these Schlieren images is not associated with ignition and combustion, but simply to the mixing of the hot jet with unburned mixture.

Schlieren and OH-PLIF sequences for ignition of combustible gas by hot burned gas are shown in Figs. 3c and d, respectively, where the imaged area covers 26.5×39 mm. The images are shown for $p_1/p_2 = 2.06$ and $d = 1.0$ mm. The first Schlieren image on Fig. 3c is captured 2578 μs after ignition in the first chamber. The time interval between the three different Schlieren frames is 40 μs and the time interval between the OH-LIF images is also 20 μs for the first, second and third LIF images and 40 μs between third and fourth LIF image. The PLIF images have been recorded approximately 2 μs after the corresponding Schlieren images. The region where ignition and subsequent combustion occurs can be clearly recognized by the sudden increase in OH-LIF intensity at $t = 2598$ μs (second OH-LIF image from the left; no corresponding Schlieren image is available for this point in time) at a distance of approximately 9 mm from the nozzle. The detection limit of the camera system is one critical factor with respect to the diagnostic analysis. However, the increase in OH concentration by several orders of magnitude during the ignition process helps in examining this process with reasonable accuracy using OH-LIF.

The interpretation of the LIF-signals is not straightforward, because the LIF-signal strength depends in a complicated way on several quantities (temperature, OH-number density, number density of species which cause quenching of the LIF-signal), and these quantities vary in a wide range in the system. It is not a priori clear if and how certain important processes in the jet (like ignition, combustion, and extinction) can be identified by the LIF-signal that they cause. As an aid to better interpret the image sequences, numerical simulations with a simple mixing reactor model [3] coupled with spectroscopic simulations [16] were performed. These simulations help in linking the observed signals (OH-LIF images) with the thermochemical state in the jet. The hot jet is represented in the simulations by a homogeneous constant-pressure reactor which is filled with hot exhaust gas with a certain initial temperature $T^{(b)}$ and initial chemical composition. To this gas, a flow of unburned hydrogen/air mixture ($T = 300$ K, $p = 1$ bar) is added with a certain mixing rate θ. Due to the addition of combustible fuel/air mixture to the hot jet, chemical reactions occur simultaneously to the mixing. The chemical source terms are calculated according to the set of elementary reactions for hydrogen/air combustion including 38 reactions of nine species [3]. The homogeneous reactor model allows large parametric studies concerning mixing rate and initial temperature. This enables us to link the OH-signal to certain characteristic states that are associated with important processes inside the jet.

The model simulations yield the mixture composition and temperature for given inlet

conditions as a function of time. From this information, the LIF-signal of the hydroxyl-radical (OH) that results after excitation with a laser-pulse of given spectral features and with a given detection bandpass was calculated. To this end, the program LASKIN [16] was used to compute the temporal evolution of the OH fluorescence intensity as a function of temperature, pressure, and chemical composition. The LIF-signal computation covers effects of the temperature dependent population of the laser-coupled ground state, line broadening of absorption lines by molecular collisions and by the Doppler-effect, as well as vibrational and rotational energy transfer from the laser-excited upper levels, and collisional quenching.

The initial composition is set to chemical equilibrium at a predefined temperature. The degree of mixing between hot gas jet and unburned gas is described by the mixture fraction ξ, defined as the fractional part of mass that stems from the burned gas. In the real jet, the mixing rate θ is not constant with respect to time. To mimic the decay of the mixing frequency with decaying shear velocity in the jet, a temporal decline of θ with decreasing mixture fraction ξ is used in the model, according to $\theta = \theta_0 \cdot \xi$, where θ_0 is the mixing rate at $\xi = 1$.

Figure 4a shows the temperature of the perfectly stirred reactor as a function of mixture fraction ξ for different initial mixing rates θ_0. The corresponding computed LIF-signals are shown in Fig. 4b. As can be seen in Figs. 4a and b for a fixed initial jet temperature ($T^{(b)} = 1487$ K), different mixing rates lead to qualitatively different behaviour: If the mixing rate is much greater than the chemical rate ($\theta_0 = 2 \times 10^4 \text{ s}^{-1}$), chemistry can not compensate for the rapid cooling, and the

system moves along the lower branch of Fig. 4a, namely the line of unreacted mixing states between unburned gas and the jet gas for different mixture fractions. The system will display virtually no OH-LIF signal in this case. The situation depicted in Figs. 3a and b is best represented by this "pure mixing branch" shown in Fig. 4.

If the chemical time scale is much smaller than the mixing time scale as represented by an initial mixing rate of $\theta_0 = 1 \text{ s}^{-1}$ in Fig. 4a, the unburned mixture is consumed instantaneously during mixing, leading to an increase in temperature. Correspondingly, there is an increase in OH number density leading to an increase in OH-LIF signal as seen in Fig. 4b. After complete mixing has occurred ($\xi = 0$), the system attains the adiabatic flame temperature corresponding to the unburned mixture. For intermediate mixing rates (as represented by the curves for $\theta_0 = 2 \times 10^3 \text{ s}^{-1}, \ldots, 1.2 \times 10^4 \text{ s}^{-1}$ in Fig. 4), the system first follows the unreacted mixing line, but eventually, the temperature rise due to exothermic reactions outbalances the temperature decrease due to the addition of cold gas, and the system again ignites, combusts and finally evolves into chemical equilibrium. The OH-LIF signal intensity in this case displays a steep rise with a pronounced "overshoot", which is associated with a steep rise in temperature. Although the LIF-measurements do not supply quantitative information about OH, the simple model calculations allow to link certain regions in the observed LIF-images with different states of the ignition/combustion process. In the measurements, only extremely weak or no LIF signals were observed in the jet directly at the nozzle exit. According to LIF-signal simulations for chemical equilibrium at different temperatures, the jet would emit LIF-signal that is
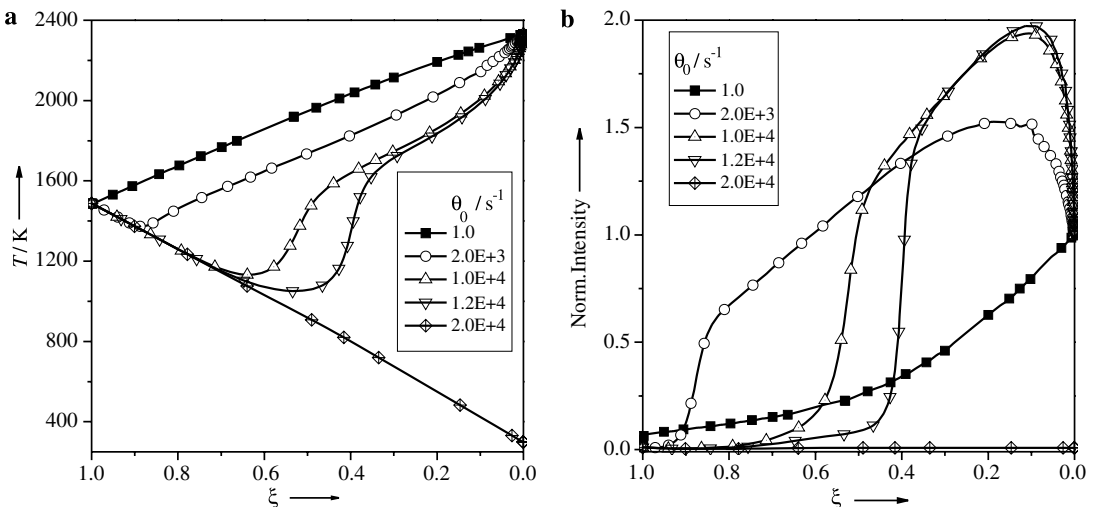

Fig. 4. Dynamic behaviour of the perfectly stirred reactor for $T^{(b)} = 1487$ K with different initial mixing rates θ_0.

detectable with the experimental setup, if its temperature was in the region around 1800 K or higher. It is therefore concluded that the heat loss of the jet to the nozzle walls is considerable, and that the jet temperatures in the experiments must be below 1800 K (compared to approximately 2390 K for chemical equilibrium without heat loss).

The ignition process is strongly influenced by temperature and mixing rate. In Fig. 5, the maximum mixing rate $\theta_{0,\,max}$ at which ignition still occurs, is shown as a function of the exhaust gas temperature $T^{(b)}$. The curve separates the initial values of the mixing rate for a given temperature that lead to ignition from the initial values that do not lead to ignition. This temperature dependence is based on the dominant effect of the temperature on the elementary reactions. As the temperature $T^{(b)}$ increases, the induction time, which describes the time between the beginning of mixing and ignition, decreases. A high jet temperature is therefore required to ignite the mixture in cases of large mixing rates to overcome the cooling due to mixing.

The calculations can be used to explain some interesting experimental results. In Table 1, the dependency of the minimum nozzle diameter required for 100% ignition with pressure ratio is shown. The different ignition probabilities are based on at least 10 experiments per configuration. For example, for a pressure ratio of 1.44 the minimum nozzle diameter required for 100% ignition of combustible gases by hot burned gases is 0.9 mm while for $p_1/p_2 = 2.06$ it is 1.0 mm. A higher outflow velocity resulting from the higher pressure difference leads to a higher mixing rate. Therefore, following Fig. 5, the nozzle diameter leading to 100% ignition has to increase with increasing pressure difference to decrease outflow velocity and increase temperature of the hot jet.
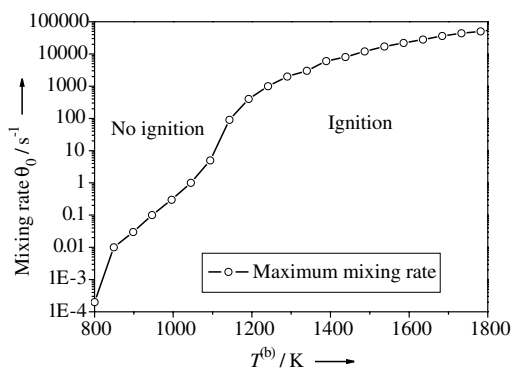
This effect of the increase in pressure ratio on the ignition behaviour can be seen in the Schlieren and PLIF images on Fig. 6 ($p_1/p_2 = 4.75$ and $d = 1.1$ mm). The imaged area starts at a distance of 29 mm from the nozzle exit and covers 26.5×39 mm. The time difference between the different Schlieren frames in Fig. 6a is 40 μs, and the first frame is recorded 3458 μs after ignition in the first chamber. The PLIF images in Fig. 6b have been recorded approximately 2 μs after the corresponding Schlieren images. The initiation of the ignition of the gases by the hot jet happens in the time interval between the first and the second Schlieren frames, as is seen in the second frame of the PLIF sequence. Compared to the situation depicted in Figs. 3c and d, the ignition inside the free jet flow starts far more away from the nozzle exit at approximately 43 mm. This increase of ignition distance from the nozzle exit inside the jet is mainly based on the higher pressure difference leading to a higher outflow velocity and mixing rate. Therefore following Figs. 4 and 5 the conditions are not favourable for ignition at the beginning and only mixing and cooling occurs. With increasing distance from the nozzle outlet, velocity and mixing decreases and finally at the experimental conditions in Fig. 6 the chemical reactions lead to an ignition, which again starts near the jet axis rather than at the sides. The localised ignition and extinction of kernels and the growth of the kernel is influenced by turbulent eddies, and the regions where OH-LIF signal is emitted are not spatially coherent. Note that there are also spot-like regions of considerably enhanced OH-LIF emission visible in Fig. 6. These bright spots can be understood using the results from the simple numerical model: They are regions that have just ignited and that are

Fig. 5. Calculated (based on the mixing reactor model) maximum initial mixing rates still leading to ignition of unburned 28% H_2/72% air mixture as a function of the exhaust gas temperature $T^{(b)}$.
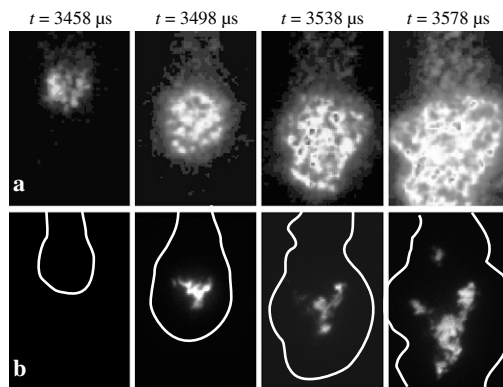

Fig. 6. (a) Simultaneous laser Schlieren and (b) OH-PLIF sequences for $p_1/p_2 = 4.75$ and $d = 1.1$ mm. The images are 39 mm in height, the top is located 29 mm away from nozzle exit. The PLIF images have been recorded approximately 2 μs after the corresponding Schlieren images.

now on the branch of high OH-LIF emission ("overshoot"), not yet having reached chemical equilibrium. In Fig. 6, regions where ignition already has occurred and combustion takes place are visible, simultaneously with regions that are just igniting. Both the combusting and the igniting regions are not spatially coherent due to the influence of the turbulent flow caused by the jet.

The OH-signal always appears well inside the boundary of the Schlieren images (drawn as white lines into the OH-LIF images in Figs. 3 and 6). This does not *per se* mean that the OH-signal source (as indicated by the occurrence of OH-LIF) is located well inside the jet (rather than close to the boundary): the Schlieren images contain line-of-sight information of a three-dimensional object, projected onto the image plane, while the LIF images genuinely contain information from a two-dimensional region (the plane of the laser-sheet). The Schlieren boundaries plotted into the LIF-images therefore yield only rough information about the boundaries of the Schlieren region in the plane of the LIF-measurement. However, in all Schlieren/LIF picture pairs that were recorded it was seen that the region of ignition (indicated by the presence of enhanced OH-LIF signal) lies well within the zone marked by Schlieren images. From the combined information from all these images, we conclude that the OH-LIF emission does not happen at the jet boundary, but well within the jet near the tip.

4. Summary and conclusion

This paper reports on studies on the ignition of near-stoichiometric hydrogen/air mixtures by hot exhaust gas jets. In an optically accessible combustion cell, hot jet ignition experiments were performed under well-defined conditions. High-speed sequences of planar OH-LIF and Schlieren images were recorded to study the ignition of unburned hydrogen/air mixture by a hot exhaust gas jet. From these high-speed image sequences, the temporal development of individual ignition events could be tracked. To aid the interpretation of the observed LIF-signals, a simple numerical simulation of the reactive mixing of exhaust gas with H_2/air mixture was combined with spectroscopic simulations of the OH-LIF signal.

The Schlieren images show that the changes in pressure ratio across the nozzle substantially change the average outflow jet velocity. The absence of appreciable amount of OH LIF-signal at the nozzle exit suggests that the gas at this location is relatively cool due to heat losses to the nozzle walls. Subsequent ignition of the combustible mixture by the hot exhaust jets can be observed in the OH-PLIF sequences. The combination of mixing reactor model/spectroscopic simulations is used

to link the observed LIF-signals with certain states (extinction, ignition, and combustion) of the hot jet/H_2-air mixing process. Especially, the interaction of turbulence and chemical reactions dominates the problem of hot jet ignition. This becomes apparent considering the locations in the jet where ignition is observed: The hot jet emerges from the nozzle with high velocity and underlies high shear stresses (strain rates) due to the contact with the surrounding H_2/air mixture. The observation that ignition occurs near the jet tip and not at the lateral sides of the jet can be explained with the different mixing behaviour of these areas. At the lateral sides the high shear stresses result in strong mixing, while at the tip mixing is reduced [17], increasing the probability of ignition in this area. The experimental data will be used as a basis for developing and validating detailed models of the hot jet ignition problem. Understanding this problem helps to improve the design of electrical equipment of the type of protection flameproof enclosure. Therefore, current experimental efforts are directed at determining instantaneous mixture fraction and temperature fields.

References

[1] E. Murase, S. Ono, K. Hanada, A.K. Oppenheim, *Combust. Sci. Technol.* 113 (1996) 167–177.
[2] IEC 60079-1, *Electrical Apparatus for Explosive Gas Atmospheres—Part 1: Flameproof Enclosures 'd'*, 2003.
[3] U. Maas, J. Warnatz, *Combust. Flame* 74 (1988) 53–69.
[4] J.D. Blouch, C.K. Law, *Combust. Flame* 132 (2003) 512–522.
[5] H.G. Im, J.H. Chen, C.K. Law, *Proc. Combust. Inst.* 27 (1998) 1047–1056.
[6] J.W. Meyer, P.A. Urtiew, A.K. Oppenheim, *Combust. Flame* 14 (1970) 13–20.
[7] H. Phillips, *Combust. Flame* 19 (1972) 187–195.
[8] Ø. Larsen, R.K. Eckhoff, *J. Loss Prev. Process Ind.* 13 (2000) 341–347.
[9] M. Beyer, Ph.D. thesis, University of Braunschweig, 1997.
[10] T. Redecker, *Classification of Flammable Gases and Vapours by the Flameproof Safe Gap and the Incendivity of Electrical Sparks.* Report W-18, Physikalisch–Technische Bundesanstalt, 1981.
[11] IEC 60079-0, *Electrical Apparatus for Explosive Gas Atmospheres—Part 0: General Requirements*, 2004.

[12] J. Warnatz, U. Maas, R.W. Dibble, *Combustion*, third ed., Springer, Berlin, 2001.
[13] A. Dreizler, S. Lindenmaier, U. Maas, J. Hult, M. Aldén, C.F. Kaminski, *Appl. Phys. B* 70 (2000) 287–294.
[14] A.C. Eckbreth, *Laser Diagnostics for Combustion Temperature and Species*, second ed., Gordon and Breach, UK, 1996.

[15] J. Hult, M. Richter, J. Nygren, M. Aldén, A. Hultqvist, M. Christensen, B. Johansson, *Appl. Opt.* 41 (2002) 5002–5014.
[16] U. Rahmann, A. Bülter, U. Lenhard, R. Düsing, D. Markus, A. Brockhinke, K. Kohse-Höinghaus, Faculty of Chemistry, Physical Chemistry I, 2003, available at <http://pc1.uni-bielefeld.de/~laskin/>.
[17] G. Bruneaux, SAE technical paper 02-SFL39, 2002.

Comments

Katharina Kohse-Höinghaus, Universität Bielefeld, Germany. Your results from the modeling seem to indicate that in some intermediate cases (between the limits of no ignition/no OH vs. complete ignition/full OH signal) there may be situations where the expected signal will not unambiguously depend on the conditions of the gas mixture. Please comment on the potential predictive capability of ignition under these intermediate conditions.

Reply. We do not attempt a complete identification of the conditions in the gas mixture (temperature, mole fractions of all species). What we do obtain from the model simulations is information about how certain characteristic processes in the system (like extinction, or ignition/combustion at high mixing rates) show up in the OH LIF images.

●

Mohy S. Mansour, NILES-Cairo University, Egypt. The boundary conditions of the hot exhaust gases are not well defined due to the shot-to-shot variations. So, validation of the numerical calculations based on the present experimental data is not accurate enough. A well defined source of hot exhaust gases, providing definite boundary conditions, should improve the validation

and interpretation of the present data. Can you comment on this?

Reply. As mentioned in the paper, the experiments are not used here to validate numerical calculations. Instead, the numerical simulations are used to aid the interpretation of the experimental results, namely the OH LIF-signals. The connection of the LIF-signal to processes like ignition or extinction is essentially the same for a wide range of boundary conditions (e.g., initial jet temperatures). For our study, therefore, uncertainty in boundary conditions was not an issue.

●

G.I. Nathan, University of Adelaide, Australia. You explained your result in terms of mixing. Did you consider the effect of strain? The mean scalar field is not a reliable measure of molecular mixing.

Reply. The effect of strain was not included in the numerical simulations presented here. We have performed similar studies using unsteady 1-D flame simulations, which do include strain effects. They deliver similar connections between OH-LIF signal and the important processes like ignition or extinction.

II

A. FRANKE[1]
W. KOBAN[2]
J. OLOFSSON[1]
C. SCHULZ[3]
W. BESSLER[2]
R. REINMANN[4]
A. LARSSON[5]
M. ALDÉN[1],✉

Application of advanced laser diagnostics for the investigation of the ionization sensor signal in a combustion bomb

[1] Lund Institute of Technology, Division of Combustion Physics, Box 118, 22100 Lund, Sweden
[2] PCI, Universitaet Heidelberg, Im Neuenheimer Feld 253, 69120 Heidelberg, Germany
[3] IVG, Universitaet Duisburg-Essen, Lotharstrasse 1, 47057 Duisburg, Germany
[4] Fiat-GM Powertrain, Advanced Engineering, 15127 Sodertalje, Sweden
[5] Swedish Defence Research Agency, Weapons and Protection Division, 14725 Tumba, Sweden

ABSTRACT The ionization sensor is an electrical probe for diagnostics in internal combustion engines. Laser-induced fluorescence (LIF) imaging of fuel, hydroxyl (OH), and nitric oxide (NO) distributions has been employed to extend our knowledge about the governing processes leading to its signal. By monitoring the flame propagation in quiescent and turbulent mixtures, the cycle-to-cycle variations in the early sensor signal was attributed to the stochastic contact between flame front and electrodes. An analysis of the relationship between gas temperature and sensor current in the post-flame gas suggests a dominant role of alkali traces in the ionization process at the conditions under study. Significant cooling of the burned gas in the vicinity of the electrodes was observed in quiescent mixtures. Imaging of the post-flame gas in turbulent combustion revealed moving structures with varying NO and OH concentrations, which were identified as sources of variation in the sensor current.

PACS 51.50.+v; 42.62.Fi; 47.27.-i

1   Introduction

The spark plug, which ignites the combustible mixture in internal combustion engines, can also act as an electrical probe for in-cylinder diagnostics. The sensor measures the electric current through the gas in the vicinity of the electrode gap. The combustion process affects the electrical properties of the gas. Thus, the sensor signal contains information about the conditions in the combustion chamber. One important advantage is that this information can be retrieved without inserting any additional equipment into the combustion chamber. Compared to the large number of applications reported in the literature [1–10], few fundamental studies have been performed. A thorough characterization of the sensor will enable a more reliable signal interpretation for feedback or feedforward control of the engine. The objective of the present investigation is to improve the knowledge about the basic processes governing the sensor behavior by using advanced optical diagnostics in the combustion chamber.

✉ Fax: +46 (0) 46-222 4542, E-mail: marcus.alden@forbrf.lth.se

The sensor signal typically consists of two distinct peaks, attributed to chemical ionization during early flame propagation and thermal ionization during main combustion, respectively. One objective of the present study was to image the flame propagation by sequential two-dimensional laser-induced fluorescence under turbulent conditions, and to investigate the consequences of turbulence for the early sensor signal. Current models for the ionization sensor signal rely on NO as the main contributor to ionization [11–14]. Thus, a second motivation for the present investigation was to examine the correctness of this assumption experimentally by using spectroscopic measurements of nitric oxide in the vicinity of the electrodes.

2   Background

2.1   *Ionization sensor*

The sensor detects the variation in ionization during the combustion process by applying a voltage of approximately 80 V across the gap of the spark plug during combustion. The signal is well-separated in time from the ignition discharge. The signal typically shows two subsequent peaks (Fig. 1). The first peak occurs when the flame is in contact with the electrodes. It is caused by chemical ionization in the reaction zone, and its magnitude is related to the local equivalence ratio close to the electrode gap. The second peak occurs close to the pressure peak and is usually attributed to thermal ionization in the post-flame zone.

Ionization in flames [15] and electrical phenomena in ionized gases [16] have been extensively studied over the last years. The number of investigations related to applications of the sensor in combustion engines is steadily growing. However, only a few fundamental studies of the ionization sensor have been performed. Reinmann et al. [17] provided a model for the current resulting from chemi-ionization in the flame front. Saitzkoff et al. [11] analyzed the ionization equilibrium in the post-flame gases in order to explain the sensor current during main combustion and relate it to the in-cylinder pressure. Wilstermann [14] presented a comprehensive investigation of the sensor including an overall model and various studies of the influence of equivalence ratio, electrode shape, and exhaust gas fraction. Andersson [18] applied the model of Saitzkoff et al. [11], and added improved submodels for
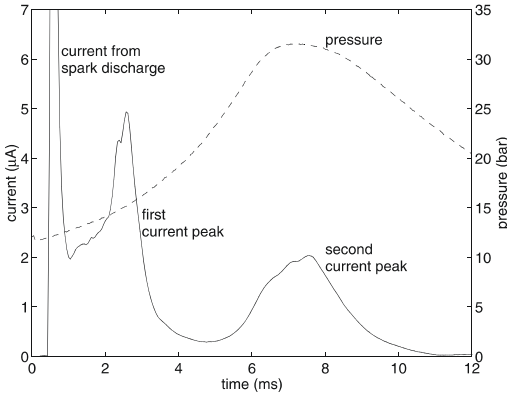
FIGURE 1   Example of a typical ion current signal and the corresponding pressure trace measured in an engine

the in-cylinder pressure, the formation of nitric oxide, and the burned gas temperature. Naoumov et al. [12] employed chemical kinetics to improve these models. Despite of the lack of any experimental evidence, all of the above mentioned models assume NO as the main contributor to post-flame ionization. This assumption appears reasonable because among the combustion products, NO is the species with the lowest ionization potential (9.27 eV) [14, 19]. Naoumov et al. [13] presented a chemical non-equilibrium simulation that included ionization modeling and proved theoretically the dominant role of NO for ionization in the post-flame gas. The present work is the first experimental study to investigate the relation of in-cylinder NO concentrations and sensor signal. Spectroscopic and electrical measurements are combined with an algorithm that allows the separation of the influence of electron donor concentration and temperature, which has been presented recently [20].

The electrical conductivity of the post-flame gas is governed by the concentration of free electrons, because they feature a significantly higher mobility than the ions. The equilibrium concentration of electrons is dominated by the exponential dependence of the equilibrium constant on the ratio E_i/T between the ionization energy of the electron donor, E_i, and the gas temperature T. The expression for the current I through the burned gas inherits this temperature sensitivity and can be written as [20]

$$I \propto \sqrt{[A]} \exp\left(-\frac{E_i^A}{2\,k_B T}\right). \tag{1}$$

Thus, the logarithm of the current (2) is a linear function of the inverse temperature with a slope proportional to the ionization potential of the ionized species, and an offset containing information about its concentration [A].

$$\ln I = \frac{1}{2}\ln[A] - \frac{E_i^A}{2\,k_B T} + \text{const.} \tag{2}$$

This relationship has been successfully applied for the analysis of current, temperature and exhaust gas data from engine measurements [20], and it is also used for the data processing in the present experiment.

A recent investigation emphasizes the importance of the contact area between flame front and cathode for both shape and magnitude of the first peak [21]. However, the conclusions relied on flame photography and were therefore limited to laminar combustion.

2.2   *Laser-induced fluorescence*

2.2.1 Nitric oxide.   In the context of this work, NO is the combustion-related species with the lowest ionization potential and was therefore expected to be the main contributor to thermal ionization. Various options exist for the detection of NO by LIF [22]. They differ in the excitation-detection scheme applied. The prospects of excitation in the A-X(0,2)-band, used in this work, were investigated by Schulz et al. [23] for combustion-relevant pressures and temperatures. Excitation at 247.94 nm together with the detection of the blue-shifted fluorescence, minimizes interference with the fluorescence from hot O_2 and inhibits detection of the broadband, red-shifted fluorescence from polycyclic aromatic hydrocarbons (PAHs) present as combustion intermediates. Figure 2 illustrates schematically the process. Excitation takes place from the second vibrational level of the electronic ground state, thus only "hot" NO will be detected. The main advantage over approaches using shorter excitation-wavelengths is that the laser light suffers less from absorption. This is important for a two-dimensional imaging technique. The absorption is attributed mainly to hot CO_2 [24]. The dependence of NO-LIF intensity I_{LIF} for weak, non-perturbing laser excitation can be derived on the base of a four-level model [25]. It is given by

$$I_{LIF} = I_{Laser} n_{NO} f_B(T) B_{ik} g_\lambda(p, T)$$
$$\times \sum_{k,j} f_{kj} \frac{A_{kj}}{\sum_l A_{kl} + Q_k(p, T)}.$$

I_{LIF} depends on the number density of the excitable molecules (which is the number density n_{NO} of the species times the Boltzmann fraction f_B giving the population of the initial level i), the Einstein B_{ik} coefficient for absorption $i \to k$, the spectral overlap $g_\lambda(p, T)$ of laser profile and NO absorption spectrum and the fluorescence quantum yield $A/(A + Q)$, where A and Q are decay rates due to spontaneous emission and electronic quenching, respectively. Q depends on
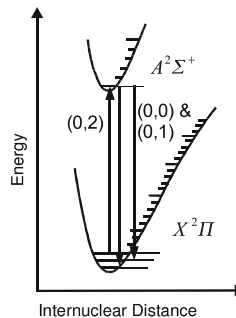

FIGURE 2
Excitation-detection scheme for NO-LIF when exciting at 247.94 nm

the local temperature and the gas composition. For NO at atmospheric pressure and above, the denominator is dominated by Q. No further depopulation processes of the excited levels like predissociation occur for the levels under study. The summation over k, j indicates that due to energy transfer processes within the excited manifold, the fluorescence signal originates from different excited rotational levels simultaneously. Therefore, a spectral transmission function f_{kj} of the detection system needs to be included. Pressure and temperature dependencies of the fluorescence signal can be simulated and corrected for [26], thus allowing quantitative evaluation of NO-mole fractions. As a further advantage of the detection scheme applied, there is a temperature independence of the NO concentration measurement within 20% from 1900 K to 3000 K, since several effects cancel [27]. Thus, no detailed knowledge about local temperatures is needed. This excitation-detection scheme has been successfully applied in high-pressure burners [23] and engines [28, 29]. The excitation wavelength is accessible by a tunable KrF excimer laser such as the EMG 150 TMSC (Lambda Physik).

2.2.2 Fuel Visualization. Imaging of fuel provides not only information about the fuel distribution but also about flame propagation because the burned gas regions will appear dark. Tracer-based fuel imaging has been successfully applied to in-cylinder measurements [30]. Our fuel (methane) cannot be directly detected by laser-induced fluorescence, and therefore requires the addition of a fluorescent tracer. A commonly used tracer for methane is acetone, since its molecular weight and diffusion coefficient are reasonably well matched [31]. It was also used in the experiments presented here.

The spectroscopic properties of acetone at combustion relevant pressures and temperatures have been extensively studied and are fairly well understood [32]. The absorption spectrum at 220–330 nm has a maximum near 275 nm. Fluorescence occurs from 350 to 550 nm with a maximum around 400 nm.

The LIF signal for broadband absorbing species and weak excitation energies can be described as

$$I_{LIF} \propto E_{laser} n_{acetone} \sigma_{abs}(T, \lambda) \varphi(T, p, \lambda) \, , \qquad (3)$$

where n is the tracer number density, σ_{abs} the absorption cross section and φ the fluorescence quantum yield. Despite a slight increase in absorption, the fluorescence signal decreases with T due to faster intersystem crossing (ISC) with higher excess energy in the S_1 state, the signal increases with pressure about 30% from 1 to 6 bar air due to vibrational relaxation to states with slower ISC.

2.2.3 Hydroxyl. The hydroxyl radical (OH) is abundant in the flame front and in the hot post-flame gases and is frequently used as a marker for the reaction zone [33, 34]. In the present investigation the frequency-doubled light from a Nd:YAG cluster pumped a dye laser. The light from the dye laser was frequency-doubled once more and tuned to excite the $Q_1(8)$ transition in the *A-X* (1,0) band at about 283 nm. The fluorescence from the (1,1) and (0,0) bands around 310 nm was detected.

3   Experimental setup

3.1   *Combustion chamber*

The combustion chamber has an approximately cubic shape with volume of 167 cm^3. It consists of three orthogonally intersecting cylindrical passages in a block of stainless steel. Each of the cylindrical passages can be sealed, either by fused silica windows, thus providing optical access, or by stainless steel plugs holding pressure sensors and electrodes. The cell has additional diagonal passages, which were connected to an air injection system and a fuel injection system for the injection of compressed preheated air and compressed methane, respectively. For exhaust gas and for the evacuation of the cell, a third diagonal passage was used. Gas flow to and from the chamber was controlled by electromagnetic valves.

In order to facilitate the interpretation of the experimental results, a simplified electrode geometry was chosen instead of a spark plug. Straight threaded stainless steel electrodes with a diameter of 2 mm and sharp tips were used. The threads provided a convenient and flexible way to attach additional disks to the electrodes in order to modify the electrode geometry. The cathode and the wall of the cell were electrically connected to a common ground. The electrode gap, located in the center of the cell, was adjusted to 1 mm.

Heating the cell to temperatures of about 400 K avoided water condensation on windows and other cooler parts, and helped to keep the windows clean, and ensured, together with the heating of the injected gas, a homogeneous temperature field.

3.2   *Optical measurements*

Figure 3 illustrates the optical setup. The temporal evolution of the combustion process in the cell was observed with a specially designed multi-frame laser/detector system. Fuel and OH were visualized in four subsequent time steps. The burst of laser pulses at the required high repetition rate was delivered by a laser cluster consisting of four individual flash-lamp pumped, Q-switched Nd:YAG lasers (BMI). The infra-red laser beams of $\lambda = 1064$ nm are frequency doubled to $\lambda = 532$ nm, and combined into a single
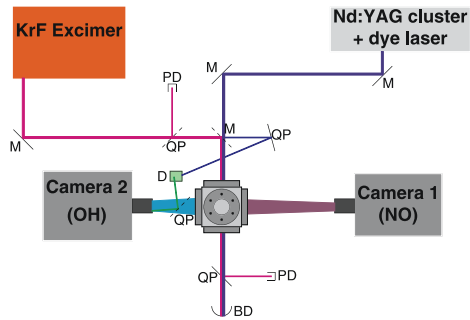

FIGURE 3   Setup used for the simultaneous detection of NO and OH or fuel. The optical path and the main elements are shown. The following abbreviations are used: QP-quartz plate, PD-photodiode, BD-beam dump, M-mirror, D-dye cuvette. Filters and lenses are not shown

beam path. The temporal separation between the pulses is adjustable from 0 to 100 ms, and during the measurement this was set in the range 1.5–3 ms. To detect the fluorescence corresponding to these rapid laser pulses, a high-speed framing camera (Hadland Photonics) was used. The light collected by the camera lens is split and guided to eight separate intensified CCD units, which can be exposed in a rapid succession synchronized with the laser. Optionally an extra image intensifier can be inserted behind the camera lens, which further increases the intensity of the signal, but more importantly converts the ultra-violet fluorescence to visible light, detectable by the camera.

For the OH visualization the pulse train from the Nd:YAG laser was used to pump a dye laser (Continuum ND60). The dye laser operates on a solution of Rhodamine 590 in methanol, and the output of the dye laser is frequency doubled to about 283 nm. A combination of spherical and cylindrical lenses formed a vertical laser sheet (20×0.7 mm^2), which was directed into the combustion cell. The OH LIF was isolated from the scattered laser light by a longpass filter ($\lambda = 295$ nm combined with a bandpass filter (UG 11) and then imaged onto the image intensifier of the framing camera. For the acetone LIF experiments the Nd:YAG laser was frequency-quadrupled ($\lambda = 266$ nm). The signal was passed through a longpass (WG 335) to supress scattered laser light.

Because of the fact that the four laser sheets in an image sequence originate from different lasers, the intensity profiles of the sheets are not identical. Their spatial intensity profiles were not identical and varied from shot-to-shot. Therefore, it was important to monitor the intensity profile on-line during the experiment. A small fraction of the light sheet was directed into a cuvette containing a solution of fluorescing dye. Via a beamsplitter the resulting signal was imaged onto the edge of the image intensifier, which allowed to correct each individual image for light sheet profile and shot-to-shot variation of pulse energy.

NO-Detection: The beam from a tunable, narrowband ($\Delta \nu = 0.4$ cm^{-1}) KrF excimer laser (Lambda Physik, EMG 150 TMSC) at 247.94 nm was formed to a horizontal light sheet (25×0.7 mm^2) using an $f = 1000$ mm cylindrical lens and aligned through the quartz windows of the cell. The focus of the lens was set behind the region of interest. Laser pulse energies (60 mJ/pulse) and laser absorption (up to 40% at peak pressure) were measured on a single-shot basis by means of two photodiodes. The laser power density of 15 MW/cm^2 is below the saturation limit [35]. The signal was imaged onto the chip of an image intensified CCD camera (LaVision, FlameStar II, equipped with an $f = 105$ mm, $f_\# = 4.5$, Nikon UV lens). A combination of four mirrors with narrow spectral reflection characteristics at 230 ± 8 nm and a short pass edge filter (Laseroptik, high reflectance at 248 nm, 0°) were used to isolate the blue-shifted NO fluorescence from any other signal, mainly from O$_2$-LIF, PAH-LIF and Rayleigh-scattered laser light. The signal from the intensified camera was digitized, stored and later processed.

The beams from the two laser systems were spatially overlapped using a 45° reflective mirror for 248 nm with good transmission characteristics at 266 nm and 283 nm. Relative to the respective cameras, the 248-nm laser beam passed the cell in front of the electrodes and the 266 nm or 283 nm beams passed behind them. Therefore, one can observe the shadow of the electrodes on the OH- and the acetone images but not on the NO images.

3.3   *Pressure and current*

The transient pressure in the constant-volume combustion chamber was measured using a flush-mounted, water-cooled, piezoelectric transducer (Kistler) connected to a charge amplifier. A second sensor provided information about the static pressure in the expansion vessel to monitor the evacuation of the combustion chamber and to obtain an indication of the amount of internal exhaust gas recirculation. Thermocouples were used to keep track of the temperature of the preheated air, the fuel, and the cell. A commercial inductive ignition system with ionization sensing capabilities (Mecel AB) has been used. For sensing the current, a voltage of about 80 V is applied across the electrode gap after the igniting discharge.

4   **Investigations**

The ion-current signal along with flame propagation and NO distribution was investigated for two distinct conditions, laminar and turbulent flame. Variable timing between gas inlet and ignition allowed varying of the degree of turbulence. A long delay (5 s) lead to calm gases near-laminar flame propagation (in the following called laminar case). Ignition shortly after gas inlet (100 ms) with the gases still moving around resulted in a turbulent flame development (in the following referred to as turbulent case).

4.1   *First peak of the sensor current*

The first peak of the sensor signal is closely related to the flame propagation during early combustion, and is explained by the electrical contact established between the electrodes by the flame front. The chemi-ionization process in the flame front depends on the equivalence ratio, and so does the magnitude of the first peak. In addition, an influence of the electrode shape and of gas flow can be observed.

4.1.1 Role of the electrodes. First, the measurement of the flame propagation by acetone LIF imaging was performed in quiescent mixtures. Figure 4 shows the current during the first few milliseconds after ignition together with a series of images illustrating the consumption of the fuel by the flame. An additional disk has been attached to the cathode (bottom electrode). When the flame reaches this disk (between 14 and 17 ms after ignition) a current peak appears. This is in agreement with the findings presented in [21], that the contact between the flame and the cathode is the bottleneck for the first peak of the sensor current.

4.1.2 Effect of turbulence. Turbulence moves and distorts the flame kernel. This may lead to deviations in the contact surface between electrodes and flame front and thus, to fluctuations in the current. Due to a more structured flame shape,
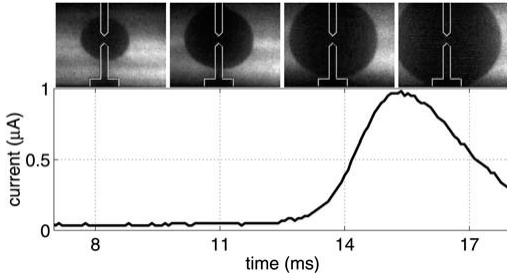
FIGURE 4   Early flame propagation (8, 11, 14, and 17 ms after ignition, imaged by fuel tracer LIF) and sensor current in quiescent mixture. Regions where the fuel has been consumed by the flame appear dark in the images. The shadow of the vertically arranged electrodes are visible, best in the image to the left. Imaged area: 29×23 mm^2
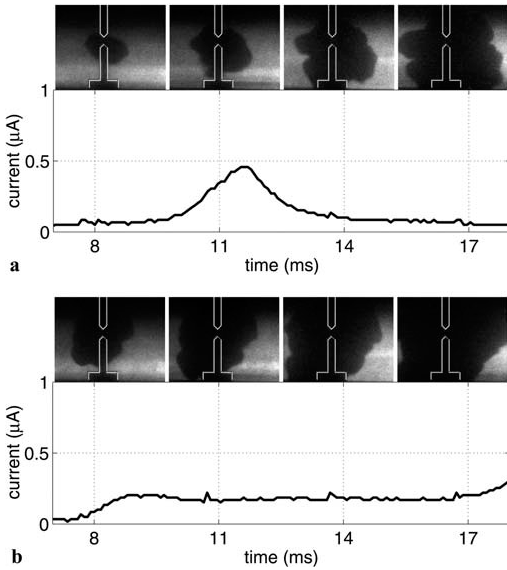

FIGURE 5   Examples of early flame propagation and sensor current in turbulent mixtures

the flame may touch the electrodes repeatedly, leading to several peaks in the early signal, which can be frequently observed in engine measurements. Figure 5 shows examples of the flame propagation in a turbulent mixture together with the signals from the current sensor. From a large number of measurements, representative examples have been selected to provide a basis for the discussion of the hypothesis mentioned above.

Similar to the laminar case, the current in Fig. 5a shows a distinct peak. However, the magnitude of the peak is reduced by a factor of 2 compared to the laminar case. An explanation is found in the corresponding images of the flame propagation: apparently, the flame covers only part of the cathode disk. The flame propagation shown in Fig. 5b deviates even more from the laminar case shown in Fig. 4. The flame reaches the left side of the disk and propagates

along the surface, covering only small parts of it at once, thus giving rise to a low yet persisting current. The degree of turbulence in the cell was not sufficient to accomplish situations when the flame kernel repeatedly gets into contact with the electrodes and multiple peaks appear in the current.

The examples given above explain the complex and varying shapes of the sensor signal during early combustion that are often observed in engines where imaging of the spark plug region is more difficult and where the involved geometry of the electrodes hampers signal interpretation [7, 9].

4.2   *Second peak of the sensor current*

The second peak of the sensor current (cf. Fig. 1) is caused by thermal ionization in the post-flame gas. Temperature and gas composition in the vicinity of the electrode gap determine the sensor current. The species with lowest ionization potential can be expected to dominate the ionization equilibrium provided that a sufficient concentration of this species is available. NO is the combustion product with the lowest ionization potential.

4.2.1 NO concentration and sensor current. The relationship between the NO concentration in the burned gas and the sensor current has been studied. The evaluation scheme shown in Fig. 6 has been used to separate the effects of temperature and the concentration of the ionized species. As a result, information about the effective ionization potential of the burned mixture is obtained. In the experiment, we found that species with an ionization potential between 4 and 5 eV dominate the ionization process, whereas the ionization potential of NO is 9.27 eV. Possible candidates in this range are potassium ($E_i = 4.34$ eV) or sodium ($E_i = 5.14$ eV). Both are present in the atmosphere at concentrations around 200 and 700 ng/m^3 [36, 37].

In addition to this information, the cycle-resolved data about the NO mole fraction close to the electrode gap obtained from the LIF measurements can be related to the offset in the linear relationship in (2). According to these results the ionization process is dominated by species with a much lower ionization energy than that of NO. Yet a weak relationship between the NO mole fraction and the ionization degree of the burned gas was observed. The abundance of NO in the burned gas may explain this observation.

4.2.2 Role of the electrodes. Figure 7a shows an example of the NO distributions recorded in quiescent mixtures 40 ms after ignition. One would expect a homogeneous distribution as is observed when seeding NO into cold air. However, the distributions we observed share a common feature, namely an area of low signal in the vicinity of the electrodes. As the laser sheet passes in front of the electrodes, this cannot be the shadow of the electrodes. The focus of the laser sheet can also be excluded as a reason for this observation, as it was placed outside the imaged area. Apparently, there are fewer detectable NO molecules in the vicinity of the electrodes. In the discussion of this observation, two effects must be considered. Both are related to temperature, which may be lower
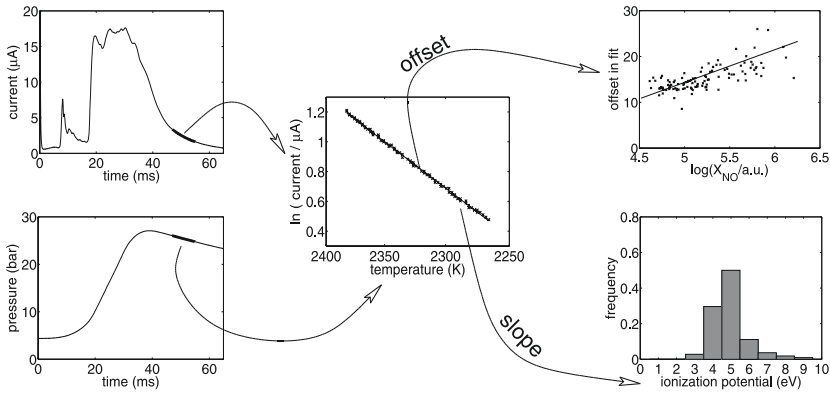
FIGURE 6   Evaluation strategy: a chunk of pressure and current data from the time after completion of combustion is selected (*left*). Gas temperature is estimated from the pressure curve with the ideal gas law. The logarithm of the current is a linear function of the inverse temperature (*middle*), with the slope giving the apparent ionization potential of the gas and an offset containing information about the concentration of the ionized species according to (2). Data from 110 cycles is compiled in the two plots to the *right*. The offset in the fit correlates with the mole fraction of NO, X_{NO} in the burned gas. The histogram below shows that species with an ionization potential around 4–5 eV dominate the ionization equilibrium

in this region because of the cooling effect of the colder electrodes. Firstly, a lower temperature leads to a lower population of the initial state used for NO detection, thus reducing the signal. However, as discussed above, the excitation and detection scheme used is fairly insensitive to local temperature fluctuations unless the temperature drops below 1900 K. Secondly, the concentration of NO itself may be lower. The formation of NO in the region cooled by the electrodes is slower and – if equilibrium is reached at all – the equilibrium concentration will be lower. Thus, the regions with low signal in fact contain less NO than the surrounding gas.

A similar behavior can be observed in the example of an OH distribution presented in Fig. 7b. The "footprint" of the electrodes is clearly visible.

4.2.3 Effect of Turbulence. Figure 8 shows sample NO distributions in turbulent combustion. A comparison with Fig. 7
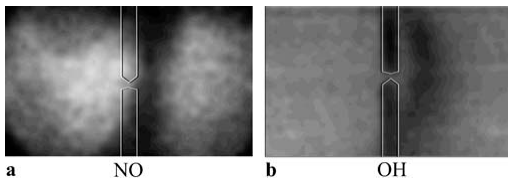

FIGURE 7   Examples of species distributions (single-shot) taken at 40 ms after ignition. The position of the electrodes in the imaged area are indicated by thin lines. Imaged area 33×20 mm^2

reveals that the regular pattern with low intensity close to the electrodes is missing. Instead, large spatial variations of the NO signal can be observed. As in the laminar case above, the variations may be caused by various processes. The combustion chamber has a rather structured shape, leading to a disadvantageous ratio of surface area to volume. Flame quenching at the wall therefore results in a relatively large fraction of unburned gas. In addition, much of the burned gas resides close to the wall and is cooled. The gas flow transports these regions of unburned or cooled burned gas to the center of the cell.

This process can also be observed in the series of species distributions in Fig. 9. While the NO image (60 ms) presents a snapshot of the NO distribution, the OH images give an impression of the evolution of the OH distribution close to the electrodes. The dark cloud in the lower left corner moves towards the electrodes at a speed of about 0.7 m/s.

This illustrates the time scale for changes of the gas composition at the electrodes. The structures with higher NO concentration visible in Fig. 8 need about 40 ms to pass the imaged area. The size of these structures ranges between 2 mm and 1 cm. Thus, the properties of the gas at the electrodes vary on a timescale of several milliseconds.

If the local gas temperature varies on this timescale, it should be visible in the relationship between the inverse average gas temperature and the logarithm of the current as a deviation from linearity. Figure 10 presents four examples of this relationship. The average gas temperature has been estimated from the pressure. Compared to e.g. Fig. 6, the deviations from linearity are more pronounced. This may indicate
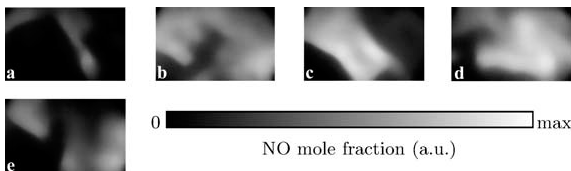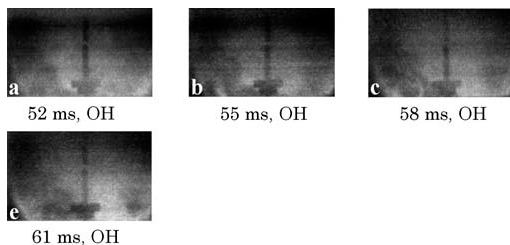

FIGURE 8   Examples of NO distributions from turbulent combustion, taken 60 ms after ignition. The gray levels are proportional to the NO mole fraction, but not calibrated. That is why arbitrary units (a.u.) are used on the scale. Imaged area: 33×20 mm^2

52 ms, OH   55 ms, OH   58 ms, OH   60 ms, NO

FIGURE 9 Series of OH images (**(a-c)** and **(e)**, imaged area: $41 \times 26\ mm^2$) and the corresponding NO distribution (**(d)**, imaged area: $33 \times 20\ mm^2$). Lighter areas correspond to higher concentration of OH and NO, respectively
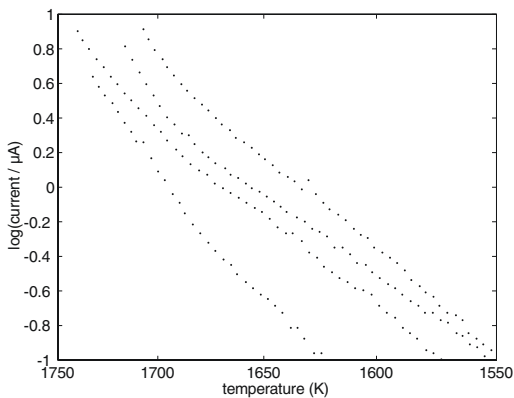

61 ms, OH

FIGURE 10 Four examples (*single cycle*) of the relationship between the logarithm of the current and the inverse average gas temperature in turbulent mixtures (100 ms mixing time). The average gas temperature has been estimated from pressure with the ideal gas law. The data cover a time interval of 16 ms. Deviations from linearity can be explained by fluctuations in the local temperature

that the local gas temperature deviates more from the average gas temperature in turbulent combustion than in quiescent combustion.

5   Summary

Laser-induced fluorescence imaging has been employed to improve the understanding of the governing processes leading to the signal of the ionization sensor. The flame propagation during early combustion was monitored under laminar and turbulent conditions using acetone LIF to study the effect on the sensor current. Based on these measurements, the cycle-to-cycle variations of the early current could be attributed to the stochastic contact between flame front and electrodes.

Imaging of NO and OH distributions in the burned gas contributed to the further understanding of the second peak of the sensor current. The mole fraction of NO, which was up to now considered to be the major species for ionization in the post-flame zone, was measured and related to the temperature-corrected ionization sensor signal. However, the relationship between gas temperature and sensor current indicated that the bulk ionization in the temperature range investigated originates from alkali traces in the atmosphere. A correlation between the NO mole fraction and the sen-

sor signal was still observed and can be expected to become more dominant under operating conditions that result in higher gas temperatures, where the alkali ionization runs into saturation.

Evidence was found for cooling of the burned gas by the electrodes. As the main part of the sensor current during late combustion is supposed to travel in the electrode gap, this observation should be considered when designing models for the sensor. Heat losses to the electrodes are significant, and gas temperature is the most important parameter for ionization.

At turbulent conditions, imaging experiments have shown strong local inhomogeneities of NO and OH concentrations in the post-flame gas. These variations pass the electrodes on a time scale of several milliseconds. We assume this to be responsible for the variations in the sensor current that reside on the same time scale.

REFERENCES

1 A. Lee, J.S. Pyko, SAE technical paper series, 950 003 (1995)
2 J. Auzins, H. Johansson, J. Nytomt, SAE technical paper series, 950 004 (1995)
3 K.N.C. Bray, N. Collings, Endeavour New Ser. **15**, 10 (1991)
4 N. Collings, S. Dinsdale, D. Eade, SAE technical paper series, 860 635 (1986)
5 Y. Ohashi, M. Koiwa, K. Okamura, A. Ueda, SAE technical paper series, 1999-01-0550 (1999)
6 M. Hellring, T. Munther, T. Rögnvaldsson, N. Wickström, C. Carlsson, M. Larsson, J. Nytomt, SAE technical paper series, 991 162 (1999)
7 M. Hellring, T. Munther, T. Rögnvaldsson, N. Wickström, C. Carlsson, M. Larsson, J. Nytomt, SAE technical paper series, 991 161 (1999)
8 H. Klövmark, P. Rask, U. Forssell, SAE technical paper series, 2000-01-1245 (2000)
9 L. Eriksson, L. Nielsen, J. Nytomt, SAE technical paper series, 960 045 (1996)
10 I. Andersson, L. Eriksson, SAE technical paper series, 2000-01-0552 (2000)
11 A. Saitzkoff, R. Reinmann, T. Berglind, M. Glavmo, SAE technical paper series, 960 337 (1996)
12 V. Naoumov, A. Demin, A. Sokolov, I. Andersson, SAE technical paper series, 2002-01-0009 (2002)
13 V. Naoumov, A. Demin, A. Sokolov, SAE technical paper series, 2003-01-0724 (2003)

14 H. Wilstermann, *Wechselspannungszündung mit integrierter Ionen-Strommessung als Sensor für die Verbrennungs- und Motorregelung* (PhD Thesis, Fortschr.-Ber. VDI **12**, Nr. 398, Gaildorf, 1999)

15 A.B. Fialkov, Prog. Energ. Combust. **23**, 399 (1997)

16 Y.P. Raizer, *Gas Discharge Physics* (Springer, Berlin 1997)

17 R. Reinmann, A. Saitzkoff, F. Mauss, SAE technical paper series, 970 856 (1997)

18 I. Andersson, *Cylinder Pressure and Ionization Current Modeling for Spark Ignited Engines* (Licentiate Thesis, Linköping University, 2002)

19 R. Reinmann, *Ionized Gases in Spark Ignition Engines* (PhD Thesis, Lund Inst. of Tech. 1998) Lund Reports on Combustion Physics, LRCP-37

20 A. Franke, P. Einewall, A. Larsson, R. Reinmann, SAE technical paper series, 2003-01-0715 (2003)

21 A. Franke, R. Reinmann, A. Larsson, SAE technical paper series, 2003-01-0714 (2003)

22 W.G. Bessler, C. Schulz, T. Lee, J.B. Jeffries, R.K. Hanson, Appl. Opt. **42**, 4922 (2003)

23 C. Schulz, V. Sick, J. Heinze, W. Stricker, Appl. Opt. **36**, 3227 (1997)

24 C. Schulz, J.B. Jeffries, D.F. Davidson, J.D. Koch, J. Wolfrum, R.K. Hanson, In: 29th Symp. Comb., Comb. Inst. (2002) p. 2725

25 A.C. Eckbreth, *Laser Diagnostics for Combustion Temperature and Species* (Gordon and Breach Publishers, Amsterdam 1996)

26 W.G. Bessler, C. Schulz, V. Sick, J. Daily, In: Joint Meeting of the Combus. Inst., Chicago, IL, (Comb. Inst. (2003))

27 W.G. Bessler, C. Schulz, M. Hartmann, M. Schenk, SAE technical paper series, 2001-01-1978 (2001)

28 F. Hildenbrand, C. Schulz, V. Sick, G. Josefsson, I. Magnusson, Ö. Andersson, M. Aldén, SAE technical paper series, 980 148 (1998)

29 C. Schulz, V. Sick, J. Wolfrum, V. Drewes, M. Zahn, R. Maly, In: 26th Symp. Comb., (1996) p. 2597

30 F. Vannobel, A. Arnold, A. Buschmann, V. Sick, J. Wolfrum, B. Cousyn, M. Decker, SAE technical paper series, 932 696 (1993)

31 J.G. Lee, D.A. Santavicca, J. Propul. Power **13**, 384 (1997)

32 M.C. Thurber, R.K. Hanson, Appl. Phys. B **69**, 229 (1999)

33 M. Alden, H. Edner, G. Holmstedt, S. Svanberg, T. Högberg, Appl. Opt. **21**, 1236 (1982)

34 S. Böckle, J. Kazenwadel, T Kunzelmann, C. Schulz, Appl. Phys. B **71**, 741 (2000)

35 C. Schulz, V. Sick, U. Meier, J. Heinze, W. Stricker, Appl. Opt. **38**, 1434 (1998)

36 S.J. Baker, Technical report, Dept. of the Env., Transport and the Regions; the Scottish Exec.; the Nat. Ass. for Wales and Dept. of the Env. in Northern Ireland (2001)

37 E. Swietlicki, S. Puri, H.C. Hansson, H. Edner, Atmos. Environ. **30**, 2795 (1996)

III

IGNITION, FLAME GROWTH AND EXTINCTION IN PREMIXED COMBUSTION DOMINATED BY A STRONGLY OSCILLATING FLOW FIELD

Annika Lindholm*, Jimmy Olofsson, Sven-Inge Möller, Johan Hult** and Marcus Aldén

Division of Combustion Physics
Faculty of Engineering LTH
Lund University, Sweden

*Siemens Industrial Turbomachinery AB
Finspång, Sweden

**Cambridge University
U.K.

Abstract

Experimental studies focused on the ignition, combustion and extinction processes in the strongly oscillating flow field have been performed. The experiments utilized a Helmholtz type pulse combustor featuring a repeatable oscillating flow field suitable for studies of the interaction between fluid dynamic and combustion related to combustion instabilities. A high repetition rate laser and camera system were used for phase locked simultaneous Laser Induced Fluorescence of OH and chemiluminescence. Results for two different operating conditions, both corresponding to lean premixed combustion of methane, are presented. These data are supplemented with cycle resolved velocity fields for one of the operating conditions. The major difference between the two operating conditions is the total mass flow rate and the inlet jet velocity. The combustion appears distinctly different for the two operating conditions. At the higher total mass flow rate, pre-ignition is observed in the beginning of the cycle. After pre-ignition OH is present although the combustion is extinct due to high fluid dynamic strain. The fresh air/fuel mixture continues to mix with combustion products from the previous cycle and becomes distributed over a major part of the combustion chamber until the almost simultaneous ignition beginning around the last quarter of the cycle. For the lower total mass flow rate, the combustion is localised to a region defined by the diverted inlet jet. Chemiluminescence is recorded throughout the cycle although the major part of the combustion takes place at the last quarter of the cycle.

Manuscript in preparation

1. Introduction

In the search for environmentally friendlier combustion systems, the number of combustion applications operated in lean premixed mode has increased. As the performance of these systems are stretched towards the operational limits the probability for occurrence of combustion instabilities or combustion induced oscillations increases significantly. Such processes may severely impair the performance of the combustion system and can lead to mechanical failure due to vibrations or the increased heat transfer [1,2]. Combustion instabilities in various applications have been extensively studied over the years as reviewed by e.g. Crocco [3], Culick [4], Barrère and Williams [5], Putnam [6], McManus et al. [7] and Renard et al. [8].

The driving processes of combustion instabilities are closely related to the dynamics of unsteady flow [1, 5, 9]. Several types of unsteady flow phenomena of importance for generation of flame instabilities can be identified. Hydrodynamic instabilities such as coherent structures in turbulent flow, e.g in mixing layers or jets can lead to unsteady heat release due to the temporal fluctuations. Vortices can also be created by acoustic interaction resulting in high sloshing velocities induced by acoustic transverse or longitudinal modes. Turbulent flames may exhibit large scale motion, this may cause pulsations in the inlet jet of fresh reactants and initiate periodic oscillation of the heat release. In this case the jet oscillates in a longitudinal acoustic mode. The flame instabilities can also be created by flame extinctions of short duration of excessive strain rates, the reactants will re-ignite when the flow perturbation diminish.

Pulse combustors and dump-combustors for hazardous waste incineration are examples of combustion applications where the advantages of controlled unsteady combustion, such as increased heat and mass transfer are utilized. The acoustic interaction with the flow field and the subsequent combustion are the same in this case as for the mechanisms responsible for the development of unwanted combustion instabilities, [10]. The reproducible oscillating combustion process in pulsating combustion is therefore suitable for studies of the effects of fluid dynamic and combustion interactions.

The fluid flow in the combustion chamber of a Helmholtz type pulse combustor is dominated by a strong toroidal vortex created when the incoming jet of fresh reactants passes the stagnation plate. Keller et. al, [10], have shown that this vortex is responsible for large scale entrainment as well as small scale mixing of fresh reactants with hot combustion residuals. The conclusion in the work cited above, which has given extensive insight regarding ignition and combustion in a strongly oscillating flow field, were drawn from phase locked ensemble-averaged measurements of the velocity field, instantaneous chemiluminescence and schlieren images. Work by others [11,12], as well as earlier work by Keller & Saito [13], show that the measured chemiluminescence never completely reaches zero during the combustion cycle. Data in Ref. [10] also show chemiluminescence at all times but not in the region of the reactants during injection. It was concluded that the ignition of the fresh reactants occurs first along the outer edges of the rolled-up toroidal vortex and develops rapidly in the centre where uniform combustion of the fresh reactants occur. Reaction was found to exist in the smaller recirculation zone behind the sudden expansion, outside the high-strain region, producing a continuous combustion source, however, this is not the source of re-ignition. Flame extinction by fluid dynamic strain is proposed to delay ignition during injection while reactants and hot products continue to mix until the strain has decreased to a level allowing ignition and subsequent almost

volumetric combustion. However, the conclusions in Ref. [10] are based on line-of-sight measurements of chemiluminescence and schlieren images and will not show any details of possible flame structures and the source of reignition can not be verified from these measurements. Furthermore, the measurements in Ref. [10] were performed for a single operating condition, although a small adjustment of the stagnation plate position may lead to considerable changes in frequency and input power.

In a previous study [14] the effect of inlet geometry, in terms of different stagnation plate positions, on the operating conditions for a Helmholtz type pulse combustor with a combustion chamber of square cross section was investigated. The temporal profile of the heat release, indicated by OH chemiluminescence, was found to vary significantly for small changes in the inlet geometry. Because of higher velocities due to increased mass flow the vortical structures reach further into the combustion chamber resulting in enhanced overall mixing and more rapid combustion. The heat release in the pre-ignition region decreases with increasing distance between the stagnation plate and the inlet. This observation supports the suggestion in Ref. [10] that flame extinction by fluid dynamic strain inhibits ignition of the fresh reactants during the injection phase and that the extinction process by nature is more pronounced for increased overall mass flow rate.

The purpose of the present study is to continue and extend the investigations presented in Ref. [14], which focused on time-resolved local measurements of pressure and heat release equivalents, to detailed experimental studies of the flame structure for two inlet geometries and corresponding operating conditions. The experimental data are used to verify possible ignition delay due to fluid dynamic strain as well as to identify possible reignition sources. Time resolved Planar Laser Induced Fluorescence (PLIF) of OH and line of sight integrated chemiluminescence images, supplemented by previously measured flow fields for one operating condition, are employed to investigate the structural changes of the flame geometry for two different inlet configurations.

2. Experimental Techniques

2.1 Experimental combustor

The Helmholtz type pulse combustor used in this study, primarily consists of a flapper valve, a combustion chamber and a tail pipe, see Fig 1. The pulse combustor system includes decouplers at the inlet and outlet. The pressure actuated flapper valve positioned inside the inlet decoupler controls the injection and mixing of fresh air/fuel mixture into the combustion chamber. The arrangement of the gas supply inside the valve and the complex flow path from the valve to the combustion chamber, ensure that a homogeneous air/fuel mixture enters the combustion chamber. During the experiments a fan working at constant speed supplies combustion air to the inlet decoupler. In order to give optical access to the combustion zone the combustion chamber walls are made of quartz, forming a square cross section (80x80 mm) with a length of 150 mm. The total volume of the combustion chamber, including the contraction cone which connects the combustion chamber to the tail pipe, is 1.5 litres. A circular stagnation plate with a diameter of 25 mm is mounted to a 5 mm rod centred to the inlet of the combustion chamber, see Fig. 1 (bottom). The inlet geometry of the combustor can be altered by adjusting the position of the stagnation plate. In this way the burner input, air flow, operating frequency and air/fuel ratio can

be modified, [14]. This configuration can operate in a stable manner for a long period of time, which is an essential condition for the measurements performed.

Fig. 1

The burner input is measured with a thermal mass flow meter and the actual burner input is calculated from the lower heating value of the methane gas used as fuel during the experiments. For emission measurements the exhaust gases are continuously sampled at a flow rate of 1 l/min through an electrically heated tube connected to the exhaust decoupler. To calculate the equivalence ratio, the oxygen concentration is measured by a paramagnetic analyser. The accuracy of the O_2 measurements are within $\pm$ 0.2 % O_2. The pressure in the combustion chamber is measured by a water cooled piezoelectric pressure transducer, located at the combustion chamber wall. A second pressure transducer is located at the combustion chamber side of the pressure actuated valve.

The flow field in the combustion chamber has previously been measured by Laser Doppler Velocimetry (LDV). To obtain cycle resolved velocity fields, the LDV and pressure signals were simultaneously sampled. By dividing the pressure cycle in 20 time bins and applying a conditional phase averaging method average pressure and velocity cycles were generated, [12].

2.2 High speed diagnostic system for Laser Induced fluorescence of OH

A high-repetition rate laser and camera system was utilized for phase locked measurements of the flame front. The OH-PLIF intensity images were collected from three different planes of the axisymmetric combustion chamber. Simultaneously, the chemiluminescence from the flame was recorded. The high speed PLIF diagnostic system collected sequences of four images with a temporal resolution of 100, 150 and 350 μs between the images. The measurements were carried out for two different operating conditions, both corresponding to lean premixed combustion.

The hydroxyl radical (OH) is involved in all hydrocarbon combustion and plays a central role in oxidation chemistry. Since OH is formed close to the flame front it is often used as a flame front marker. An example where OH PLIF has been used for studies of flame front structures in SI engines can be found in reference [15]. OH is formed by fast two-body reactions and is consumed by slower three-body recombination reactions [16]. In a premixed flame the OH produced at the flame front is slowly consumed in the burnt gases, and thus acts as a marker of both the flame front and, partially, of the burnt gases. In the present work a unique high speed laser diagnostic system, which previously has been applied to studies of non-premixed jet flames [17] and IC engines [18], has been used.

The laser diagnostic set-up shown in Fig. 2 is used to obtain the OH fluorescence images. At the upper left corner the combustion chamber top view indicates the location of the three different planes A = centre plane, B = centre + 15 mm and C = centre + 30 mm. OH is excited by using the $Q_1(8)$ transition in the $A^2\Sigma^+ \leftarrow X^2\Pi$ system, corresponding to a wavelength around 283 nm. To generate this wavelength, a dye laser is pumped by a multiple-YAG laser system (BMI/CSF-Thomson), consisting of four individual Nd:YAG lasers. The time separation between the pulses from these lasers can be adjusted from 0 up to 100 ms, and when performing the experiment it

was set to be 100 – 325 µs, in order to fully capture the motion of the turbulent reacting flow. The pulses from the individual Nd:YAG lasers are aligned and frequency doubled to 532 nm before pumping the dye laser (Continuum ND60). Laser radiation of 283 nm is finally produced by frequency doubling of the output from the dye laser, operating on a Rhodamine 590 dye solution in methanol. The energy in a single laser pulse at 283 nm was about 5 mJ for a pulse separation of 100 µs, and 10 mJ for 325 µs pulse separation. The laser light is formed to a laser sheet, 60 mm wide and 0.3 mm thick. This laser sheet is then directed into the combustion chamber through the top quartz plate, generating fluorescence light from the OH radicals in the intersection with the flame. The four rapidly sequenced OH-PLIF images are detected by a high-speed framing camera, consisting of eight intensified CCD cameras. An eight-facet pyramidal prism placed behind the camera lens, splits the incoming fluorescence light onto the individual CCD cameras. With an individual Multi Channel Plate, MCP, in front of each CCD working as a shutter, it is possible to expose the CCD cameras in a rapid sequence. This procedure was synchronized with the laser system, enabling imaging of the fluorescence light originating from each of the four laser pulses. When performing the experiment every other CCD camera is used to image the fluorescence light. The other four CCD cameras are used to image spontaneous emission from the flame shortly after each laser pulse. Since the fluorescence light from OH is emitted in the ultra-violet region and the beam splitter optics in the camera is made of glass, an extra image intensifier is added to the framing camera to convert the fluorescence to visible light, detectable by the CCD cameras. To discriminate against laser light scattered from surfaces, a long-pass filter transmitting wavelengths above 295 nm is placed in front of the camera lens. The image area was around 70 mm in height and 50 mm in width. Since the laser sheet intensity profile varies slightly from shot to shot, the profile is measured for each laser shot. To do this, 4 % of the intensity is split off from the laser sheet by a quartz plate, right before entering the combustion chamber. This reflected laser sheet is directed into a transparent cell containing a homogenously mixed solution of a fluorescing dye. The fluorescence from the dye is directed onto the camera objective by a second quartz plate. This results in images where the top rows contain the dye fluorescence, i.e. the laser intensity profile, and the rest of the image contains the OH fluorescence from the combustion chamber. Intensity fluctuations in the images due to variations in laser intensity profile could then be compensated for by using this additional information. Each series consists of four sets of images, consisting of one OH-LIF image and one chemiluminescence image (exposure time 16 µs), with a time separation of 100, 150 or 325 µs between the sets.

Fig. 2

2.3 Data post-processing

The imaging system is synchronised with the operating cycle of the pulse combustor by means of the two pressure signals. In order to step through the operating cycle a pulse generator creates a trigger pulse with a programmable delay relative to the well defined zero crossing of the rising valve pressure signal. The trigger pulse is used to initiate the first laser pulse. Because of cycle-to-cycle variations it is not possible to know the exact operating frequency of the actual operating cycle in advance. A trigger pulse from the CCD-camera is transferred to the gate of one of the clocks on the data acquisition board initiating the start of collecting the pressure from

the combustion chamber and valve. In this way, the exact time, within 1 µs, in the actual pressure cycle is recorded together with the corresponding image.

Reynold's time-averaging for oscillating, unsteady turbulent flows is used to deduce the pressure, the organised unsteady component and the turbulent component. This method has been used earlier by Dec et al. [19]. In the post processing of the data the pressure signal is filtered in a second order Butterworth bandpass filter with cut-off-frequencies of 40 and 500 Hz and the negative zero crossing of combustion chamber pressure is used to identify the beginning of a cycle. The pressure cycle is divided into 145 time bins and averaged over a number of cycles. After the mean operating cycle was deduced a cubic spline calculated the mean pressure for the instant in the cycle when each series of images was recorded and out of ten series for the same delay the one closest to the mean pressure cycle was chosen.

During post-processing of the collected images the background level, recorded without combustion was subtracted from both PLIF and emission images. The OH PLIF images were then divided by the laser intensity profile, which was measured on-line. This compensates for fluctuations and inhomogeneities in the laser pulse energy and profile. Finally, noise in the PLIF images was reduced by filtering, using the technique described in Ref. [20], which smoothes additive image noise by generating statistics in a local neighbourhood and comparing them to the expected values.

3. Results and Discussion

Measurements were carried out for two different operating conditions corresponding to two different inlet geometries and equivalence ratios, Cases 1 and 2, see table 1. The gas supply pressure, p_g, and the inlet decoupler pressure, p_{id}, are given relative to atmospheric pressure.

Tab. 1

Velicity fields are available from previous LDV measurements [12], carried out for the operating condition corresponding to Case 1 in this study. These measurements, indicate that the flow field was found to be dominated by a high velocity entraining jet incorporating large axial and transversal velocity fluctuations. Thus this case is suitable for investigations of extinction processes in a strongly oscillating flow field. The second operating condition is obtained by moving the stagnation plate closer to the inlet and thereby creating an inlet geometry with increased pressure drop and lower air flow rate into the combustor. To accommodate the decreased air flow, the gas supply pressure was lowered to give an overall equivalence ratio of 0.85. The change in inlet geometry of a pulse combustor will cause the air and fuel flow to automatically adjust itself to a certain degree resulting in a subsequent change in operating frequency and pressure amplitude. This choice of operating conditions for Case 2, is used to investigate how the injection, ignition and combustion processes are affected by the decreased total mass flow rate through the combustor and hence the decreased velocity of the entraining jet.

6

To determine the opening and closing times of the valve, the pressure on the combustion chamber side of the valve was measured simultaneously with the pressure in the combustion chamber. The ensemble-averaged pressure and pressure fluctuations are shown for the two test cases in Fig. 3. Given the measured pressure, p_{id}, in the inlet decoupler, it can be observed that the valve is closed approximately between $t/\tau \approx 0.7$, and $t/\tau \approx 0.875$ for Case 1 and between $t/\tau \approx 0.975$ and $t/\tau \approx 0.05$ for Case 2, τ denotes the time of one cycle. For case 1, $\tau \approx 16$ ms, and for Case 2, $\tau \approx 10$ ms. To be noted is also the large pressure fluctuations for Case 2, indicating a more unstable operation of the pulse combustor for this case.

Fig. 3

Ensemble-averaged velocity fields from LDV superposed on measured instantaneous OH images at the centre plane A, Case 1, are shown for four different instants of the operating cycle, see Fig 4. These instants correspond to $t/\tau = 0.025$, 0.275, 0.475 and 0.675. In order to retain as much information as possible, the instantaneous OH images are scaled separately between the different instants in Fig 4. Ensemble-averaged axial, v''_{ax}, and transversal, v''_{tr}, velocity fluctuations are also included.

Fig. 4

At time $t/\tau = 0.025$ the onset of injection has already started and the inlet jet can be observed in the areas showing slightly higher intensity of the axial and transversal velocity fluctuations. Structures of OH can be seen emanating from the stagnation plate towards the combustion chamber wall near the inlet, corresponding to the interface between the diverted inlet stream and the low velocity stagnation region behind the stagnation plate. As the injection phase reaches its peak ($t/\tau \approx 0.275$), two clearly visible vortices downstream of the stagnation plate can be observed causing higher velocities in the centre core. OH is now visible in a structure following these vortices, corresponding to the distinct interface between regions with high, respectively low intensity of velocity fluctuations. Further on, the high velocity fluctuations are localized to the inlet jet and the downstream side of the vortex, whereas the second half of the combustion chamber and the centre core right behind the stagnation plate exhibit low velocity fluctuations. Close to ignition at time, $t/\tau = 0.475$, there is no distinct OH except at the downstream edge of the laser sheet corresponding to low velocity fluctuations. The inlet jet has now slowed down but the velocity of the counter flow region in the centre core is close to its maximum. Small but homogenous velocity fluctuations in the centre core extending over a large part of the combustion chamber indicates efficient mixing between fresh reactants and burnt gases. During peak of combustion at time, $t/\tau \approx 0.675$, the velocities are low and small homogenous velocity fluctuations are observed in most parts of the combustion chamber.

Experimental data from chemiluminescence and OH-LIF measurements, corresponding to cycle times $t/\tau = 0$, 0.3, 0.5 and 0.7 are presented in Fig. 5. The chemiluminescence images are line-of-sight measurements integrated over the entire depth of the combustion chamber. The OH images are presented at their actual position and size during the measurements, where sheet A is the centre plane, sheet B is centre plane + 15 mm and sheet C is the centre plane + 30 mm (as indicated earlier in Fig. 2). It is important to underline that OH-intensity between different sheets and data for the two different cases cannot be compared. The relative OH concentrations can, however, be compared for the same sheet and case.

Fig. 5

For Case 1 (Fig. 5, upper part) there is chemiluminescence close to the inlet surrounding the stagnation plate at the beginning of the operating cycle. The OH-intensity images from planes A, B and C shows the entraining jet as it enters and partly mixes with the residual burnt gases from the previous cycle. At the interface between fresh air/fuel mixture and residual gases there are small flamelet like structures, indicating early ignition or pre-ignition along the outer edges of the entraining jet at low velocities. This flame is partly extinguished but partly distributed along the edges of vortices created by the entraining jet as can be seen at $t/\tau = 0.3$ in Fig. 5. This differs from the chemiluminescence measurements, where there is no sign of chemiluminescence in the region of the reactants during injection at high velocities and high velocity fluctuations. At the centre core there is an evenly distributed pool of OH in the ground state. Plane C shows only small islands of OH towards the inlet of the combustion chamber, indicating that this plane is now dominated by the fresh air/fuel mixture transported by the entraining jet. Chemiluminescence appears late in the cycle at time $t/\tau \geq 0.5$ when ignition is about to start. From Fig 4 ($t/\tau = 0.475$) it is evident that there are structures of OH that may act as ignition sources. This shows that OH at ground level is present during the entire injection phase but there is no OH^* or CH^* (excited state). Tuning the dye-laser output wavelength off the OH-resonance line confirms that the detected signal really originates from OH fluorescence. At time, $t/\tau = 0.7$, combustion reaches its maximum intensity, featuring strong OH-intensity in all the measured planes. Assuming that the flame front can be deduced by finding the largest gradient in the OH images, it can be observed that no distinct flame front exists in this very lean case.

For Case 2 (Fig. 5, lower part), the injection phase has not been initiated at time, $t/\tau = 0$, and there are yet no signs of an entraining jet. The chemiluminescence image shows that reactions are taking place close to the inlet pipe but the main combustion have not been initiated at this time. At the next instant, one can distinguish the entraining jet and the flame located near the edges of the toroidal vortex. The flame location is indicated by the appearance of strong chemiluminescence in the same region. Combustion is present during the entire cycle and peaks at $t/\tau \approx 0.525$-0.560. Due to increased inlet decoupler pressure and decreased combustion chamber pressure there is a net flow of reactants into the combustion chamber during a major part of the operating cycle. The flame front is nearly laminar, slightly wrinkled but distinguishable. The structures corresponding to the outer edges of the toroidal vortex are clearly visible. Behind the flame, an evenly distributed region of OH slowly decaying from combustion and transported towards the combustion zone can be observed.

In Fig 6(a-b), instantaneous OH images for the first part of the operating cycle for Case 1 (sheet A, B) and Case 2 (sheet B) are presented. The chemiluminescence images are also included, corresponding to the area visualised in the OH images displayed in the row above. The chemiluminescence images are taken 1 µs after the corresponding OH image. The selected part of the operating cycle illustrates the injection, extinction and ignition phase for the two measured cases. As previously mentioned, the OH-intensity is scaled within one set of images and can be compared. The intensity in the images ranges from black (low) to white (high).

The entraining air/fuel jet is clearly observed in Fig 6a, sheet B, where the entire injection, extinction and ignition phase is presented. The valve opens before the combustion cycle is

completed. During the first part of the cycle, when the velocity of the inlet jet still is moderate, there are clearly mixing and reactions taking place. Residual OH at ground level from the previous combustion cycle serves as a marker between fresh reactants and burnt gases. From the two measured sheets it can be deduced that a pool of OH radicals is present. This pool is partly extinguished and partly transported towards the centre core and the inlet, as can be seen in the sequence from sheets A and B. The main ignition starts at $t/\tau \approx 0.5$, see the chemiluminescence images, and emanates from the centre core spreading outwards. At this time the dark region represents a mixture of residual hot gases from the previous cycle and the fresh air/fuel mixture. Ignition occurs early in the cycle along the interface between the outer edges of the entraining toroidal vortex and the evenly distributed OH pool remaining from the previous combustion cycle. The region where reactions occurs is flushed down in the combustion chamber and enters the region of the centre core where it ignites the fresh reactants. At ignition time there is no pool of remaining OH in the ground state present in the centre core, since it has been flushed downstream towards the inlet of the combustion chamber. The small reacting pockets emanating from the inlet toroidal vortex seem to be responsible for the initiation of the main combustion in the centre core. No distinguishable flame front can be identified, rather the combustion seems to start simultaneously at different locations.

For Case 2, the valve is closed during the negative zero crossing of the pressure, see Fig. 3 (right). This is confirmed by the OH images from Fig. 6b, which at $t/\tau =0$ show no sign of an entraining jet in the evenly distributed zone of OH at ground level. At $t/\tau = 0.04$ a flame can be observed close to the inlet. Due to the low velocities, the jet is ignited in the remaining radical pool directly as it enters the combustion chamber. The chemiluminescence images also show that combustion takes place in this area. As the jet momentum increases, it can be observed that the flame is located along the outer edges of the toroidal vortex, with an evenly distributed radical pool of OH on one side and the fresh air/fuel mixture on the other side. This can be observed at $t/\tau = 0.5$, where there is a strong signal from the chemiluminescence image, almost no signal of OH from sheet B but, as shown in Fig. 5, a strong signal from OH at sheet C. Later in the cycle the air/fuel mixture has reached the centre core and the combustion takes place in an almost volumetric way. A more distributed reaction zone develops in a region close to the walls. In this case the fluid dynamic strain in the entraining jet is not high enough to delay combustion.

Fig. 6

4. Concluding remarks

To investigate the ignition and extinction processes in a strongly oscillating flow field, a high repetition rate diagnostic laser system for measuring time resolved Planar Laser Induced Fluorescence from OH was used. The measurements were carried out, for two different inlet geometries and total mass flow rates, in a reproducible oscillating flow field generated by the combustion process in a Helmholtz type pulse combustor. Both operating conditions correspond to lean premixed combustion, where the change in total mass flow rate is achieved by altering the stagnation plate position and decreasing the supply pressure of the methane gas used as fuel. This allows investigations of how the injection, ignition and combustion processes are affected by the decreased total mass flow rate through the combustor and hence the decreased velocity of the entraining jet of fresh air/fuel mixture into the combustion chamber. The integrated

chemiluminescence from the combustion process in the combustion chamber was measured simultaneously with the OH-LIF measurements.

The results indicate that the heat release distribution depends on the inlet jet velocity which significantly affects the injection, mixing and ignition processes. At high inlet jet velocities (stagnation plate position 25 mm from inlet) no chemiluminescence is observed during the injection phase, indicating delayed ignition due to fluid dynamic strain as proposed in Ref. [10]. After ignition, combustion is observed in a region extending over almost the entire combustion chamber, except for the region close to the inlet. However, OH is observed during the early injection phase, when the inlet velocities have not reached their maximum values. This indicates pre-ignition that later is extinguished. The OH radicals emanating from the possible pre-ignition may be transported by the toroidal vortices and may play an important role in the subsequent ignition. There is no distinguishable flame front, rather ignition starts in small islands which develop into flamelet like structures. The experimental data for this operating condition indicate that a major part of the heat release is located to the regions closer to the walls. A large amount of the heat release takes place in the second (downstream) half of the combustion chamber, no heat release occurs in the inlet region. At low inlet jet velocities (stagnation plate position 13 mm from inlet) a completely different behaviour is observed. The flame is localized to a smaller part of the combustion chamber close to the inlet and the stagnation plate. Chemiluminescence is observed during the entire cycle. From the OH-intensity images it can be observed that the reaction zone seems to be located along the edges of the entraining air/fuel jet. The experimental data also verify the presence of a radical pool which is suggested in Ref. [10] as a possible ignition source. The flame front is almost laminar, wrinkled but distinguishable, the structures corresponding to the outer edges of the toroidal vortex is clearly visible. Later in the cycle the transport of the air/fuel mixture has reached the centre core and the combustion takes place in an almost volumetric way. A more distributed reaction zone is located in a region close to the walls. The chemiluminescence data show that the heat release is concentrated to the inlet region of the combustion. A large amount of the fuel in the diverted inlet jet is consumed before this jet reaches the combustion chamber walls.

References

[1]   S.M. Candel, *Proc. Combust. Inst.* 24 (1992) 1277-1296.
[2]   J. E. Dec, J.O. Keller, V.S. Arpaci, *Int. J. Heat Mass Transfer* 35 (9) (1992) 2311-2325.
[3]   L. Crocco., *Proc. Combust. Inst.* 10 (1965) 1101-1128.
[4]   F.E.C. Culick, in: F.E.C. Culick, M.V. Heitor, J.H. Whitelaw (Eds.) *Unsteady Combustion.* Kluwer Academic Publishers, Dordrecht, The Netherlands, 1996, p. 173.
[5]   M. Barrère, F.A. Williams, *Proc. Combust. Inst.* 10 (1969) 169-181.
[6]   A.A. Putnam, *Combustion-Driven Oscillations in Industry*. American Elsevier, New York, 1971.
[7]   K.R. McManus, T. Poinsot, S.M. Candel, *Prog. Energy Combust. Sci.* 19 (1993) 1-29.
[8]   P.-H. Renard, D. Thévenin, J.C. Rolon, S.M. Candel, *Prog. Energy Combust. Sci.* 26 (2000) 225-282.
[9]   A.K. Gupta, D.G. Lilley, N. Syred, *Swirl Flows*. Abacus Press, Kent, U.K., 1984.
[10] J.O. Keller, P.K. Barr, R.S. Gemmen, *Combust. Flame* 99 (1994) 29-42.
[11] D. Reuter, B.R. Daniel, J. Jagoda, B.T. Zinn, *Combust. Flame* 65 (1986) 281-290.
[12] A. Lindholm, A., *Time resolved flow fields and heat release in pulse combustors,* ISSN 0282-1990, Department of Heat and Power Engineering, LTH, Lund, Sweden, 1995.
[13] J.O. Keller, K. Saito, *Combust. Sci. Tech.* 53 (1987) 137-163.
[14] S.I. Möller, A. Lindholm, *Combust. Sci. Tech.* 149 (1999) 389-406.
[15] H. Becker, A. Arnold, R. Suntz, P. Monkhouse, J. Wolfrum, R, Maly, W. Pfister, *Appl. Phys. B*, 50 (1990) 473-478.
[16] H.B. Najm, P.H. Paul, C.J. Mueller, P.S. Wyckoff, *Combust. Flame* 113 (1998) 312-332.
[17] C.F. Kaminski, J. Hult, M. Aldén, *Appl. Phys. B* 68 (1999) 757-760.
[18] J. Hult, M. Richter, J. Nygren, M. Aldén, A. Hultqvist, M. Christensen, B. Johansson, *Appl. Optics* 41 (2002) 5002-5014.
[19] J.E. Dec, J.O. Keller, I. Hongo, *Combust. Flame* 83 (1991) 271-292.
[20] J.S. Lee, *Optical Engineering* 25 (5) (1986) 636-643.

Table 1
Operating conditions for the pulse combustor during measurements

Case	Power Input (kW)	Operating freq. (Hz)	Stagnation plate position (mm)	Equivalence ratio ϕ	P_g (kPa)	P_{id} (kPa)
1	14.8	62	25	0.55	1.25	1.07
2	12.4	99	13	0.85	1.05	1.23

Air inlet with fan

Inlet decoupler
with mixing valve
Volume: 25 l.

Flue gas

Inlet tube
Length: 210 mm.
Inner diam.: 20 mm.

Tail pipe
Length: 1340 mm.
Inner diam.: 36 mm.

Exhaust decoupler
Volume: 35 l.

Combustion chamber
Volume: 1.5 l.
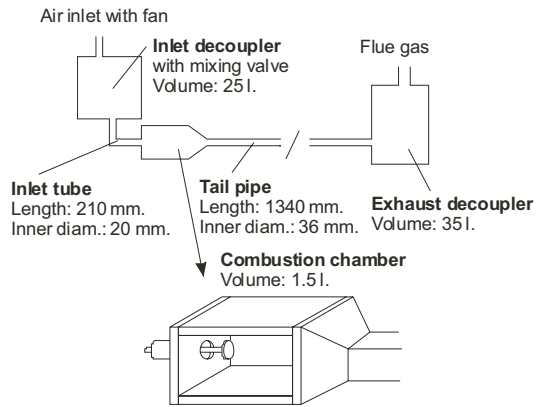
Figure 1. Schematic of the pulse combustor and square combustion chamber.
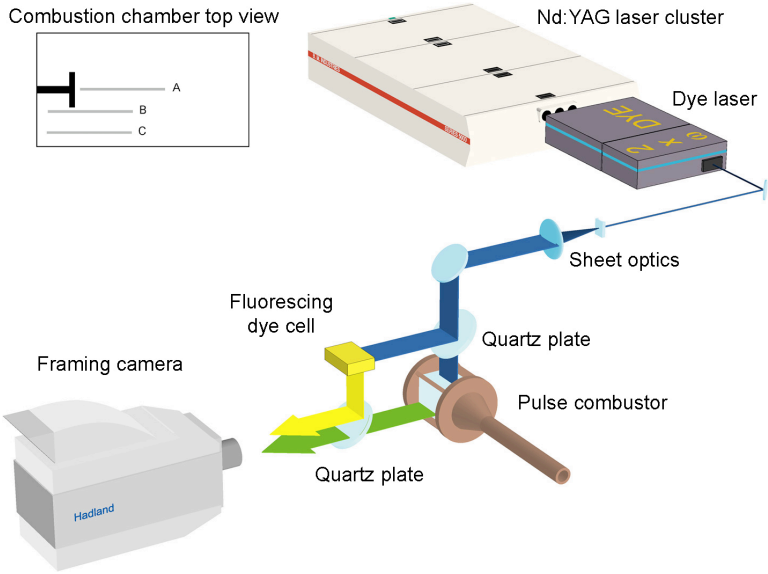
Figure 2. Set-up for the high speed diagnostic system for Laser Induced Fluorescence of OH and combustion chamber top view showing the location of the three different planes A = centre plane, B = centre + 15 mm and C = centre + 30 mm.
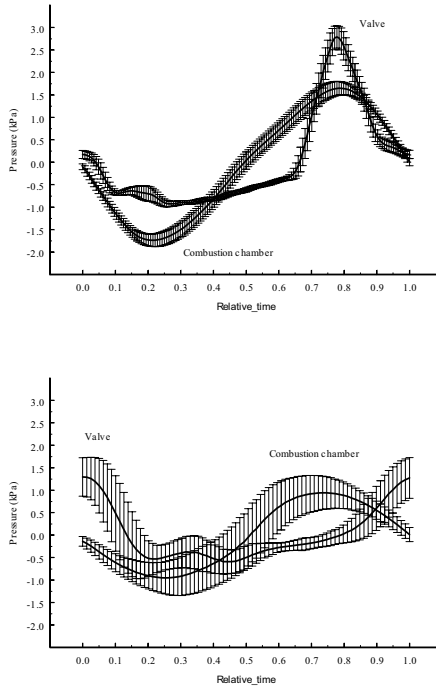
Figure 3. Pressure in the combustion chamber and the valve for the two different operation conditions, corresponding to lean premixed combustion. Top: Power input = 14.8 kW, equivalence ratio = 0.55, stagnation plate position = 25 mm, operating frequency = 62 Hz. Bottom: Power input = 12.4 kW, equivalence ratio = 0.85, stagnation plate position = 13 mm, operating frequency = 99 Hz.
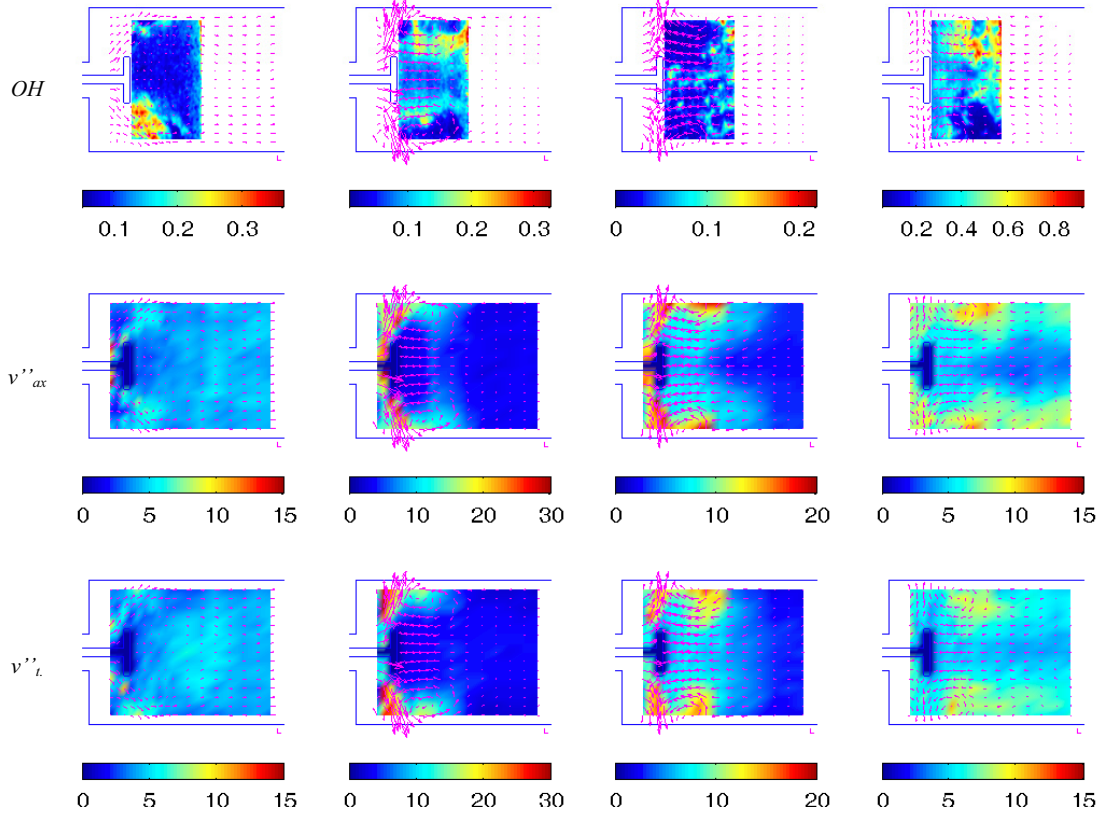
Figure 4. Ensemble averaged velocity fields at four instants of the operating cycle superposed on measured instantaneous OH images (top row), axial velocity fluctuation, v''ax (middle row), and transversal velocity fluctuations, v''tr (bottom row). Operating conditions: Power input = 14.8 kW, equivalence ratio = 0.55 and operating frequency = 62 Hz. Reference velocity vectors (lower right corner) represent 10 m/s.
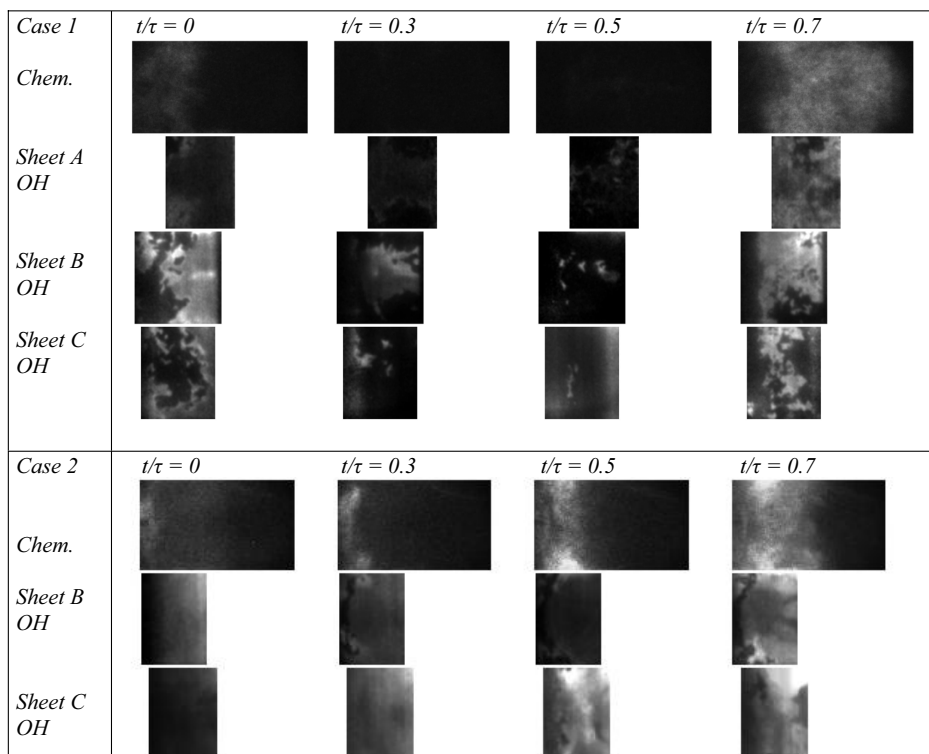
Figure 5. Experimental data for Case 1 (upper half) and Case 2 lower half. From top to bottom: chemiluminiscence, OH at plane A, B, and C (Case 1) and plane B and C (Case 2). From left to right: normalized cycle time t/τ = 0, 0.3, 0.5 and 0.7.

Case 1: Sheet B (time separation between images = 325 μs)
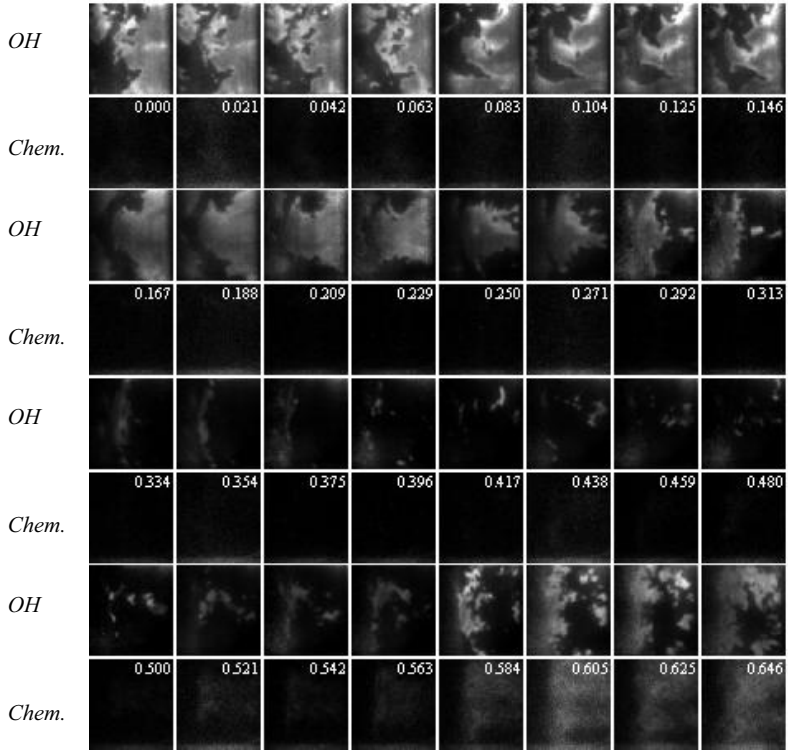
Figure 6(a). Instantaneous OH images from plane B, case 1. The chemiluminescence images correspond to the area visualised in the OH images and are taken 1 μs after the OH image displayed in the row above. The images are arranged from left to right, top to bottom. The first four images represents a time sequence from the same operating cycle with a time step indicated above the series, the next four also belongs to the same sequence but from a different operating cycle, and so forth. The intensity in the images ranges from black (low) to white (high).

Figure 6(b). Instantaneous OH images from plane B, case 2. The chemiluminescence images correspond to the area visualised in the OH images and are taken 1 μs after the OH image displayed in the row above. The images are arranged from left to right, top to bottom. The first four images represents a time sequence from the same operating cycle with a time step indicated above the series, the next four also belongs to the same sequence but from a different operating cycle, and so forth. The intensity in the images ranges from black (low) to white (high).

IV

Simultaneous PIV/OH-PLIF, Rayleigh thermometry/OH-PLIF and stereo PIV measurements in a low-swirl flame

Per Petersson, Jimmy Olofsson, Christian Brackman, Hans Seyfried, Johan Zetterberg, Mattias Richter, Marcus Aldén
Department of Combustion Physics, Lund University, SE-221 00 Lund, Sweden

Mark A. Linne
Sandia National Laboratories, PO Box 969, Livermore, CA 94551-0969 USA
Fax 925-294-2276, email mlinne@sandia.gov

Robert K. Cheng
Environmental Energy Technologies Division, Ernest Orlando Lawrence National Laboratory, Berkeley, California, 94720 USA

Andreas Nauert, Dirk Geyer, Andreas Dreizler
FG Energie- und Kraftwerkstechnik, TU Darmstadt, Petersenstr. 30, 64287 Darmstadt, Germany

In this paper, we describe the diagnostic techniques for simultaneous velocity and relative OH distribution, simultaneous temperature and relative OH distribution and for 3-component velocity mapping. Data extracted from the measurements include statistical moments for inflow fluid dynamics, temperature, conditional velocities and scalar flux. The work is a first step in the development of a detailed Large Eddy Simulation (LES) validation database for a turbulent, premixed flame. The low-swirl burner used in this investigation has many of the necessary attributes for LES model validation, including a simplified interior geometry, it operates well into the thin reaction zone for turbulent premixed flames, and flame stabilization is based entirely upon the flow-field and not upon hardware or pilot flames.

Copyright

1. Introduction

One emerging approach to lower NOx emissions for applied combustion processes is based upon lean premixing of fuel and air. To achieve lowest NOx emissions in practical devices, it is desirable to operate these flames close to their lean blow-off limit (LBO). As one example, this concept is commonly applied to modern prototype gas turbine combustors. Unfortunately, lean operation in combustors makes them prone to thermo-acoustic instabilities and flame extinction. To mitigate such problems during the development of new combustors, a more detailed understanding based upon a deterministic numerical simulation of swirling turbulent premixed flames is necessary.[1,2]

The emerging design tools for lean premixed combustors are based upon large eddy simulation[3,4] (LES). At its present stage of development, underlying models {'subgrid' models most often transferred from Reynolds averaged Navier Stokes (RANS) simulations} need to be validated in the context of LES. Although turbulent premixed flames (classified as oblique,[5] envelope[6] and unattached flames[7,8]) have been extensively studied experimentally, at present just a few databases suitable for LES validation exist (see e.g. reference [6]). Such a validation database should contain information similar to the databases provided for non-premixed target flames studied recently in the framework of the TNF workshop.[9] Most important are well characterized inflow and boundary conditions, information on statistical moments of velocity, temperature, and species concentrations at various locations, structural information such as thermal dissipation, flame surface density, reaction progress, and turbulent length and time scales. In a combined effort such a database is currently being developed by the authors of this paper. In the work reported here simultaneous PIV (particle image velocimetry) and multi-shot OH-PLIF (planar laser-induced fluorescence), and simultaneous filtered Rayleigh thermometry and multi-shot OH-PLIF and stereo PIV experiments are presented.

A suitable generic burner for stabilizing lean premixed flames is required in order to develop a validation database. The design features of the burner nozzle should make it easy to apply structured meshes common to most research-codes used for numerical simulation of turbulent flames. Complex fluid-flow structures such as intense recirculation zones or even coherent motion, and pilot flames for stabilization should be avoided. Despite these constraints, however, a nozzle geometry that is applicable to industrial applications is desirable. The low-swirl concept initiated in 1995 by Cheng and co-workers[10,11] meets most of these conditions. The main characteristics are a detached flame that propagates freely in a diverging, intensely turbulent flow-field. Thus, very lean flames can be stabilized in a divergent flow that slows in a linear fashion without producing recirculation. This concept has been shown to generate very low NOx-levels and is a promising solution for attaining ultra-low emission targets { < 5 ppm NOx (15% O_2) in stationary gas turbines[12]}.

Low-swirl flames have been investigated in a number of laboratories. Unfortunately, no standard design has been employed. Most of the studies use a set of four tangential air-jets that superimpose a weak swirl on the turbulent flow of the premixed fuel/air stream.[8,13-16] In other studies the swirl was generated by an annular swirler.[12,17] Although flame series have been partly investigated,[14] these different low-swirl flames have served primarily for investigation of the validity of different regime diagrams,[14,15] to compare emission characteristics with high swirling flames,[12] to investigate systematic changes in flame structure by varying the ratio between turbulence intensity and laminar flame speed (u'/s_l),[8] and by varying flame speeds, flow

acceleration and flame crossing frequencies.[13] The operational conditions of these previous studies differ too much to be used collectively for LES validation purposes.

For this project a new low-swirl burner was designed. The burner design includes an annular swirler consisting of eight curved vanes used in connection with a perforated plate fitted to the entrance of the center channel (Fig. 1). This choice of swirl generation was made to avoid dilution of the lean gas mixture by four tangential air jets. Three copies of the newly designed burner were made for comparative studies in different locations. Reproducibility between several burners was then of paramount importance. To reproduce the same swirl condition in three different burners in three locations would be more certain with fixed vanes than with air jets. The matched burners were fabricated in the same machine shop at the same time, and tolerances were very tightly held.

2. Experimental methods

The low-swirl burner used here is different from the original design[8] in that eight vanes are used to impart swirl in the flow rather than four tangential jets. In addition, this burner has a nozzle with a long bezel on the outside so that the inner flow does not change area before exiting into the surroundings. The inner diameter of the nozzle is 50 mm. This design also avoids generating any recirculation at the nozzle exit. Furthermore, the burner assembly was mounted in a 600 mm wide co-flow of air. This necessitated a "slim" outer shape of the burner, and any obstacles (e.g. air swirler tubes) in the co-flow needed to be avoided. A wide co-flow was necessary to ensure that no dust particles were entrained from the laboratory environment. This is crucial especially for single-shot 1D Raman and conventional Rayleigh measurements on the same flames where dust caused optical break down otherwise.[18] All mass flows were controlled by electronic mass flow controllers (Bronckhorst).

Two operational points were selected for study, LSF-1 (27kW) and LSF-2 (40kW), both with a fuel-air ratio ϕ = 0.62 (see Table 1). The flames were classified to lie within the thin reaction zone of the revised regime diagram.[19] To infer this designation, the laminar flame speed s_l and the corresponding laminar flame thickness l_f were based on data taken from a flamelet library.[20] Taylor's hypothesis of frozen turbulence was used to obtain the integral length scales from measured LDV time series.

For flows such as this one, the swirl-number S is expected to land in the range of 0.5,[21] but to accurately calculate the value of S based upon geometry is difficult because it depends upon the pressure drop across the various flow channels (the holes in the perforated plate and the swirler channels in this case). Here, stereo PIV data taken in the horizontal plane for flow LSF-1 at a position 2 mm above the nozzle were used to calculate the swirl-number, based on the ratio of the axial flux of tangential momentum over the axial flux of axial momentum. In the current configuration a relatively large fraction is passing through the perforated plate, about 40% by volume, yielding a swirl-number $S \approx 0.55$.

Two separate laser systems were used for simultaneous PIV/PLIF measurements. The counter-propagating laser beams were formed into overlapping sheets to illuminate a planar region of the flame, crossing the vertical centerline of the burner. A schematic diagram of the setup is shown in Fig. 2. A similar arrangement was used for the simultaneous Rayleigh thermometry/PLIF measurements. To simplify the alignment of the setup special alignment tools where manufactured. One tool had a transparent grid for the alignment of the cameras, and one tool had a centered slit for alignment of the counter-propagating laser sheets and for PIV sheet thickness

control. The tools had a perfect fit in the burner nozzle and could easily be mounted for alignment.

For PIV the beams from two frequency doubled Nd:YAG lasers (Quantel) were overlapped to provide successive Mie scattering from the seed particles. In the probe volume the light sheet had a height of 60 mm and a thickness of ~ 700 µm for the 2-component measurements and ~ 1 mm for 3-component measurements. The energy in each pulse was approximately 40 mJ and the pulse separation was optimized for each field-of-view and choice of interrogation window. When the full width of the flame was imaged the field-of-view was approximately 60 x 50 mm² and a relatively short pulse separation, $\Delta t = 30 – 50$ µs, was applied to capture high axial and out of plane velocities in the outer part of the flame. When only the low velocity core of the flow-field was investigated the field-of-view was 30 x 25 mm² and a $\Delta t = 100 – 200$ µs could be used. For imaging an interline-transfer CCD camera (Flowmaster 3S, La Vision) with 1280 x 1024 pixels was used. For the evaluation of the velocities, a cross-correlation algorithm with an adaptive multipass method developed by LaVision was used.   The spatial resolution for the PIV measurements equals the sizes of the interrogation windows, for both cases 32 x 32 pixels, and the sheet thickness. Hence, the spatial resolution is about 0,8 mm × 0,8 mm× 0,7 mm (1mm for stereo PIV) for the high spatial resolution case, and 1,6 mm × 1,6 mm × 0,7 mm (1mm for stereo PIV) for the low spatial resolution case.

For stereo PIV a second CCD camera (Imager Intense 1376 x 1040, La Vision) was installed and both cameras were fitted with Scheimpflug adaptors. The angle between the image plane of the cameras and the object plane was 45 degrees. A two-level calibration plate (La Vision) was used for alignment of the laser sheet, cameras, and for sheet thickness adjustment (~1mm). With the two-level plate two different calibration planes can easily be imaged without moving the plate. To relate the coordinate system of the two cameras to the laboratory reference frame, four mapping functions are necessary, one for each calibration plane. The mapping functions are based on a pinhole model (software Davis 7.0, La Vision) that also makes it possible to use a "self-calibration" procedure based on cross-correlation on simultaneous exposed images by the two cameras. In case of any displacement between the calibration plate and the light sheet a field of disparity vectors is created and used for misalignment corrections.[22]

0.5µm-sized dry $ZrSiO_4$ particles were used as seed material. Velocity fluctuations up to 7 kHz could be resolved with a slip of less than 1%. Two seeders were installed to provide seeding to the methane/air mixture and the co-flowing air individually. To assure stable and reproducible seeding densities, $ZrSiO_4$ was sieved into a bypass of the respective gas flows. For this purpose a combination of static mesh and rotating brush was installed at the bottom of an adequately dimensioned $ZrSiO_4$ storage tank. The speed of the motor driving the rotating mesh and the bypass-ratio determined the seeding density. The seeding density was adjusted to meet the standard PIV criterion of a minimum of 10 particles in the interrogation windows, even in the hot expanded region.

In order to achieve laser-induced fluorescence from OH and to track the OH propagation in time, the multi-YAG laser cluster at LTH Lund was used (see Fig. 3). The system is described thoroughly in reference [23]. The cluster consists of four individual, Q-switched Nd:YAG lasers (BMI), with an output wavelength of 532 nm. Each of these was used to pump a dye laser (Sirah) operating on a Rhodamine 590 dye solution in methanol. The problems with beam profile deterioration and severe pulse energy losses, which occur when a single dye laser is pumped by a rapid burst from the multi-YAG, are circumvented when using several dye lasers. The outputs from the dye lasers were then frequency doubled and superimposed to a single beam path by

means of dichroic mirrors. The UV laser beams were formed into sheets of thickness ~ 300 μm in the probe volume region. The energy in each pulse was approximately 2mJ. OH radicals were excited via the $Q_1(8)$ transition of the (v'=1, v''=0) band in the A-X system at approximately 283 nm [24] with a fairly temperature-insensitive population distribution in the $N = 8$ level. Fluorescence from the A-X (1,1) and (0,0) bands (near 310 nm) was detected using a UV lens (Nikkor, $f = 105$mm, f/# = 4.5). A bandpass filter and a *UG11*-filter (Schott) suppressed spurious light efficiently, while long pass OH detection filters included a high reflector from 275 – 295 nm and a highly transmissive filter for wavelengths greater than 295 nm.

To allow for multi-frame, time-resolved PLIF images, a high-speed framing camera (Hadland) with eight individual ICCD modules was used,[23] enabling acquisition of up to eight frames in a rapid succession. The camera was fitted with an image intensifier unit for UV detection and the smallest resolvable unit for this arrangement was about 300μm. For this investigation a sequence of four PLIF images were captured with this camera with a Δt = 200 – 400 μs. The time delay was chosen so that the flame front motion could be studied. For each OH-PLIF sequence, a PIV recording was synchronized with the second image in the sequence. The PIV and PLIF imaging were controlled from different computers. The synchronization of the 8Hz PIV lasers and the 10Hz LIF lasers was achieved with external timing equipment. For each investigated flame condition 1500 joint PIV and OH-PLIF sequences were collected in order to generate statistics.

For higher spatial resolution fluorescence detection a second interline-transfer CCD camera (Imager Intense 1376 x 1040, La Vision) was equipped with an image intensifier (Hamamatsu). With this set up and a field of view of 34x26 mm^2 the smallest resolvable unit was about 100μm. By using two of the Nd:YAG lasers in the laser cluster a sequence of two OH-PLIF images could be captured for tracking the flame front movement. The camera was connected to the PIV computer, allowing both PIV raw data and OH-PLIF images to be collected and stored in the same image file. This simplified the data evaluation considerably. Laser irradiance profiles were recorded online by reflecting the laser sheets into a cell containing fluorescing dye. The resulting dye LIF signals were imaged onto the detector concurrently with the OH-PLIF images. The beam profiles were used in a post-processing step to normalize OH-PLIF data on a shot-by-shot basis. Previous experience has established that OH and dye PLIF signals are linear when the system is operated as they were in this work.

For Rayleigh thermometry the filtered Rayleigh scattering (FRS)[25] approach was used. FRS exploits the fact that Doppler-broadening increases with temperature. By using a narrow band excitation for Rayleigh scattering in connection with an atomic or molecular notch filter resonant with the excitation wavelength in front of a camera system, increasing Doppler widths are converted to enlarged leakage around the notch, generating increasing signal levels. By proper calibration and modeling of the convolution between spectral profiles of the laser, notch, and Doppler width, signal strengths can be transformed into temperatures. The present FRS approach is described in detail in reference [26]. In brief, a single-longitudinal mode pulsed (90 ns) alexandrite laser (PAL 101, Light Age Inc.) with a line width of 100 MHz and a pulse energy of 30 mJ was tuned on the resonance of single-isotope atomic mercury Hg^{202} at 254 nm. Mercury was contained at 300 K in a 7 cm long quartz cell (10^{-3} Torr) directly in front of an ICCD camera (Roper Scientific PIMAX). The mercury absorption notch width of ~ 2 GHz is dominated by Doppler broadening under these conditions. The use of isotope-enhanced mercury simplified the absorption profile of the filter to produce a single hyper-fine line structure. This facilitated a proper notch filter model. The Rayleigh scattering line profile was modeled with the S6-model to

include Brillouin contributions and the total Rayleigh cross section in the burned gases was estimated with the unburned gases. The cross section for a burned gas composition for complete reaction of methane differs from that of the unburned gases by less than 1.3%. The potential of FRS to suppress Mie scatter from seed particles is an attractive feature; the goal being simultaneous PIV and FRS. In the present study the seeding density required for good PIV spatial resolution was relatively high, to facilitate extraction of statistical moments across the flame front. Unfortunately, the Mie scattering from particles in the flow proved too large to be removed by the atomic filter. Future experiments will reduce the seed density so that only features at typical LES grid scales and larger are imaged simultaneously with FRS. For this investigation simultaneous FRS and multi-shot OH-PLIF were captured in a similar manner as for the PIV/OH-PLIF imaging. For each investigated flame condition 600 joint FRS and OH-PLIF sequences were collected in order to generate statistics.

3. Results and discussions

The measurement techniques, the specific flow rates and the equivalence ratios selected for this work are somewhat different from those of Cheng and co-workers,[8,10-14,16,17] but the findings of the program described here are consistent with the results published by that group.

Figure 4 shows an ensemble averaged image of 500 stereo PIV recordings for LSF-2. One can see that the flow slows approximately linearly with height, reaching a very slow zone in the core at x = 61 mm, and that no mean tangential component (e.g. swirl) exists in the core. In the core region turbulent flames are hydrodynamically stabilized where the mean flow has slowed to a point where it matches the flame propagation. The swirling flow at the outer edge is symmetric and reproducible, offering opportunities for investigation of a sheared, stratified premixed flame. Stereo PIV taken in horizontal planes demonstrates that the eight vanes actually impose a small but observable structure in the swirling flow, but this does not propagate to the center and it decays with height. Figure 5 shows a combined PIV/OH-PLIF image of the LSF-2 flame, and it illustrates a common, reoccurring flame shape.

To capture the inflow conditions, stereo PIV was applied to the outlet of the annular swirl assembly and at the outlet of the nozzle as it entered the surroundings. Radial profiles of mean and fluctuations of velocity components at the exit of the swirler are presented in Fig. 6. These results were acquired with the nozzle removed, thereby imposing a radial component that does not exist at that location when the nozzle is in place. The data are useful as a specific test of a swirler model, however, if the swirler has been included in a computational domain. One can observe that there are significant differences between the data extracted just above a swirler passage and those extracted just above a swirler vane, but this is not surprising. The profiles, however, are fairly symmetric. Next, radial profiles of mean and fluctuations of velocity components at the exit of the nozzle are presented in Fig. 7. One can observe relatively symmetric mean profiles, no swirl at the center, and the rms values reach a minimum at the centerline.

Figure 8 shows a single shot FRS temperature recording (top) followed by a sequence of four OH-PLIF images with a $\Delta t = 400$ µs. It can be seen from the OH field that the inner part of the flame, where the flow is close to two dimensional in average, is not changing significantly. In the outer regions the swirl, the average flow velocity and flow fluctuations are all increasing in strength. All these factors increase the interaction between the flame and the flow and rapid changes in observed flame structure can occur. The single shot FRS recording is synchronized with the second image in the OH-PLIF sequence. The resolution in the single shot FRS image is

sufficient to match the PLIF and FRS images and to deduce temperature data around the flame front, the single-shot signal-to-noise ratio for FRS in the present setup is 5-10:1 depending on temperature.

Figure 9 contains radial profiles of temperature from both LSF-1 and LSF-2, acquired using FRS. The adiabatic flame temperature for such a flame is 1705 K, which is almost reached in the post-flame zones (at 40 – 45 mm, the flow is almost always in the burnt flame zone), especially for LSF-2. The rms values for each profile are also shown and they indicate wide variation in temperature at each location, especially for LSF-1. Note also that the peak temperature for LSF-1 at x = 35.4 mm is well below 1700 K. This is caused mainly by the fact that measurements are made sometimes in burnt and sometimes in unburned gases due to the large-scale structures of the flame front, (see Fig. 5), and front dynamics. This fact can also explain the high rms fluctuations encountered.

A two dimensional plot of the Reynolds mean reaction progress variable $\bar{c}$ is shown in Fig. 10 for flow LSF-2. The mean reaction progress variable, $\bar{c}$, is 0 in the unburned state and 1 in the fully reacted state. Values between 0 and 1 correspond to locations within the turbulent flame brush. A binary mask is created from the instantaneous OH-PLIF images, indicating only burned and unburned zones. By ensemble averaging of all instantaneous mask images (approximately 6000 images) provides the Reynolds mean reaction progress.[27-29] Axial plots of $\bar{c}$ are shown in Fig. 11. From these one can extract the mean flame front location (at $\bar{c}$ = 0.5); for LSF-1 it is 33 mm and for LSF-2 it is 32 mm. In addition, the distance between $\bar{c}$ = 0.1 and $\bar{c}$ = 0.9 can be taken as the width of the flame brush; it is equal to 17 mm for LSF-1 and 15 mm for LSF-2.

The results from the simultaneous PIV and PLIF measurements where used to determine conditional velocities (see below) and for increased understanding of the flame/flow interaction. Figure 12 shows a combined PIV/OH-PLIF image in the upper part of the flame for LSF-2. In this region of the flame the flow-field is more complicated and the flame-flow interaction strong. The entrainment of air also successively dilutes the air fuel mixture and extinction can finally occur. This phenomenon was important to study and became a challenge to capture in the ongoing LES modeling of the present flame.[30]

Conditional velocities were extracted using combined PIV and OH-PLIF images at three different radial positions (centerline, 6 mm from the centerline, and 12 mm from the centerline). As shown in Fig. 5 the flame is highly contorted and for this reason, conditional velocities were extracted normal to the flame front. For each radial location data was collected from 5 adjacent cells, centered around the investigated radial location, with a cell size of 32 x 32 pixels. The flame front location for each OH image was identified near the center, and at the left and right border of each cell. Using these data the best corresponding velocity vector on both sides of the flame front could be taken from the PIV data. Therefore, only velocity vectors immediately adjacent to the flame front (within about 1 mm) are considered. This corresponds to strip-conditioned velocities introduced in reference [28]. Also, local flame front angle was determined for extracting the velocity components normal to the flame front. The influence of flame front angle on the conditional velocities was further investigated by processing data with low flame angle (<45) and steep flame angles (>45) respectively. No conclusive differences in the conditional data were observed for these two flame angle intervals. Uncertainties due to particle thermophoretic transport were estimated in reference [28] for premixed methane/air flames of

$\phi = 0.6$ to be $\bar{u}_{TP,b} = 0.02 \, \text{m/s}$ at the burnt side and independent of strain. This value is low compared to mean velocities at locations where $\bar{c} = 0.5$ and can be thus neglected.

The conditional velocity data for $\bar{c} = 0.5$ are presented in Table 2. The quantities $\bar{u}_b$ and $\bar{u}_u$ denote conditional mean velocities in the burnt and unburnt region deduced from the conditional PIV data. For flame LSF-1 and for all three radial positions considered, $\bar{u}_b$ exceeds $\bar{u}_u$ by approximately 40%, which is clearly above the uncertainties related to thermophoretic transport. Thus, counter-gradient diffusion associated with thermal expansion and acceleration of fluid passing the flame front dominates in this flow. For flame LSF-2 the Reynolds number is higher than in case LSF-1. However, the measurements of the conditional velocities indicate as well that $\bar{u}_b$ exceeds $\bar{u}_u$ but only by approximately 20%. Counter-gradient diffusion still dominates this flame.

As is obvious from table 2, the conditional turbulence level increases with increasing radial position. This is in accordance with trends depicted in Fig. 7 b). Enhanced velocity fluctuations farther away from centerline are due to higher shear.

Scalar fluxes were extracted from this data by applying the BML model,[31] as described in references [28, 32, 33], via the following:

$$\overline{\rho \widetilde{u''c''}} = \bar{\rho} \tilde{c} \left(1 - \tilde{c}\right) \left(\overline{u_b} - \overline{u_u}\right) \tag{1}$$

The Favre-averaged reaction progress $\tilde{c}$ is calculated from:

$$\tilde{c} = \frac{\bar{c}}{\bar{c} + \dfrac{\rho_u}{\rho_b}\left(1 - \bar{c}\right)} \tag{2}$$

Densities in the burnt (ρ_b) and unburned regions (ρ_u) are taken from laminar flamelet calculations assuming adiabatic conditions (CHEM1D,[34] 16-step reaction mechanism[35]). The Reynolds mean reaction progress variable $\bar{c}$ is taken from the ensemble averaged binarised instantaneous OH images as previously described.

The calculated scalar fluxes are also contained in Table 2. More data will be extracted from new measurements higher up in the flame brush, for $\bar{c} > 0.8$.

4. Conclusions

A number of laser diagnostics were applied to a low-swirl flame to measure flow-field velocity, relative OH distribution, and temperature. In keeping with the spatial orientation of LES, imaging and statistical moments extracted from the images are emphasized. In this paper, we report statistical moments for inflow fluid dynamics, temperature, and conditional velocities. In addition, the progress variable was extracted from the OH distributions and from this the scalar flux was deduced. This paper has described initial results in the development of a detailed validation database for a turbulent, premixed flame.

The low-swirl design has been chosen for this work because it has many of the necessary attributes for LES model validation, including a simplified interior geometry, it operates well

into the thin reaction zone of the regime diagram, and flame stabilization based entirely upon the flow-field and not upon hardware or pilot flames. Initial experiments have demonstrated that a stable and symmetric flame can be achieved and that various regions of the flame offer opportunities to study two dimensional turbulent flames in the core, while the outer edge offers the opportunity to investigate stratified lean premixed flames with local extinction.

Future work will focus on further analysis of the data, additional temperature measurements and measurement of the flow inside the nozzle. The data will be organized in a useable form and made available together with information on boundary conditions and estimated measurement accuracies to model developers wishing to make use of it.

References

1. R. J. Santoro, "Applications of laser-based diagnostics to high pressure rocket and gas turbine combustor studies," *AIAA* (1998) 98-2698.
2. A. Dreizler, J. Janicka, "Diagnostic challenges for gas turbine combustor model validation," *Applied Combustion Diagnostics*, K. Kohse-Höinghaus, J. Jeffries eds. (Taylor & Francis, 2002), pp. 561.
3. H. Pitsch, "Large-Eddy simulation of turbulent combustion," *Annu. Rev. Fluid Mech*. 38 (2006) pp. 453-482.
4. J. Janicka, A. Sadiki, "Large Eddy simulation of turbulent combustion systems," *Proc. Comb. Inst.* 30 (2005) 537-548.
5. A. Soika, F. Dinkelacker, A. Leipertz, "Measurement of the resolved flame structure of turbulent premixed flames with constant Reynolds number and varied stoichiometry," *Proc. Comb. Inst.* 27 (1998) 785-792.
6. Y-C. Chen, N. Peters, G. A. Schneemann, N. Wruck, U. Renz, M.S. Mansour, "The detailed structure of highly stretched turbulent premixed methane-air flames," *Combust. Flame* 107 (1996) 223-244.
7. E.J. Stevens, K.N.C. Bray, B. Lecordier," Velocity and scalar statistics for premixed turbulent stagnation flames using PIV" *Proc. Comb. Inst*. 27 (1998) 949-955.
8. B. Bédat, R.K. Cheng, "Experimental study of premixed flames in intense isotropic turbulence," *Combust. Flame* 100 (1995) 485-494.
9. R.S. Barlow, International Workshop on Measurement and Computation of Turbulent Non-Premixed Flames, http://www.ca.sandia.gov/TNF/.
10. Chan, C.K., K.S. Lau, W.K. Chin, R.K. Cheng, "Freely propagating open premixed turbulent flames stabilized by swirl," *Proc. Comb. Inst*. 24 (1992) 511-518.
11. Cheng, R.K., D.T. Yegian, M.M. Miyasato, G.S. Samuelsen, R. Pellizzari, P. Loftus, C. Benson," Scaling and development of low-swirl burners for low-emission furnaces and boilers" *Proc. Comb. Inst*. 28 (2000) 1305-1313.
12. M. R. Johnson, D. Littlejohn, W. Nazeer, K.O. Smith, R.K. Cheng, "A comparison of the flowfields and emissions of high-swirl injectors and low-swirl injectors for lean premixed gas turbines," *Proc. Combust. Inst.* 30 (2005) 2867-2874.
13. R.K. Cheng, "Velocity and scalar characteristics of premixed turbulent flames stabilized by weak swirl", *Combust. Flame* 101 (1995) 1-14.
14. R.K. Cheng, I.G. Shepherd, B. Bédat, L. Talbot," Premixed turbulent flame structures in moderate and intense isotropic turbulence" *Combust. Sci. and Tech*. 174 (2002) 29-59.
15. C. Kortschik, T. Plessing, N. Peters, "Laser optical investigation of turbulent transport of temperature ahead of the preheat zone in a premixed flame," *Combust. Flame* 136 (2004) 43-50.
16. T. Plessing, C. Kortschik, N. Peters, M.S. Mansour, R.K. Cheng, "Measurements of the turbulent burning velocity and the structure of premixed flames on a low swirl burner," *Proc. Combust. Inst*. 28 (2000) 359-366.
17. R.K. Cheng, D. Littlejohn, W. Nazeer, K.O. Smith, "Laboratory studies of the flow field characteristics of low-swirl injectors for adaptation to fuel-flexible turbines, " *ASME Turbo Expo* (2006) GT2006-90878.

18. D. Geyer, A. Kempf, A. Dreizler, J. Janicka, "Scalar dissipation rates in isothermal and reactive turbulent opposed-jets: 1D-Raman/Rayleigh experiments supported by LES," *Proc. Combust. Inst.* 30 (2005) 681-689.
19. N. Peters, *Turbulent Combustion*, (Cambridge University Press, 2000), p. 78.
20. P. Wang, X. S. Bai, "Large Eddy simulation of turbulent premixed flames using level-set G-equation," *Proc. Combust. Inst*. 30 (2005) 583-591.
21. D. Littlejohn, A.J. Majeski, S. Tonse, C. Castaldini, R.K. Cheng, "Laboratory investigation of an ultra-low NOx premixed combustion concept for industrial boilers," *Proc. Combust. Inst*. 29 (2002) 1115-1121.
22. B. Wieneke, "Stereo-PIV using self-calibration on particle images," *Exp. In Fluids* 39 (2005), 267-280.
23. J. Hult, M. Richter, J. Nygren, M. Aldén, A. Hultqvist, M. Christensen, B. Johansson. "Application of a high-repetition-rate laser diagnostic system for single-cycle-resolved imaging in internal combustion engines" *Applied Optics* vol. 41, No. 24 (2002).
24. LIFBASE: Database and spectral simulation, http://www:sri.com/psd/lifbase/.
25. R.B. Miles, J.N. Forkey, W.R. Lempert, "Filtered Rayleigh scattering measurements in supersonic/hypersonic facilities," *AIAA* (1992) 92-3894.
26. J. Zetterberg, Z.S. Li, M. Afzelius, M. Aldén, "Applications of a single-longitudinal-mode alexandrite laser for diagnostics of combustion interest," *Rev. Sci. Instrum.* 75 (2004) 3208-3215.
27. P. A. M. Kalt, J. H. Frank, R. W. Bilger, "Laser imaging of conditional velocities in premixed propane/air flames by simultaneous OH PLIF and PIV," *Proc. Combust. Inst*. 27 (1998) 751-758.
28. J. H. Frank, P. A. M. Kalt, R. W. Bilger, "Measurement of conditional velocities in turbulent premixed flames by simultaneous OH PLIF and PIV," *Combust. Flame* 116 (1999) 220-232.
29. A. Nauert, A. Dreizler, "Conditional velocity measurements by simultaneously applied laser Doppler velocimetry and planar laser-induced fluorescence in a swirling natural gas/air flame," *Z. Phys. Chem*. 219 (2005) 635-648.
30. K-J. Nogenmyr, P. Petersson, X. S. Bai, A. Nauert, J. Olofsson, C. Brackman, H. Seyfried, J. Zetterberg, Z.S. Li, M. Richter, A. Dreizler, M. Linne, M. Aldén, "Large Eddy Simulation and experiments of stratified lean premixed methane/air turbulent flames," *Proc. Combust. Inst.* 31 (2007), 1467-1475.
31. K.N.C. Bray, P.A. Libby, J.B. Moss, "Flamelet crossing frequencies and mean reaction rates in premixed turbulent combustion". *Combust. Sci. Tech.* 41 (1984) 143–172.
32. P. A. M. Kalt, Y-C. Chen, R. W. Bilger, "Experimental investigation of turbulent scalar flux in premixed stagnation-plate flames", *Combust. Flame*, 129 (2002) 401-415.
33. D. Most, F. Dinkelacker, A. Leipertz, "Direct determination of the turbulent flux by simultaneous application of filtered Rayleigh scattering thermometry and particle image velocimetry", *Proc. Combust. Inst.* 29 (2002) 2669-2677.
34. CHEM1D, A one-dimensional laminar flame code, Eindhoven University of Technology, http://www.combustion.tue.nl/chem1d.
35. M.D. Smooke, V.Giovangigli, "Reduced Kinetic Mechanisms and Asymptotic Approximations for Methane-Air Flames", M.D. Smooke ed., (Springer, 1991), p. 1R28.

Tables

Table 1.
Operational points and characteristics of lean premixed methane/air flames.

Flow designator	u_{exit} [m/s]	Re_{exit}	P [kW]	Φ
LSF-1	6.2	20,000	27	0.62
LSF-2	9.3	30,000	40	0.62

Table 2.

Conditional velocities and scalar fluxes at $\bar{c} = 0.5$ for the flames described in Table 1.

Flow designator	location	$\bar{u}_b$ [m/s]	rms_b [m/s]	$\bar{u}_u$ [m/s]	rms_u [m/s]	$\overline{\rho u''c''}$ [kg/sm²]
LSF-1	cl[§]	0.46	0.35	0.33	0.34	0.01095
LSF-1	6 mm from cl	0.51	0.46	0.37	0.46	0.01149
LSF-1	12 mm from cl	0.28	0.72	0.20	0.60	0.00663
LSF-2	cl	0.49	0.44	0.41	0.45	0.00694
LSF-2	6 mm from cl	0.37	0.55	0.31	0.58	0.00495
LSF-2	12 mm from cl	0.20	0.78	0.16	0.81	0.00211

§ cl denotes centerline

List of Figure Captions

Fig. 1. a) Cross-section of burner without swirl assembly. Premixed air and fuel enters via four nozzles (two visible) and passes several perforated plates before reaching the swirler. b) swirl assembly; arrow marks the location where the assembly is installed.

Fig. 2. Schematic sketch of the experimental setup for simultaneous PIV/OH-PLIF measurements.

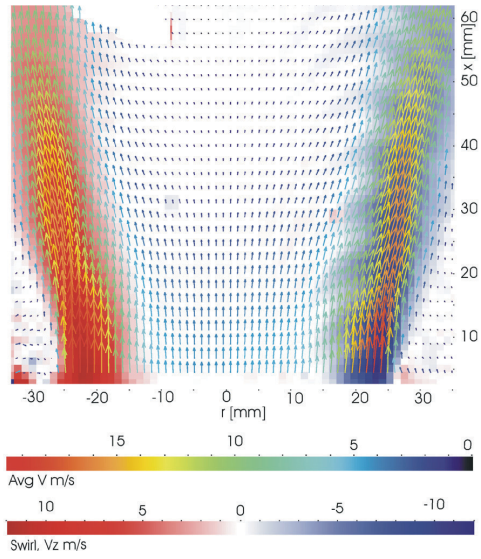Fig. 3. (Color online) The multi-YAG laser cluster at LTH Lund.

Fig. 4. Ensemble average of 500 single-shot stereo PIV images for LSF-2 (flow is going into the paper on the right side; note that a few vectors where lost in the upper left of the image).

Fig. 5. (Color online) A combined single-shot PIV/OH-PLIF image for LSF-2 (r=radial distance, x=height above nozzle).
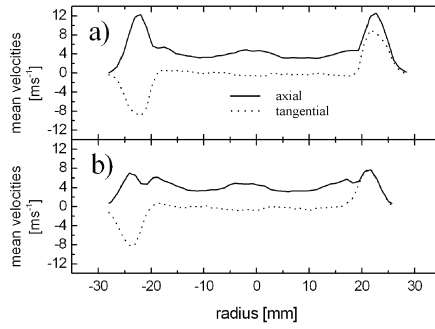
Fig. 6. Exit velocity profiles of swirler for LSF-1 (2 mm downstream): a) mean axial and tangential velocities crossing over the center of a flow passage, b) mean axial and tangential velocities crossing over the center of a vane.
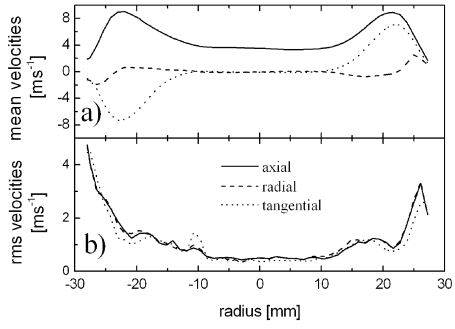
Fig. 7. Exit velocity profiles of nozzle for LSF-1 (2 mm downstream): a) mean axial, radial, and tangential velocities, b) respective rms values.
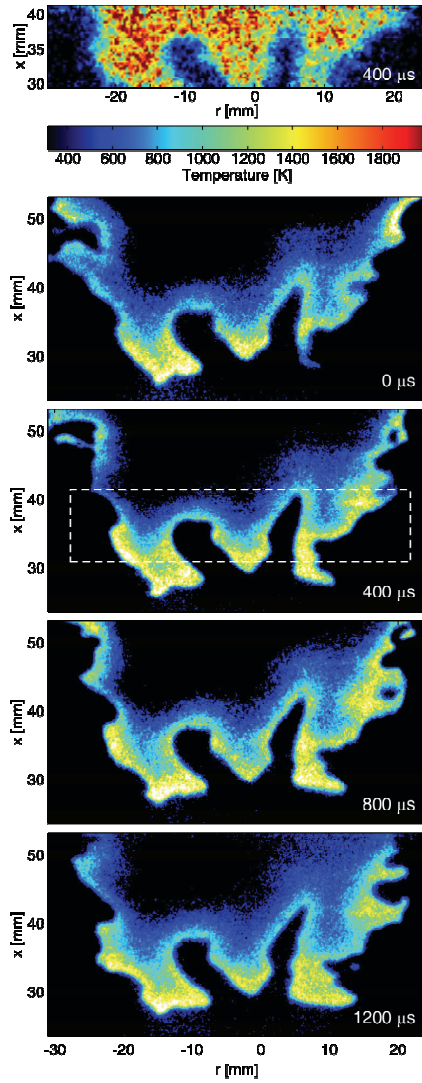
Fig. 8. A single shot FRS temperature image (top) followed by a sequence of four OH-PLIF images with a $\Delta t = 400$ µs.
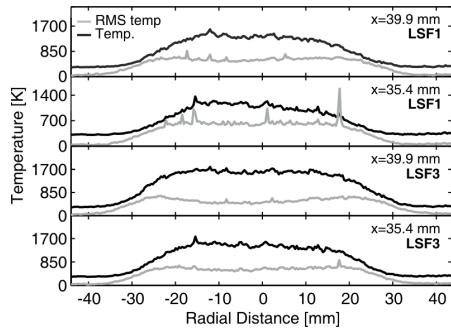
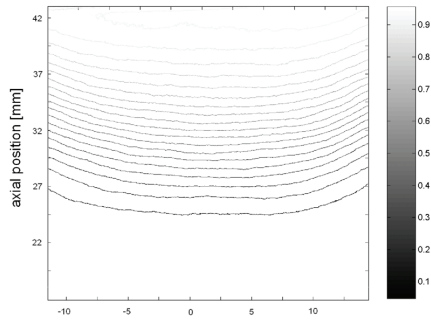Fig. 9. Radial profiles of temperature and rms values.

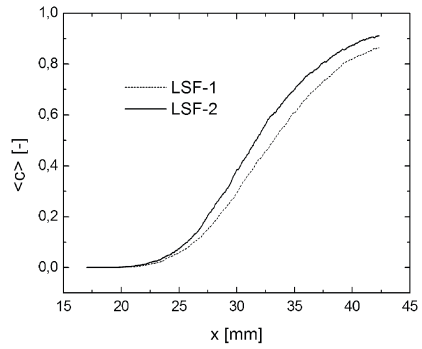Fig. 10. Contour plot of the mean reaction progress variable for LSF-2.

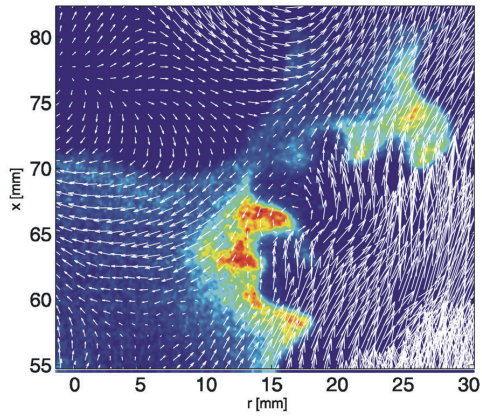Fig. 11. Axial dependence of the mean reaction progress variable.

Fig. 12. (Color online) A combined single-shot PIV/OH-PLIF image in the upper part of the flame for LSF-2.

Fig. 1. a) Cross-section of burner without swirl assembly. Premixed air and fuel enters via four nozzles (two visible) and passes several perforated plates before reaching the swirler. b) swirl assembly; arrow marks the location where the assembly is installed.

Fig. 2. Schematic sketch of the experimental setup for simultaneous PIV/OH-PLIF
measurements.

Fig. 3. (Color online) The multi-YAG laser cluster at LTH Lund.

Fig. 4. Ensemble average of 500 single-shot stereo PIV images for LSF-2 (flow is going into the paper on the right side; note that a few vectors where lost in the upper left of the image).

Fig. 5. (Color online) A combined single-shot PIV/OH-PLIF image for LSF-2 (r=radial distance, x=height above nozzle).

Fig. 6. Exit velocity profiles of swirler for LSF-1 (2 mm downstream): a) mean axial and tangential velocities crossing over the center of a flow passage, b) mean axial and tangential velocities crossing over the center of a vane.

Fig. 7. Exit velocity profiles of nozzle for LSF-1 (2 mm downstream): a) mean axial, radial, and tangential velocities, b) respective rms values.

Fig. 8. A single shot FRS temperature image (top) followed by a sequence of four OH-PLIF images with a Δt = 400 µs.

Fig. 9. Radial profiles of temperature and rms values.

Fig. 10. Contour plot of the mean reaction progress variable for LSF-2.

Fig. 11. Axial dependence of the mean reaction progress variable.

Fig. 12. (Color online) A combined single-shot PIV/OH-PLIF image in the upper part of the flame for LSF-2.

V

Chemiluminescence sensor for local equivalence ratio of reacting mixtures of fuel and air (FLAMESEEK)

Y. Hardalupas [a,*], M. Orain [a], C. S. Panoutsos [a], A.M.K.P. Taylor [a],
Jimmy Olofsson [b], Hans Seyfried [b], Mattias Richter [b], Johan Hult [b],
Marcus Aldén [b], Fredrik Hermann [c], Jens Klingmann [c]

[a] *Mechanical Engineering Department, Imperial College London, Exhibition Road, London SW7 2AZ, UK*
[b] *Department of Combustion Physics, Lund Institute of Technology, P.O. Box 118, SE-22100 Lund, Sweden*
[c] *Department of Heat and Power Engineering, Lund Institute of Technology, P.O. Box 118, SE-22100 Lund, Sweden*

Abstract

This paper describes a Cassegrain optics-based chemiluminescence sensor (CS) for measurements in gas turbine combustors. The chemiluminescence sensor measures the equivalence ratio of reacting fuel and air mixtures, and can identify the flame location, in partially premixed flames. It has the potential for monitoring the degree of premixedness of reacting fuel and air in industrial gas turbine combustors, where operation with lean premixed mixtures is important for reduction of NO_x emissions. The spatial resolution of the sensor is evaluated by comparing OH^* chemiluminescence measurement from the CS with laser induced OH fluorescence, in the cone-shaped premixed flame of a Bunsen burner. The ability of the sensor to measure in a modified micro-gas turbine environment burning a methane/air, as well as, a methane/water/air flame (humidified flame) is also demonstrated.
© European Communities, 2004. Published by Elsevier Ltd. All rights reserved.

1. Introduction

Lean premixed combustion is an important method for the reduction of NO_x emissions from industrial gas turbine combustors. Operating in a lean-premixed mode has the advantage of

---

* Corresponding author. Tel.: +44-20-7594-7057; fax: +44-20-7823-8845.
E-mail address: y.hardalupas@imperial.ac.uk (Y. Hardalupas).

avoiding high-temperature, stoichiometric combustion that increases thermal NO_x. Lean fuelling, however, currently has the overriding disadvantage that combustion induced oscillations arise which can destroy the machine. One theory is that these oscillations arise during fuel lean operation because of a feedback mechanism involving appropriately-phased time-dependent fluctuations of equivalence ratio of the reacting mixture. An instrument which could measure spatial and temporal variations of the equivalence ratio of air with fuel could be useful both in the context of verifying the origin of the combustion induced oscillations and in terms of having the simplicity to measure spatial and temporal inhomogeneity of the premixed mixture in industrial gas turbines. The chemiluminescent sensor described in this paper is potentially able to provide these measurements.

An optical sensor with the ability to measure the fuel/air premixedness and resolve the local flame front, was developed, evaluated and will be tested in a real gas turbine environment, in the context of a project entitled "FLAMESEEK" (FLAME sensors for efficient engine cycles), funded by the European Commission through the fifth framework programme. The partners in FLAMESEEK project include Rolls–Royce Power Engineering plc (UK), Imperial College London (UK), University of Twente (The Netherlands), Lund University (Sweden), Foundation for Research and Technology Hellas/Institute of Chemical Engineering and High Temperature Chemical Processes (Hellas) and Alstom Power SE AB (Sweden).

It has been known for many years that the chemiluminescence from flame excited radicals such as OH^*, CH^*, C_2^*, and CO_2^* can be used to measure aspects of combustion. Recently, for example, Higgins et al. [1,2], and Docquier et al. [3], have used the excited chemiluminescent intensities from OH^* and CH^* to measure the equivalence ratio of premixed, fuel-lean methane/air flames, although their measurements were not spatially resolved because they measured the global chemiluminescence of the flame by using a fiber and a quartz lens. Kojima et al. [4], have reported spatially-resolved measurements of OH^*, CH^* and C_2^* of laminar premixed methane/air flames, but they studied fuel-rich flames.

In this paper, a Cassegrain optics-based chemiluminescence sensor will be presented and its ability to resolve flame fronts will be shown by its comparison with OH PLIF. Then the applicability of the CS at an atmospheric modified micro-gas turbine environment will be assessed. The ability of the sensor to measure equivalence ratio at a CH_4/H_2O/air humidified flame will be demonstrated, and the important effect of the humidity to the measured equivalence ratio by the CS will be studied.

2. The chemiluminescence sensor

The variation of chemiluminescence intensity with flame equivalence ratio and flame strain rate was evaluated in a flow allowing independent variations of flow conditions and combustion parameters, such as bulk flow strain rate and flame equivalence ratio. The so-called "counterflow" burner geometry is suitable for that purpose, because it allowed us to operate the burner within a wide range of flame equivalence ratios and bulk flow strain rates: the spatially stabilized flat flame front was close to the stagnation plane, which had constant stretch rate along the reaction zone. Finally, it offers excellent optical access for measurements. The counterflow geometry used for this work follows the work of Mastorakos [5], Fig. 1. It comprised two opposed brass pipes with inner
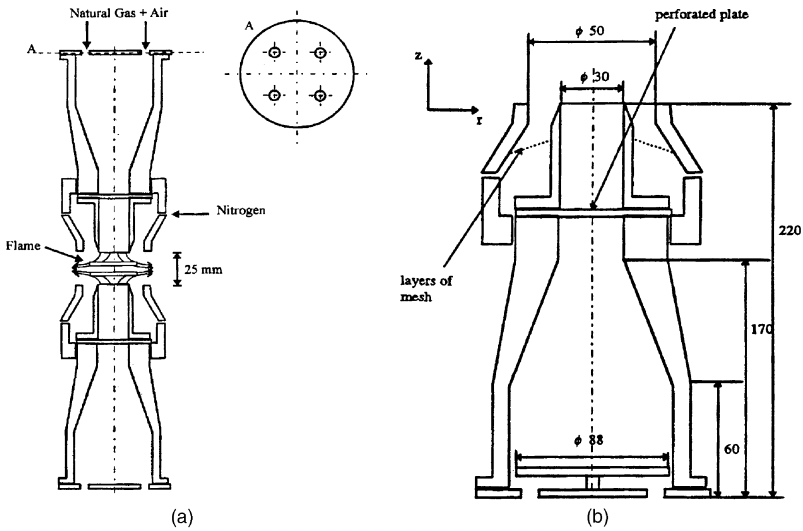
Fig. 1. (a) Counterflow burner geometry and (b) detailed sketch of the lower duct (dimensions in mm).

diameter of $D = 30$ mm, separated by a distance 2H, which can be adjusted to any value up to 200 mm via a vertically moveable lower pipe. The counterflow burner has been described in detail in [6]. The bulk exit velocity of each jet from the pipe, V_0, was varied between 1 and 5 m/s. This corresponds to a bulk flow strain rate, S, ranging from 80 to 400 s^{-1}. The bulk flow strain rate was evaluated as follows:

$$S = \frac{2V_0}{2H}.$$ (1)

The equivalence ratio Φ of the premixed mixture was varied from 0.7 to 1.3 for most of the cases studied.

2.1. Instrumentation

The chemiluminescence sensor comprised a Cassegrain optical system, shown in Fig. 2, similar to that of Akamatsu et al. [7]. The use of mirrors, rather than lenses, avoided the generation of chromatic aberrations for different wavelengths, in contrast to lenses (refractive elements), which cannot be corrected for chromatic aberrations over a wide range of wavelengths. The collected light from the CS was focused onto a pinhole placed in front of an optical fiber, which was connected to a purpose-built *photo detector unit* (Fig. 2). The light was split into three parts using two dichroic mirrors for the three wavelengths considered. Each part was directed onto appropriate interference filters specific to the radical considered, at 310.4 nm for the OH*, 430.5 nm for the CH*, and 516 nm for the C_2^*. The collected light intensities were transformed into electrical signals by three photomultipliers. The temporal signals of OH*, CH* and C_2^* were filtered by a low-pass filters, and digitized simultaneously using a 12-bit A/D card. The MICRO system had a
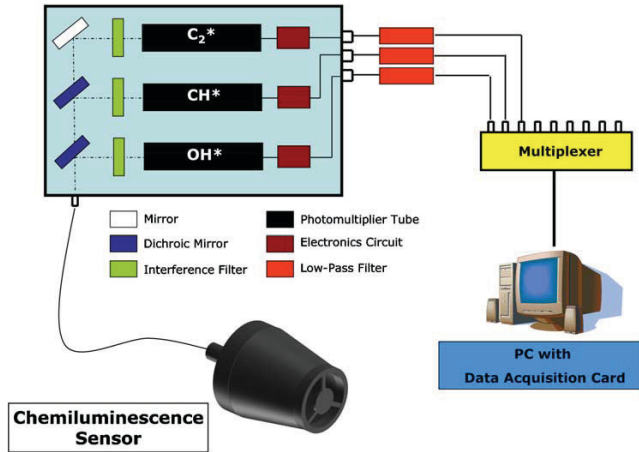
Fig. 2. The chemiluminescence sensor and the photo detector unit.

300 mm focal length, with diameter of primary and secondary mirrors of 150 and 50 mm respectively. This produced a probe volume with nominal diameter and length of 200 microns and 1.6 mm, respectively, according to Akamatsu et al. [7].

2.2. Data processing

Raw intensity signals from the photomultipliers were recorded and then processed according to the following steps:

- A threshold was selected for the raw intensity CH^* signal. This allows detection of signals from the reaction sheet above the background noise.
- Samples which were above the threshold for the CH^* signal were identified. These samples were considered to arise from chemical reaction in the optical probe volume. The corresponding points in time in the OH^* intensity signal were identified to evaluate the instantaneous OH^*/CH^* ratio. Within the interval of the signal record being above the threshold, we identified the maximum values of the CH^* and OH^* signals. If the maxima of the intensities coincided (i.e. they occurred within a temporal tolerance of $2/f_s$, where f_s was the sampling frequency), we calculated the instantaneous value of the OH^*/CH^* ratio from these two maxima. The idea underlying this processing was that only the maxima of the intensities were representative of the local instantaneous reaction rate and equivalence ratio and that intensities before or after the maximum (in a given interval) are typical of chemical reaction initiation or termination.
- The mean and rms of the fluctuation of the samples of the OH^*/CH^* ratio, determined as above, were calculated from the instantaneous OH^*/CH^* ratio taking into account the different efficiencies of the interference filters, dichroic mirrors and the response of the photocathodes at the wavelengths considered. The conversion factors of the current optical system that were used to convert measured intensity ratio into real intensity ratio are:

$$\frac{I_{\text{OH}}^{\text{real}}}{I_{\text{CH}}^{\text{real}}} = 2.720 \frac{I_{\text{OH}}^{\text{meas}}}{I_{\text{CH}}^{\text{meas}}}, \tag{2}$$

where I^{meas} and I^{real} represent, respectively, the measured and the real chemiluminescence intensity of the radical considered.

2.3. Calibration of CS for natural gas

Calibration experiments were performed with the counter-flow burner using UK natural gas (94% methane, CH_4) over an equivalence ratio range of 0.7–1.3 and a bulk strain rate range of 160–320 s^{-1}. The measured OH*/CH* chemiluminescent intensity ratio was found to be independent of the strain rate, and monotonically dependent on the equivalence ratio. The dependence of OH*/CH* ratio on the equivalence ratio, Φ, was approximated by the following curve fit ([8]):

$$\frac{\text{OH}^*}{\text{CH}^*} = 0.497 + 2.107 \exp(-(\Phi - 0.7)/0.260). \tag{3}$$

For all flow conditions and for a given value of Φ, the OH*/CH* ratio was within 5% of the value given by Eq. (3), which leads to an uncertainty of approximately 0.05 for determination of flame equivalence ratio for $\Phi \leqslant 1.0$. For $\Phi > 1.0$, the chemiluminescent technique could not measure flame equivalence ratio accurately with uncertainties being larger, of the order of 0.1–0.2. Therefore, the curve fit, Eq. (3), may be used only for equivalence ratios less than 1.0. The monotonic dependency of the OH*/CH* intensity ratio on equivalence ratio makes the instrument a useful instrument for measuring local flame equivalence ratio in a real burner operating with natural gas at atmospheric pressure. The calibration of the CS for natural-gas-fuelled flames has been described in more detail in Refs. [6,8].

3. Evaluation of the CS with OH PLIF

The spatial resolution of the CS has been evaluated using spatial and temporal resolved planar laser-induced fluorescence, PLIF, of the OH flame radical. The laser technique used in order to evaluate the spatial resolution of the CS, was spatially and temporally resolved planar laser-induced fluorescence, PLIF, of the OH flame radical. The laser source was a cluster consisting of four standard flash-lamp pumped Nd:YAG lasers (BMI, France). The fundamental laser wavelength is 1064 nm. Each laser in the cluster consists of a Q-switched oscillator and a single amplifier, emitting laser pulses with duration of 7 ns. The four laser beams are aligned and frequency doubled according to the scheme shown in Fig. 3.

With this laser cluster a sequence of laser pulses with very short time separation can be obtained, enabling temporally resolved studies of turbulent combustion phenomena. However, the high-temporal resolution capability of the Nd:YAG laser cluster was not used during the present experiments, since the flame studied was a stable laminar Bunsen-burner flame.

The 532 nm output from the Nd:YAG laser cluster was converted to other wavelengths using a dye laser, pumped by the Nd:YAG laser cluster. The dye laser (ND60, Continuum) is narrowband
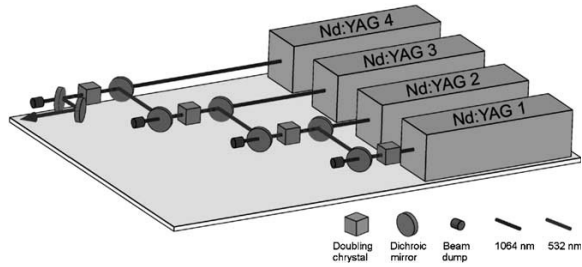
Fig. 3. Schematic overview of the Nd:YAG laser cluster, consisting of four Nd:YAG lasers of LTH.

(0.2 cm^{-1}) and has tunable wavelength with a harmonic generation unit attached to it. For excitation of the OH radical laser light with a wavelength close to 283 nm is used. This wavelength is generated using a Rhodamine 590 dye solution in methanol, with subsequent frequency doubling of the dye laser output using a KDP crystal.

The laser-induced fluorescence images were recorded using an ICCD camera (LaVision Flamestar II), with an image area of 576×384 pixels, and a dynamic range of 14 bit.

A Bunsen burner was used for these experiments, which established an axially symmetric cone-shaped stable flame, when operated with premixed reactants. The radius of the inner nozzle of the burner was $R = 5$ mm. The burner was fuelled by natural gas and air, and the mixture was fully premixed before exiting the nozzle with equivalence ratio, $\phi = 0.85$. The experimental set-up is shown in Fig. 4.
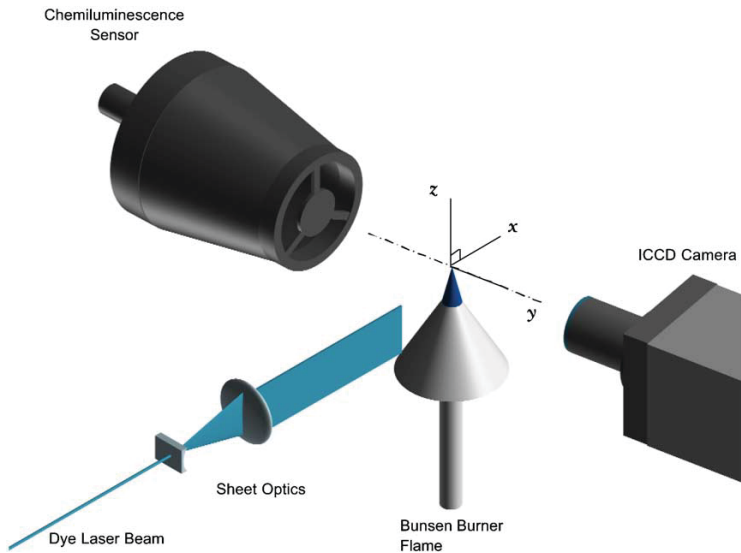

Fig. 4. The experimental setup for OH PLIF and chemiluminescence measurements in the Bunsen-burner flame.

The measurements of the excited species OH*, CH* and C_2^* were performed at a distance of $z = 5$ mm downstream of the exit of the burner. Radial profiles of chemiluminescent intensity were measured in two orthogonal directions at this axial location. For the first direction, the probe volume of the sensor was traversed along the *x*-axis (Fig. 4), reached the reaction zone and collected emitted light "tangentially" to the flame sheet and moved across until it reached the reaction zone on the other side of the burner axis. The chemiluminescence intensity measurements when the probe volume was inside the reaction zone were very little influenced by background emissions and, therefore, the measurements were mainly due to the reaction in the probe volume and this radial profile is associated with '*point measurements*'.

A typical *x*-direction profile ("*point measurement*") of the CS is shown in Fig. 5, where the chemiluminescence intensity from OH* is compared with the results from the OH PLIF measurements, at the same height above the burner tip ($z = 5$ mm). The figure shows that, for both measurement techniques, two intensity maxima are located at the same "radial" (i.e. *x* location) positions (symmetrical about the burner axis). However, the PLIF measurements show a wider OH intensity profile outside the reaction zone. However, this is expected since the PLIF technique excites the ground state OH radicals, which are abundant downstream of the reaction zone, in the post-flame gases. The CS, on the other hand, detects only the natural chemiluminescence from the excited radicals formed in the reaction zone. Therefore, since there is no "combustion" in the post-flame gases, the chemiluminescence intensity from OH* radicals is very low outside the reaction zone. The good agreement for the radial location of the intensity maxima from the LIF and the CS measurements indicates that this is the location of the reaction zone. Nevertheless, the CS measurements indicate a larger intensity around the centerline of the burner where a reaction zone is certainly not present. This signal is due to the collection of light from the flame present outside the probe volume, in front and/or behind the probe volume.
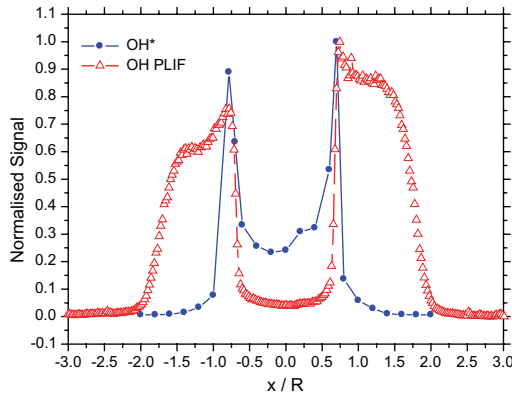

Fig. 5. Comparison between the OH and OH* intensities measured by OH PLIF and the chemiluminescence sensor respectively. The intensities are normalised with the maximum intensity measured with each instrument and the radial distance is normalised with the burner radius.

4. Measurements with the CS in an atmospheric pressure micro-gas turbine combustor

In order to test the ability of the CS to measure in an environment closer to that of a practical gas turbine, we evaluated the sensor's ability to measure the degree of premixedness of the fuel/air mixture, in a modified micro-gas turbine combustor, running at atmospheric pressure. Unfortunately, the limited optical access to the combustor chamber did not allow us to resolve the flame front, since we could not measure tangentially to the flame, but the ability of the sensor to measure the degree of premixedness under different operating conditions—including a humidified flame—was shown.

The combustion chamber originates from a Volvo micro-gas turbine (VT 40), with operating characteristics for the engine at full load being 4 bar (combustor pressure), 147 kW (thermal power), 600 °C (inlet air temperature) and 355 g/s (air mass flow). The combustor was modified to operate at atmospheric pressure with the corresponding values being 45 kW, 372 °C and 88 g/s, respectively. The combustor operated with natural gas. The inlet air stream could be humidified up to 20% at full load before entering the combustor chamber.

Natural gas was supplied to the pilot burner (diffusion flame) and to the main burner (premixed flame). Consequently, the combustion chamber had the capability for both premixed and non-premixed operating modes. The pilot flame can be characterized as a slightly lean diffusion flame. A part of the air entered through the primary swirler and was mixed with the fuel before it entered the combustion chamber, and this is shown schematically in Fig. 6. The pilot flame was attached to the outer ring of the pilot burner. Before the main flame was swirl-stabilized in the combustor chamber, the fuel/air mixture was premixed. The mixing process started in the secondary swirler, in which the natural gas was perpendicularly injected to the air stream; additional air was added
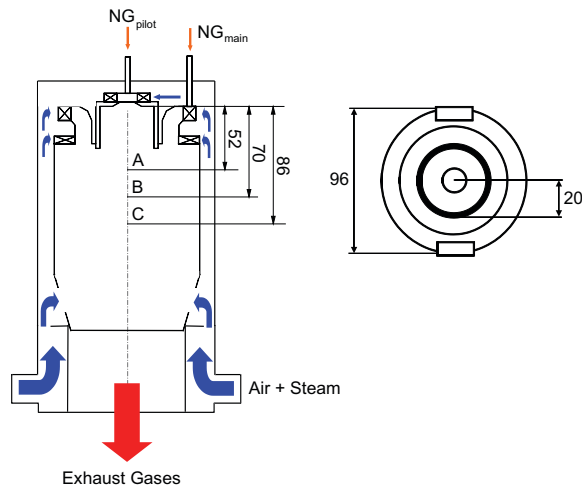

Fig. 6. Left: Flow schematic of the atmospheric combustion rig. Right: The combustion chamber seen from the exhaust gases end.

to the stream in the tertiary swirler. The secondary and tertiary swirlers are counter flowing, which is likely to improve mixing.

Moreover, the combustor has been equipped with two side windows and one bottom window, all in fused silica, providing optical access to the combustion zone. The optical access made it possible to perform measurements with laser/optical-based techniques. In Fig. 7 one of the side windows of the combustor is depicted. The side windows of the combustion chamber, were situated on either side of the diameter of the chamber and were double walled. These windows made it possible to achieve optical access from the fuel/air inlet in the primary zone down to the dilution zone. The window at the bottom of the flue gas channel allowed additional optical imaging of both the flame structure and the flow field. The measurements with the CS were performed through the side window shown in Fig. 7.

During the experiments the atmospheric combustor was operated at three conditions, referred to as GT1, GT2 and GT3, the characteristics of which are presented in Table 1. The two first cases, GT1 and GT2, were without humidified air, whereas in GT3, 8.1 kg H_2O/kg air is used. For all cases, the pilot flame was used *only* during the ignition of the burner. Measurements were performed only under *nominally* premixed fuel/air operation of the combustor, although partially premixed mixture was expected to occur during combustion in the chamber and the measurements presented below confirmed this expectation.

The measurements of the chemiluminescent intensity of the excited radicals of OH^*, CH^* required for measurement of the equivalence ratio, ϕ, were performed at three different planes, A, B and C, and for three different operating conditions of the burner. Plane A was closer to the
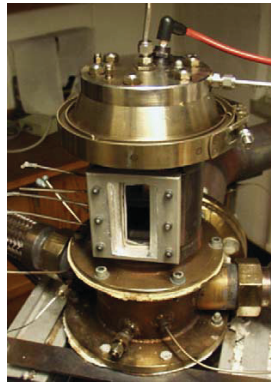

Fig. 7. The side window of the atmospheric combustion chamber.

Table 1
The characteristics for each of the three operating conditions

Case	m_{air} [g/s]	m_{fuel} [g/s]	T_{in} [°C]	Ω [kg H_2O/kg air]	$T_{exhaust}$ [°C]
GT1	83	0.64	340	0	691
GT2	83	0.615	341	0	671
GT3	83	0.637	330	8.1	667

swirlers of the burner at a distance of 52 mm from the exit of the swirlers, and planes B and C were at 70 and 86 mm below this exit, respectively. The position of the different planes where measurements were performed can be seen in Fig. 6.

The optical access of the side windows was nominally 30 mm, but was reduced to approximately 27 mm because of the insulation material that was used for the placement of the windows. This arrangement made impossible chemiluminescence sensor measurements tangentially to the flame, which would have given the best spatial resolution. So, during the measurements the CS probe volume was placed as close to the flame front as possible, but signal was collected from the background before and after the probe volume.

The CS was traversed along the x-axis (Fig. 8), and its probe volume was focused inside the burner at a distance of 40 mm from the outer window, which is equal to $r/R_B = 0.24$, where $R_B = 50$ mm is the radius of the inner flame tube of the burner. The different stations where the measurements were performed can be seen visualized by the median dotted line (red dotted line in the web version) shown in Fig. 8.

The measured mean values of the equivalence ratio, for the operating condition GT1, and for the different planes A, B and C, are shown in Fig. 9. The corresponding distributions of the probability functions (PF) of the equivalence ratio of the reacting mixture, ϕ, can be seen in Fig. 10. The values of equivalence ratio of the fuel/air mixture are richer at planes A and C, and slightly leaner at plane B. The same trend was observed for the operating condition GT2, shown in Fig. 11. The operating conditions GT1 and GT2 are quite similar in composition, so no large variations in the time-averaged value of the measured equivalence ratio would be expected. The difference in the measured mean value between operating conditions GT1 and GT2 was of the order of 0.05. The distributions of ϕ are wider at plane A, presumably because the measurements were closer to the mixing region of the fuel/air streams, confirming that the mixture was only partially premixed. The observed discrepancies in the PF of ϕ at the edge of the profiles, i.e. for $r/R = -0.6$ of Fig. 10, plane A, are caused by the limited optical access of the CS at the edges of the combustion chamber.

A humid $CH_4/H_2O/air$ flame ("wet" flame) was also studied during the experiments at the atmospheric combustor. The percentage of humidity was 8.1% (kg H_2O/kg air). The air flow rate
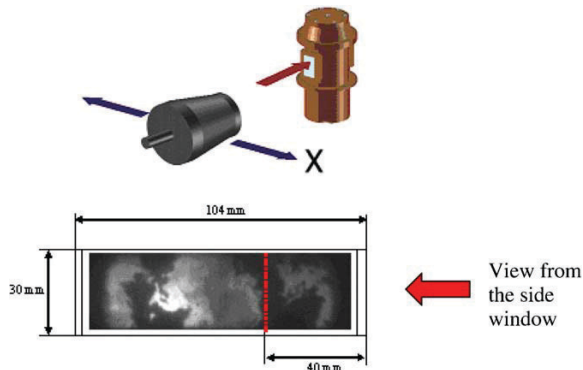

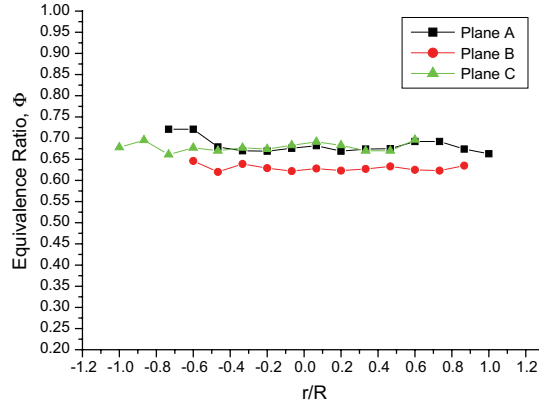Fig. 8. Measurement stations of the chemiluminescence sensor.

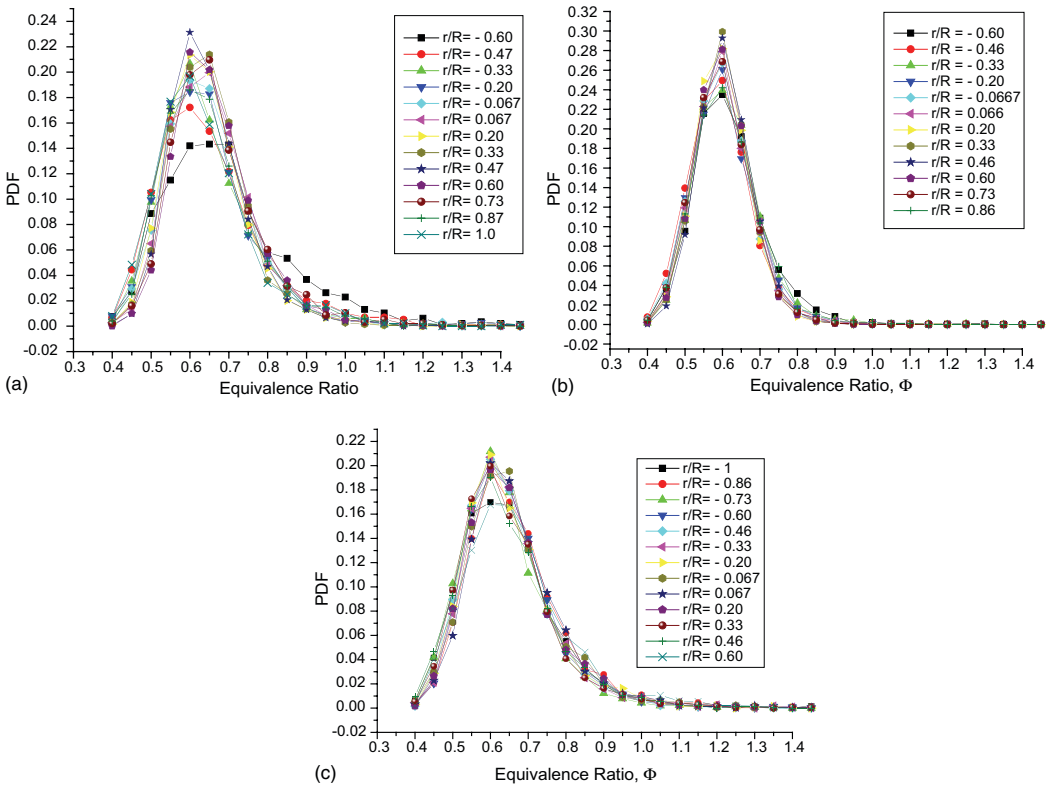Fig. 9. Mean values of equivalence ratio for the operating condition GT1, at planes A, B and C.

Fig. 10. PF distributions of the equivalence ratio for operating condition GT1, at planes A, B and C.
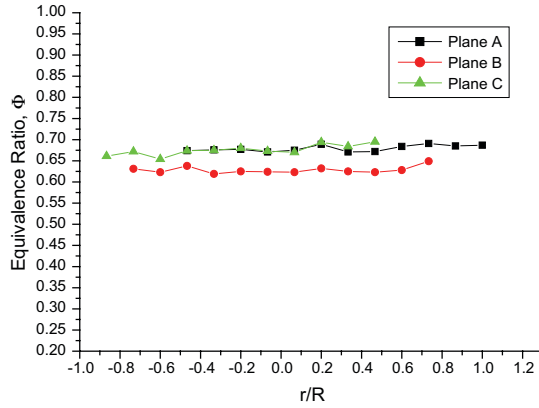
Fig. 11. Mean values of equivalence ratio for operating condition GT2, at planes A, B and C.

and the fuel flow rate were exactly the same as for operating condition GT1, so the results from the humid flame are plotted together with the results for operating condition GT1 at plane C in Fig. 12, and in Fig. 13 the PF of the equivalence ratio are presented. It can be observed that there is a good agreement between the mean values of equivalence ratio of the humidified flame and the CH_4/air flame, suggesting that the addition of water at the combustor did not influence the ratio of the OH^*/CH^* excited radicals, and therefore the equivalence ratio. Another encouraging indication from these measurements is that the CS has the ability to measure in a humidified flame environment.
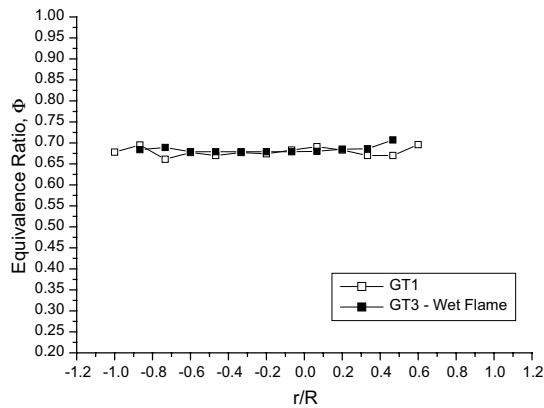

Fig. 12. Distribution of the mean values of the equivalence ratio for the humidified flame and the operating condition GT1, measured at plane C.
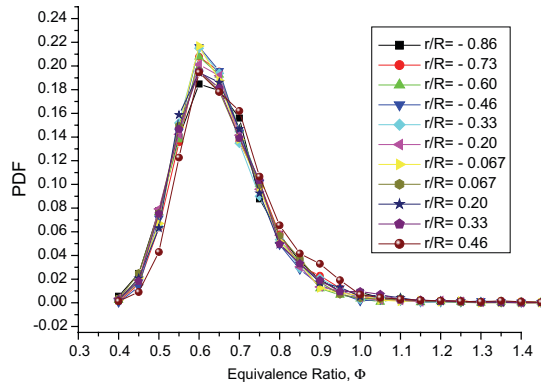
Fig. 13. PF curves for the values of equivalence ratio for the operating condition GT3—humidified flame, measured at plane C.

5. Conclusions—Future work

A chemiluminescence-based technique that has the potential of measuring flame equivalence ratio in a real gas turbine environment was presented in this paper. A Cassegrain telescope optical arrangement was used to provide spatially and temporally resolved intensity measurements, which detected the local flame structure. The calibration of the technique for natural-gas-fuelled flames under atmospheric pressure and variable strain rate has been described. The OH^*/CH^* intensity ratio has the potential for measuring flame equivalence ratio of the reacting mixture in flames at atmospheric pressure burning natural gas. The technique can measure equivalence ratio in lean and stoichiometric mixtures, but higher uncertainties appear for rich mixtures.

1. The evaluation of the CS with OH PLIF has shown that both techniques detected the reaction zone at the same radial position in a Bunsen burner.
2. However, the spatial resolution of the Chemiluminescence sensor is good when the probe is traversed such that the flame sheet is tangential, rather than normal to, the flame. This is due to the fact that when the probe volume of the sensor is located at the center of the flame, the spatial resolution of the sensor is reduced, because the sensor collects light from regions in front and/or behind the probe volume. This may not be a problem if generous optical access can be made available allowing measurement tangentially to the flame front, but can become a serious drawback when such optical access is not available.
3. The ability of the sensor to measure the equivalence ratio in a micro-gas turbine combustor working at atmospheric pressure but otherwise under conditions similar to that of a real gas turbine (air and fuel flow rates, preheating and humidified flame) show that the sensor has the potential for monitoring the degree of premixedness of reacting fuel and air in stationary gas turbine combustors, where operation with lean premixed mixtures is important for reduction of NO_x emissions.

The important effect of pressure to the existing natural gas calibration of the CS is going to be studied in the future, in order to measure the fuel/air degree of premixedness at an industrial gas turbine environment.

Acknowledgement

References

[1] B. Higgins, M.Q. McQuay, F. Lacas, J.C. Rolon, N. Darahiba, S. Candel, Systematic measurements of OH chemiluminescence for fuel-lean, high-pressure, premixed, laminar flames, Fuel 80 (2001) 67–74.
[2] B. Higgins, M.Q. McQuay, F. Lacas, S. Candel, An experimental study on the effect of pressure and strain rate on CH chemiluminescence of premixed, fuel-lean methane/air flames, Fuel 80 (2001) 1583–1591.
[3] N. Docquier, F. Lacas, S. Candel, Closed-loop equivalence ratio control of premixed combustors using spectrally resolved chemiluminescence measurements, Proc. Combust. Inst. 29 (2002) 139–145.
[4] J. Kojima, Y. Ikeda, T. Nakajima, Spatialy resolved measurement of OH^*, CH^* and C_2^* chemiluminescence in the reaction zone of laminar methane/air premixed flames, Proc. Combust. Inst. 28 (2000) 1757–1764.
[5] E. Mastorakos, Turbulent combustion in opposed jet flows, PhD Thesis, University of London, UK (1993).
[6] M. Orain, Experiments with gas and liquid-fuelled flames, PhD Thesis, University of London, UK (2001).
[7] F. Akamatsu, T. Wakabayashi, S. Tsushima, Y. Mizutani, Y. Ikeda, N. Kawahara, T. Nakajima, The development of a light-collecting probe with high spatial resolution applicable to randomly fluctuating combustion fields, Meas. Sci. Technol. 10 (1999) 1240–1246.
[8] Y. Hardalupas, M. Orain, Spatially and temporally resolved heat release rate and equivalence ratio measured using chemiluminescence emission from flames, Combust. Flame 2003, (in press).

VI

High-Speed PLIF Imaging for Investigation of Turbulence Effects on Heat Release Rates in HCCI Combustion

H. Seyfried, J. Olofsson, J. Sjöholm, M. Richter, M. Aldén
Division of Combustion Physics, Department of Physics, Lund University, Faculty of Engineering

A. Vressner, A. Hultqvist, B. Johansson
Division of Combustion Engines, Department of Energy Sciences, Lund University, Faculty of Engineering

PO Box 118, S-221 00 Lund, Sweden

ABSTRACT

High-speed laser diagnostics was utilized for single-cycle resolved studies of the fuel distribution in the combustion chamber of a truck-size HCCI engine. A multi-YAG laser system consisting of four individual Nd:YAG lasers was used for planar laser-induced fluorescence (PLIF) imaging of the fuel distribution. The fundamental beam from the lasers at 1064 nm was frequency quadrupled in order to obtain laser pulses at 266 nm suitable for excitation of acetone that was used as fuel tracer. Bursts of up to eight pulses with very short time separation were produced, allowing PLIF images with high temporal resolution to be captured within one single cycle event. The system was used together with a high-speed framing camera employing eight ICCD modules, with a frame-rate matching the laser pulse repetition rate. The combustion evolution was studied in terms of spatial distribution and rate of fuel consumption for different engine hardware configurations as well as operating conditions e.g. different stoichiometries and combustion phasing. Two different piston crown geometry were used for altering the degree of turbulence in the combustion chamber. In addition to the optical investigations, the impact of turbulence effects was also studied by calculating the rate of heat-release and combustion phasing from the pressure trace.

INTRODUCTION

Homogeneous Charge Compression Ignition (HCCI) engines are well known for high efficiency and low emissions of Nitrogen Oxides (NOx) and particulate matter [1, 2]. One of the negative issues with HCCI is how to control the combustion phasing since its only governed by the pressure and temperature history of the charge. If the load is too high and/or the combustion timing is too advanced the combustion rates will be very fast and thus also pressure rise rates which not only causes excessive noise but could also lead to engine damage. A strategy for decreasing the combustion rates is for example charge dilution by Exhaust Gas Recirculation (EGR) which slows down the reaction rates. Another approach could be to change the flow conditions in the cylinder. This can be done using a Variable Valve Actuation (VVA) with valve timings set in such way that different amount of swirl is produced inside in the combustion chamber. An alternative is geometry generated turbulence which has been studied in this paper, where piston geometry in form of a square bowl in piston with a narrow squish region forces the gas down into the bowl causing turbulent conditions.

PRIOR WORK

The effect of geometry generated turbulence on Rate of Heat Release (ROHR) has been studied in earlier work by Christensen et al. [3, 4]. It was found that the ROHR could be decreased about 50% and the combustion duration doubled by the use of a bowl compared to a disc shaped combustion chamber during similar operational conditions. This means that the load can be increased by the use of bowl geometries with acceptable pressure rise rates. The turbulence level was measured by Laser Doppler Velocimetry (LDV) and found to be twice as high at Top Dead Centre (TDC) with the bowl geometry. However it was not clear if the decreased ROHR was entirely due to turbulence effects or due to other effects caused by the geometry. Therefore it is appropriate to divide the conditions caused by the geometry into direct and indirect effects:

1. Direct effects could be the turbulence effect on chemical kinetics.

2. Indirect effects are for example boundary layer thickness, temperature distribution, heat losses and charge homogeneity.

Kong et al. [5], modeled the direct effect of turbulent flow on chemical kinetics by the eddy breakup concept using CFD with detailed chemical kinetics code. The model predicted the longer combustion duration in the bowl case due to increased wall heat transfer, but more comprehensive CDF models are needed to predict turbulence and heat transfer accurately.

Another theory for explaining the decreased ROHR and increased combustion duration could be that the geometry causes a sort of 2-stage combustion where the ignition first occurs in the bottom of the bowl where the hot residuals probably are located and as time proceeds the combustion propagates out in the squish volume during the early stages of the expansion stroke. This would probably be due to charge stratification in either temperature, air/fuel ratio or a combination of both. In the disc shaped combustion chamber the temperature distribution is expected to be more even as the residuals would be better mixed with the fresh charge. In contradiction to this one might argue that the high turbulence found in the bowl case should result in even better mixing compared to the pancake geometry, resulting in a less stratified charge in terms of lambda and temperature. However, at an early stage before the onset of combustion it is reasonable to believe that residuals are trapped in the bowl.

PRESENT WORK

Since the prior studies, based on pressure measurements and LDV, did not reveal the different contributions of direct and indirect effects due to geometry generated turbulence causing the slower ROHR in the bowl case further studies are necessary to explore the phenomenon.

In this paper planar laser-induced fluorescence, PLIF with an excitation wavelength of 266 nm was used for fuel visualization for two different piston geometries. The fuel used was ethanol and given that this is a non-fluorescent fuel a fluorescent tracer species was added. In general a suitable tracer should have the appropriate characteristics, e.g. spectrally separated absorption and fluorescence regions and ideally the fluorescence should be independence on temperature, pressure and composition of the surrounding gas. Other crucial features are that the tracer must follow the fuel and be consumed during the combustion in order to avoid tracer buildup and it must not influence the combustion process itself [6].

Acetone (CH_3COCH_3) has shown a number of advantages as a tracer molecule in PLIF imaging measurements [7, 8, 9]. Due to its broad absorption characteristics in the UV region (225 to 320 nm) the molecule is accessible with common high-energy, pulsed lasers, e.g. Nd:YAG and Excimer lasers. Subsequent fluorescence occurs between 350 and 550 nm. The differences in boiling point and diffusion coefficients between the tracer and the fuel are less of an issue in the presented measurements since they are performed with port injection. The long residence time in the port in combination with the position of the injector, upstream of the inlet valve, allow significant time for evaporation and mixing.

Generally, the fluorescence yield of acetone shows a temperature dependence. Depending on the excitation wavelength, the yield can increase or decrease with increasing temperature. In these experiments, employing excitation at 266 nm, the sensitivity to temperature change is fair [9, 10, 11]. Pyrolysis of acetone is another potential source of error. Experiments performed by Yip et al. [12] revealed no significant pyrolysis of acetone below 1000K. This implies that measurements during the heat release (1200-1500 K) may actually measure acetone pyrolysis and not consumption. However, pyrolysis is of course a step towards eventually oxidizing the fuel. In earlier investigations by the authors the optically detected start of consumption of acetone matches well with the start of the heat release calculated from the pressure trace for this fuel/tracer combination. Furthermore, simultaneous PLIF imaging of acetone and chemiluminescence imaging has also indicated the desired correlation between the disappearance of signal from acetone and the increase in chemiluminescence intensity [13].

EXPERIMENTAL

ENGINE SETUP

The engine used in this study was a six cylinder Scania D12 truck sized diesel engine converted to HCCI operation by the use of port fuel injection (PFI). The engine was in single cylinder operation, meaning that only one cylinder was operational while the rest were motored. A piezoelectric water-cooled Kistler 7061B pressure transducer was used to monitor the in-cylinder pressure and this information was used to control the phasing of combustion by changing the inlet air temperature with an electrical heater. Some vital engine data can be found in Table 1.

Table 1 Geometrical data of the Scania D12 Engine

Displaced volume	1966 cc
Stroke	154 mm
Bore	127.5 mm
Connecting rod	255 mm
Exhaust valve open	82° BBDC
Exhaust valve close	38° ATDC
Inlet valve open	39° BTDC
Inlet valve close	63° ABDC
Valve lift inlet	14 mm
Valve lift exhaust	14 mm
Fuel Injection	PFI
Fuel	Ethanol/Acetone: 90%/10%

Combustion Chambers

Two different combustion chambers were tested in this study, one disc shaped combustion chamber and one with a square bowl in piston. With the disc shaped combustion chamber the swirling motion of the charge is believed to be pretty undisturbed during the compression stroke. This geometry is used as a baseline and reference case to the main object of interest in this study, the square bowl in piston. When using a square shaped combustion chamber with a narrow squish region a strong squish motion forces the swirling motion of the charge into the bowl during the compression stroke creating a turbulent environment, especially in the corners of the bowl.

The engine was equipped with a quartz window in the piston and a 45 degree mirror which enables optical access from beneath. Further a quartz liner was situated just below the cylinder head enabling optical access from the side. This setup has been used for numerous studies before with the disc shaped combustion chamber. For this geometry the quartz window in the piston is squeezed in between two titanium retainers preventing the window from coming off during operation, see Figure 1. With the square bowl in piston geometry the upper part of the piston was entirely made of quartz glass in order to get optical access from the side to study the combustion inside the bowl. This means that the quartz piston could not be mounted in the same way as for the disc geometry. Instead the quartz piston was glued onto a titanium piston crown holder, where the glue is the only thing preventing the quartz piston from coming off. A sketch of this geometry can be found in Figure 2. It should also be mentioned that the bowl has equal sides, 47 mm, while the depth is 37.4 mm.
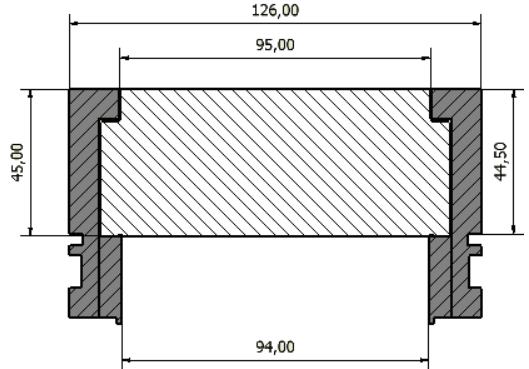

Figure 1 Sketch showing a cross section of the disc piston with the most important dimensions. White area is quartz and gray is titanium. All dimensions in mm.
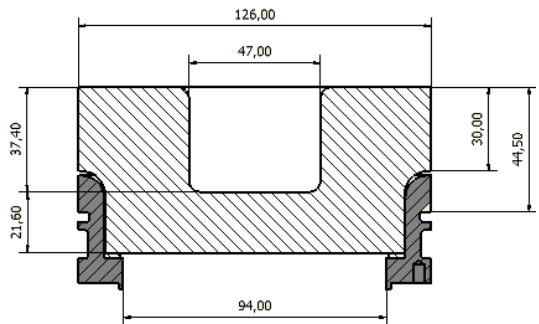

Figure 2 Sketch showing a cross section of the square bowl in piston with the most important dimensions. White area is quartz and gray is titanium. All dimensions in mm.

Some geometrical properties of the two combustion chambers used can be found in Table 2. During the preparation of the experiments the idea was to use the same compression ratio of 18:1 for both geometries, with a squish distance of 1 mm in the bowl case. However due to expansion of the piston extension and the glue caused by elevated temperatures and mass forces, especially at gas exchange TDC, the squish distance was increased to 1.75 mm in the bowl case which causes an difference in CR between the geometries. In order to investigate the effect of the difference in CR, measurements were performed with the disk geometry for both CR 18.0:1 and 17.2:1. The comparison showed no significant difference concerning rate of heat release and combustion duration. For these parameters the cycle-to-cycle fluctuations in the

3

combustion phasing showed a greater impact then the difference in CR. The measurements also revealed a difference of 0.5 percentage units in net indicated efficiency.

Table 2 Geometric properties of the combustion chambers used.

	Disc	Bowl
CR	18.0:1	17.2:1
Squish Distance	7.45 mm	1.75 mm
Topland Height	44.5 mm	44.5 mm

From Table 2 it can also be seen that the topland height is quite high for both geometries. This is due to optical access limiting the possibility to mount the piston rings as high as would be preferred. Since a large topland volume will trap fuel which is oxidized during the lower pressure of the expansion stroke the combustion efficiency is expected to drop a few units. However the most important thing is that the topland height is the same for both geometries.

Table 3 presents the operating conditions for the two different combustion chamber geometries. A number of operational points were tested during the measurements. However the table is limited to the operating conditions for the data presented in this paper.

Table 3 Operating conditions for both geometries. Parameters presented are air/fuel equivalence ratio (λ), crank angle of 50% burned (CA50), indicated mean effective pressure (IMEP), pressure derivative (dP), intake air pressure (P_{Intake}), inlet air temperature (T_{Intake}), combustion duration (CA10-CA90) and net indicated efficiency ($\eta_{Indicated, net}$).

Geometry	Disc	Bowl	Disc	Bowl
λ	3.3	3.3	3.7	3.7
CA50 [CAD ATDC]	8	8	8	8
IMEP [Bar]	2.81	2.79	2.17	2.16
dP [Bar/CAD]	3.50	1.10	2.20	0.97
P_{Intake} [Bar]	0.97	0.97	0.97	0.97
T_{Intake} [°C]	89	96	100	107
CA10-CA90 [CAD]	7.4	16.8	8.4	17.6
$\eta_{Indicated, net}$ [%]	40.8	39.1	39.9	39.0

OPTICAL SETUP

In order to visualize the fuel, or acetone, in the combustion chamber, Planar Laser-Induced Fluorescence (PLIF) was used. Cycle-resolved imaging of this type puts high demands on the repetition rate of the laser source and for this purpose a custom made multi-YAG laser cluster was used. The cluster consists

of four separate laser channels of Nd:YAG type, each operating with a repetition rate of 10 Hz and with a fundamental laser wavelength of 1064 nm. For superimposing the four beam paths and for frequency doubling of the laser radiation to 532 nm, a specially designed beam combining scheme was used. In this scheme the beam from laser 1 is frequency doubled to 532 nm using a second harmonic generating (SHG) crystal, after which the frequency doubled beam is separated from the fundamental beam by means of a dichroic mirror. The fundamental beam from laser 2 is then combined with the frequency doubled beam from laser 1, by using a second dichroic mirror reflecting in the green and transmitting in the IR. The beams are directed through a second SHG where the doubled beam from laser 1 passes unaffected while the fundamental from laser 2 is frequency doubled. This procedure is repeated for all the four lasers, and thus the laser system has a single output from which the pulses at 532 nm from the four lasers are emitted. Before the output the beams are directed through a forth harmonic generator (FHG), frequency doubling the green beams to 266 nm, which is used to excite the acetone. The laser system allows for opening of the Q-switch twice during one flash lamp discharge, extending the number of pulses from four to eight. The eight pulses can be emitted in a rapid succession and the time separation between two consecutive pulses, when firing eight pulses with equal time separation, can be set to values as short as 6.25 μs. A more thorough description about the multi-YAG laser system can be found in Ref. 14.

In order to detect the acetone fluorescence generated by the rapid laser pulse burst, a high-speed framing camera was used. The framing camera employs a single optical input in front of which a Bernard-Halle lens (f=+100 mm, f#=2) was mounted. An image intensifier is placed at the optical entrance of the camera in order to enhance the sensitivity of the detector and to enable UV detection. The intensified signal is split up with an eight-facet prism onto eight individual intensified CCD modules. Each module consists of a CCD image sensor (384x576 pixels) and a micro channel plate (MCP). The MCP further intensifies the signal and it also functions as an electronic shutter. To enable exposure of the CCD image sensors in a rapid succession, the MCPs are synchronized with the laser pulse train.

Figure 3 shows a schematic of the experimental setup used. To gain two-dimensional information of the fuel distribution the laser beam from the multi-YAG laser cluster was expanded to a horizontal laser sheet using a set of spherical and cylindrical lenses. The laser sheet was directed into the HCCI engine through the quartz cylinder liner and focused in the center of the combustion chamber. In the case with the piston square bowl, the sheet was positioned half way up from the bottom of the bowl. The fluorescence from the acetone was imaged perpendicular to the sheet, through the

quartz piston via a UV enhanced mirror in the piston extension onto the high-speed framing camera. To prevent scattered laser light from reaching the CCD detectors, two optical filters were used; one quartz cuvette with liquid N.N.-Dimethyl-formamide blocking 266 nm, and one short-pass filter with a cut-off wavelength at 500 nm to avoid interference from the remaining 532 nm laser light.
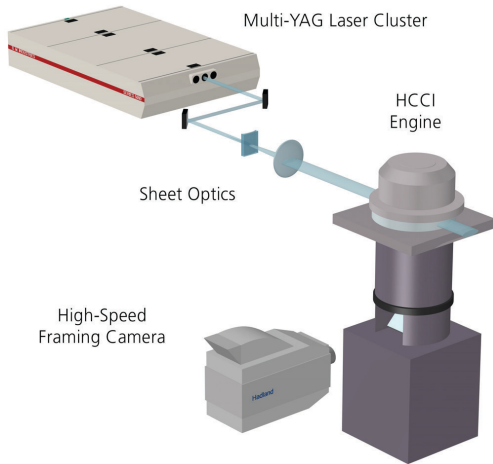

Figure 3 Schematic of the experimental setup.

During the presented measurements the engine speed was kept constant at 1200 rpm. This corresponds to a combustion cycle frequency of 10 Hz which matches the overall repetition rate of the laser system. A pulse from a crank angle encoder was used to fire the laser system at the desired position.

The multi-YAG laser system was operated in double pulse mode, resulting in an energy of approximately 20 mJ per pulse at 266 nm. The time-separation between two consecutive images was varied from 70 μs up to 140 μs, corresponding to 0.5 CAD (crank angle degree) and 1 CAD respectively. In order to suppress the background radiation, the camera exposure time was set to 50 ns for each image acquisition.

RESULTS

The combustion development for the two engine geometries was studied in terms of fuel consumption and rate of heat release for different stoichiometries (lambda values) and combustion phasing. PLIF sequences with seven image frames showing the fuel distribution in a single engine cycle were recorded. The initial width of the laser sheet was 31 mm for both engine geometries. However, for the square bowl geometry the solid quartz piston introduces a strong focusing effect on the sheet, which has to be compensated for. This compensation was done by making the sheet divergent instead of parallel before entering the combustion chamber. It was difficult to fully compensate for the focusing and a slight convergence remained, resulting in a sheet width of 26 mm, at the exit of the square bowl.

To enable subtraction of undesired laser scattering from the fuel PLIF measurements, also images without combustion present were acquired. In order to compensate the PLIF images for imperfections in the laser sheet intensity profile, these profiles were also recorded. This was done by recording PLIF image sequences early in the cycle before the combustion has started, thus were the fuel distribution was uniform. From these images an intensity profile matrix was created. This matrix has the same size as the images with recorded fuel consumption, and the fuel consumption sequences were then divided by the profile matrix pixel by pixel in order to compensate for these variations.

In Figure 4 image sequences showing the fuel distribution within one cycle for the disc and square bowl geometry respectively, are presented. Measurements were performed for λ=3.3, λ=3.7 and λ=4.1, and the examples shown in the figure originates from λ=3.7. It should be noted that prior to the onset of combustion the fuel distribution appeared to be homogeneous for all stoichiometries investigated. Bright regions indicate the fuel whereas dark regions indicate where fuel consumption has occurred. The figure also includes schematics of the combustion chamber geometries, in which the dashed lines correspond to the laser sheet positions. As can be seen in the upper part of Figure 4, fuel consumption starts at multiple ignition points in the cylinder for the disc geometry, which is most likely due to temperature inhomogenities in the charge. The corresponding rate of heat release curve is shown in Figure 6. The time positions of the individual frames are indicated by the seven marks. The figure also confirms a rapid combustion and high peak heat release. A closer look at the images in the sequence also indicates that the decrease in fuel concentration is gradual, without sharp concentration gradients, and the lack of flame-front-like propagation. Although the last frame shows virtually no presence of fuel, the plot in Figure 6 reveals that there is still some heat to be released at this point. This discrepancy can be due to the PLIF imaging being a two-dimensional technique showing only a cross section of the combustion chamber. This means that there might be, and probably is, fuel outside the imaged area, e.g. the volumes close to the walls and the crevices cannot be accessed. Another possibility that might contribute is that the tracer species (acetone) does not perfectly represent the fuel (ethanol) in terms of
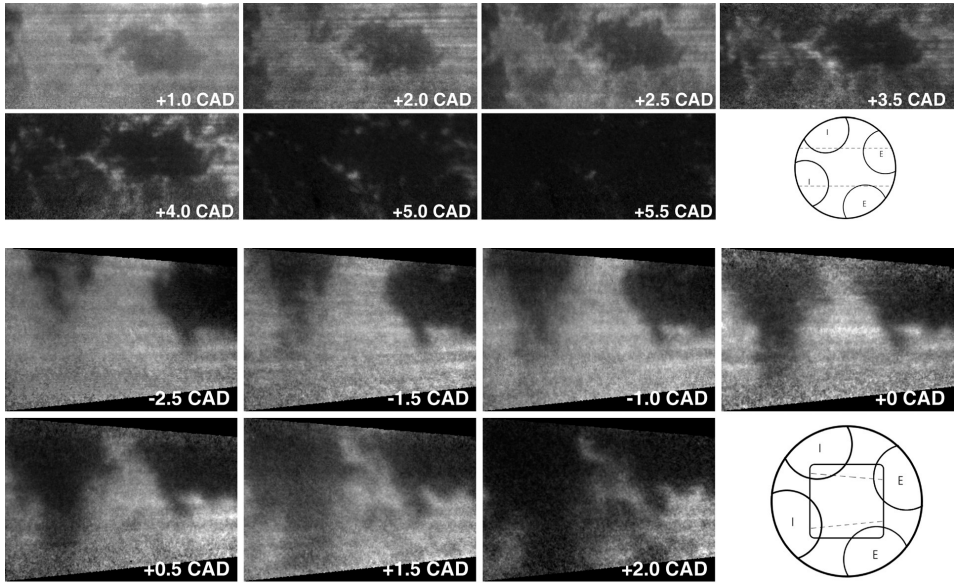
Figure 4 Image sequences of seven single shot PLIF images showing the fuel consumption for the two piston geometries at λ=3.7. The upper sequence represents the disc piston case with an imaged area of 30 mm x 67 mm, whereas the lower sequence represents the bowl piston case with an imaged area of 30 mm x 45 mm.
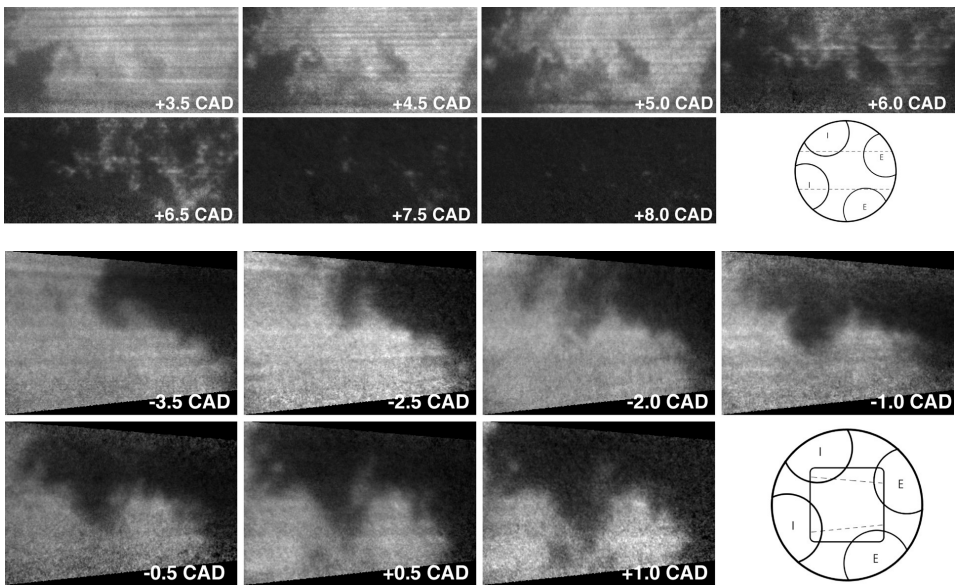

Figure 5 Image sequences of seven single shot PLIF images showing the fuel consumption for the two piston geometries at λ=3.3. The upper sequence represents the disc piston case with an imaged area of 30 mm x 67 mm, whereas the lower sequence represents the bowl piston case with an imaged area of 30 mm x 45 mm.

pyrolysis/oxidation at this late phase of the combustion process. However, the most likely reason is that the heat release at this late phase represents combustion of decomposed fuel, mainly in the form of carbon-monoxide.

For the combustion process involving the square bowl geometry a clearly different behavior is seen, see the lower part of Figure 4. Ignition occurs only in a few positions, resulting in slower rate of fuel consumption. Moreover, this seems to give rise to a more flame-front-like combustion behavior, and hence much sharper concentration gradients. Whether this is an effect of the increased degree of turbulence induced by the bowl piston or of hot residual gas remaining in the bowl is yet to be determined. In the rate of heat release for this case, presented in Figure 7, a slower combustion and a lower peak heat release can be seen as compared to the disc piston geometry. Also PLIF image sequences for the two piston geometries at λ=3.3 are presented, see Figure 5. As can be seen, the images show the same trends as for the leaner case.
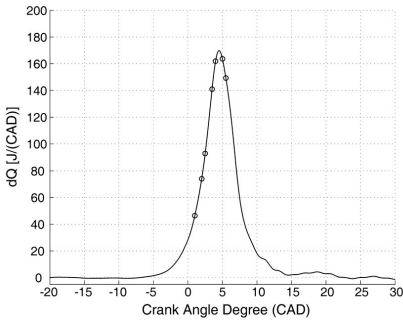

Figure 6 Rate of heat release measured for the disc piston geometry. Corresponding PLIF sequence is presented in the upper part of Figure 4.
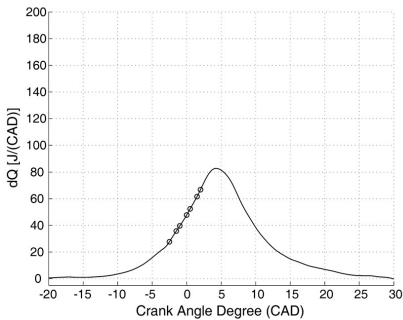

Figure 7 Rate of heat release measured for the square bowl piston geometry. Corresponding PLIF sequence is presented in the lower part of Figure 4.

A way to more thoroughly distinguish between flame-front-like combustion with sharp gradients and multiple-ignition combustion with more gradual fuel consumption is to study the intensity histogram in the fuel PLIF images. The sharp gradients resulting from the flame front give rise to two well separated intensity levels in the images corresponding to burned and unburned areas, whereas gradual fuel oxidation results in a more even distribution between the gray levels in the images. In Figure 8, such histograms are shown for the disc geometry (left) and the square bowl geometry (right), both determined for λ=3.3. The presented data is extracted from the images in Figure 5. In the figure the number of pixels is presented using different scales for the two cases.
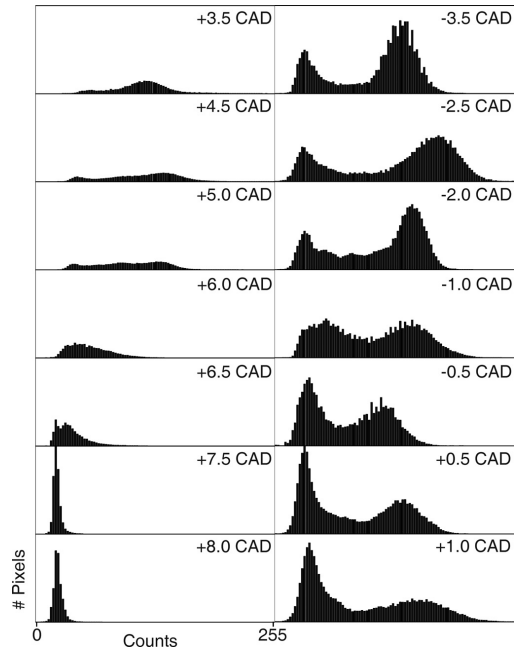

Figure 8 Intensity histograms for the disc geometry (left) and the square bowl geometry (right), both determined for λ=3.3. Data extracted from the images in Figure 5.

In the case with the disc geometry it is seen that the intensity is distributed over the dynamic range in the beginning of the fuel consumption. As the combustion proceeds the representation of low-intensity contribution (low fuel content) is increased. This is well in agreement with what has been previously concluded in this and in prior work [13]. The square bowl geometry induces a different behavior as shown in the histogram presented

in the right part of Figure 8. For this case a well separated bimodal intensity distribution is seen over the entire image sequence. Initially the peak representing bright areas dominates over the peak representing dark areas. The combustion development causes a redistribution between the two peaks, were the bright peak is decreasing and the dark peak is growing, without first passing through the mid-dynamic range in between the two peaks. In the middle of the sequence (-1 CAD) an even distribution between the bright and dark peeks is seen. This bimodal behavior is typical for flame front propagation, e.g. in spark ignition engines.

SUMMARY AND CONCLUSION

High-speed fuel tracer PLIF imaging was performed in an HCCI engine running with two different piston geometries, one flat and one with a square bowl. From earlier work the square bowl piston was known to generate high turbulence intensity, in the positions investigated by LDV, and also a significantly lower rate of heat release compared to the flat piston. The main scope of the presented study was to use optical techniques to investigate the spatial behavior of the combustion phenomena in order to gain knowledge about the processes generating the reduced rate of heat release when running with the square bowl piston.

The results revealed, as expected, multiple ignition kernels and a gradual oxidation of the bulk charge through distributed reactions for the flat piston geometry. For the square bowl piston there are instead very few isolated ignition kernels. Furthermore, the progression of the following combustion shows remarkably similarities to conventional flame front propagation. Possible causes for this behavior are that hot residuals are trapped in the deep square bowl or/and heat transfer from the bowl walls. This introduces a hot zone with steep temperature gradients in the bowl. The pressure and temperature history of the charge in the bowl is such that ignition is promoted first in this area. The early flame front like combustion in the hot zone continues until the colder mixture is reached. At present there is not enough PLIF data from the topland volume and from the upper part of the bowl to make certain conclusions, but line of sight chemiluminescence imaging performed by Vressner et al. [15] indicates that the colder charge burns later, when the conditions become favorable, in a fashion similar to what is seen for the flat piston. Similar phenomena are described by Sankaran et al. [16] who studied the effects of non uniform temperature distribution on the ignition of lean homogeneous mixtures. The high turbulence intensity shown in earlier LDV work might be seen as a contradiction to this hypothesis. However, LES modeling of the square bowl geometry by Bai et al. [17] indicates that the gas in the bowl actually has a low flow speed and thus long residence time facilitating sufficient heat transfer. In the above mentioned paper, this also found to be the reason for the increased combustion duration

for the square bowl. From the presented study the experimental results point towards temperature stratification as the main explanation for the extended burn duration. However, additional work is required in order verify and distinguish the influences from temperature stratification and from turbulence.

ACKNOWLEDGMENTS

CONTACT

Hans Seyfried, Division of Combustion Physics, Lund University, Faculty of Engineering. PO Box 118, S-221 00 Lund, Sweden. E-mail: hans.seyfried@forbrf.lth.se.

REFERENCES

1. Aoyama, T., Hattori, Y., Mizuta, J. and Yasuo, S, "An Experimental Study on Premixed-Charge Compression Ignition Gasoline Engine", SAE 960081.
2. Christensen, M., Hultqvist, A., and Johansson, B., "Demonstrating the Multi-Fuel Capability of a Homogeneous Charge Compression Ignition Engine with Variable Compression Ratio", SAE 1999-01-3679.
3. Christensen, M., Johansson, B. and Hultqvist, A., "The Effect of Combustion Chamber Geometry on HCCI Operation", SAE 2002-01-0425.
4. Christensen, M. and Johansson, B., "The Effect of In-Cylinder flow and Turbulence on HCCI Operation", SAE 2002-01-2864.
5. Kong, S.-C.,Reitz, R.D., Christensen, M. and Johansson, B., "Modeling the Effects of Geometry Generated Turbulence on HCCI Engine Combustion", SAE 2003-01-1088.
6. Schulz, C., Sick, V., "Tracer-LIF diagnostics: quantitative measurement of fuel concentration, temperature and fuel/air ratio in practical combustion systems", *Progress in Energy and Combustion Science*, 2004.
7. Thurber, M. C., Grisch, F., Hanson, R. K., "Temperature imaging with single- and dual-wavelength acetone planar laser-induced fluorescence", *Optics Letters*, Vol. 22, No. 4, 1997.
8. Thurber, M. C., Grisch, F., Kirby, B. J., Votsmeier, M., Hanson, R. K., "Measurements and modeling of acetone laser-induced fluorescence with implications for temperature-imaging diagnostics", *Applied Optics*, Vol. 37, No. 21, 1998.
9. Thurber, M. C., M., Hanson, R. K., "Pressure and composition dependence of acetone laser-induced

fluorescence with excitation at 248, 266, and 308 nm", *Applied Physics B*, Vol. 69, 1999.

10. Grossman, F., Minkhouse, P. B., Ridder, M., Sick, V., Wolfrum, J., "Temperature and pressure dependence of the laser induced fluorescence of gas-phase acetone and 3-pentanone", *Applied Physics B*, Vol. 62, 1996.

11. Grossmann, F., Monkhouse, P. B., Riddler, M., Thurber, M. C., Grisch, F., Kirby, B. J., Votsmeier, M., Hanson, R. K., "Measurements and modeling of acetone laser-induced fluorescence with implications for temperature-imaging diagnostics", *Applied Optics*, Vol. 37, No. 21, 1998, pp 4963-4978.

12. Yip, B., Miller, M. F, Lozano, A., Hanson, R. K, "A combined OH/acetone planar laser-induced fluorescence imaging technique for visualizing combusting flows", *Experiments in Fluids*, Vol. 17,1994,.pp 330-336.

13. Hultqvist, A., Christensen, M., Johansson, B., Nygren, J., Richter, M., Hult, J., Aldén, M., "The HCCI Combustion Process in a Single Cycle- High-Speed Fuel Tracer LIF and Chemiluminescence Imaging", SAE 2002-01-0424, 2002.

14. Hult, J., Richter, M., Nygren, J., Aldén, M., Hultqvist, A., Christensen, M., Johansson, B., "Application of a high speed laser diagnostic system for single-cycle resolved imaging in IC engines", *Applied Optics*, 40:5002, 2002.

15. Vressner, A., Hultqvist, A., Johansson, B., "Study on Turbulence Effects in HCCI Combustion using High-Speed Cycle-Resolved Chemiluminescence Imaging", submitted to the SAE World Congress 2007.

16. Sankaran, R., Im, H. G., Hawkes, E. R., Chen, J. H., "The effects of nonuniform temperature distribution on the ignition of a lean homogenous hydrogen-air mixture", 30th Symposium (International) on Combustion, 2004.

17. Yu, R.X., Bai, X.S., Vressner, A., Hultqvist, A., Johansson, B., Olofsson, J., Seyfried, H., Sjöholm, J., Richter, M., Aldén, M., "Effect of Turbulence on HCCI Combustion", submitted to the SAE World Congress 2007.

ABBREVIATIONS

ABDC: After Bottom Dead Centre

ATDC: After Top Dead Centre

BBDC: Before Bottom Dead Centre

BTDC: Before Top Dead Centre

CR: Compression Ratio

HCCI: Homogeneous Charge Compression Ignition

TDC: Top Dead Centre

PFI: Port Fuel Injection

VII

Development of high temporally and spatially (three-dimensional) resolved formaldehyde measurements in combustion environments

J. Olofsson,[a] M. Richter, and M. Aldén
Division of Combustion Physics, Lund Institute of Technology, Lund 22100, Sweden

M. Augé
Institut Francais du Pétrole (IFP), Ecole Centrale Paris,
Laboratoire d'Energétique Moléculaire et Macroscopique, Combustion (EM2C), Paris, France

In the present article a multi-YAG laser cluster and a framing camera have been applied for ultrahigh framing rate and three-dimensional measurements of formaldehyde distribution in flames and engines. The measurement technique utilizes a laser/detection system which has been adopted for the generation of eight laser pulses at 355 nm. By combining these lasers with a framing camera, short movies showing the formaldehyde distributions in combustion phenomena can be recorded, by means of planar laser-induced fluorescence. The technique is successfully demonstrated in a laboratory flame as well as in an engine. In addition to the temporally resolved experiments also three-dimensional measurements are performed by sweeping the eight generated laser sheets across the flame by the use of a fast scanning mirror. By proper triggering of the laser sweep and the detector a three-dimensional image showing the formaldehyde distribution in the flame can be created, which is also demonstrated. © *2006 American Institute of Physics.*
[DOI: 10.1063/1.2165569]

I. INTRODUCTION

Laser diagnostic techniques may constitute the tool that during the last decade has made the most impact for a deepened understanding of combustion and flow processes. This statement is based on outstanding features of these techniques such as nonintrusiveness in combination with high temporal and spatial resolutions. These techniques are reviewed from a more fundamental aspect as well as with numerous applications, e.g., in Refs. 1–4. Maybe the most important development in the area of laser diagnostics in combustion processes is the use of two-dimensional visualization of fluorescence emission, planar laser-induced fluorescence (PLIF), which has found widespread applications also in various industrial devices, for example, reciprocating engines and gas turbines, see, e.g., Refs. 5–8. Until the late 1990s the PLIF technique has more or less been limited to single-shot registrations with a repetition rate of up to about 10–30 Hz, which is clearly not adequate for real-time analyses of turbulent combustion phenomena. Such studies require special techniques and dedicated hardware.

In the late 1990s a laser/detector system which consists of a cluster of four double pulse Nd:yttrium aluminum garnet (YAG) lasers in combination with an ultrahigh repetition rate framing camera was developed for recording eight temporally resolved PLIF images with a repetition rate up to the megahertz range.[9] This system has been applied for studies of various combustion phenomena, e.g., ignition and flame development,[10] internal combustion (IC) enginestudies,[11] and

three-dimensional visualization.[12] All of these experiments have been performed by using the second or fourth harmonic of the Nd:YAG lasers at 532 and 266 nm, respectively, either for excitation of a tracer added to the fuel (3-pentanone or acetone) or for pumping a dye laser with the second harmonic which by frequency doubling could be used for excitation of the OH radical at 282 nm.

In the present article we demonstrate how the YAG laser cluster as described above has been redesigned to enable the generation of laser pulses at 355 nm rather than the original 532 and 266 nm. After the laser and beam combining system was rebuilt its performance was demonstrated by successful temporally resolved measurements of formaldehyde in flames and in an engine. Formaldehyde is a crucial species in the low-temperature region of combustion and a key species in autoignition and knock phenomena. Recently its presence in homogeneous charge compression ignition (HCCI) engines has also been demonstrated.[13,14] In addition to the temporally resolved formaldehyde measurements, the article also demonstrates the possibility for three-dimensional visualization of this species in a flame.

II. EXPERIMENT

To obtain a laser source emitting laser pulses at 355 nm with a sufficiently high repetition rate required to perform time-resolved two-dimensional (2D) experiments on turbulent combustion phenomena, the multi-YAG laser cluster (BMI) at the Lund Institute of Technology was redesigned. Originally set up as a laser source for 532 and 266 nm radiation, the cluster consists of four individual flash-lamp pumped, *Q*-switched Nd:YAG lasers mounted on a common

---

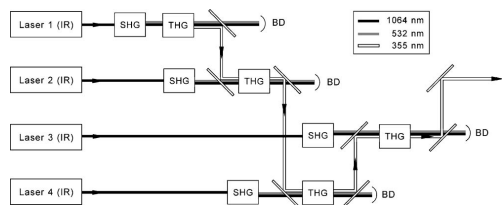[a]Author to whom correspondence should be addressed; electronic mail: jimmy.olofsson@forbrf.1th.se

FIG. 1. Layout of the laser frequency tripling and beam combining systems. SHG, THG; second- and third-harmonic generator, respectively. BD; beam dump.

baseplate. For a detailed description of the originally de-signed laser cluster the reader is referred to Refs. 9–11. Each of the Nd:YAG lasers produces pulses with a repetition rate of 10 Hz at the fundamental wavelength of 1064 nm with a pulse energy of ~1 J and a pulse duration of 7 ns. For gen-erating laser radiation at 355 nm and for combining the four beams into a common optical output, a beam combining scheme was designed, shown in Fig. 1. The IR beam from laser 1 is frequency doubled to 532 nm in a second-harmonic generating (SHG) crystal. Radiation at 355 nm is then pro-duced by the mixing of the second-harmonic beam with the remaining part of the fundamental IR beam in a third-harmonic generating (THG) crystal. In order to spectrally isolate the 355 nm beam a dichroic mirror reflecting the 355 nm beam and transmitting the IR and green beams is used. The spectrally isolated third-harmonic beam from laser 1 is then combined with the fundamental and second-harmonic beams from laser 2. This is achieved by using a second di-chroic mirror reflecting 355 nm and transmitting the other wavelengths. After beam combination, the three beams pass through the THG of laser 2. The third-harmonic beam passes unaffected, whereas the fundamental and second-harmonic beams are mixed to produce a second beam at 355 nm. This is repeated for all the lasers until all the beams are frequency tripled and aligned onto each other creating a single output beam.

The lasers can be fired in a series, in which the time delay between the consecutive lasers can be individually set from 0 up to 100 ms. This results in a rapid burst of four pulses at the laser output. However, the lasers can also be run in double pulse operation, which is achieved by opening the Q-switch twice during one flash-lamp discharge. In this man-ner a laser pulse burst with a maximum of eight pulses is obtained. The time separation between the two double pulses from one laser can be set to values from 25 to 145 μs. The upper limit is given by the length of the flash discharge and the lower limit is governed by the gain buildup time in the cavity. However, by interleaving the double pulses from the four lasers the time separation between the pulses can be reduced to 6.25 μs(=25/4 μs).

In the present study the ability to apply the system for two- and three-dimensional visualizations of formaldehyde in different combustion environments was investigated. The laser pulses exiting at the common output of the Nd:YAG cluster are reflected by a dichroic mirror of the same type as those used in the beam combining scheme described above.
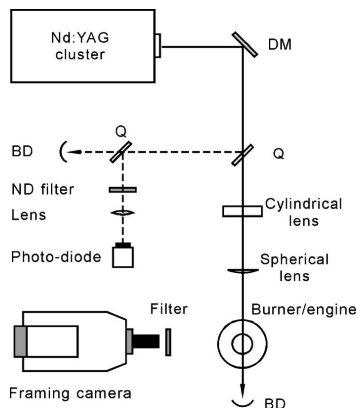

FIG. 2. Experimental setup used for high repetition rate formaldehyde mea-surements. Q; quartz plate. DM; dichroic mirror.

Thus, most of the residual IR and green beams are transmit-ted and led to a beam dump enhancing the spectral isolation of the 355 nm beam.

A general experimental setup for the experiments carried out is shown in Fig. 2. A small fraction of the beam is linked off from the beam path by a reflection from a quartz plate (Q), and the intensity of the reflection is further reduced by a neutral density filter and then focused on an UV sensitive photodiode. With the photodiode connected to an oscillo-scope this allows for on-line monitoring of the individual laser-pulse intensity, and additionally it provides a full over-view of the time separation between the pulses.

Most of the beam is, however, transmitted through the quartz plate and directed through two lenses shaping the cir-cular beam into a narrow sheet with dimensions suitable for the specific combustion phenomenon to be studied. The laser sheet is focused in the center of the combusting volume to be studied. The fluorescence from the exited formaldehyde mol-ecules within the laser sheet is imaged on a detector posi-tioned perpendicularly to the sheet. For detection a high-speed framing camera is used. The camera employs a single optical input, in front of which a quartz $f=100$ mm camera lens, Bernard-Halle, was placed to collect the light. Behind the optical input, an eight-facet pyramid beam splitter redi-rects the light onto eight individual intensified charge-coupled device (ICCD) units. Each of these units consists of a CCD image sensor and a microchannel plate (MCP), func-tioning as an image intensifier as well as an electronic shut-ter. To enable exposure of the eight CCD image sensors in a rapid succession, the MCPs are synchronized with the laser pulses. The time between two consecutive images in an im-age sequence can be as short as 10 ns.

Optionally, an extra image intensifier can be inserted be-hind the camera lens, and this has two major advantages. It increases the sensitivity of the detector system and it also makes the system UV sensitive by converting the UV radia-tion into visible light, detectable by the rest of the system. With this option the minimum time between two consecutive images is increased to about 1 μs.

The laser/detector system can be triggered in different ways, which makes the system versatile and useful in several types of applications. The laser can be internally triggered, operating at 10 Hz repetition rate. This type of triggering is used, e.g., in continuous combustion phenomena such as a flame from a burner nozzle. Another possibility is to trigger the system on an external event. One example of such an event is a specific crank angle in an engine operation cycle which is to be studied. In both cases, following the trigger pulse, the lasers are fired individually with a preset time separation, and the MCPs in the framing camera are triggered individually by the lasers. Although the laser/detector system is designed for up to eight full size images, only seven images were recorded in the reported experiments due to one malfunctioning CCD unit.

III. MEASUREMENTS

A. Preparatory flame measurements

The objective of this part of the work was to determine the feasibility of time-resolved PLIF experiment with the multi-YAG laser operating at 355 nm to detect formaldehyde and to spectrally assure the choice of proper spectral filters for the 2D measurements. Although, the band excited at 355 nm (band A-X 4_1^0) shows a weak absorption coefficient,[15] it is still an attractive choice of excitation wavelength since it is easily obtained at high-energy levels by a frequency tripled Nd:YAG laser. It could be argued whether it would be a better choice to pump a dye laser to reach a wavelength on the absorption peak in order to obtain stronger fluorescence. This technique would probably work well in a single-shot experiment, but with the high repetition rate required in the present study, other problems are likely to occur. For example, if the dye solution in the cuvette is not completely exchanged between two consecutive pulses, the pulse energy in the consecutive pulses would be significantly decreased. Also the quality of the beam intensity profile would deteriorate as the pulse separation is deceased.[11]

The experiments were carried out using a stable, water-cooled conical burner equipped with a 10 mm diameter nozzle, which was supplied with air and dimethylether (DME) as fuel. The gases were supplied to an inlet at the base of the burner and the flow was regulated by two flow meters. DME $[(CH_3)_2O]$ was used as fuel primarily due to the high concentrations of formaldehyde it produces, as reported by Konno *et al.*.[16]

The four lasers of the multi-YAG cluster described in Sec. II were operated in both single- and double-pulse modes. The examples presented were captured in single pulse mode where the system typically produced an output energy of 70 mJ/pulse at 355 nm. Each pulse had a duration of 7 ns and the time separation between consecutive pulses was set to 100 μs. Since only four pulses interact with the flame, four CCD detectors of the framing camera, equipped with a UV lens (f=100 mm, $f/2$, Bernard-Halle), were synchronized to the laser pulses. The gate width of each MCP was 50 ns.

The fluorescence signal, occurring between 350 and 550 nm in the electronic transition $X\ ^1A_1$-$A\ ^1A_2$, was captured ei-

FIG. 3. (Color online) Time-resolved images of PLIF of formaldehyde in a laminar premixed flame.

ther with a CCD coupled to a spectrometer or directly by a CCD through a set of filters which were selected to correspond to this spectral region and to eliminate laser reflections. A band-pass filter centered at 360 nm, BG3, [full width at half maximum (FWHM)=170 nm, transmittance 85%] was used to eliminate reflections from residual 532 nm laser emission, and a long-pass filter, GG385, was used to eliminate the 355 nm laser reflections.

Four such time-resolved images are shown in Fig. 3. In these images a thin region that corresponds to the inner cone of the flame can be observed but nothing inside or outside this zone. This region corresponds to the reaction zone where intermediate species such as formaldehyde are formed.[17] Since the flame is laminar and the time separation between images is short, no changes in time and space can be observed. Still this experiment proves that high-speed PLIF experiments on formaldehyde using the multi-YAG laser operating at 355 nm is feasible and can provide data with decent signal-to-noise ratio. The next step was thus to try to implement the technique to an optical engine as described below.

B. Engine experiments

For the purpose of developing and trying out measurement techniques, a small four-stroke spark ignition (SI) engine was modified to provide optical access to the combustion chamber. The single-cylinder engine with a side-valve layout was originally designed for mobile electric power generation. The side-valve design made it convenient to replace the standard flat cylinder head with a window-equipped substitute. Since it is a production-type engine, except for the optical cylinder head, lubricant oil can get past the piston rings and enter the combustion chamber. In view of the optical properties, this results in quite a harsh environment for performing laser diagnostics. A positive aspect of this would be that if a technique proves to work in this particular test engine it could be expected to perform even better in a state of the art, oil free (dry cylinder liner), optical engine.

The previously described laser and detector system was used to perform high-speed PLIF imaging of formaldehyde in this engine. The capability of firing up to eight laser pulses in a rapid sequence was utilized to perform true cycle-resolved measurements. The standard technique for generating cycle-resolved measurements of species distributions is to make one recording from each engine cycle at subsequent crank angles. In order to cover a large crank angle range, the data recorded from different cycles are then combined. However, because of the cycle-to-cycle variations found in combustion engines, this strategy has an averaging effect on the results. In the ideal case, all the measurement data should be recorded from a single cycle.[23] For the case of formaldehyde, this has previously not been feasible, due to the lack of high-
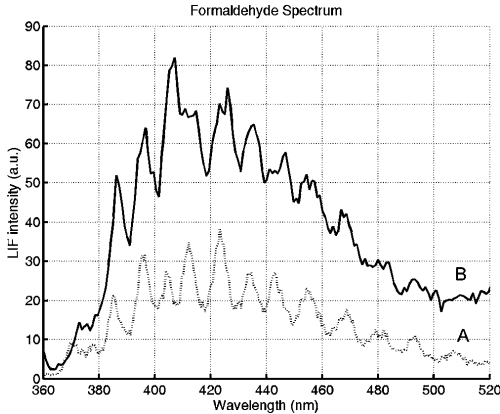
FIG. 4. Laser-induced spectra from formaldehyde in a flame, A, and in an engine, B.

FIG. 6. Optical layout for three-dimensional imaging of formaldehyde.

ratio (~10), indicating a high potential for high-speed measurements also in full size optical engines.

C. Three-dimensional visualization

Two-dimensional visualization of species in combustion environments provides very important information about the combustion process studied, and by extending the technique by high repetition rate imaging, the time evolution of turbulent combustion phenomena can also be studied. However, in some applications the two-dimensional information is not sufficient to reveal all the desired information. For example, in planar laser-induced fluorescence small flame islands can be seen, which appear to have no physical connection to the main flame zone. However, it cannot be concluded whether these flame islands are, in fact, isolated or if they are just an effect of the three-dimensional main flame bending in and out of the laser sheet. This information can only be revealed by measurements covering all three spatial dimensions.

Three-dimensional (3D) laser-induced fluorescence measurements can be performed by recording a stack of closely spaced PLIF images. By using a rapidly scanning mirror the laser sheet can be swept though the measurement volume and the fluorescence from each plane can be recorded by a CCD detector. Here it is of great importance that the fluorescence from all planes is recorded faster than the characteristic time scale of the process studied. This approach has previously been used for 3D visualization, see, e.g., Refs. 19–21.

In this section it is presented how the high repetition rate of the multi-YAG laser/framing camera system has been used to capture 3D LIF images of formaldehyde distribution in a flame. The experimental setup is illustrated in Fig. 6. The multi-YAG system was used with the lasers working in double pulse mode resulting in a burst of eight laser pulses. The time separation between the pulses was set to about 13 μs. To sweep the laser beams a scanning galvanometric mirror (GSI Lumonics) was used, with the scanning frequency set to 40 Hz and the sweep amplitude adjusted to obtain a suitable sheet spacing. The mirror directed the beams through a cylindrical lens ($f = -100$ mm) and a spherical lens ($f = +1000$ mm). In order to obtain parallel laser sheets the scanning mirror was placed in the focal plane of the spherical lens. This created a laser sheet with the height of ~45 mm and a sheet spacing of 1.1 mm. The focus of the laser sheets was positioned right above the center of the

speed tunable laser sources. In these tests, optical grade methanol was used as fuel and the engine was run at medium load. A crank angle encoder served as triggering source for the laser/detector system. Prior to the high-speed imaging experiments, spectroscopic measurements were made in the engine. The aim of this experiment was to assure that the fluorescence emission from the engine originates from formaldehyde, which was done by comparing the engine spectrum to known flame emission spectra showing the formaldehyde features.[18] For this purpose, the framing camera in the setup of Fig. 2 was replaced by a grating spectrometer coupled to an ICCD camera. A quartz lens was mounted in front of the filter in order to collect the fluorescence and focus it onto the spectrometer slit. As shown in Fig. 4, the formaldehyde emission spectrum from the flame, line A, does very well resemble the spectrum from the engine shown by line B.

The experimental setup for the high-speed imaging is quite similar to the one presented in Fig. 2. The results are shown in Fig. 5. The first image was recorded at top dead center (TDC) and the following images were recorded with a delay of 80 μs (corresponding to 1.15 CA at 2400 rpm) between the recordings. The PLIF images in Fig. 5 were recorded by using ~25 mJ in each of the eight laser pulses. Although, these engine tests were not performed in an oil-free environment, the results revealed a good signal-to-noise
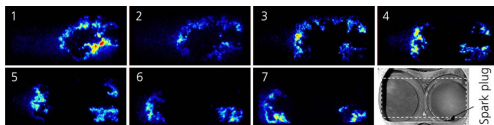

FIG. 5. (Color online) Formaldehyde can be seen in front of the propagating flame front. The time separation between the images is 80 μs and the engine is running at around 2400 rpm. Note that this image series is collected within a single engine cycle. The dotted line in the photograph in the lower rightmost part of the figure marks the imaged area.
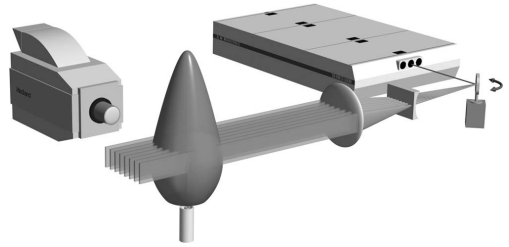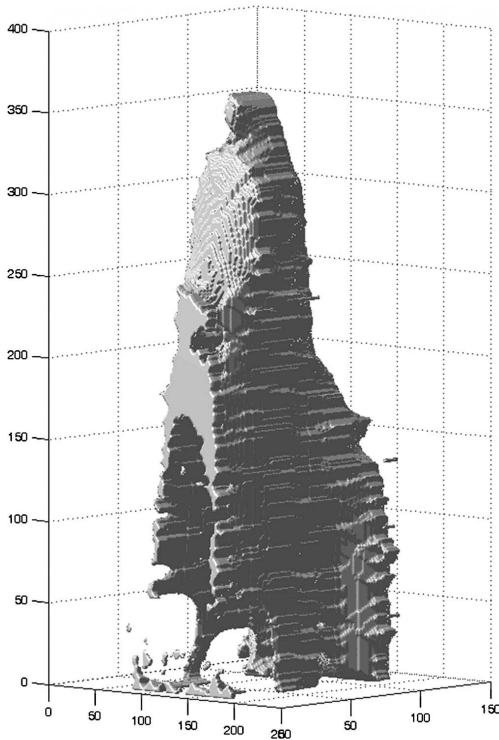
FIG. 7. Three-dimensional visualization of formaldehyde in a flame.

nozzle of the burner. The flame studied was the premixed DME/air flame described in Sec. III A.

The formaldehyde fluorescence was detected by the framing camera on which a Nikon $f=50$ mm lens was mounted and the same optical filters as described above were used. The signal from a function generator was used in order to synchronize the laser/detector system with the scanning mirror by creating a trigger signal of 10 Hz phase locked to the signal which governs the scanning of the mirror. In this manner it was ensured that the laser was firing at the same position in the mirror sweep every time. The camera was synchronized with the laser in the same manner as described in Sec. II.

Prior to assembling the stack of 2D images into a 3D surface, each 2D image was converted from an 8 bit image to a binary image by means of signal thresholding, separating fluorescence areas from the background. A 3D surface of the formaldehyde distribution in the flame was finally created with the use of the multiple binary 2D images. This was achieved by shape-based interpolation between the laser planes.[22] In Fig. 7 the 3D surface of the formaldehyde distribution is shown as recorded by a single sweep of the multi-YAG laser beams.

IV. DISCUSSION

We have in the present article described the redesign of a laser system, consisting of a Nd:YAG laser cluster producing a burst of laser pulses at 355 nm, which together with a framing camera, has been used for ultrafast visualization of formaldehyde in a laboratory flame and in an engine. The laser/detector system has also been used for three-dimensional visualization of formaldehyde. By sending the laser pulses to a rapidly scanning mirror and by proper triggering of the framing camera, the spatially resolved 2D images of formaldehyde could be put together forming a 3D image of the species distribution in the flame.

The possibilities for temporally resolved and 3D visualization of formaldehyde may be an important tool in future combustion applications, e.g., studies of autoignition and knock phenomena as well as experiments in HCCI engines. The plans for the near future include moving this high-speed imaging system into an engine research laboratory to measure formaldehyde in an HCCI engine.[24] From previous experiments it is known that the HCCI combustion possesses a heterogeneous structure both during the cool-flame and the main combustion. The spatial distribution of formaldehyde in the early cool-flame phase can reveal information on how stratified the charge is. Following the evolution of the ignition event in time is of major interest. As is known, the combustion rate in HCCI engines is very high. In addition, the spatial pattern of the combustion varies from cycle to cycle. Thus, it would not be sufficient for this upcoming study to use conventional techniques, in which one image per cycle is recorded.

The development of a laser cluster producing 355 nm laser beams is also important, not only because of the possibilities for formaldehyde detection, it may also open the possibilities for temporally and spatially resolved detection of species whose absorption bands require pumping of a tunable dye laser at 355 nm. This is the case for CH, absorbing at 430 nm, C_2, absorbing at 516 nm, and NO, absorbing at 226 nm (frequency doubling of 452 nm). All these species may now be investigated by high-speed 2D or 3D visualization. In addition to these species there are also several species requiring a two-photon excitation process in the near vacuum ultraviolet (vuv) spectral region, e.g., CO, O, H, and H_2O, which might be possible to detect temporally resolved formaldehyde by pumping a dye laser in the blue-green spectral region by 355 nm followed by frequency doubling to the near vuv spectral region.

[1] A. C. Eckbreth, *Laser Diagnostics for Combustion Temperature and Species*, 2nd ed. (Gordon and Breach, London, UK, 1996).

[2] *Applied Combustion Diagnostics*, edited by K. Kohse-Höinghaus and J. B. Jeffries (Taylor & Francis, New York, 2002).

[3] J. Wolfrum, *Twenty-Seventh Symposium (International) on Combustion* (The Combustion Institute, Pittsburgh, 1998), pp. 1–41.

[4] K. Kohse-Höinghaus, Prog. Energy Combust. Sci. **20**, 203 (1994).

[5] S. Einecke, C. Schulz, and V. Sick, Appl. Phys. B: Lasers Opt. **B71**, 717 (2000).

[6] B. Baeuerle, J. Warnatzand, and F. Behrendt, *Proceedings of the 26th International Symposium on Combustion* (The Combustion Institute, Pittsburgh, 1996), p. 2619.

[7] U. E. Meier, D. Wolff-Gassmann, and W. Stricker, Aerosp. Sci. Technol.

4, 403 (2000).

[8] F. Dinkelacker, A. Soika, D. Most, D. Hofmann, A. Leipertz, and W. Polifke, *Proceeding of the 27th International Symposium on Combustion* (The Combustion Institute, Pittsburgh, 1998), pp. 857–865.

[9] C. F. Kaminski, J. Hult, and M. Aldén, Appl. Phys. B: Lasers Opt. **B68**, 757 (1999).

[10] C. F. Kaminski, J. Hult, M. Aldén, S. Lindenmaier, A. Dreizler, U. Maas, and M. Baum, *Proceedings of the 28th International Symposium on Combustion* (The Combustion Institute, Pittsburgh, 2000), pp. 399–405.

[11] J. Hult, M. Richter, J. Nygren, M. Aldén, A. Hultqvist, M. Christensen, and B. Johansson, Appl. Opt. **41**, 5002–5014 (2002).

[12] J. Hult, A. Omrane, J. Nygren, C. F. Kamiski, B. Axelsson, R. Collin, P. E. Bengtsson, and M. Aldén, Exp. Fluids **33**, 265 (2000).

[13] N. Graf, J. Gronki, C. Schulz, T. Baritaud, J. Cherel, P. Puret, and J. Lavy, SAE Technical Report No. 2001-01-1924, 2001.

[14] R. Collin, J. Nygren, M. Richter, M. Aldén, L. Hildingsson, and B. Johansson, SAE Technical Report No. 2003-01-3218, 2003.

[15] J. E. Harrington, and K. C. Smyth, Chem. Phys. Lett. **202**, 196 (1993).

[16] M. Konno, S. Kajitani, Z. Chen, K. Yoneda, H. Matsui, and S. Goto, SAE Technical Report No. 2001-01-3504, 2001.

[17] A. Burkert, D. Grebner, D. Mäller, W. Triebel, and J. König, *Proceeding of the 28th International Symposium on Combustion* (The Combustion Institute, Pittsburgh, 2000), pp. 1655–1661.

[18] R. J. H. Klein-Douvel, J. Luque, J. B. Jeffries, G. P. Smith, and D. R. Crosley, Appl. Opt. **39**, 3712 (2000).

[19] G. Kychakoff, P. H. Paul, I. V. Cruyningen, and R. K. Hanson, Appl. Opt. **26**, 2498 (1987).

[20] B. Yip, R. L. Schmitt, and M. L. Long, Opt. Lett. **13**, 96 (1988).

[21] J. Nygren, J. Hult, M. Richter, M. Aldén, M. Christensen, A. Hultqvist, and B. Johansson, *Proceeding of the 29th International Symposium on Combustion* (The Combustion Institute, Pittsburgh, 2002), pp. 679–685.

[22] J. Andersson, M.S. thesis, Lund Institute of Technology, 2000.

[23] A. Hultqvist, M. Christensen, B. Johansson, M. Richter, J. Nygren, J. Hult, and M. Aldén, SAE Technical Report No. 2002-01-0424, 2002.

[24] R. Collin, J. Nygren, M. Richter, M. Aldén, L. Hildingsson, and B. Johansson, *Proceedings of the Sixth International Symposium on Diagnostics and Modeling of Combustion in Internal Combustion Engines*, Yokohama, Japan, 2004, pp. 319–325.

VIII

High-Speed LIF Imaging for Cycle-Resolved Formaldehyde Visualization in HCCI Combustion

J. Olofsson, H. Seyfried, M. Richter and M. Aldén
Division of Combustion Physics, Lund Institute of Technology

A. Vressner, A. Hultqvist and B. Johansson
Division of Combustion Engines, Lund Institute of Technology

K. Lombaert
Laboratoire de Mécanique Physique, Université Pierre et Marie Curie,
CNRS-UMR 7068, 2, Place de la Gare de Ceinture
78210 Saint Cyr l'Ecole, France

Lund Institute of Technology
PO Box 118
S-221 00 LUND
Sweden

ABSTRACT

High-speed laser diagnostics was utilized for single-cycle resolved studies of the formaldehyde distribution in the combustion chamber of an HCCI engine. A multi-YAG laser system consisting of four individual Q-switched, flash lamp-pumped Nd:YAG lasers has previously been developed in order to obtain laser pulses at 355 nm suitable for performing LIF measurements of the formaldehyde molecule. Bursts of up to eight pulses with very short time separation can be produced, allowing capturing of LIF image series with high temporal resolution. The system was used together with a high-speed framing camera employing eight intensified CCD modules, with a frame-rate matching the laser pulse repetition rate. The diagnostic system was used to study the combustion in a truck-size HCCI engine, running at 1200 rpm using n-heptane as fuel. By using laser pulses with time separations as short as 70 μs, cycle-resolved image sequences of the formaldehyde distribution were obtained. Thus, with this technique it is possible to follow the formaldehyde formation and consumption processes within a single cycle. The combustion evolution was studied in terms of the rate and spatial structure of formaldehyde formation and consumption for different engine operating conditions, e.g. different stoichiometries. Also, the impact on the rate of heat-release was investigated.

INTRODUCTION

Homogeneous Charge Compression Ignition (HCCI) is a hybrid between the well-known Spark Ignition (SI) and Compression Ignition (CI) engine concepts. As in an SI engine fuel and air are premixed in the inlet system into a more or less homogeneous charge. During the compression stroke the pressure and temperature of the mixture increases and reaches the point of auto ignition at several locations simultaneously [1]; i.e. the mixture burns without the help of any ignition system, just as in a CI engine. Since ignition occurs at multiple points, the integrated combustion rate becomes very high. Therefore, highly diluted mixtures or Exhaust Gas Recirculation (EGR) have to be used in order to limit the rate of combustion [2]. Without sufficient mixture dilution, problems associated with extremely rapid combustion and knocking-like phenomena will occur, as well as excessive NO_X production. On the other hand, an overly lean mixture will result in incomplete combustion or even misfire. The big challenge with this combustion concept is auto ignition timing control since this is only depending on the pressure and temperature conditions. Combustion control can be done by adjusting operational parameters as inlet air temperature, fuel amount and EGR rate [3, 4]. The major advantages of HCCI compared to the diesel engine are low NO_X emissions and, depending on the fuel, virtually no soot [5]. The benefit of HCCI compared to the Spark Ignition (SI) engine is the much higher part load efficiency since the HCCI engine is running unthrottled [6]. The toughest

challenge is controlling the ignition timing over a wide load and speed range [7, 8]. Another challenge is to obtain an acceptable power density. The power density is limited by combustion noise and high peak pressures. At low loads, the rather high emissions of unburned hydrocarbons (HC) and carbon monoxide (CO), in combination with low exhaust temperatures, present an additional challenge [9]. By applying unthrottled HCCI combustion at part load in SI engines, efficiency can be improved by 40-100%. Emerging technologies for variable valve timing, with the intent of using these as means of controlling the combustion timing in HCCI engines [10], may well lead the way for the first application of the HCCI combustion mode in practice.

Formaldehyde is usually formed as an intermediate species when combusting hydrocarbons. The formation occurs through low-temperature oxidation in an early phase of the ignition process. The generated formaldehyde is then being consumed in the following combustion process. Formaldehyde is also associated with the low-temperature reactions that occur when certain mixtures of hydrocarbon fuels and air are close to the explosion limit. Hence, the low-temperature reactions (cool flames) and the early phase of the main heat release in an HCCI engine can be investigated by probing the formation and consumption of formaldehyde. Conventional planar laser induced fluorescence from formaldehyde, i.e., with one image captured per engine cycle, has been used earlier in investigations of the Controlled Auto Ignition (CAI) combustion concept [11] and for characterization of HCCI combustion [12, 13, 14]. In the latter publication it was reported how the concentration of formaldehyde increased as the Low Temperature Reactions (LTR) progressed. In the same study, the spatial formation and consumption of formaldehyde appeared to be highly heterogeneous. In terms of cycle-to-cycle stability it could be concluded that the formation during the LTR was quite stable whereas the consumption during the main heat release showed substantially more fluctuations. This means that although the cycle-to-cycle variations in terms of in-cylinder pressure are known to be reasonably small, the spatial variations of the combustion from one cycle to another can be quite significant. The heat release when running HCCI is also known to be very rapid. This combination of fast consumption and fluctuating combustion phasing introduces an averaging effect when performing conventional LIF measurements where one image is recorded per cycle. In order to really capture the details of such processes it is necessary to follow a single cycle event.

In this work the early phase of ignition and main combustion in an HCCI engine were investigated with high-speed laser-induced fluorescence, LIF, of formaldehyde. For this purpose a tailor made YAG-laser cluster combined with a high speed framing camera were used. This approach was used to generate unique single-cycle resolved measurements.

EXPERIMENTAL

ENGINE SETUP

The engine used for the work presented was an inline six-cylinder, 2.0 liter/cylinder *Scania* D12 diesel engine, converted to single cylinder HCCI operation.

Type:	Four-valve diesel engine
Displaced volume:	1966 cc
Bore:	127.5 mm
Stroke:	154 mm
Compression ratio:	11.2:1
Exhaust valve open:	34° BBDC @ 0.15 mm lift
Exhaust valve close:	6° BTDC @ 0.15 mm lift
Inlet valve open:	2° BTDC @ 0.15 mm lift
Inlet valve close:	31° BBDC @ 0.15 mm lift
Valve lift exhaust:	14.1 mm
Valve lift inlet:	14.1 mm
Inlet valve diameter:	44 mm
Exhaust valve diameter:	41 mm

Table 1. Data for the Scania D12 optical engine.

In order to provide for optical access the engine was equipped with an elongated piston and a 30 mm high quartz liner. The engine was also modified to operate with port-fuel injection, which generates a principally homogeneous charge. To have an optically transparent and non-fluorescent fuel, pure n-heptane was used. The compression ratio was set to 11.2:1 and the engine was run with lambda values between 3.2 and 4.5. The engine runs reported in this work were performed with a fixed inlet air temperature of 38° C.

A water cooled Kistler pressure transducer, placed 50 mm from the centre of the bore axis, was used for in-cylinder pressure capture. A photo of the engine can be seen in Figure 1 and a table containing some vital engine specifications of the *Scania* D12 is shown in Table 1.

The inlet air was preheated with an electrical heater to initiate HCCI combustion with the selected compression ratio and fuel type. The experiments on the engine were conducted under the operating conditions shown in Table 2. The rich limit was limited by too rapid combustion and high in-cylinder pressures.
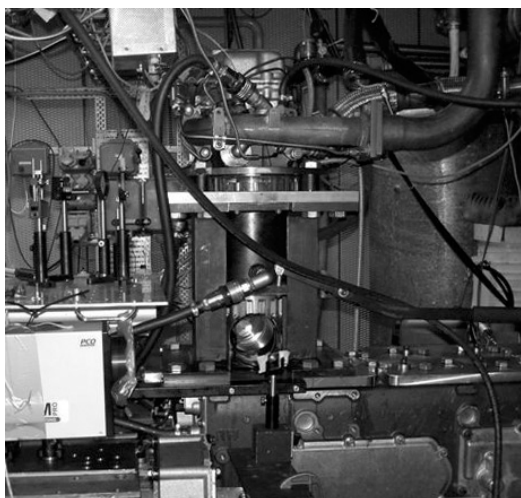
Figure 1. The modified Scania D12, the engine used for all the experiments conducted.

Engine speed:	1200 rpm
Lambda:	3.2 – 4.5
Inlet air temperature:	38° C
Inlet air pressure:	1 bar absolute
Fuel:	N-Heptane

Table 2. Operational parameters.

OPTICAL SETUP

The formaldehyde LIF measurements were performed by exciting the formaldehyde molecules in the A-X$^1_0$ band, using the third harmonic (355 nm) from the multi-YAG cluster. The laser cluster consists of four separate laser channels of Nd:YAG type, each operating with a repetition rate of 10 Hz and with a fundamental laser wavelength of 1064 nm. For superimposing the four beam paths and for frequency tripling of the laser radiation to 355 nm, a specially designed beam combining scheme was used, shown in Figure 2. In this scheme the beam from laser 1 was frequency doubled to 532 nm in a second harmonic generating (SHG) crystal, after which the frequency doubled beam together with the remaining part of the fundamental is mixed in a third harmonic generating (THG) crystal to generate laser radiation at 355 nm. The tripled beam is separated from the doubled and fundamental beams by means of a dichroic mirror. The frequency doubled beam

from laser 2 is then combined with the tripled beam from laser 1, by using a second dichroic mirror reflecting in the UV and transmitting in the green and IR. The beams are directed through a second THG where the tripled beam from laser 1 passes unaffected while the fundamental and doubled beams from laser 2 are frequency tripled. This procedure is repeated for all the four lasers, and thus the laser system has a single optical output from which the pulses at 355 nm from the four lasers are emitted. The laser system allows for opening of the Q-switch twice during one flash lamp discharge, extending the number of pulses from four to eight. The eight pulses can be emitted in a rapid succession, and the time separation between two consecutive pulses can be set to values as short as 6.25 μs.
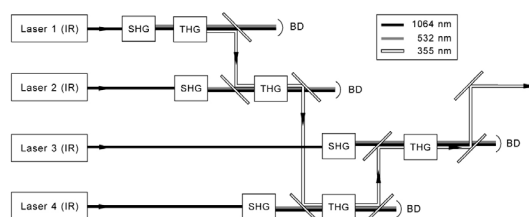

Figure 2. The beam combining scheme for generation of laser radiation at 355 nm with the multi-YAG laser system.

In order to detect the fluorescence generated by the rapid laser pulse burst, a high-speed framing camera was used. The framing camera employs a single optical input in front of which a Bernard-Halle camera lens (f=+100 mm, f#=2) is mounted. An image intensifier is placed at the optical entrance of the camera in order to enhance the sensitivity of the detector. The intensified signal is split up with an eight-facet prism onto eight individual intensified CCD modules. Each module consists of a CCD image sensor (384x576 pixels) and a micro channel plate (MCP). The MCP further intensifies the signal and it also functions as an electronic shutter. To enable exposure of the CCD image sensors in a rapid succession, the MCPs are synchronized with the laser pulse train. In the configuration presented, the detector system can acquire image sequences with an image time separation down to 1 μs.

To gain two-dimensional information of the formaldehyde distribution the laser beam from the multi-YAG laser system was passed through an f=-100 mm cylindrical lens and an f=+500 mm spherical lens to form a narrow, laser sheet. The laser sheet, approximately 40 mm in width, was directed into the HCCI engine through the quartz cylinder liner and focused in the center of the combustion chamber. The fluorescence signal from the formaldehyde was imaged perpendicular to the sheet,
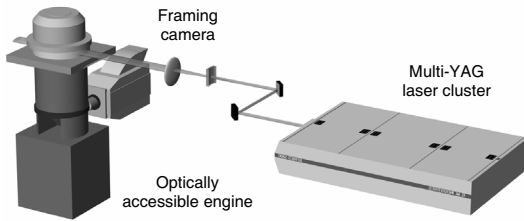
3

Figure 3. Schematic of the experimental setup.

through the quartz piston via a UV enhanced mirror in the piston extension onto the high-speed framing camera. In front of the camera two optical filters were mounted, a long-pass filter, GG385, to eliminate the laser scattering at 355 nm, and a short-pass filter with a cut-off wavelength at 500 nm to avoid interference from the remaining 532 nm laser light. A schematic of the experimental setup for the formaldehyde LIF measurements is shown in Figure 3. In Figure 4 the field-of-view of the camera is shown, and the dashed line corresponds to the area of the laser sheet.

In order to synchronize the engine with the laser/detection system the engine speed was kept constant at 1200 rpm, corresponding to a combustion cycle frequency of 10 Hz. This matches the overall repetition rate of the laser system. A pulse from a crank angle encoder was used to fire the laser system at the desired position.

The multi-YAG laser system was operated in double pulse mode, resulting in an energy of approximately 45 mJ per pulse at 355 nm. The time-separation between two consecutive images was kept constant at 70 μs, corresponding to 0.5 CAD (crank angle degree), throughout the measurements. In order to suppress the background radiation, the camera exposure time was set to 50 ns for each image acquisition. Due to one malfunctioning CCD module in the framing camera, only seven images were acquired in the present study.
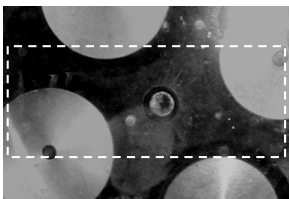
Figure 4. Image of the field-of-view. The dashed box show the LIF detection area, with dimensions 35 mm x 90 mm.

RESULTS

Seven pulse LIF sequences of the formaldehyde distribution within one stroke in the HCCI engine were recorded. The combustion development was studied in terms of the rate of formaldehyde formation and consumption for different load conditions, i.e. by varying the stoichiometry (lambda value). The formaldehyde formation occurs in the early low-temperature reactions (cool flame) of the ignition process, while the consumption is located at the early phase of the main heat release. The imaged region inside the combustion chamber corresponds to an area of 35 mm x 90 mm. To be able to subtract the undesired laser scattering from the formaldehyde LIF measurements, also images without combustion present were acquired. The fluorescence signal was approximately ten times stronger than the background level, providing a satisfactory signal-to-noise ratio. In order to compensate the LIF images for imperfections in the laser intensity profile, these profiles were also recorded [15]. This was done by recording LIF image sequences in a CAD range were the formaldehyde distribution was uniform, thus between the completion of the formaldehyde formation and the beginning of the consumption.

In Figure 5 image sequences of seven images showing the formaldehyde consumption within one cycle event for λ=4.5, λ=4.0, and λ=3.5, are presented. In the images the formaldehyde consumption can be followed within the main combustion process for the different running conditions. Regions where formaldehyde consumption has occurred appear dark, while bright regions indicate the presence of formaldehyde. From the images it is evident that the formaldehyde consumption becomes more rapid as the fuel mixture becomes richer. This is in agreement with traditional heat release analysis which shows an increased rate of heat release for richer mixtures. It can also be seen that the consumption process occurs at an earlier stage for fuel richer mixtures. From earlier experiments it is known that the ignition temperature decreases slightly with lambda. This implies that the combustion phasing becomes more advanced for richer mixtures if the inlet temperature is kept constant. The spatial structure of the formaldehyde distribution during the consumption phase looks quite similar to what was found in an earlier investigation using high-speed fuel tracer LIF [15], indicating that visualization of formaldehyde, under certain circumstances, can be an alternative to fuel tracer LIF. In that paper [15] it was shown how the combustion progressed through distributed reactions throughout the entire bulk volume and this without traditional flame front propagation. Supporting those results, the formaldehyde images also clearly show that the ignition occurs at multiple points simultaneously and as can be seen, also the consumption of formaldehyde is lacking normal flame propagation.
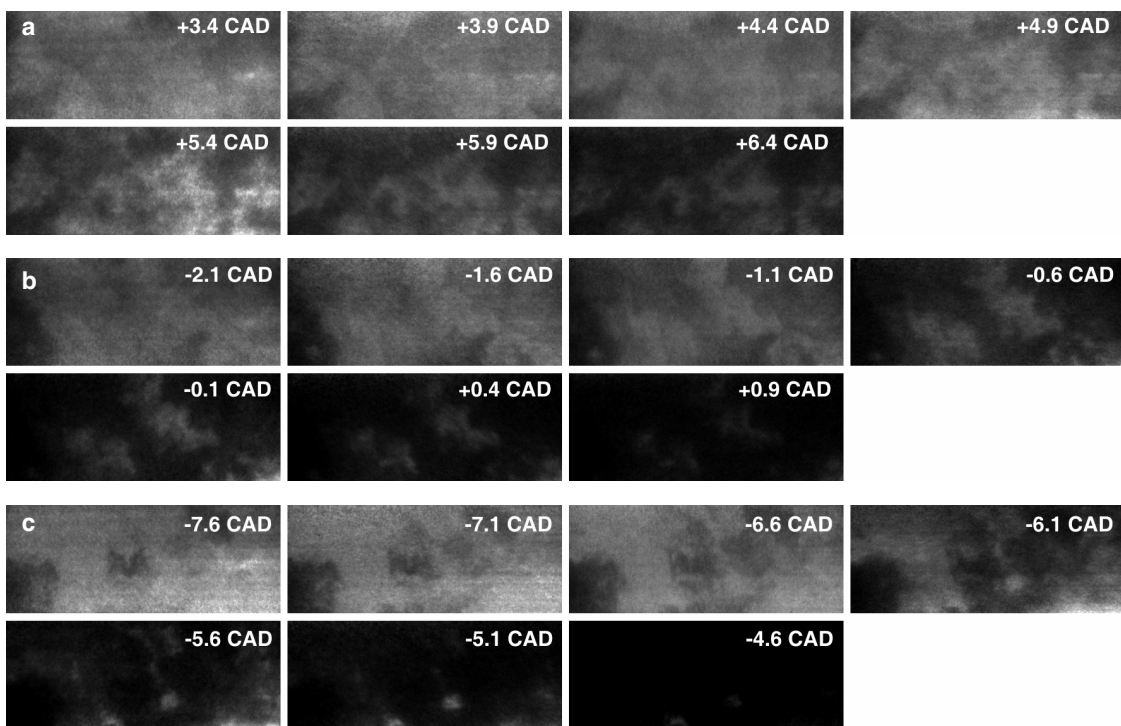
Figure 5. A sequence of seven single-shot PLIF images showing the formaldehyde consumption is depicted for each the three stoichiometries λ=4.5 (a), λ=4.0 (b), and λ=3.5 (c).
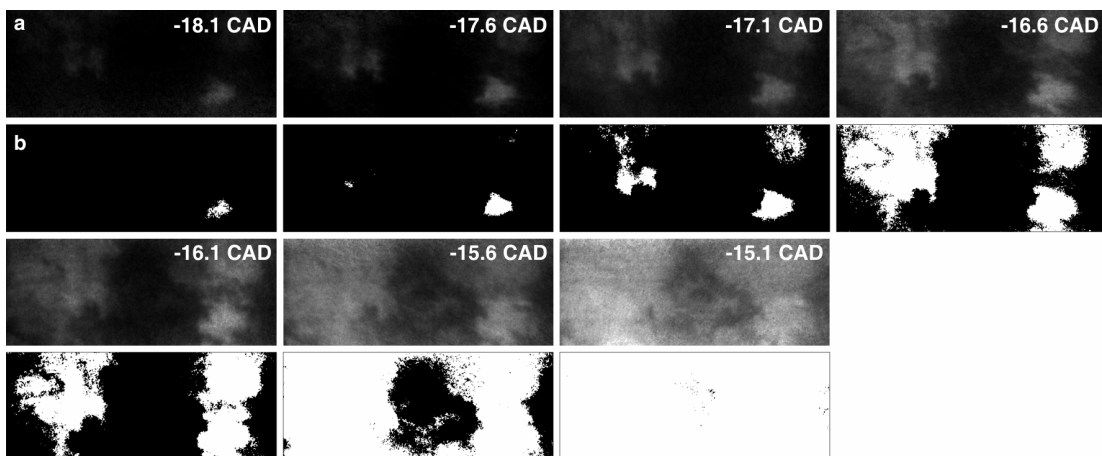

Figure 6. Binary images (b) were accomplished by applying a threshold to the grayscale images (a), marking image areas containing LIF signal as white, and leaving areas lacking signal as black. An example is shown for the formaldehyde formation running the engine at λ= 4.5.

For the purpose of studying the spatial distribution during formaldehyde formation and consumption in the engine, the surface fraction of LIF signal covering the imaged area was determined. To determine the surface fraction binary images, rather than grayscale images, are desired. Binary images were accomplished by applying a threshold to the grayscale images, marking image areas containing LIF signal as white, and leaving areas lacking signal as black. The threshold level was placed just above the noise level of the detector and equally set for all sequences evaluated. In Figure 6 an example is shown for the formaldehyde formation running the engine at $\lambda=4.5$. It should be noted that thresholding does not always provide a perfect representation of the signal areas in the images. However, even in the case of $\lambda=4.5$, which is the leanest mixture used in the present study and thus the formaldehyde LIF signal-to-noise ratio is the lowest, thresholding still gives an acceptable result.

To illustrate the cycle-to-cycle variations, the heat release traces from 25 independent cycles (black curves) and the corresponding mean heat release trace (white curve), are presented in Figure 7. As can be seen, the cycle-to-cycle variations are larger for the main heat release compared to the heat release of the cool flame, confirming the low temperature reactions to be more stable. These variations support the need for single-cycle studies of the formaldehyde formation and consumption processes.
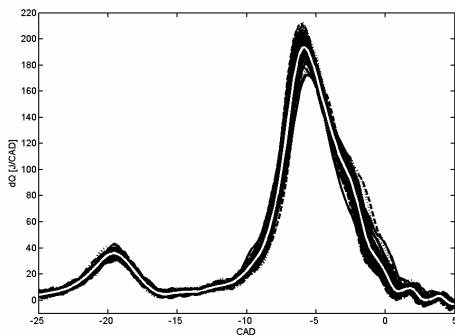

Figure 7. Heat release traces from 25 independent cycles (black curves) and the corresponding mean heat release trace (white curve) for $\lambda=3.5$.

In Figure 8 one can see how the phasing of the combustion changes with lambda. With increased amount of fuel the cool flame combustion phasing advances. Note that the duration for the cool flame seems to be constant for the different stoichiometries studied, thus independent of load. It is expected that the

heat release rate during the cool flame increases, when additional fuel is injected. However, this effect can be seen only as a slight increase of the peak values in Figure 9. In spite of this, the amount of heat released during the cool flame period compared to the heat released during the main combustion is lower with higher load. The heat release for the main combustion advances and the rate of heat release increases with increasing amount of fuel. This can be explained by the faster kinetics following a more fuel-rich mixture. In addition, the greater amount of heat released in each cycle increases the cylinder temperature, thus advancing the combustion.
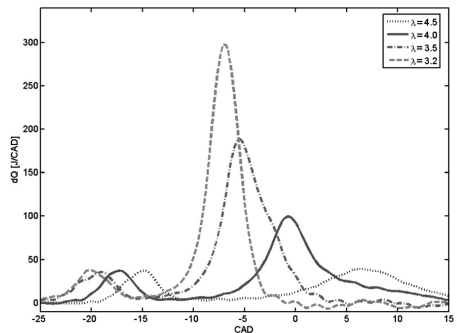

Figure 8. Mean heat release traces for the four different stoichiometries studied.

The binary images were integrated in order to determine the fraction of surface covered by formaldehyde signal. The cycle-resolved surface fraction was plotted together with the corresponding rate of heat release curve for each of the four stoichiometries studied. In Figure 9 this is shown for the formaldehyde formation. Figure 10 shows the cycle-resolved surface fractions and the corresponding heat release curves for the formaldehyde consumption. Cycle-to-cycle variations cause fluctuations in the formation/consumption phasing; hence the complete process is not always covered by the seven laser pulses. However, the variations are sufficiently small to not influence the mutual order of the curves for the stoichiometries studied.

As previously mentioned, the combustion phasing advances as the fuel/air-mixture becomes richer. As can be seen in the upper part of Figure 9, this yields for the formaldehyde formation as well. However, this is not the case for $\lambda=3.2$, since this condition is close to the fuel-rich limit of operation, and therefore instabilities in engine operation induces uncertainties in measurement data. Figure 9 also shows that the rate of formaldehyde formation increases for fuel-leaner stoichimometries. A

probable cause could be that since the cool flame has a later phasing, the cylinder has reached a higher temperature at the start of the low-temperature reactions, resulting in a more rapid formaldehyde formation.
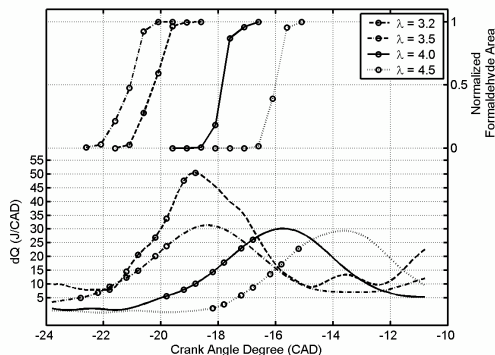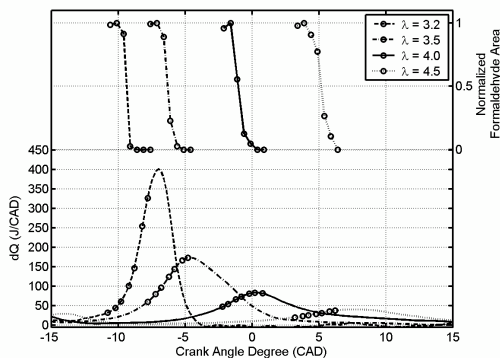

Figure 9. The cycle-resolved surface fraction acquired at formaldehyde formation is shown together with the corresponding rate of heat release curve for each of the four stoichiometries studied.

In Figure 10 it can be seen how the surface fraction with formaldehyde signal shrinks with increasing rate for lower lambda values. Earlier experiments performed with one image captured per engine cycle revealed similar trends. However, by employing high-speed single-cycle resolved measurements the averaging effect introduced by the jittering of the combustion phasing from cycle-to-cycle is avoided.

Figure 10. The cycle-resolved surface fraction acquired at formaldehyde consumption is shown together with the corresponding rate of heat release curve for each of the four stoichiometries studied.

SUMMARY AND CONCLUSION

1. Two-dimensional visualization showing the formation and consumption of formaldehyde was performed in an optical engine, within a single cycle, using a high speed PLIF system.

2. By utilizing high-speed diagnostics, the averaging effect introduced by cycle-to-cycle variations of combustion phasing could be avoided.

3. By resolving a single cycle event it could be verified that the formation and consumption of formaldehyde occurs gradually through distributed reactions. The phasing of these reactions varies for different parts of the combustion chamber, resulting in the heterogeneous structure.

4. The decay of the formaldehyde concentration is clearly more rapid for richer mixtures, whereas the duration in CAD's in which formaldehyde is being formed seems to be less dependent on stoichiometry.

5. The spatial structure of formaldehyde LIF recorded in the consumption phase show properties similar to that of fuel LIF. This strongly indicates that visualization of naturally occurring intermediates such as formaldehyde, under certain circumstances, can be an alternative to fuel tracer LIF. This is especially interesting when running heavier fuel fractions considering that no suitable tracers exist for this purpose.

ACKNOWLEDGMENTS

CONTACT

Corresponding author: Jimmy Olofsson, Division of Combustion Physics, Lund Institute of Technology, PO Box 118, S-221 00, LUND, Sweden, phone: +46 46 2220353, fax: +46 46 2224542, e-mail: jimmy.olofsson@forbrf.lth.se.

REFERENCES

1. A. Hultqvist, M. Christensen, B. Johansson, A. Franke, M. Richter, M. Aldén: "A Study of the Homogeneous Charge Compression Ignition Combustion Process by Chemiluminescence Imaging", SAE1999-01-3680

2. M. Christensen, B. Johansson: "Influence of Mixture Quality on Homogeneous Charge Compression Ignition", SAE9824541

3. T. Aoyama, Y. Hattori, J. Mizuta, Y. Sato: "An Experimental Study on a Premixed-Charge Compression Ignition Gasoline Engine", SAE960081

4. J-O. Olsson, O. Erlandsson, B. Johansson: "Experiments and Simulation of a Six-Cylinder Homogeneous Charge Compression Ignition (HCCI) Engine", SAE2000-01-2867

5. M. Christensen, A. Hultqvist, B. Johansson: "Demonstrating the Multi Fuel Capability of a Homogeneous Charge Compression Ignition Engine with Variable Compression Ratio",SAE1999-01-3679

6. M. Christensen, P. Einewall, B. Johansson: "Homogeneous Charge Compression Ignition (HCCI) Using Iso-octane, Ethanol and Natural Gas-A Comparison to Spark Ignition Operation",SAE972874

7. J-O. Olsson, P. Tunestal, B. Johansson: " Closed-Loop Control of an HCCI Engine", SAE2001-01-1031

8. J-O. Olsson, P. Tunestal, G. Haraldsson, B. Johansson: "A Turbo Charged Dual Fuel HCCI Engine", SAE2001-01-1896

9. O. Erlandsson, B. Johansson, F. A. Silversand: "Hydrocarbon (HC) Reduction of Exhaust Gases from a Homogeneous Charge Compression Ignition (HCCI) Engine Using Different Catalytic Mesh-Coatings", SAE2000-01-1847

10. D. Law, J. Allen, D. Kemp, G. Kirkpatrick, T. Copland: "Controlled Combustion in an IC-Engine with a Fully Variable Valve Train", SAE2001-01-0251

11. N. Graf, J. Gronki, C. Schulz, T. Baritaud, J. Cherel, P. Duret, and J. Lavy: "In-cylinder Combustion Visualization in an Auto-Igniting Engine using Fuel Tracer- and Formaldehyde-LIF Imaging", SAE2001-01-1924.

12. Robert Collin, Jenny Nygren, Mattias Richter, Marcus Aldén, Leif Hildingsson, Bengt Johansson: "Simultaneous OH- and formaldehyde-LIF measurements in an HCCI engine", SAE2003-01-3218

13. Robert Collin, Jenny Nygren, Mattias Richter, Marcus Aldén, Leif Hildingsson, Bengt Johansson: "The Effect of Fuel Volatility on HCCI Using Simultaneous Formaldehyde- and OH-PLIF", SAE2004-01-2948

14. Robert Collin, Jenny Nygren, Mattias Richter, Marcus Aldén, Leif Hildingsson, Bengt Johansson: "Studies of the Combustion Process with Simultaneous Formaldehyde and OH PLIF in a Direct-Injected HCCI Engine", COMODIA Paper ID: 23

15. Anders Hultqvist, Magnus Christensen, Bengt Johansson, Mattias Richter, Jenny Nygren, Johan Hult, Marcus Aldén: "The HCCI Combustion Process in a Single Cycle – High-Speed Fuel Tracer LIF and Chemiluminescence Imaging", SAE2002-01-0424

DEFINITIONS, ACRONYMS, ABBREVIATIONS

CI	Compression Ignition
CO	Carbon monoxide
EGR	Exhaust Gas Recirculation
HC	HydroCarbons (unburned)
HCCI	Homogeneous Charge Compression Ignition
IMEP	Indicated Mean Effective Pressure
NO_X	The sum of nitrogen oxides
SI	Spark Ignition
λ	Relative air-fuel ratio

IX

Optical Diagnostics of Laser-Induced and Spark Plug-Assisted HCCI Combustion

M. Weinrotter, E. Wintner
Photonics Institute, Vienna University of Technology

K. Iskra, T. Neger
Institute of Experimental Physics, Graz University of Technology

J. Olofsson, H. Seyfried, M. Aldén
Division of Combustion Physics, Department of Physics, Lund Institute of Technology

M. Lackner, F. Winter
Institute of Chemical Engineering, Vienna University of Technology

A. Vressner, A. Hultqvist, B. Johansson
Division of Combustion Engines, Department of Heat and Power Engineering

ABSTRACT

HCCI (Homogeneous Charge Compression Ignition), laser-assisted HCCI and spark plug-assisted HCCI combustion was studied experimentally in a modified single cylinder truck-size Scania D12 engine equipped with a quartz liner and quartz piston crown for optical access. The aim of this study was to find out how and to what extent the spark, generated to influence or even trigger the onset of ignition, influences the auto-ignition process or whether primarily normal compression-induced ignition remains prevailing. The beam of a Q-switched Nd:YAG laser (5 ns pulse duration, 25 mJ pulse energy) was focused into the centre of the cylinder to generate a plasma. For comparison, a conventional spark plug located centrally in the cylinder head was alternatively used to obtain sparks at a comparable location. No clear difference in the heat releases during combustion between the three different cases of ignition start could be seen for the fuel of 80/20 iso-octane/n-heptane used. However, with optical diagnostic methods, namely PLIF (Planar Laser-Induced Fluorescence), Schlieren photography and chemiluminescence imaging, differences in the combustion process could be evaluated.

INTRODUCTION

In an HCCI engine air and fuel are premixed and as the piston is reaching TDC (*Top Dead Center*) the mixture auto-ignites at several locations simultaneously [1]. Since ignition occurs at multiple points, the integrated combustion rate becomes very high. Therefore, highly diluted mixtures or EGR (Exhaust Gas Recirculation) have to be used in order to limit the rate of combustion [2]. However, the big challenge with this combustion concept is auto-ignition timing control since this is only depending on pressure and temperature conditions at TDC. Combustion control can be done by adjusting operational parameters as inlet air temperature, fuel amount and EGR rate [3,4]. Normally, cycle to cycle variations in terms of IMEP (*Indicated Mean Effective Pressure*) are very low [5,6] in HCCI combustion but, with late combustion timing, cycle to cycle variations increase and the combustion becomes unstable. By using an additional heat source in form of a spark, either electrical or by a laser-induced plasma, advancement of the auto-ignition timing can be achieved [7]. The major advantages of HCCI mode compared to diesel engine operation are low NO_x emissions and, depending on the fuel, virtually no soot [8]. The benefit of HCCI compared to SI (*Spark Ignition*) combustion is the much higher part load efficiency [9]. The toughest challenge is controlling the ignition timing over a wide load and speed range [10,11]. Another challenge is to obtain an acceptable power density. The power density is limited by combustion noise and high peak pressures. At low loads, the rather high emissions of unburned hydrocarbons and carbon monoxide, in combination with low exhaust temperatures, present an additional challenge [12]. By applying unthrottled HCCI combustion at part load in SI engines, efficiency can be improved by 40-100%. Emerging technologies for variable valve timing, with the intent of using these as a means of controlling the combustion timing in HCCI engines [13],

may well lead the way for the first application of the HCCI combustion mode in practice.

In this work, HCCI combustion was either combined with a well-timed laser-induced plasma generated by a short laser pulse (5 ns) or a conventional spark plug ignition inside a combustion chamber of a six cylinder internal combustion engine. To overcome the difficulties of controlling the ignition timing an attempt was made to trigger HCCI combustion by spark plug or laser-induced ignition and observe this process by different optical diagnostic methods. PLIF, Schlieren photography and chemiluminescence imaging were applied. This work is a continuation of the work of Kopecek et al. [7] where the concept of a "laser triggered HCCI combustion" was proven. In the experiments presented the transition of spark ignition to auto-ignition should be analyzed.

A 10 mm NGK CR7E motorcycle spark plug and a Q-switched Nd:YAG solid-state laser have been used as alternative ignition sources. The focused short laser pulse leads to non-resonant breakdown [14] in the focal area followed by the formation of a hot dense plasma starting the combustion process. Such laser-induced plasmas are capable to ignite combustible mixtures like reported first by ref. [15]. Laser ignition offers several advantages in comparison to conventional spark plug ignition, like the ability to ignite leaner mixtures, arbitrary positioning of the ignition location and the potential of reduced service demand when applying monolithic, diode-pumped solid-state lasers. Highly developed spark plugs for stationary gas engines have a lifetime between 2,000 - 4,000 h in comparison to a laser ignition system with lifetimes of about 10,000 h. Further on, the ignition delay and overall combustion time are shorter and multi-point ignition can be applied more easily to enhance the combustion properties of ultra-lean mixtures [16,17].

The first experiments concerning a laser-ignited internal combustion engine were done by [18], demonstrating successful operation at leaner mixtures than being possible using conventional spark plugs. Furthermore, a natural gas engine was successfully operated in SI mode by a Q-switched laser running for a first test period of 100 hours without any interruption due to window fouling or other disturbances [19]. Also laser ignition and its advantages with respect to the potential future fuel hydrogen have been already investigated by [20]. A modified conventional gasoline engine was run by [24] on a daily basis including cold starts for over 200 hours. In recent experiments a 6 mm diameter entrance window and a much smaller and simplified laser system like the one described in this work was used. Preliminary results show reasonable reliability and motivate further investigation and development of laser ignition systems.

EXPERIMENTAL SETUP

ENGINE

The engine used for the tests was an inline six-cylinder Scania D12 diesel engine, converted to HCCI operation

by using port fuel injection. The engine worked in single cylinder operation and optical access was enabled by a quartz liner and a quartz piston crown. The combustion chamber was of a disc shaped design and the compression ratio was chosen to be 11.2:1 for optimal optical access. A water cooled Kistler pressure transducer, placed 50 mm from the centre of the bore axis, was used for in-cylinder pressure capture. A photo of the engine can be seen in Fig. 1 and some vital engine specifications of the Scania D12 are shown in Table 1.
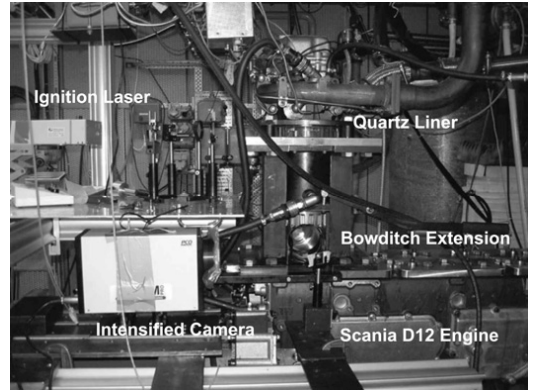

Figure 1: The modified Scania D12, the engine used for all the experiments conducted.

Displaced volume	1966 cc
Stroke	154 mm
Bore	127.5 mm
Connecting rod	255 mm
Compression ratio	11.2:1
Exhaust valve open	34° BBDC @ 0.15 mm lift
Exhaust valve close	6° BTDC @ 0.15 mm lift
Inlet valve open	2° BTDC @ 0.15 mm lift
Inlet valve close	31° BBDC @ 0.15 mm lift
Valve lift exhaust	14.1 mm
Valve lift inlet	14.1mm

Table 1: Technical specifications of the Scania D12 engine.

The inlet air was preheated by an electrical heater to initiate HCCI combustion with the selected compression ratio and fuel type. The experiments on the engine were conducted under the operating conditions shown in

Table 2. An air/fuel ratio of λ = 2.9 seemed to be the lean limit for successful combustion timing advancement using either spark formation method. The rich limit was limited by too rapid combustion and high in-cylinder pressures. The engine load for λ = 2.8 was 2.8 bar and for λ = 3.1 2.4 bar (IMEP). Due to high heat transfer to metal and glass parts at high load, adjustments of the inlet air temperature in the range of 2 °C had to be made in order to keep the combustion phasing constant.

Engine speed	1200 rpm
Lambda (λ)	2.7 - 3.2
Inlet air temperature	175 - 200°C
Inlet air pressure	1 bar absolute
Fuel	80% Iso-octane and 20% n-heptane

Table 2: Operational parameters of the engine.

IGNITION LASER

A Q-switched, flashlamp pumped Nd:YAG solid-state laser was employed to generate a plasma inside the combustion chamber of the engine for each cycle. Details and pulse energy can be found in Table 3. The laser pulse could be released at arbitrary crank angle positions and any rotation speeds by applying a special trigger interface. However, normally the speed was kept constant at 1200 rpm during the whole measurement requiring a constant pulse repetition rate of 10 Hz. A three-lens system (Extension-(1), collimating-(3), focusing-lens (4)) focused the beam through a quartz liner into the center of the cylinder, about 1 mm below the cylinder head (see Fig. 2). An additional cylindrical lens (2) had to be employed to compensate the effect of the quartz liner. A schematic drawing of the experimental setup with the ignition laser can be seen in Fig. 3.

Type	Nd:YAG
Wavelength	1064 nm
Pulse duration	5 ns
Pump source	Flashlamp
Pulse energy applied	25 mJ

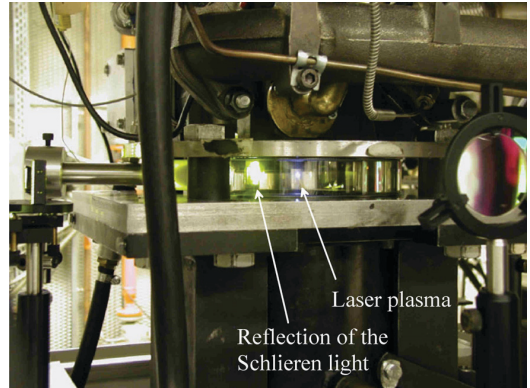Table 3: Specifications of the laser employed

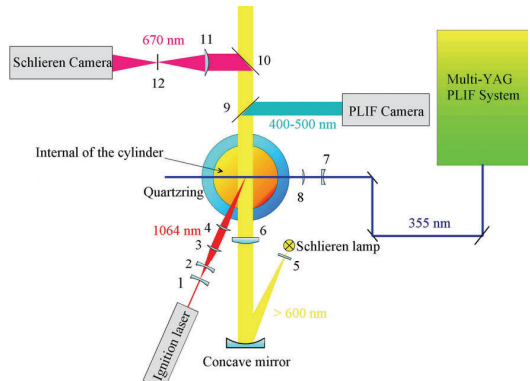Figure 2: Blue laser plasma in the center of the figure with yellow Schlieren light

Figure 3: Experimental setup I; Schlieren / PLIF (vertical laser sheet): 1-Extension lens, 2-Cylinder lens(Ignition laser), 3-Collimating lens, 4-Focusing lens(f=100mm), 5-Filter (long pass cutoff 600nm), 6-Cylinder lens (Schlieren), 7-Cylinder lens (PLIF), 8-Focusing lens (PLIF), 9-Beamsplitter (reflecting 400-500nm), 10-Beamsplitter (reflecting 670nm), 11-Focusing lens (Schlieren), 12-Schlieren aperture (Knife-edge)

SCHLIEREN IMAGING

Schlieren photography was conducted in the plane of the focal spot of the igniting laser or the spark plug. As the index of refraction in gases is strongly dependent on density, areas with gradients of temperatures or pressures have considerable effect on the propagation of light. As a consequence, the refraction angle is proportional to the first derivative of these parameters. The experimental setup I is depicted in Fig. 3. Collimated light from a high pressure Mercury discharge lamp was directed through the combustion chamber. The focusing lens (11) has two functions: i) it focuses the unscattered part of the incoming parallel light and ii) it images a real and inverted picture of the scattered light on the CCD chip of an intensified camera. Now the parallel part of the beam is cut out by placing an aperture (12) in the focal region in a way that it covers

the focused light but enables the scattered part to pass around the focal area. Hence, regions with high temperature or pressure refract the parallel light and it can pass the aperture. To compensate the negative cylindrical lens effect of the quartz liner providing optical access to the engine, a compensating positive cylindrical lens (6) was inserted in the beam path before the cylinder. The difficulties due to engine motion, restricted optical access and distortion resulted in a somewhat reduced image size and quality, but nevertheless the effect of laser ignition on the onset of combustion could be clearly observed.

CHEMILUMINESCENCE IMAGING

Chemiluminescence imaging was performed by viewing through the quartz of the piston crown and a 45° mirror using the Bowditch extension scheme (see Fig. 1). A schematic drawing of the experimental setup II can be found in Fig. 4. The imaging system consisted of an intensified camera system equipped with UV optics and a dielectric coated beamsplitter (13), reflecting chemiluminescence emission around 308 nm while allowing passage for the fluorescence light of formaldehyde lying in the spectral range 400 nm and longer. The chemiluminescence images were recorded with an exposure time of 100 µs (0.72 CAD (*C*rank *A*ngle *D*egree)) unless otherwise stated. Spectral investigation of the emitted radiation revealed a distinct signature around 308 nm originating in the A-X emission band of OH and a broad underlying unstructured spectrum which can be attributed to carbon monoxide. Therefore, the images reveal not the exact location of the flame front but give a good overview of the occurence and development of flame kernels in the HCCI combustion process.
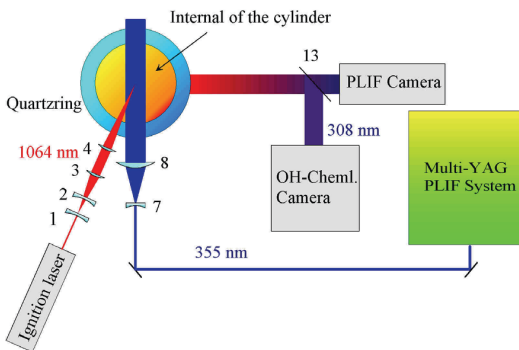

Figure 4: Experimental setup II; Chemiluminescence / PLIF (horizontal laser sheet): 1-Extension lens, 2-Cylinder lens (Ignition laser), 3-Collimating lens, 4-Focussing lens (f=100mm), 7-Cylinder lens (PLIF), 8-Focussing lens (PLIF), 13-Beam splitter (reflecting 308nm)

PLIF IMAGING

In order to capture the rapid combustion features in HCCI combustion, a high-speed imaging system was used. The formaldehyde LIF measurements were performed using a multi-YAG laser system. It consists of a cluster of four individual Q-switched Nd:YAG lasers with a fundamental wavelength of 1064 nm. The laser beams are frequency-doubled to 532 nm, combined with the neighboring beams by means of dichroic mirrors, and effectively frequency-tripled to yield a wavelength of 355 nm by sum frequency generation of the fundamental and the second harmonic. Eventually the four beams are aligned into a single optical output to be used in the experiments. By opening the Q-switch twice during one flashlamp discharge each laser can produce a double pulse, allowing a total of eight laser pulses to be fired in a rapid sequence. When operating in this fashion, the time separation between two consecutive pulses can be set to values as short as 6.25 µs. This short time-separation enables cycle-resolved LIF measurements, and provides sufficient temporal resolution for resolving the characteristic time scales in the turbulent environment of the HCCI engine.

In order to detect the LIF signal from the rapid laser pulses, a high-speed framing camera was used. In front of the optical input of the camera an f = 100 mm camera lens was mounted. Behind the optical input an eight-facet pyramid beam splitter directs the light onto eight individual intensified CCD modules. Each CCD module employs a 576 times, 384 pixel array with an 8 bit dynamic range, and an MCP (*M*icro *C*hannel *P*late) for exposure gating and signal intensification. The gating of each MCP is individually programmable and was synchronized with the laser pulses. In order to increase the overall sensitivity of the detection system an additional image intensifier was placed between the camera lens and the eight-facet prism. By using this intensifier unit, the minimum time separation between two consecutive images can be increased to 1 µs. However, this is not a limitation in the present application. For a detailed description of the laser/detector system, the reader is referred to [21-23].

For the formaldehyde LIF visualization the laser beam from the multi-YAG cluster was formed into a laser sheet by a combination of cylindrical (7) and spherical lenses (8) and directed into the combustion chamber of the HCCI engine via the quartz liner. To gain more thorough spatial information of the formaldehyde distribution, two different measurements were performed. The first setup (experimental setup I) included a laser sheet perpendicular to the cross section of the engine cylinder (see Fig. 3). In this case the fluorescence was imaged at a right angle through the quartz liner onto the framing camera. The second setup (experimental setup II) used a laser sheet in the cross sectional plane of the cylinder, and the fluorescence signal was imaged through the quartz piston via a UV enhanced 45° mirror in the piston extension onto the high-speed camera (see Fig. 4). In all LIF measurements performed, the time separation

between two consecutive images was set to 70 µs corresponding to 0.5 CAD of the engine. In front of the camera lens a long-pass filter with a cut-off wavelength of 385 nm was mounted, eliminating scattered laser light at 355 nm and transmitting the formaldehyde fluorescence. Since a small fraction of laser radiation at 532 nm from the frequency doubling process may still remain in the laser beam, an additional short-pass filter with a cut-off wavelength at 500 nm was used.

In the picture series the bright areas correspond to formaldehyde which is produced during the cool flame stadium prior to full compression some 20 CAD BTDC (*B*efore *T*op *D*ead *C*entre). The dark areas are depicting a consumption of formaldehyde which can be described as the burned regions in the mixture.

RESULTS AND DISCUSSION

The stabilizing effect of laser ignition has previously been reported by Kopecek et al. [7] using methane as fuel for HCCI combustion. The aim of this work was to get an insight into the mechanism of different supporting ignition sources on the onset and development of the combustion process by using a fuel which is more closely related to automotive applications. As n-heptane yields a good signal for formaldehyde PLIF diagnostics, a mixture of 80 % isooctane and 20 % n-heptane was chosen. The authors also tried a 50/50 % mixture yielding, however, no effect in combination with any ignition source (laser, spark plug) because of the too low octane number.

In unsupported HCCI, the mixture ignites at several spots throughout the compressed volume. Ignition timing and location are determined by the temperature and pressure history and the degree of inhomogeneity of the mixture. The concept of flame front propagation seems to loose its validity, leading to the term "controlled knock" for HCCI. Therefore, the idea of supporting HCCI ignition by additional spark plug or laser plasma ignition is not as straightforward as it seems.

UNSUPPORTED HCCI

A sequence of pictures recorded by PLIF imaging with vertical laser sheet (experimental setup I) during one particular cycle can be seen in Fig. 5. The pictures reveal the multipoint flame development structure during a combustion sequence. In all picture sequences of unsupported HCCI the formaldehyde consumption, which can be taken as a marker of the starting combustion, begins near the cylinder walls (left and right side of the pictures) like it can be observed in Fig. 5.
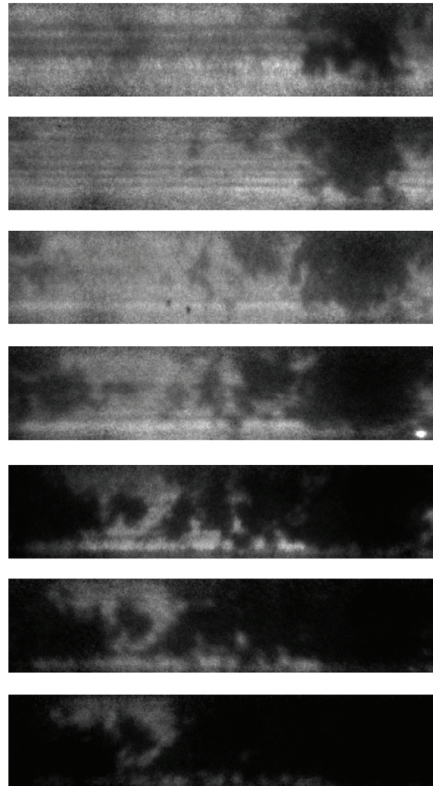

Figure 5: PLIF picture sequence; unsupported HCCI; vertical laser sheet (experimental setup I); λ = 2.8; first picture at 11.4° CA ATDC (After Top Dead Center); interval 0.5° CA; image size: 1.2 x 5.4 cm
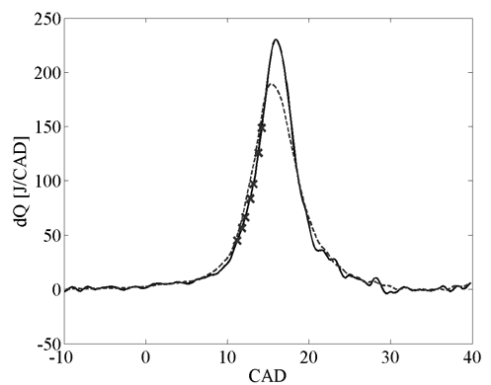

Figure 6: Heat release; unsupported HCCI; λ = 2.8; solid line corresponds to the PLIF picture series in Fig. 5; dots indicate the CAD when the PLIF pictures are taken; dashed line: average of 100 cycles, 50 taken before and 50 after the heat release indicated by the solid line

Fig. 6 shows the corresponding heat release (solid line) to the PLIF picture sequence in Fig. 5 measured during one cycle. The dots on the solid line indicate the CAD when the PLIF pictures were taken. The dashed line shows the average heat release of 100 cycles; 50 cycles before the heat release for the PLIF pictures (solid line) was taken and 50 cycles after. The COV IMEPnet was 0.21 bar and the COV in terms of CA50 was 3.20 CAD thus the cycle to cycle variations were large. As a result of this no clear difference in combustion characteristics (combustion timing, maximum pressure,…) could be observed between unsupported-, laser assisted- and spark plug-assisted HCCI combustion mode.

The resulting density and temperature gradients throughout the volume cause the even more grainy structure in the Schlieren image presented in Fig. 7. The used Schlieren camera was only able to take one picture per cycle. So the images were recorded one by one for every cycle, shifting the timing with a minimum interval of 0.5 CAD between the consecutive images. The images of the Schlieren setup cover a region of approximately 2 x 2 cm including the location of the spark plug and the laser plasma, respectively.
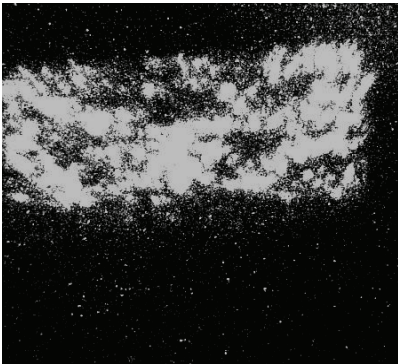

Figure 7: Schlieren picture; unsupported HCCI; (experimental setup I); λ = 2.8; image size: 2 x 2 cm; at 13° CA ATDC

Fig. 8 shows a PLIF picture sequence viewed through the quartz piston crown via the 45° mirror, like depicted in the experimental setup II in Fig. 4 applying a horizontal PLIF laser sheet. Hence these pictures are perpendicular to the ones in Fig. 5. Again, it can be seen that the combustion (formaldehyde consumption, dark regions) starts near the cylinder walls and proceeds through the unburned mixture.
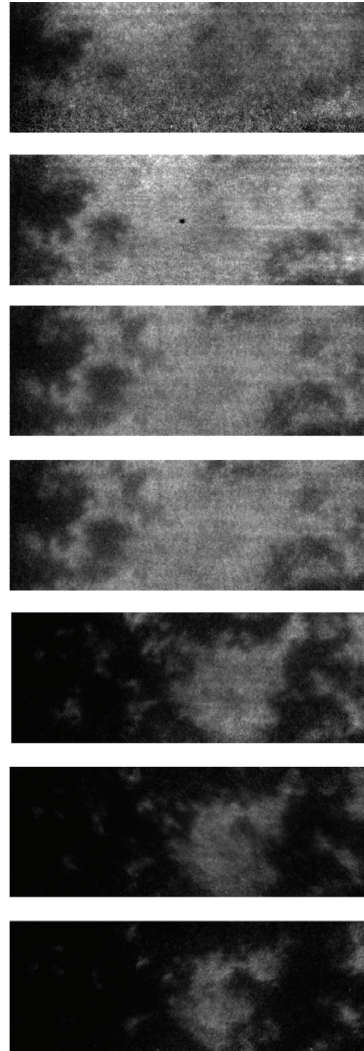

Figure 8: PLIF picture sequence; unsupported HCCI; horizontal laser sheet (experimental setup II; λ = 2.8; first picture at 11.4° CA ATDC; interval 0.5° CA; image size: 3.5 x 9 cm

Through the beamsplitter (13 in Fig. 4) it was possible to take chemiluminescence pictures at the same time like the PLIF pictures were taken as shown e.g. in Fig. 8. In Fig. 9, the whole combustion area can be seen from the bottom via the 45° mirror. The pictures are yielding just averaged intensity information over the line of sight (i.e. the vertical axis of the cylinder). The combustion starts at some points mostly close to the wall like in the PLIF pictures (Fig. 8), but the exact locations show erratic behavior from cycle to cycle. Consecutively, flame development starts at more and more points until the whole mixture is consumed. Both, the arbitrary locations

of ignition and the fast heat release typical for HCCI are clearly visible in these sequences.
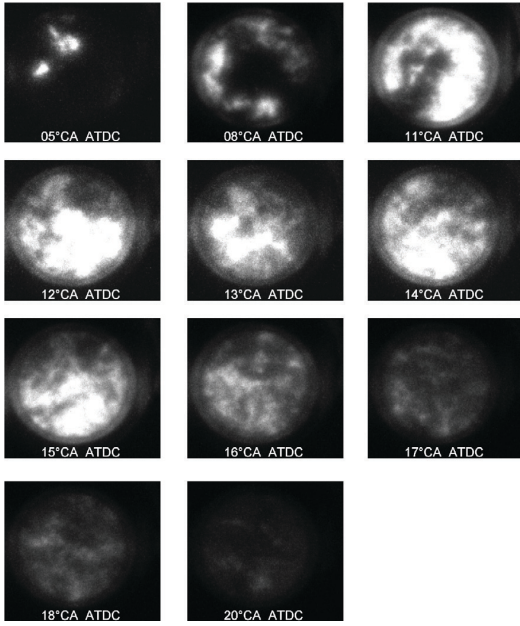

Figure 9: Chemiluminescence pictures (308 nm); unsupported HCCI; (experimental setup II); image size: 14 x 14 cm; λ = 2.8

LASER-ASSISTED HCCI

The second part of the experiments involved HCCI combustion for which starting was attempted by a laser-induced plasma at 25° CA BTDC. Earlier ignition timing was also tested, but no effect could bee seen in the images. The laser pulse energy was about 25 mJ and the pulse length was 5 ns. The air/fuel equivalence ratio λ had the value 2.8. With leaner mixtures than λ = 2.8 no effect of the laser or spark plug ignition could be seen.

Fig. 10 depicts a PLIF picture sequence with a vertical laser sheet (experimental setup I). In contrast to the unsupported HCCI case in Fig. 5, a clear "flame front" structure can be seen, which can be attributed to be caused by the ignition plasma. This effect of the laser plasma on the onset of combustion was not as pronounced at all cycles. The PLIF pictures showed all degrees of influence of additional ignition from strong flame front propagation to no effect at all. This erratic behavior is a result of a high COV (*Coefficient of Variation*) value like mentioned above and obscured the effect of laser ignition in the rate of heat release curves. Two reasons might contribute to these somewhat faint results: The ignition timing of the laser was too early, a fact determined by the limits of optical access. This problem could be overcome by using a laser entrance window in the cylinder head which was not available at

that time. And the second feature unfavorable for pronounced supported ignition is the low octane number of the fuel used in these experiments. More appropriate fuels would be pure isooctane or gasoline for these test conditions. On the other hand these fuels would be a bad choice for the PLIF experiments due to the absence of formaldehyde.
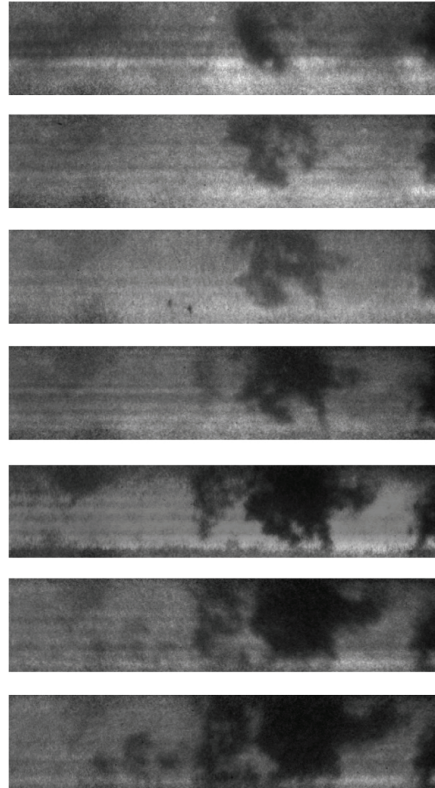

Figure 10: PLIF picture sequence; laser-assisted HCCI; vertical laser sheet (experimental setup I); λ = 2.8; first picture at 11.4° CA ATDC; interval 0.5° CA; ignition time: -25° CA BTDC; image size: 1.2 x 5.4 cm

The corresponding heat release (solid line) to the above depicted PLIF picture sequence can be found in Fig. 11. Like in Fig. 6, the dots on the solid heat release indicate the CAD when the PLIF pictures were taken. The dashed line shows the average heat release of 100 cycles; 50 cycles before the heat release for the PLIF pictures (solid line) was taken and 50 cycles after. The COV IMEPnet was 0.05 bar and the COV in terms of CA50 was 1.66 CAD.
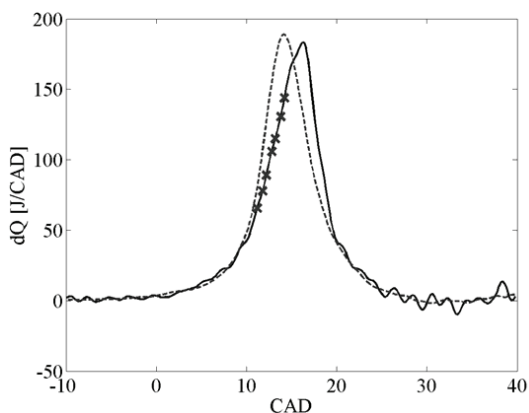
Figure 11: Heat release; laser-assisted HCCI; λ = 2.8; ignition time: -25° CA BTDC; solid line corresponds to the PLIF picture series in Fig. 5; dots indicate the CAD when the PLIF pictures are taken; dashed line: average of 100 cycles, 50 taken before and 50 after the heat release indicated by the solid line

The PLIF picture sequence in Fig. 12 taken through the quartz bottom piston via the 45° mirror shows again like the PLIF pictures in Fig. 10 an expanding "flame front" structure. In addition to that, also "normal" HCCI combustion starts from the left cylinder wall.
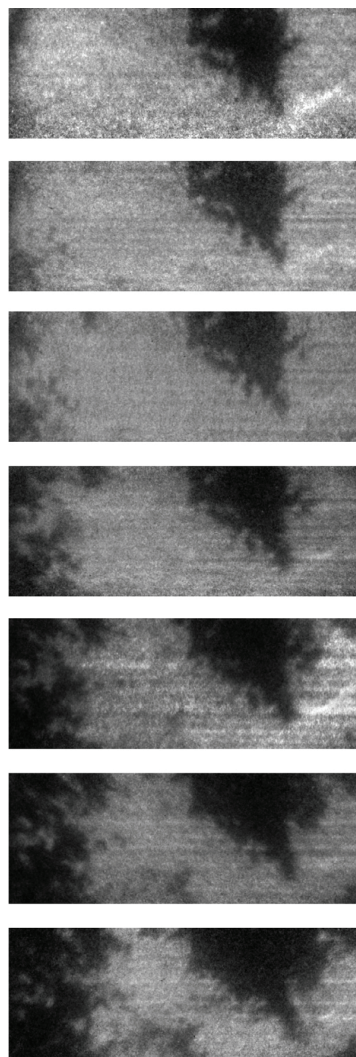

Figure 12: PLIF picture sequence; laser-assisted HCCI; horizontal laser sheet (experimental setup II); λ = 2.8; first picture at 11.4° CAD ATDC; interval 0.5° CA; ignition time: -25° CA BTDC; image size: 3.5 x 9 cm

In the chemiluminescence pictures in Fig. 13 viewed through the quartz piston, also some kind of flame front can be observed. In comparison to the unsupported HCCI combustion case in Fig. 9 where the combustion starts mainly near the cylinder walls, in these images an intensity peak can be observed in the middle of the cylinder. But it has to be pointed out that these pictures are taken from different cycles because the used intensified camera was only able to take one picture in a cycle.
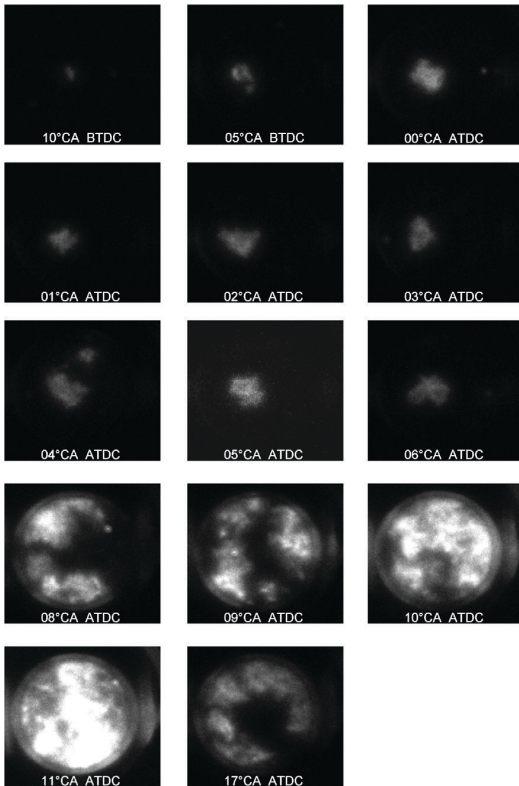
Figure 13: Chemiluminescence pictures (308 nm); laser-assisted HCCI; (experimental setup II); image size: 14 x 14 cm; λ = 2.8; ignition time: -25° CA BTDC

Fig. 14 shows Schlieren pictures through the quartz liner (experimental setup I). Again, it has to be taken into account that just one picture per cycle could be taken. One can see the growing combustion volume when the piston is going down from 0 to 20 CAD ATDC. But also in the Schlieren pictures it can be observed that the combustion is starting mainly from the middle of the combustion chamber in comparison to unsupported HCCI were the combustion starts mostly near the cylinder walls.
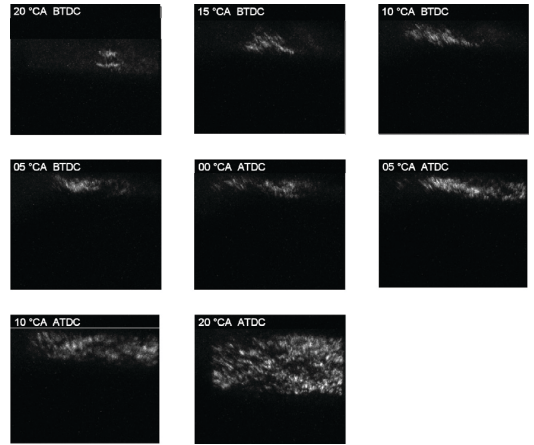

Figure 14: Schlieren pictures; laser-assisted HCCI; (experimental setup I); image size: 2 x 2 cm; λ = 2.8; ignition time: -25° CA BTDC

Cycle to cycle variations between corresponding images recorded at the same CAD were quite large. However, PLIF image sequences recorded during one cycle suggest that a Schlieren series would show similar flame front like behavior but requires an additional expensive multiexposure camera system, if one wants to compare both methods. The Schlieren images were considered illustrative and informative as well, but including all corresponding images from unsupported and spark plug assisted HCCI was omitted for brevity.

SPARK PLUG-ASSISTED HCCI

Beside laser-assisted HCCI also spark plug-assisted HCCI was investigated. The spark plug was positioned in the center of the cylinder head. The ignition timing was the same as for the laser-assisted case (25° CA BTDC) and the same air/fuel equivalence ratio of 2.8 was used. Like in the laser-assisted case, no effects of the spark in the images could be found if an earlier ignition time was chosen.

Again something like an "expanding flame front structure" can be seen in the PLIF picture sequence with the vertical laser sheet (experimental setup I) in Fig. 15. No big difference to the laser-assisted HCCI combustion case in Fig. 10 could be observed. But again as a result of a big COV-value sometimes nearly no effect of the spark could be observed and sometimes it was possible. The same behavior for the spark plug-assisted HCCI can be found in the chemiluminescence pictures in Fig. 16.
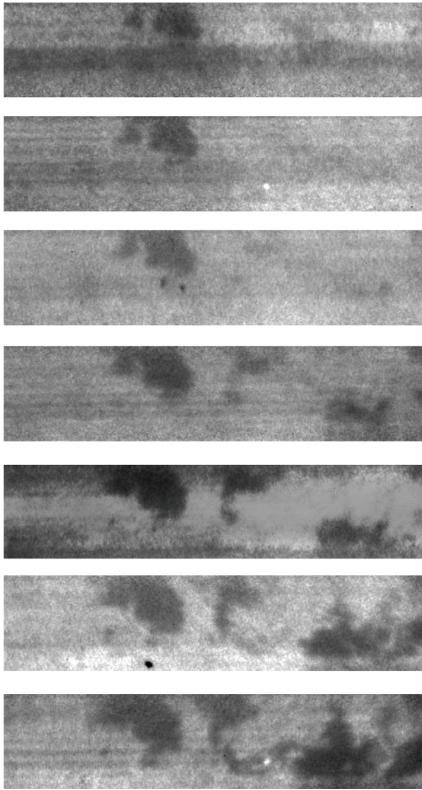
Figure 15: PLIF picture sequence; spark plug-assisted HCCI; vertical laser sheet (experimental setup I); λ = 2.8; first picture at 11.4° CA ATDC; interval 0.5° CA; ignition time: -25° CA BTDC; image size: 1.2 x 5.4 cm

Finally the heat release of the spark plug-assisted HCCI combustion is depicted in Fig. 17. Again, like in the other cases large cycle to cycle variations were present. The COV IMEPnet was 0.27 bar and the COV in terms of CA50 was 3.01 CAD. Hence, the conclusion of the heat release datas is that the COV was too big so no clear difference in the combustion characteristics of the three different combustion modes can be extracted.
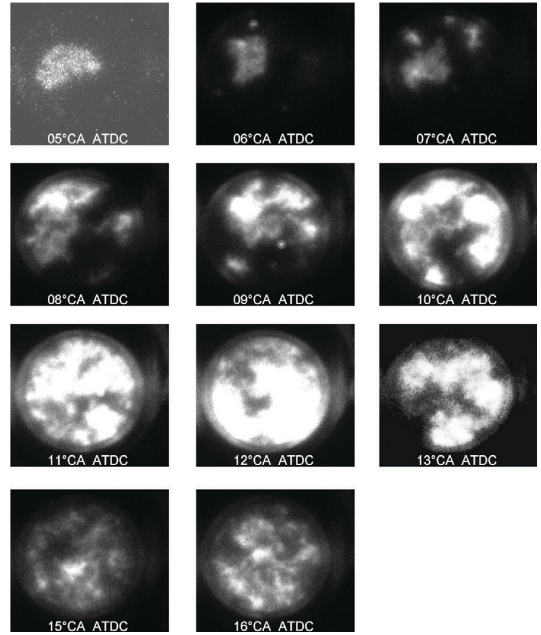

Figure 16: Chemiluminescence pictures (308 nm); spark plug-assisted HCCI; (experimental setup II); image size: 14 x 14 cm; λ = 2.8; time: -25° CA BTDC
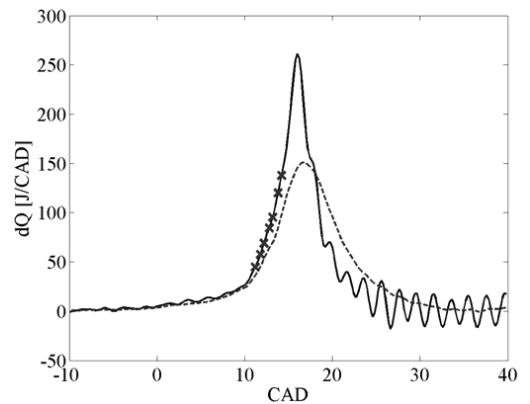

Figure 17: Heat release; spark plug-assisted HCCI; λ = 2.8; ignition time: -25° CA BTDC; solid line corresponds to the PLIF picture series in Fig. 5; dots indicate the CAD when the PLIF pictures are taken; dashed line: average of 100 cycles, 50 taken before and 50 after the heat release indicated by the solid line

CONCLUSION

The effect of spark plug and laser plasma ignition on the ignition timing of a research engine running in HCCI mode was investigated. The fuel used in these experiments consisted of a mixture of 80 % isooctane and 20 % n-heptane. The engine allowed comprehensive optical diagnostics by different laser spectroscopic, optical and imaging techniques in addition to the standard monitoring devices like pressure transducers and exhaust gas analysis. Unlike in the case of methane, where the effect of laser ignition on the HCCI process was evident in the pressure and heat release curves [7], the influence of additional ignition sources on a mixture with easier autoignition properties like n-heptane is more subtle. The heat release curves show no significant effect on the overall performance of the engine whether unsupported HCCI or spark/laser-assisted mode were investigated because the cycle-to-cycle have been too large. But the optical diagnostics reveal that, beginning at the ignition point, a flame structure develops and propagates in the first CAD in a way similar to conventional SI engines. This indicates that when using other fuels than n-heptane being less prone to autoignition like isooctane or gasoline, the effect of laser or spark plug ignition on the combustion rate or ignition timing can be expected to be more pronounced like in the case of methane. Another explanation to the weak effect of either method of support could be that the HCCI combustion starts at the walls in this particular engine [1] and thus the ignition source that would heat up the charge and advance the auto-ignition timing should be placed closer to the cylinder wall. The obvious difference in the flame development between unsupported and laser or spark plug supported HCCI having been observed by different imaging techniques emphasize the value of additional diagnostic techniques together with standard engine diagnostics.

ACKNOWLEDGMENTS

REFERENCES

1. A. Hultqvist, M. Christensen, B. Johansson, A. Franke, M. Richter, M. Aldén: "A Study of the Homogeneous Charge Compression Ignition Combustion Process by Chemiluminescence Imaging", SAE1999-01-3680
2. M. Christensen, B. Johansson: "Influence of Mixture Quality on Homogeneous Charge Compression Ignition", SAE9824541
3. T. Aoyama, Y. Hattori, J. Mizuta, Y. Sato: "AnExperimental Study on a Premixed-Charge Compression Ignition Gasoline Engine, SAE960081
4. J-O. Olsson, O. Erlandsson, B. Johansson: "Experiments and Simulation of a Six-Cylinder Homogeneous Charge Compression Ignition (HCCI) Engine", SAE2000-01-2867
5. S. Onishi, S. Hong Jo, K. Shoda, P. Do Jo, S. Kato: "Active Thermo-Atmosphere Combustion (ATAC) – A New Combustion Process for Internal Combustion Engines", SAE790501
6. R.H. Thring: "Homogeneous-Charge Compression-Ignition (HCCI) Engines", SAE892068
7. H. Kopecek, E. Wintner, M. Lackner, F. Winter, A. Hultqvist: "Laser-stimulated Ignition in a Homogeneous Charge Compression Ignition Engine", SAE2004-01-0937
8. M. Christensen, A. Hultqvist, B. Johansson: "Demonstrating the Multi Fuel Capability of a Homogeneous Charge Compression Ignition Engine with Variable Compression Ratio",SAE1999-01-3679
9. M. Christensen, P. Einewall, B. Johansson: "Homogeneous Charge Compression Ignition (HCCI) Using Iso-octane, Ethanol and Natural Gas- A Comparison to Spark Ignition Operation", SAE972874
10. J-O. Olsson, P. Tunestal, B. Johansson: " Closed-Loop Control of an HCCI Engine", SAE2001-01-1031
11. J-O. Olsson, P. Tunestal, G. Haraldsson, B. Johansson: "A Turbo Charged Dual Fuel HCCI Engine", SAE2001-01-1896
12. O. Erlandsson, B. Johansson, F. A. Silversand: "Hydrocarbon (HC) Reduction of Exhaust Gases from a Homogeneous Charge Compression Ignition (HCCI) Engine Using Different Catalytic Mesh-Coatings", SAE2000-01-1847
13. D. Law, J. Allen, D. Kemp, G. Kirkpatrick, T. Copland: "Controlled Combustion in an IC-Engine with a Fully Variable Valve Train", SAE 2001 World Congress, March 2001, Detroit, MI, USA
14. P.D. Ronney: "Laser versus conventional ignition of flames", Opt. Eng. **33** (2), 510-521, 1994.
15. F.J. Weinberg, J.R. Wilson: "A Preliminary Investigation of the Use of Focused Laser Beams for Minimum Ignition Energy Studies", Proc. Roy. Soc. London, A **321**, 41-52, 1971.
16. H. Kopecek, H. Maier, G. Reiser, F. Winter, E. Wintner: „Laser Ignition of Methane-Air mixtures at High Pressures", Experimental Thermal and Fluid Science **27**, 499-503, 2003.
17. M. Weinrotter, H. Kopecek, M. Tesch, M. Lackner, F. Winter, E. Wintner: "Laser ignition of ultra-lean methane-hydrogen-air and hydrogen-air mixtures under engine-like conditions", Experimental and Thermal fluid science, article in press.
18. J.D. Dale, P.R. Smy, R.M. Clements: "Laser Ignited Internal Combustion Engine – An Experimental Study", SAE-780329, Detroit, 1978.
19. H. Kopecek, S. Charareh, M. Lackner, C. Forsich, F. Winter, J. Klausner, G. Herdin, E. Wintner: „Laser Ignition of Methane-Air Mixtures at High Pressures

and Diagnostics", ASME, ICES2003-614, Austria, 2003.

20. M. Weinrotter, H. Kopecek, M. Lackner, F. Winter, E. Wintner: "Application of Laser Ignition to Hydrogen-Air Mixtures at High Pressures", International Journal of Hydrogen Energy, article in press.

21. C.F. Kaminski, J. Hult, M. Aldén, Appl Phys B **68**, 757-760, 1999.

22. C.F. Kaminski, J. Hult, M. Aldén, S. Lindenmaier, A. Dreizler, U. Maas, M. Baum, In Twenty-Eight Symposium (International) on Combustion, The Combustion Institute, Pittsburgh, 399-405, 2000.

23. J. Hult, M. Richter, J. Nygren, M. Aldén, A. Hultqvist, M. Christensen, B. Johansson, Appl. Optics B 41, 5002-5014, 2002.

24. J. Graf, M. Weinrotter, H. Kopecek, E. Wintner, Laser Ignition, Optics and Contamination of Optics in an I.C. Engine. ASME Internal Combustion Engine Division, Fall Technical Conference, ICEF2004-833, USA, 2004.

CONTACT

Martin Weinrotter, Vienna University of Technology, Photonics Institute, Gusshausstrasse 27, 1040 Wien, Austria, email: martin.weinrotter@tuwien.ac.at

DEFINITIONS, ACRONYMS, ABBREVIATIONS

HCCI	Homogeneous Charged Compression Ignition
Nd:YAG	Neodymium Yttrium Aluminum Garnet
PLIF	Planar Laser-Induced Fluorescence
TDC	Top Dead Center
EGR	Exhaust Gas Recirculation
IMEP	Indicated Mean Effective Pressure
NO$_x$	The sum of nitrogen oxides
SI	Spark Ignition
BBDC	Before Bottom Dead Center
ABTD	After Bottom Dead Center
BTDC	Before Top Dead Center
ATDC	After Top Dead Center
λ	Relative air-fuel ratio
CAD	Crank Angle Degree
MCP	Micro Channel Plate
COV	Coefficient of Variation